Development of a cavity-enhanced Fourier transform spectrometer based on optical frequency combs for laboratory astrophysics

Romain Dubroeucq

COLLEGE SCIENCES DE LA MATIERE
DOCTORAL DES MOLECULES
BRETAGNE ET MATERIAUX

Université de Rennes

THÈSE DE DOCTORAT DE

L'UNIVERSITÉ DE RENNES

ÉCOLE DOCTORALE N° 638
Sciences de la Matière, des Molécules et Matériaux
Spécialité : *Physique*

Par
Romain Dubroeucq

Development of a cavity-enhanced Fourier transform spectrometer based on optical frequency combs for laboratory astrophysics

Développement d'un spectromètre à transformée de Fourier en cavité par peigne de fréquences optiques pour l'astrophysique de laboratoire

Thèse présentée et soutenue à Rennes, le 12 décembre 2023
Unité de recherche : Institut de Physique de Rennes (IPR) UMR CNRS 6251

Rapporteurs avant soutenance :

Olivier PIRALI, Directeur de recherche, CNRS, Université Paris-Saclay
Marco MARANGONI, Professeur d'université, Politecnico di Milano

Composition du Jury :

Président :	Hugues GUILLET DE CHATELLUS, Directeur de recherche, CNRS, Université de Rennes
Examinatrice :	Hélène FLEURBAEY, Chargée de recherche, CNRS, Université Grenoble-Alpes
Dir. de thèse :	Lucile RUTKOWSKI, Chargée de recherche, CNRS, Université de Rennes
Co-dir. de thèse :	Robert GEORGES, Professeur d'université, Université de Rennes

Remerciements / Acknowledgements

Je voudrais remercier toutes les personnes ayant participé à mes travaux de thèse ces trois dernières années. Je tiens d'abord à remercier tous les membres du DPM à l'IPR, pour les discussions, les échanges et les rires que nous avons eus le midi, dans un couloir du labo ou en group meeting. Je tiens ensuite à remercier tous les ingénieurs et techniciens qui m'ont grandement aidés dans la conception et le développement des instruments, Jean-Charles Potier, Ewen Gallou, Olivier Moustier, Jonathan Thiévin et Jonathan Courbe. I also deeply thanks the people I met in Toruń, Piotr Masłowski for welcoming me in his lab and of course Dominik Charczun, for all the long hours in the lab, around a drink or a ramen. Je voudrais sincèrement remercier tous mes camarades non-permanents de l'IPR, Amélie, Myriam, Marion, Julien, Solène, Elliot, Julien, Alberto, Maxime, Yohann, Alexis, Adrien et ceux que j'oublie, sans qui ces trois années au labo, en conférences ou en ville n'auraient pas été les mêmes. Et je remercie tellement Robert Georges, mon directeur de thèse, pour ton soutien et tes constantes pertinence, motivation et bonne humeur. Enfin, je remercie indéfiniment Lucile Rutkowski, ma directrice de thèse, pour m'avoir tant appris et inlassablement soutenu et motivé durant toute cette thèse. Merci pour toutes les connaissances que tu m'as transmises et toutes les compétences que j'ai pu acquérir en travaillant avec toi. J'ai hâte d'avoir des nouvelles de la manip dans le futur ! Je voudrais aussi remercier toute les personnes extérieures à la recherche qui m'ont accompagnées pendant ce doctorat, à commencer par mes parents, ma soeur et ma grand-mère. Je veux aussi particulièrement remercier tous les amis qui rendent Rennes si facile et agréable à vivre : Yohann, Mathieu, Mathilda, Marion, Maël, Flore, Carole, Florine, Julia, Amalia, Antoine, Clément, Aurélia, Armand, Aymeric, Isabella et les autres. Petite place spéciale pour toi Yvan, pour ces plus de trois années de colocation merveilleuse avec toi. A toi aussi Buffy le chat, tu es un monstre mais je t'aime beaucoup. Et enfin, mille milliards de mercis à toi Laure-Anne, merci de ton soutien incroyable, tout est parfait depuis deux ans avec toi. Je ne peux achever ces remerciements sans bien évidemment citer les merveilleuses personnes qui travaillent ou ont travaillé à la cafétéria du Diapason, Amandine, Sylvie, Colas et les autres, pour vos merveilleuses quiches qui furent le carburant de cette thèse.

Table of Contents

Acronyms

AOM	Acousto-Optic Modulator.
AWG	Arbitrary Waveform Generator.
CEAS	Cavity-Enhanced Absorption Spectroscopy.
CFD	Computational Fluid Dynamics.
CRDS	Cavity Ring-Down Spectroscopy.
cw	Continuous-Wave laser.
DAQ	Acquisition board.
DBM	Double-Balanced Mixer.
DCS	Dual-Comb Spectroscopy.
DDG	Digital Delay Generator.
DDS	Direct Digital Synthesizer.
DFG	Difference Frequency Generation.
EOM	Electro-Optic Modulator.
FFT	Fast-Fourier Transform.
FID	Free-Induction Decay.
FSR	Free Spectral Range.
FTS	Fourier Transform Spectrometer.
FWHM	Full-Width at Half-Maximum.
HeNe	Helium-Neon laser.
HTP	Hartmann-Tran Profile.

NEA Noise equivalent absorption.
NEA^{1s} Noise equivalent absorption at 1s averaging time per spectral element.
NSD Noise Spectral Density.

OFC Optical Frequency Comb.
OPD Optical Path Difference.
OPO Optical Parametric Oscillator.

PDH Pound-Drever-Hall.
PI Proportional Integrator.
PZT PieZo-electric Transducer.

QCL Quantum Cascade Laser.
QF Quality Factor.

RMS Root-Mean Square.
RMSE Root-Mean Square Error.

SE Standard Error.
SHG Second-Harmonic Generation.
SI International System of Units.
SNR Signal-to-Noise Ratio.

VIPA Virtually-Imaged Phased Array.
VP Voigt Profile.

Résumé en français

L'invention du peigne de fréquences optiques (OFC) à la fin des années 1990 à partir de lasers femtosecondes à modes bloqués a révolutionné le domaine de la métrologie de précision temps-fréquence, en fournissant un moyen direct de relier les fréquences optiques et micro-ondes. Avant l'avènement de ces lasers, des chaînes de multiplication de fréquence massives, partant de la seconde du Système International d'unités (SI) définie par les horloges atomiques à micro-ondes ^{133}Cs, étaient nécessaires pour combler le fossé vers les fréquences optiques, en utilisant une série d'oscillateurs à verrouillage de phase (Hollberg *et al.*, 2005 ; Diddams *et al.*, 2020). Les peignes de fréquences ont remplacé ces systèmes encombrants et complexes par un seul laser femtoseconde à modes bloqués. Ces lasers peuvent synthétiser 10^5-10^6 modes optiques également espacés en fréquence, et avec une stabilité de 1 sur 10^{18}. Ils permettent une conversion directe de fréquences micro-ondes à optiques et d'optiques à micro-ondes, ainsi qu'une mesure précise de la fréquence. Cela a ouvert la voie à la comparaison des horloges atomiques, à la mesure de transitions optiques (Udem *et al.*, 1999a), aux différences de fréquences optiques entre des lasers (Udem *et al.*, 1999b, Reichert *et al.*, 1999 Diddams *et al.*, 2000a), de fréquences optiques (absolues) de lasers (Diddams *et al.*, 2000b) ainsi que la première horloge atomique entièrement optique (Diddams *et al.*, 2001) avec une stabilité à long terme meilleure que les horloges atomiques définissant les standards SI (Udem *et al.*, 2002). Dans les années qui ont suivi, plusieurs autres démonstrations ont eu lieu : la stabilisation complète d'un peigne de fréquence (Jones *et al.*, 2000), une horloge moléculaire optique (Ye *et al.*, 2001), le test de constantes fondamentales (Bize *et al.*, 2003) et la synthèse optique de précision d'un signal micro-onde (Diddams *et al.*, 2003). La moitié du prix Nobel de physique 2005 a été attribuée à Ted Hänsch et John Hall pour leur contribution à la métrologie des fréquences optiques et l'invention des peignes de fréquence optiques (Hall, 2006, Hänsch, 2006).

Les applications des peignes de fréquence se sont rapidement étendues au-delà de leur champ d'application initial, à savoir la métrologie de précision. Une liste non exhaustive

contient : l'étalonnage précis des spectrographes astronomiques (Murphy *et al.*, 2007), la génération d'impulsions XUV et attosecondes (Keller, 2003, Baltuška *et al.*, 2003), la spectroscopie moléculaire de précision (Sugiyama *et al.*, 2023) et la détection de gaz à l'état de traces (Alden *et al.*, 2017), la microscopie cohérente (Potma *et al.*, 2002) et la télémétrie précise (Minoshima & Matsumoto, 2000). En particulier, le développement de sources fiables émettant dans l'infrarouges moyen a permis d'atteindre une haute sensibilité de détection pour les applications de chimie physique (Weichman *et al.*, 2019).

La spectroscopie par peigne de fréquences offre la possibilité d'une large couverture spectrale, d'une résolution temporelle rapide et d'une grande sensibilité. Cela a permis la première détection simultanée et quantitative d'espèces clés impliquées dans les réactions chimiques, à savoir les réactifs, les espèces transitoires et les produits (Fleisher *et al.*, 2014 ; Hoghooghi *et al.*, 2023). Cette capacité a ouvert la voie à la mesure des taux de réaction et des rapports de branchement avec un biais minimal. Ces travaux ont été réalisés soit à température ambiante, soit à haute température, mais aucun n'a encore réussi à mesurer des taux de réaction précis aux températures pertinentes pour la chimie interstellaire. L'objectif de cette thèse est le développement d'un instrument capable de relever un tel défi. Cet instrument devrait être capable de détecter de multiples espèces, avec une résolution temporelle de l'ordre de la microseconde, sensible à des densités moléculaires aussi faibles que 10 molécules/cm^{103}.

L'idée générale de notre approche repose sur un spectromètre à transformée de Fourier à absorption renforcée par cavité optique fonctionnant dans l'infrarouge moyen et sondant un écoulement uniforme supersonique, comme illustré sur la figure 1. L'environnement froid est obtenu *via* l'expansion supersonique de l'échantillon, ce qui permet d'obtenir des températures effectives de quelques dizaines de kelvins, et sera finalement combiné avec une technique de photolyse par laser pulsé. Les écoulements supersoniques sont le coeur du Département de Physique Moléculaire de l'Institut de Physique de Rennes (IPR), historiquement pour la cinétique de réaction avec la technique CRESU (Cinétique de Réaction e Ecoulement Supersonique Uniforme). Ils ont été largement utilisés avec les techniques de fluorescence induite par laser, de spectrométrie de masse, de spectroscopie à micro-ondes et de spectroscopie à cavité optique dans l'infrarouge proche (Rowe & Canosa, 2022). La nouveauté de ce projet doctoral est l'ajout de la spectroscopie d'absorption par peigne de fréquences à la liste des techniques compatibles avec les environnements du CRESU. Le défi à relever était double : **1)** concevoir un spectromètre capable de résoudre la microseconde sans réduire la couverture spectrale et **2)** réaliser des mesures de spectroscopie

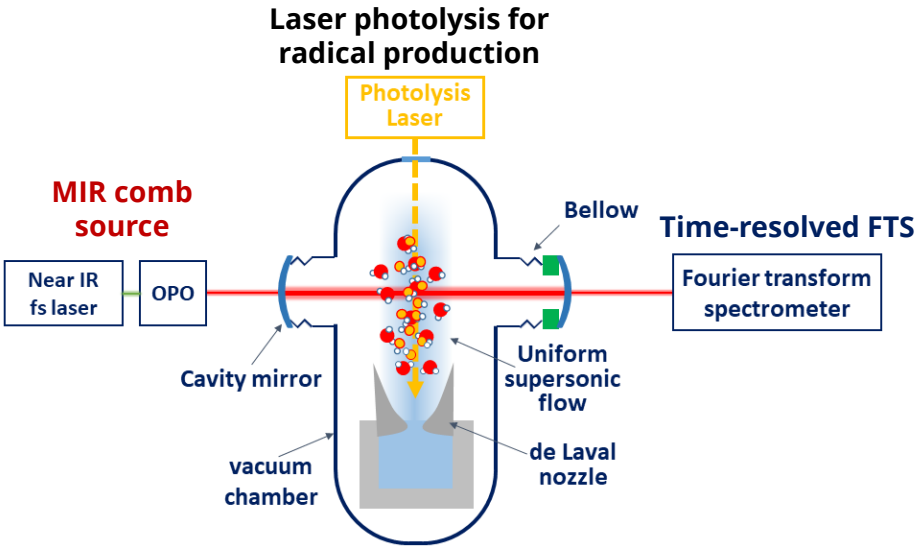

Figure 1 : Schéma de l'instrument en cours de développement à l'IPR. Un laser excimère est utilisé pour générer des radicaux par photolyse d'un gaz précurseur détendu dans un écoulement supersonique uniforme. L'échantillon moléculaire est sondé transversalement à la direction de l'écoulement par spectroscopie à cavité optique basée sur un peigne de fréquences dans l'infrarouge moyen. La transmission de la cavité est analysée à l'aide d'un spectromètre à transformée de Fourier résolu en temps.

de précision dans les conditions difficiles créées par les grands groupes de pompage nécessaires à la génération d'écoulements supersoniques. La première partie du défi nous a amenés à concevoir une nouvelle technique spectroscopique, la spectroscopie par temps de déclin de cavité par transformée de Fourier, reposant sur un spectromètre à transformée de Fourier (FTS) résolu en temps. Pour cette première étape de développement, nous sommes restés dans la gamme de télécommunications de l'infrarouge proche, où les dispositifs optoélectroniques sont facilement disponibles et comparativement moins chers que leurs homologues de l'infrarouge moyen.

Dans le premier chapitre, nous détaillerons les bases des peignes de fréquence optiques (OFC). Nous passerons rapidement en revue les différents types de sources de peignes de fréquences, et nous présenterons les actionneurs et les schémas de contrôle pour stabiliser un peigne de fréquences optiques. Dans une deuxième section, nous présenterons la source peigne de fréquences utilisée tout au long de cette thèse. La troisième section sera consacrée à l'examen des différents spectromètres existants pour la spectroscopie par peigne de fréquences. La quatrième section se concentrera sur la spectroscopie à transformée de Fourier et l'impact de sa fontion d'instrument (ILS) sur les spectres d'absorption,

ainsi que sur la méthode utilisée pour récupérer des spectres sans ILS avec une résolution des modes du peigne. Cette section se terminera par la présentation du spectromètre à transformée de Fourier à scan rapide utilisé tout au long de cette thèse.

Le deuxième chapitre portera sur la spectroscopie d'absorption dans l'infrarouge par cavité optique. La première section se concentrera sur la signature spectrale des molécules dans l'infrarouge, l'origine de la forme des raies d'absorption, les mécanismes d'élargissement de ces raies en fonction des conditions de température et de pression et les différents profils d'absorption nécessaires pour modéliser les spectres d'absorption moléculaires. La deuxième section sera consacrée aux cavités Fabry-Perot, détaillant leurs modes spatiaux et fréquentiels, leurs fonctions de transfert en transmission et en réflexion utilisées pour modéliser les spectres d'absorption obtenus avec une cavité optique, l'accord des modes spatiaux et fréquentiels nécessaire pour coupler un OFC à la cavité, la réponse transitoire de la cavité et son application à la spectroscopie par temps de déclin de cavité (CRDS). La dernière section de ce chapitre détaillera les schémas d'asservissement électroniques nécessaires pour effectuer des mesures spectroscopiques précises d'absorption renforcée par cavité optique à l'aide d'un peigne de fréquences.

Le troisième chapitre présentera la technique CRDS par transformée de Fourier (FT-CRDS). La première section passera en revue l'état de l'art des techniques CRDS à large bande. La deuxième section entrera dans les détails de la première démonstration de la technique FT-CRDS, couvrant le dispositif expérimental, l'acquisition et le traitement des données, l'application à la mesure de l'air ambiant, la comparaison des performances avec la spectroscopie d'absorption par cavité (CEAS) ainsi que les limites de la technique. La troisième section présentera un dispositif FT-CRDS amélioré, développé conjointement avec Dominik Charczun et Piotr Masłowski de l'université de Toruń en Pologne. Ce dispositif a été appliqué à une mesure précise du CO dans l'argon. La section présentera les résultats ainsi que leur budget d'incertitudes, et une comparaison avec une mesure précédente utilisant la CRDS. Le nouveau dispositif permet de décupler la sensibilité grâce à une modification de l'approche de stabilisation. Les résultats de ce chapitre ont été publiés dans un article de démonstration de faisabilité dans Optics Express (Dubroeucq & Rutkowski, 2022) et la deuxième installation a été publiée dans les actes de CLEO/EQEC en 2023 (Dubroeucq *et al.*, 2023a).

Le dernier chapitre portera sur le couplage des jets supersoniques avec la spectroscopie en peigne renforcée par cavité optique. La première section présentera les principes de base des jets supersoniques et passera en revue leurs applications en spectroscopie. La

deuxième section présentera le dispositif expérimental, en détaillant le couplage peigne-cavité, les supports de miroir de cavité conçus pour amortir les vibrations mécaniques dues au groupe de pompage, le schéma de stabilisation du peigne et de la cavité ainsi que l'appareil générants les jets supersoniques. La deuxième section couvrera la spectroscopie d'un jet supersonique d'acétylène dilué dans l'argon. Elle présentera le traitement des données permettant d'obtenir le spectre final, le modèle de transmission de la cavité utilisé pour ajuster les données expérimentales, l'étalonnage de la réflectivité des miroirs de la cavité avec la technique FT-CRDS et les conditions du jet obtenues. Les résultats préliminaires ont été publiés dans les actes de CLEO/EQEC en 2023 (Dubroeucq *et al.*, 2023b).

En conclusion, nous avons à présent développé deux parties essentielles de l'instrument de spectroscopie par peigne de fréquences optiques pour la cinétique des réactions froides (voir la figure 2).

Premièrement, nous avons démontré qu'un FTS résolu en temps est capable de résoudre des événements dépendant du temps à l'échelle de la microseconde. Nous l'avons soumis au test le plus rigoureux qui soit en l'appliquant à une technique de CRDS multiplexée, la FT-CRDS. Nous avons montré que les éléments spectraux individuels pouvaient être récupérés sans ambiguïté après la transformation de Fourier. Nous pensons donc avoir atteint les spécifications requises en matière de résolution temporelle et de large couverture spectrale pour la cinétique des réactions. Au cours du processus, la technique FT-CRDS s'est avérée suffisamment prometteuse pour faire l'objet d'une étude plus approfondie. La première étape consistait à augmenter la finesse de la cavité jusqu'aux valeurs typiques utilisées en CRDS sans réduire la largeur de bande spectrale, ce qui a déjà été réalisé à l'Université de Toruń. Nous y montrons que la FT-CRDS a un potentiel de sensibilité au-delà du profil de Voigt. Les prochaines étapes comprendront : **1)** la combinaison avec les méthodes de résolution *sub-nominal* et d'entrelacement (Maslowski *et al.*, 2016 Rutkowski *et al.*, 2018) afin de parvenir à une spectroscopie d'absorption sans étalonnage à la fois sur l'axe de l'intensité et de la fréquence, et **2)** le transfert technique vers l'infrarouge moyen.

Deuxièmement, nous avons démontré la mesure d'un échantillon dans un jet supersonique par spectroscopie d'absorption renforcée par cavité basée sur des peignes de fréquences. Nous avons appliqué le système à la spectroscopie d'un jet d'acétylène dilué dans l'argon, et nous avons entrelacé 18 spectres *sub-nominal* pour obtenir un spectre à une température de 8,5 K. Néanmoins, l'analyse spectroscopique en cours a mis en évidence

des questions restées sans réponse : **1)** la ligne d'absorption la plus forte présente un profil étrange, encore inexpliqué ; **2)** les jets de fente devraient produire différentes températures de vibration, de rotation et de translation ($T_{vib} > T_{rot} > T_{trans}$), ce qui n'a pas été vérifié ici. La densité estimée de l'acétylène au cœur du jet était de $6{,}0\times10^{13}$ molécule/cm^3, soit trois ordres de grandeur plus élevés que les densités minimales des espèces transitoires à 10^{10} molécule/cm^3. Pour accroître la sensibilité, on peut soit augmenter la longueur d'interaction, soit sonder des lignes d'absorption plus fortes. La première option consiste à augmenter la finesse de la cavité, qui pourrait facilement être multipliée par un facteur de 2 à 5 pour atteindre une densité détectable de 10^{13} sans compromettre la résolution temporelle. Le second objectif sera atteint en transférant la technique dans l'infrarouge moyen, où les sections efficaces des raies d'absorption moléculaires sont 2 à 3 ordres de grandeur plus élevées.

Les perspectives immédiates du développement du dispositif expérimental sont la mise en œuvre d'une nouvelle source DFG, couvrant la région 3-10 µm (Soboń *et al.*, 2017 ; Sotor *et al.*, 2018). Cette source est un peigne de fréquences et peut être stabilisée à la fois sur le taux de répétition et la fréquence de décalage grâce à l'ajout d'un AOM sur le bras erbium de la DFG (Lee *et al.*, 2017). Cela permettra d'asservir le peigne sur une cavité optiques, dont l'arrivée est prévue pour les prochains mois. À terme, ce spectromètre dans l'infrarouge moyen sera couplé à une chambre supersonique et à un laser pulsé de photolyse pour réaliser la première spectroscopie infrarouge de précision d'espèces radicalaires.

Introduction

The invention of the optical frequency comb (OFC) in the late 1990s from modelocked femtosecond lasers revolutionized the field of precision time and frequency metrology, by providing a direct way of linking optical and microwave frequencies. Before their advent, large-scale frequency multiplication chains starting from the SI standard set by ^{133}Cs microwave atomic clocks were necessary to bridge the gap to optical frequencies, using a series of phase-locked oscillators (Hollberg *et al.*, 2005 ; Diddams *et al.*, 2020). Frequency combs replaced these bulky and complex systems with a single femtosecond modelocked laser. These laser could synthesize 10^5-10^6 optical modes equally spaced in frequency, and with a stability of 1 part in 10^{18}. They provide direct microwave-to-optical and optical-to-microwave conversion as well as a precise frequency ruler. This opened the way for the comparison of atomic clocks, the measurement of optical transitions (Udem *et al.*, 1999a), optical frequency differences between lasers (Udem *et al.*, 1999b, Reichert *et al.*, 1999 Diddams *et al.*, 2000a) and optical frequencies of lasers (Diddams *et al.*, 2000b) as well as the first all-optical atomic clock (Diddams *et al.*, 2001) with a long-term stability better than the atomic clocks defining the SI standards (Udem *et al.*, 2002). In the following years, several other demonstrations went by : the full stabilization of a frequency comb (Jones *et al.*, 2000), an optical molecular clock (Ye *et al.*, 2001), testing of fundamental constants (Bize *et al.*, 2003) and optical precision synthesis of microwave signal (Diddams *et al.*, 2003). Half of the 2005 Physics Nobel prize was awarded to Ted Hänsch and John Hall for their contribution to optical frequency metrology and the invention of optical frequency combs (Hall, 2006, Hänsch, 2006).

The applications of frequency combs soon broadened beyond their original scope of precision metrology. A non-exhaustive list contains : precise calibration of astronomical spectrographs (Murphy *et al.*, 2007), XUV and attosecond pulse generation (Keller, 2003, Baltuška *et al.*, 2003), precision molecular spectroscopy (Sugiyama *et al.*, 2023) and trace gas sensing (Alden *et al.*, 2017), coherent microscopy (Potma *et al.*, 2002) and precise distance ranging (Minoshima & Matsumoto, 2000). In particular, the develop-

ment of reliable mid-infrared sources enabled sensitive detection for physical chemistry applications (Weichman *et al.*, 2019).

Frequency comb spectroscopy offers the potential for broad spectral bandwidth together with fast time resolution and high sensitivity. This opened up for the first simultaneous and quantitative detection of the key species involved in chemical reactions, namely reactants, transient species and products (Fleisher *et al.*, 2014 ; Hoghooghi *et al.*, 2023). This capability paved the way for measuring reaction rates and branching ratios with minimal bias. These works have been performed either at room temperature or at high temperature, but none have succeeded yet at measuring accurate reaction rates at the temperatures relevant to interstellar chemistry. The aim of this thesis is the development of an instrument capable of tackling such a challenge. Such an instrument should be able to detect multiple species, with a microsecond-level time resolution, sensitive to molecular densities as low as 10^{10} molecule/cm^3.

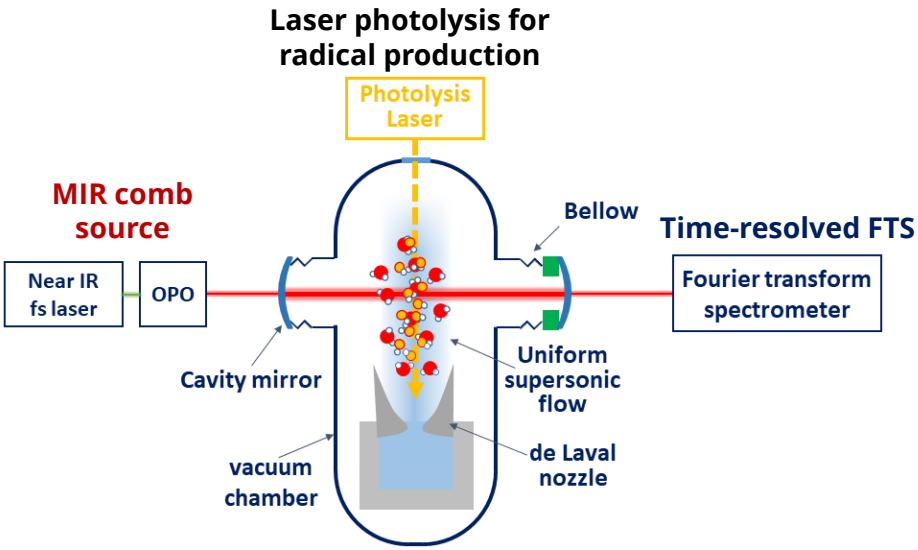

Figure 2 : Schematic of the instrumentation being developed at IPR. An excimer laser is used to generate radicals through photolysis of a precursor gas expanded in a uniform supersonic flow. The molecular sample is probed transversally to the flow direction using cavity-enhanced spectroscopy based on a mid-infrared frequency comb. The cavity transmission is analyzed with a time-resolved Fourier transform spectrometer.

The general idea of our approach relies on a cavity-enhanced absorption Fourier transform spectrometer operating in the mid-infrared probing a supersonic uniform flow, as illustrated on figure 2. The cold environment is obtained *via* supersonic expansion of the sample yielding effective temperatures down to few tens of kelvins and will be ultima-

tely combined with pulsed-laser photolysis. Supersonic flows are the workhorse of the Molecular Physics Department at the Institute of Physics of Rennes (IPR), historically for reaction kinetics in the CRESU technique (CRESU is a french acronym standing for reaction kinetics in uniform supersonic flows). They have been extensively employed with laser-induced fluorescence, mass spectrometry, microwave spectroscopy and near-infrared cavity ring-down spectroscopy (Rowe & Canosa, 2022). The novelty of this doctoral project is the addition of frequency comb absorption spectroscopy to the list of techniques compatible with CRESU environments. The challenge to tackle was double: **1)** designing a spectrometer capable of resolving the microsecond without reducing the bandwidth and **2)** performing precision spectroscopy in the harsh conditions created by the large pumping groups required in generating supersonic flows. The first part of the challenge led us to design a new spectroscopic technique, Fourier transform cavity ring-down spectroscopy, relying on a time-resolved Fourier transform spectrometer. For this first stage of development, we remained in the near-infrared telecom range where optoelectronics devices are readily available and comparatively cheaper than their mid-infrared counterparts.

In the first chapter, we will detail the basics of optical frequency combs (OFCs). We quickly review the different types of comb sources and introduce the actuators and control schemes for stabilizing an OFC. In a second section, the comb source used throughout this thesis is presented. The third section is dedicated to the review of the different spectrometers of frequency comb spectroscopy. The fourth section concentrates on Fourier transform spectroscopy and the impact of its instrumental lineshape (ILS) on absorption spectra as well as the method used to retrieve ILS-free spectra with comb mode resolution. This section ends on the presentation of the fast-scanning Fourier transform spectrometer used throughout this thesis.

The second chapter will cover infrared cavity-enhanced absorption spectroscopy. The first section focuses on the spectral signature of molecules in the infrared, the origin of the lineshapes of absorption lines, the broadening mechanisms of those lineshapes depending on the temperature and pressure conditions and the different absorption profiles needed to model molecular absorption spectra. The second section is dedicated to Fabry-Perot cavities, detailing their spatial and frequency modes, their transmission and reflection transfer functions used to model cavity-enhanced absorption spectra, the frequency and spatial mode matching required to coupled an OFC to the cavity and the cavity transient response and its application to cavity ring-down spectroscopy (CRDS). The last section of this chapter details the locking schemes necessary to perform precise cavity-enhanced

absorption spectroscopic measurements with a frequency comb.

The third chapter will present the Fourier transform CRDS technique (FT-CRDS). The first section reviews the state-of-the-art of broadband CRDS techniques. The second section goes into the details of the first demonstration of FT-CRDS, covering the experimental setup, the data acquisition and processing, the application to ambient air measurements, the performances comparison with cavity-enhanced absorption spectroscopy (CEAS) and the technique limitations. The third section presents an improved FT-CRDS setup developed jointly with Dominik Charczun and Piotr Masłowski from Toruń University in Poland. This setup was applied to a precise measurement of CO in argon. The section presents the results along with their uncertainty budget, and a comparison with a previous measurement with CRDS. The new setup allows a tenfold increase of the sensitivity thanks to a modification of the stabilization approach. The results of this chapter have been published in a proof-of-concept paper in Optics Express (Dubroeucq & Rutkowski, 2022) and the second setup was published in the CLEO/EQEC proceedings in 2023 (Dubroeucq *et al.*, 2023a).

The final chapter will focus on the coupling of supersonic jets with cavity-enhanced comb spectroscopy. The first section presents the basic principles of supersonic jets and a review of their applications in spectroscopy. The second section presents the experimental setup, detailing the comb-cavity coupling, the cavity mirror mounts designed to dampen mechanical vibrations due to the pumping group, the stabilization scheme and the supersonic jet apparatus. The second section covers the spectroscopy of a supersonic jet of acetylene seed in argon. It presents the data processing yielding the final spectrum, the cavity transmission model used to fit the experimental data, the calibration of the cavity mirrors reflectivity with FT-CRDS and the retrieved jet conditions. The preliminary results have been published in the CLEO/EQEC proceedings in 2023 (Dubroeucq *et al.*, 2023b).

1 – Optical frequency combs and Fourier transform spectroscopy

Optical frequency combs (OFCs) provide a stable comb of evenly spaced optical frequencies, with a single comb containing tens of thousands of teeth. Each tooth (or mode) is equivalent to a narrow-linewidth single mode laser. Frequency combs can then be used as a broadband light source for spectroscopy while providing high frequency resolution and spectral density, like continuous-wave (cw) laser diodes (Weichman *et al.*, 2019). We can distinguish two ways of performing spectroscopy with an OFC, depending on whether the OFC is used or not as the probe interrogating a sample. If the comb is the probing source, it is often referred to as direct frequency comb spectroscopy. In the opposite case, a cw laser is used as the probe and its absolute frequency is monitored with a wavemeter. In addition, a beatnote between the cw laser and the OFC gives a relative frequency precision and accuracy beyond the wavemeter performances. The comb is then used as a frequency ruler, in the so-called comb-assisted or comb-referenced spectroscopic techniques (Maddaloni *et al.*, 2013).

This chapter will focus on the fundamental principles of frequency combs and direct frequency comb spectroscopy. In the following sections, we will detail the principles of optical frequency combs, the presentation of the OFC source used throughout this thesis, the different spectrometers for direct frequency comb spectroscopy and the implementation of Fourier transform spectroscopy with an OFC.

1.1 Fundamentals of optical frequency combs

1.1.1 Time and frequency formalism

Optical frequency combs were first identified from stabilized Titanium-Sapphire (Ti:Sa) femtosecond modelocked lasers (Reichert *et al.*, 1999). In the time domain, a modelocked

femtosecond laser emits a train of femtosecond pulses, depicted on the top part of figure 1.1. The pulses are separated in time by τ_{rep} the pulse repetition period:

$$\tau_{rep} = 2L/v_g, \tag{1.1}$$

where L is the length of the laser cavity and v_g is the pulse group velocity in the cavity. For each pulse, we identify the carrier in red with τ_c its period, and the envelope in dashed grey with $\Delta\tau_p$ the width of the envelope. The pulses are quasi-identical, except for an increasing phase slip between the carrier and the envelope from one pulse to another. This carrier-envelope phase slip increases by a constant amount, the carrier-envelope offset $\Delta\phi_{ceo}$. It originates from residual dispersion inside the laser cavity, which induces a small difference between the phase and group velocity:

$$\Delta\phi_{ceo} = 2\pi\frac{\tau_{rep}}{\tau_c}\, c\left(\frac{1}{v_g} - \frac{1}{v_\phi}\right), \tag{1.2}$$

with v_ϕ the phase velocity and c the celerity of light in vacuum.

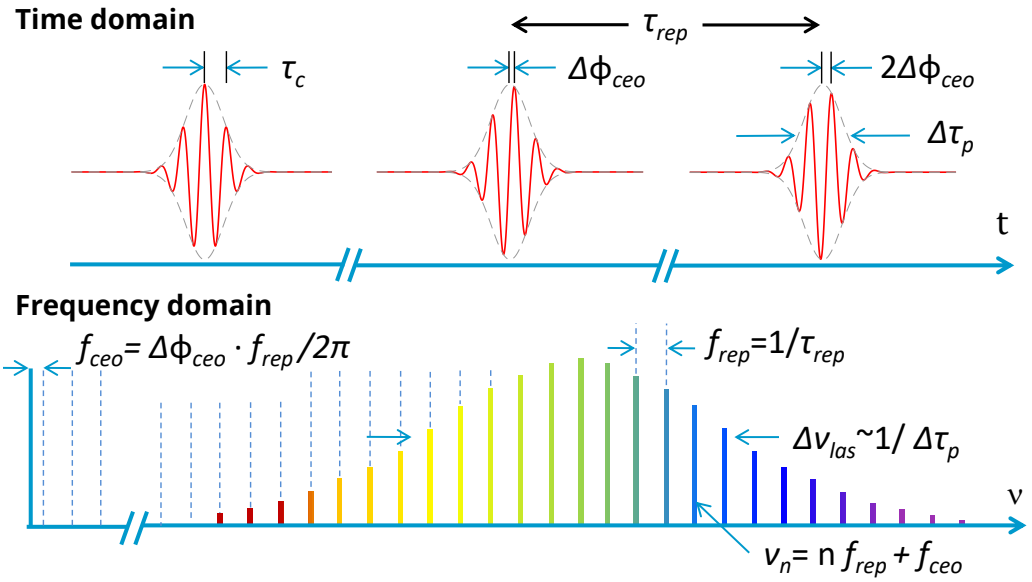

Figure 1.1 : The top panel shows a time domain representation of a train of pulses by a femtosecond modelocked laser, with the carrier period τ_c, the pulse period τ_{rep} and the pulse width $\Delta\tau_p$. There is a pulse-to-pulse phase slip between the envelope (grey) and the carrier (red) that increases by a constant amount $\Delta\phi_{ceo}$. The bottom panel displays the Fourier transform of the pulse train, which exhibits a comb-like figure with discrete teeth, each one representing a given comb mode in the frequency domain.

The time dependent electric field associated to the single m^{th} pulse then is:

$$E_{pulse}(t) = E_{envelope}(t - m\tau_{rep})e^{i(2\pi\nu_c(t-m\tau_{rep})+m\Delta\phi_{ceo})}, \tag{1.3}$$

where the carrier of frequency $\nu_c = 1/\tau_c$ is modulated in time by the envelope, with $E_{envelope}(t)$ the function describing its temporal shape. Assuming a Gaussian pulse of width $\Delta\tau_p$, we have:

$$E_{envelope}(t) = E_0 \cdot e^{-\left(\frac{t}{\Delta\tau_p}\right)^2}, \tag{1.4}$$

with E_0 the peak electric field. The electric field describing the pulse train is then the sum of the electric fields of successive pulses:

$$E_{train}(t) = \sum_n E_{envelope}(t - m\tau_{rep}) e^{i(2\pi\nu_c(t-m\tau_{rep})+m\Delta\phi_{ceo})}. \tag{1.5}$$

The comb structure in the frequency domain is then obtained by taking the Fourier transform of $E_{train}(t)$:

$$\begin{aligned}
\hat{E}_{train}(\nu) &= \int_{-\infty}^{+\infty} \sum_n E_{envelope}(t - m\tau_{rep}) e^{i\left(2\pi\nu_c(t-m\tau_{rep})+m\Delta\phi_{ceo}\right)} e^{-i2\pi\nu t}\, dt, \\
&= E_0 \sum_n e^{i\left(m\Delta\phi_{ceo}-2\pi\nu_c n\tau_{rep}\right)} \int_{-\infty}^{+\infty} e^{-\left(\frac{t-m\tau_{rep}}{\Delta\tau_p}\right)^2} e^{i2\pi(\nu_c-\nu)t}\, dt, \\
&= E_0 \Delta\tau_p \sqrt{\pi} \sum_n e^{\frac{-(2\pi(\nu-\nu_c))^2\Delta\tau_p^2}{4}} e^{i(m\Delta\phi_{ceo}-2\pi\nu_c n\tau_{rep})} e^{i2\pi(\nu_c-\nu)\, m\, \tau_{rep}}, \\
\hat{E}_{train}(\nu) &= E_0 \Delta\tau_p \sqrt{\pi} \sum_n e^{\frac{-(2\pi(\nu-\nu_c))^2\Delta\tau_p^2}{4}} e^{i(m\Delta\phi_{ceo}-2\pi\nu m\tau_{rep})}.
\end{aligned} \tag{1.6}$$

The second exponential term in the sum of equation 1.6 implies that the frequency domain representation of the pulse train exhibits evenly-spaced, discrete frequencies for which the phase of consecutive pulses adds coherently, hence the name of "frequency comb". These frequencies verify that:

$$\Delta\phi_{ceo} - 2\pi\nu_n\tau_{rep} = 2\pi n, \tag{1.7}$$

with n and integer. The solution for the frequencies is then:

$$\nu_n = \frac{n}{\tau_{rep}} + \frac{\Delta\phi_{ceo}}{2\pi\tau_{rep}}. \tag{1.8}$$

Taking $f_{rep} = 1/\tau_{rep}$ the repetition rate and $f_{ceo} = \Delta\phi_{ceo} \cdot f_{rep}/2\pi$ the carrier-envelope offset frequency (usually shortened to offset frequency), yields the expression for the discrete comb frequencies in the optical domain:

$$\nu_n = nf_{rep} + f_{ceo}, \tag{1.9}$$

with $0 \leq f_{ceo} < f_{rep}$. The comb spectrum is displayed on the bottom part of figure 1.1. Each discrete colored line is a comb "tooth" or mode, evenly-spaced by f_{rep}. At the frequency origin, the hypothetical "first" comb mode is shifted by f_{ceo}. The first exponential

term in the sum of equation 1.6 indicates that, with a pulse whose envelope is Gaussian, the frequency domain representation of the comb exhibits a Gaussian envelope as well, with a full-width at half-maximum (FWHM) inversely proportional to the pulse width $\Delta\nu_{las} \sim 1/\Delta\tau_p$. The broader the comb spectrum, the shorter the pulse. The comb spectrum is also centered on ν_c the carrier frequency.

The two frequencies f_{rep} and f_{ceo} typically lie in the hundreds of MHz range, giving $n = 10^5 - 10^6$. For example, a frequency comb emitting near 1550 nm ($\sim$ 200 THz) with a FWHM of 80 nm ($\sim$ 10 THz) with f_{rep} = 100 MHz, has 100,000 modes centred on $n \sim 2 \times 10^6$. Equation 1.9 represents the marvel of frequency combs: their deterministic nature. Only two degrees of freedom in the radiofrequency range, f_{rep} and f_{ceo}, allow to control hundreds of thousands of phase-coherent frequencies in the optical domain. To monitor these two degrees of freedom, a photodetector whose bandwidth is higher than f_{rep} can detect the amplitude modulation of the optical pulse train. However, no information about f_{ceo} is retrieved, as consecutive comb modes have the same offset frequency. A scheme called *f-2f* interferometry was then developed to detect the comb offset frequency, described in section 1.1.3 (Telle *et al.*, 1999; Jones *et al.*, 2000).

The next section will cover the different systems that can generate frequency combs, especially in the infrared part of the electromagnetic spectrum.

1.1.2 Comb sources

While frequency combs originated from Ti:Sa femtosecond modelocked lasers, many other types of sources have been developed in the past two decades (Fortier & Baumann, 2019), covering different regions of the electromagnetic spectrum, from the terahertz to the extreme ultra-violet (Picqué & Hänsch, 2019).

Most of the commercial "turn-key" frequency combs are based on rare-earths doped fiber-based oscillators, mainly ytterbium, erbium and thulium respectively covering the 1, 1.5 and 2 µm regions (Schibli *et al.*, 2004; Kim & Song, 2016; Fortier & Baumann, 2019). While fiber combs can be engineered to reach the mid-infrared region in the 3-5 µm range (Duval *et al.*, 2015), the main techniques to generate frequency combs at higher wavelengths are optical parametric oscillators (OPO, Adler *et al.*, 2009; Leindecker *et al.*, 2011) and difference frequency generation (DFG, Erny *et al.*, 2007; Gambetta *et al.*, 2008). Both techniques rely on non-linear crystals to generate radiation at lower frequencies in the infrared from a source in the near-infrared. OPO and DFG combs are commonly used for spectroscopic applications (Weichman *et al.*, 2019), as they reach

the molecular fingerprint regions at 3-5 µm (Heckl *et al.*, 2016; Soboń *et al.*, 2017) and 8-10 µm (Iwakuni *et al.*, 2018; Lee *et al.*, 2017). Intra-pulse DFG or combining OPOs and DFGs may even yield radiation further in the infrared (Kowligy *et al.*, 2019; Steinle *et al.*, 2016).

Mid-infrared frequency combs have also been obtained from quantum cascade lasers (QCLs, Hugi *et al.*, 2012) and interband cascade lasers (ICLs, Bagheri *et al.*, 2018). While the spectral bandwidth of QCL combs are usually narrower than DFG or OPO combs, they can reach high optical power even in the far-infrared, on the order of the watt at 8 µm (Jouy *et al.*, 2017). Due to the compactness of QCL lasers, QCL combs usually have a repetition rate on the order of 10 GHz, which, in principle, make them less suitable for spectroscopy applications. Nonetheless, spectroscopy with QCL and ICL combs has been demonstrated (ibid.; Sterczewski *et al.*, 2017). Terahertz frequency combs have also been obtained with QCLs (Burghoff *et al.*, 2014).

Another type of frequency combs worth mentioning is the micro-resonator combs, often referred to as "micro-combs" or "Kerr combs", which have attracted considerable attention in the past decade (Del'Haye *et al.*, 2007; Kippenberg *et al.*, 2011). Although their repetition rates are in the 100 GHz range, their chip-scale manufacturability and their silicon-compatibility open up the way to "spectroscopy on a chip" (Yu *et al.*, 2016).

The next section is dedicated to the *f-2f* interferometer which gives access to of f_{ceo}.

1.1.3 *f-2f* interferometer

The carrier-enveloppe offset frequency requires a *f-2f* interferometer to be measured, described on figure 1.2. This interferometer was first proposed by Telle *et al.* (1999), and involves a non-linear process, second harmonic generation (SHG). A frequency comb with an octave spanning spectrum, implying that the highest frequency is equal to twice the lowest frequency, propagates in a highly non-linear fiber to generate a supercontinuum spectrum. The supercontinuum is then focused into a SHG crystal to produce a second harmonic spectrum. The lowest frequency comb mode of the fundamental spectrum, of frequency $\nu(m) = mf_{rep} + f_{ceo}$, is then frequency-doubled to $2\nu(m) = 2(mf_{rep} + f_{ceo})$. The nearest comb mode is then the highest frequency comb mode from the fundamental spectrum $\nu(2m) = 2mf_{rep} + f_{ceo}$.

Their beatnote can be recorded with a photodetector and a microwave spectrum analyzer.

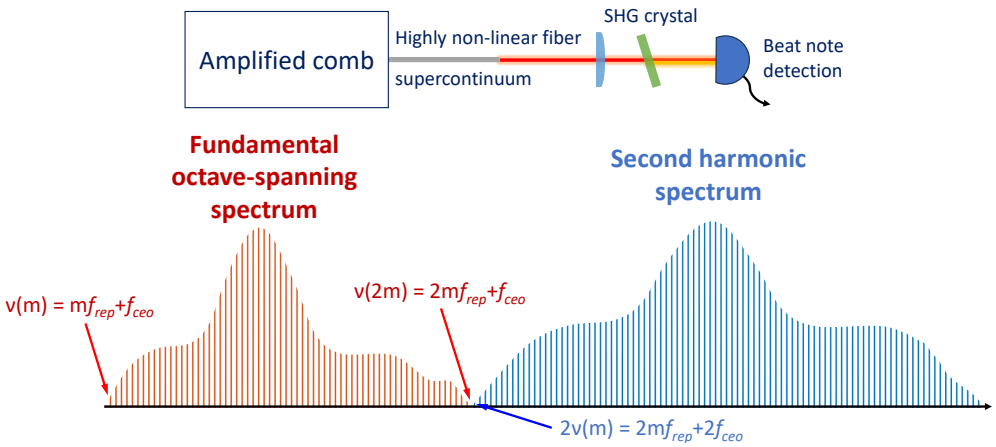

Figure 1.2 : Schematic of a *f-2f* interferometer. The amplified comb is fibered to highly non-linear fiber to generate a supercontinuum, which is then focused into a SHG crystal to generate a second harmonic spectrum. The beatnote between the highest frequency comb mode of the fundamental spectrum and the lowest frequency comb mode of the harmonic spectrum is monitored with a photodetector and yields f_{ceo}.

Their frequency difference then yields f_{ceo}, as:

$$2\nu(m) - \nu(2m) = (2mf_{rep} + 2f_{ceo}) - (2mf_{rep} - f_{ceo}) = f_{ceo}. \tag{1.10}$$

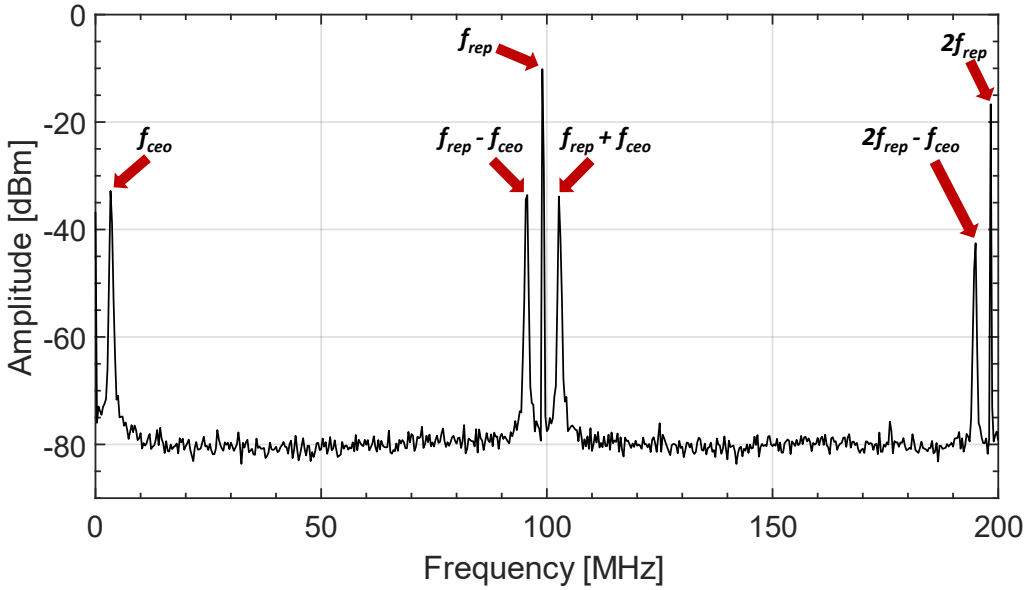

Figure 1.3 : Output signal of an *f-2f* interferometer shown on a spectrum analyzer. From left to right, we observe the beatnotes corresponding to f_{ceo}, $f_{rep} - f_{ceo}$, f_{rep}, $f_{rep} + f_{ceo}$, $2f_{rep} - f_{ceo}$ and $2f_{rep}$. Measured with RBW = 30 kHz.

The RF spectrum monitored output of a *f-2f* interferometer is shown on figure 1.3,

with a resolution bandwidth (RBW) of 30 kHz. As frequency increases, we can see from left to right on the frequency axis the beatnotes corresponding to f_{ceo}, $f_{rep} - f_{ceo}$, f_{rep}, $f_{rep} + f_{ceo}$, $2f_{rep} - f_{ceo}$ and $2f_{rep}$.

The next section will present the Erbium:fiber (Er:fiber) frequency comb used throughout this thesis.

1.2 Er:fiber frequency comb

1.2.1 Oscillator, actuators and outputs

The laser is a ModeHybrid from Mode-Locked Technology, with its block diagram shown on figure 1.4. The oscillator is an Er:fiber frequency comb, emitting in the near-infrared at 1550 nm. The repetition rate of the comb is $f_{rep} = 100$ MHz. A fiber port gives access to the oscillator output ($\sim$ 1 mW), and a BNC (for Bayonet Neill–Concelman) connector allows to monitor the f_{rep} beatnote. The oscillator spectrum is shown on figure 1.5. The comb repetition rate and offset frequency can be tuned with five actuators: a stepper motor, an intracavity electro-optic modulator (EOM), fast and slow piezoelectric transducers (PZT) and the oscillator pump current.

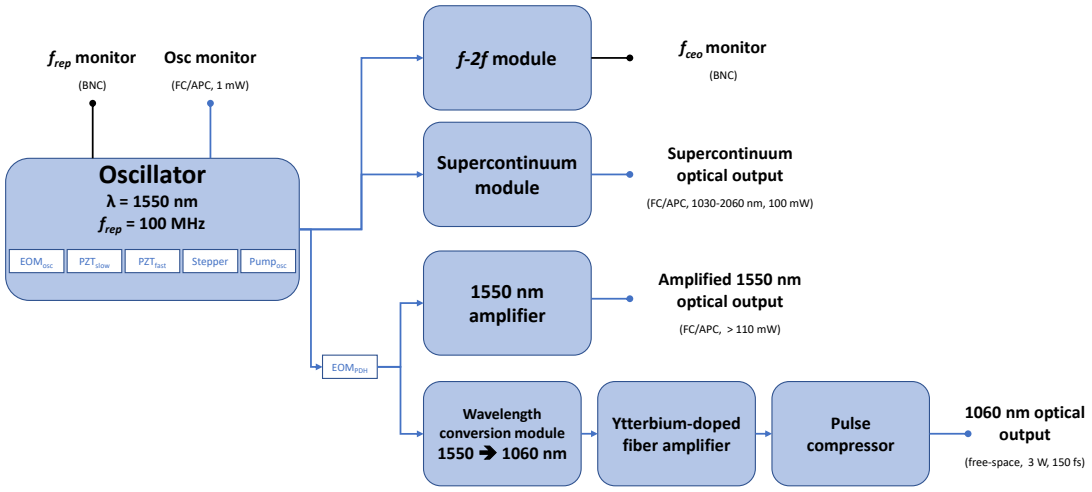

Figure 1.4 : Block diagram of the ModeHybrid frequency comb. An Er:fiber oscillator emitting near 1550 nm is split in four different outputs: the oscillator output, the amplified 1550 nm output, the supercontinuum output (spanning 1030-2060 nm), and a 3W 1060 nm output. The f_{rep} value is monitored through a coaxial output, and a *f-2f* interferometer module gives access to f_{ceo}.

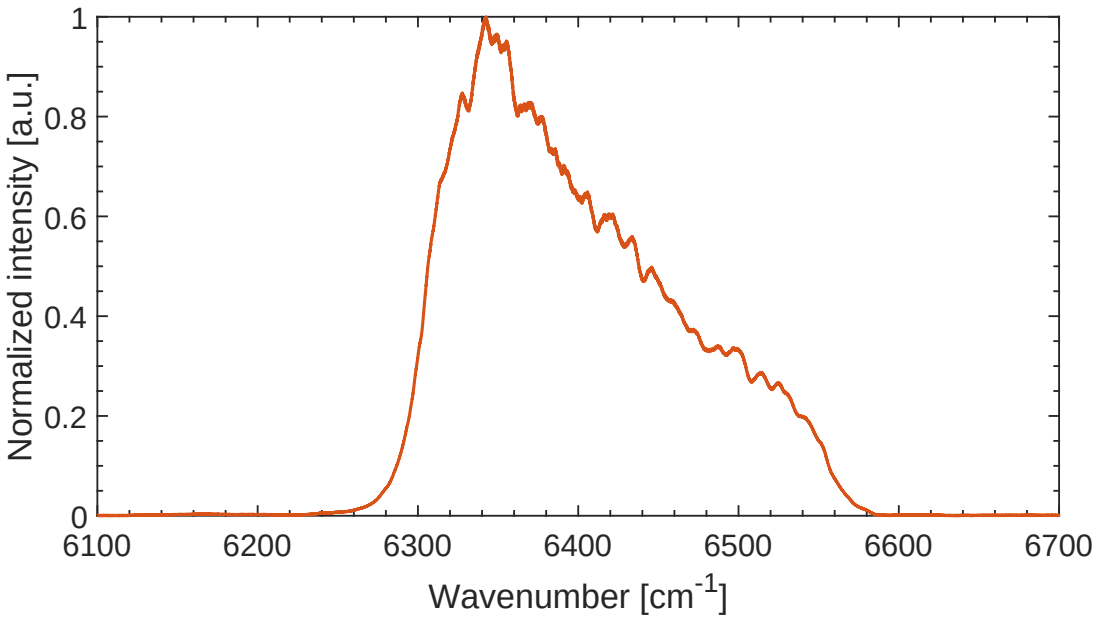

Figure 1.5 : Spectrum from the oscillator output of the frequency comb.

The impact of each actuator on f_{rep} and f_{ceo} as a change in frequency per volt applied is summarized on table 1.1. It should be noted that the slow PZT and the pump current both induce a comparable variation of f_{rep} and f_{ceo} per volt applied, while both frequencies are much more sensitive to the intracavity EOM.

Table 1.1 : Change on f_{rep} and f_{ceo} depending on the voltage applied to each of the laser actuators.

Actuators	PZT SLOW	PZT FAST	EOM osc	Pump current
f_{rep} change [Hz/V]	12.3	0.3	244	8.4
f_{ceo} change [MHz/V]	0.49	-	138	1

The oscillator light is then split in three ways. The first one goes to the *f-2f* module, which has a BNC output to monitor the f_{ceo} beatnote. The second one is stretched in a highly nonlinear fiber to yield a supercontinuum, whose output ($\sim$ 100 mW) is accessible with a fiber port. The supercontinuum spectrum, displayed on figure 1.6, almost covers 2000 cm^{-1} (1030-2060 nm). This output could be used as a precise relative frequency reference for continuous-wave lasers used in cavity ring-down spectroscopy (see section 2.2.4.2) in a comb-assisted spectroscopy scheme (Maddaloni *et al.*, 2013), provided that the comb modes are stabilized to a sub-MHz level in the optical domain.

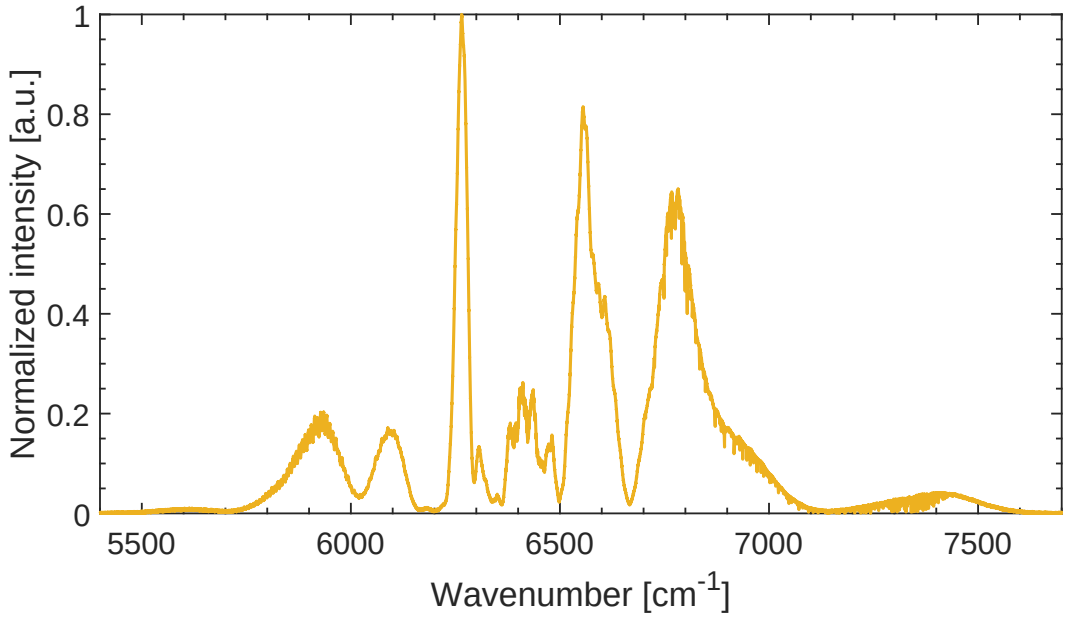

Figure 1.6 : Spectrum of the comb supercontinuum output. It spans 2000 cm^{-1} from 5700 to 7700 cm^{-1}. Absorption features visible between 6700 and 7500 cm^{-1} come from water vapor present in the laboratory air.

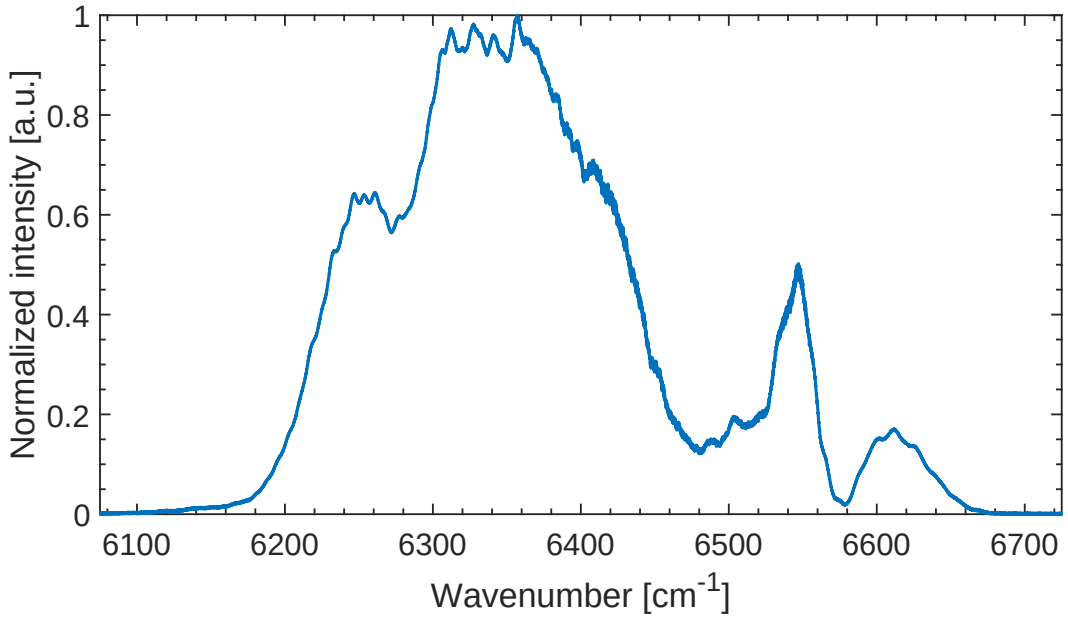

Figure 1.7 : Spectrum of the comb amplified output. It spans 500 cm^{-1} from 6200 to 6700 cm^{-1}. Note the noisy part of the baseline between 6350 and 6550 cm^{-1}, inherent to the amplifier.

The third one is fibered to an EOM, to generate sidebands from the comb modes at the modulation frequency. The light is split again in two fibers after the EOM. The first one is amplified with an Erbium-doped fiber amplifier, yielding an amplified 1550 nm output with 110 mW of output power. The amplified light is accessible with a fiber port. The corresponding spectrum is shown on figure 1.7. The second one goes through a wavelength conversion module, shifting the central frequency of the spectrum from 1550 to 1060 nm. It is amplified by an ytterbium-doped fiber amplifier, and the laser pulse is compressed in a pulse compressor. The 1060 output is free-space, with 3W of output power, and will be used to pump an OPO to generate a mid-infrared frequency comb.

1.2.2 Beatnotes stabilization

Either degree of freedom of the frequency comb, f_{rep} and f_{ceo} can be stabilized with the different actuators of the laser. Figure 1.8(a) compares the beatnote of a free-running f_{ceo} with beatnotes of a locked f_{ceo}.

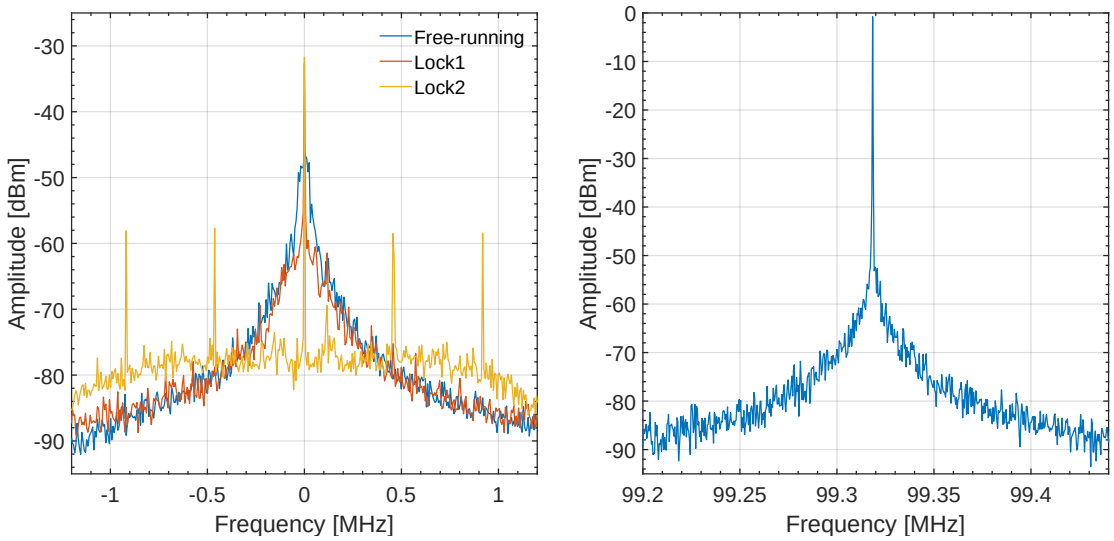

Figure 1.8 : (a) - Comparison of free-running and locked f_{ceo} beatnotes with a resolution of 300 Hz. The error signal for the lock was obtained with a phase detector and an arbitrary waveform generator. We observe three conditions: free-running (blue), locked (phase detector linear range = 256π, red), locked (phase detector linear range = 32π, yellow). A significant reduction in the beatnote width is observed when f_{ceo} is locked to a frequency reference, and as the phase detector linear range decreases. **(b)** - Beatnote of f_{rep} locked to a frequency reference with a 100 Hz resolution.

The offset frequency was compared in a phase-detector with the output of an arbitraty waveform generator (AWG). The phase detector output was fed to a proportional-integrator (PI) servo-controller (NewFocus LB1005S) with a PI corner of 30 kHz and a -20 dB gain. The servo controls the comb oscillator intracavity EOM to lock f_{ceo} to the frequency set on the AWG. When the lock is on with a phase detector linear range of 256π, there is a significant reduction of the beatnote linewidth, as seen from the red trace compared to the free-running f_{ceo} in the blue trace. The yellow trace displays the locked f_{ceo} beatnote with the phase detector linear range reduced to 32π. A significant reduction of the linewidth is observed, although resonance peaks are visible on each side of the beatnote.

The same lock can be performed on f_{rep} with the PZT actuators. The locked f_{rep} beatnote is shown on figure 1.8(b). No comparison is made here to a free-running f_{rep} as the spectrum analyzer used has a maximum resolution of 100 Hz, which is too low to differentiate between the locked and free-running case.

The next section will cover the spectrometers used in direct frequency comb spectroscopy.

1.3 Direct frequency comb spectroscopy

As frequency combs are broadband sources, one requires a spectrometer to analyze the light transmitted by the studied sample. The following subsections will describe the main categories of spectrometers used with frequency combs. The spectrometers can be separated into two main families: the dispersion techniques (virtually imaged phased array spectrometer, grating spectrograph and Vernier spectrometer) and the Fourier transform techniques (Fourier transform spectrometer and dual-comb spectrometer).

Throughout this section, the noise-equivalent absorption at 1s averaging time per spectral element will be often mentioned. This quantity is commonly used in frequency comb spectroscopy to assess and compare the performances of spectrometers. It is defined as:

$$\mathrm{NEA}^{1s} = \alpha_{min}\sqrt{\frac{T_{acq}}{M}}, \tag{1.11}$$

with α_{min} the minimum detectable absorption, T_{acq} the acquisition time and M the number of resolved spectral elements. NEA^{1s} is expressed in cm^{-1} $\mathrm{Hz}^{-1/2}$ per spectral element.

1.3.1 Grating spectrograph

The most simple dispersing spectrometer is a spectrograph, coupling a diffraction grating and a imaging CCD array. The light diffracted by the grating is integrated by the CCD array. Grilli *et al.* (2012) presented a setup where the comb is coupled to an enhancement cavity, and the cavity output is analyzed by a grating spectrograph. They reported a remarkable sensitivity of the setup, with $\mathrm{NEA}^{1s} = 1.5{\times}10^{-11}$ cm^{-1} $\mathrm{Hz}^{-1/2}$. The same apparatus was later used for *in situ*, real-time measurements of highly reactive halogenated radicals. While the instrument was compact and transportable, its spectral resolution was limited to 15 GHz, constraining measurements to atmospheric conditions, which is generally the case with grating spectrographs.

We will now cover the other types of dispersing spectrometers.

1.3.2 VIPA spectrometer

A simple dispersing spectrometer is made of a diffraction grating to spatially disperse the comb light onto a detector array to record the spectrum. However, the resolution is then limited by the diffraction grating itself, whose resolution is too low to resolve individual comb modes. Another approach requires a cross-disperser, coupling a grating with a virtually imaged phased array etalons (VIPA). The VIPA etalon was first presented by Shirasaki (1996) for telecommunications applications (Xiao & Weiner, 2004). It is a plane parallel solid etalon whose internal reflections interfere in a way that different frequencies leave the etalon at different angles. The VIPA has very high angular dispersion, 30 to 40 times higher than a conventional dispersion grating, but a lower free-spectral range (FSR) in the tens or hundreds of GHz, which depends on the etalon thickness and the refractive index of the material.

A basic VIPA spectrometer is described on figure 1.9(a): after passing through the sample, the comb light is coupled as a plane beam with a cylindrical lens into the VIPA at a slight angle, and the different beams exiting the etalon are cross-dispersed by a dispersion grating and imaged onto a 2D CCD camera. A schematic of the output of the spectrometer onto the camera is displayed on figure 1.9(b). The red dots are the resolved comb modes, separated by the comb mode spacing along the vertical axis and by the VIPA FSR along the horizontal axis, with the whole vertical range containing one VIPA FSR. The 1D spectrum is then reconstructed by following the vertical alignments of comb modes, starting from the bottom of each new line, as shown on the right part of the figure

with the white dots. Figure 1.9(c) shows a typical image recorded by the camera. The two black lines represent the limits of one VIPA FSR. Each dot corresponds to a resolved comb mode, with different colors corresponding to their respective intensities. Darker colours correspond to higher optical power. Some brighter spots are visible, corresponding to modes absorbed due to molecular absorption.

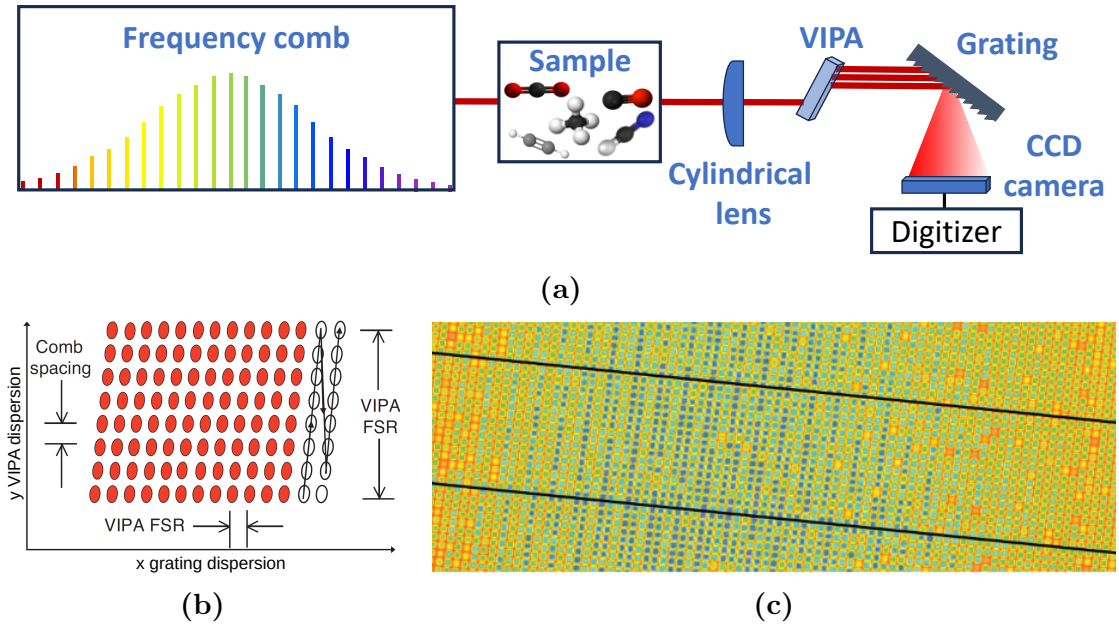

Figure 1.9 : (a) - Schematic of a VIPA spectrometer. The comb light is focused as a plane with a cylindrical lense in the VIPA aperture. The VIPA diffracted beams are then cross-dispersed with a grating, and imaged onto a CCD camera. **(b)** - Schematic of the output of a VIPA spectrometer recorded onto a camera. The resolved comb modes (red dots) are separated by the comb mode spacing along the y axis and by the VIPA FSR along the x axis. The full y range corresponds to one VIPA FSR. The frequency axis is shown on the right part of the image, with black arrows on white dots. **(c)** - Image from a camera. Each dot correspond to a resolved comb modes. The different colors correspond to different intensities of the comb modes, the darker the more optical power. Some brighter spots are visible, due to molecular absorption of certain comb modes. **(b)** and **(c)** reproduced from Diddams *et al.* (2007).

The typical performances of a VIPA spectrometer are:

- frequency resolution $\leq$ 1 GHz,
- compatible with enhancement cavities,
- spectral coverage $<$ 100 cm^{-1},
- time resolution $\sim$ 10 µs,

- acquisition rate depending on the camera, typically in the hundreds of Hz,
- $NEA^{1s} = 10^{-10}$ cm^{-1} $Hz^{-1/2}$ per spectral element.

The first demonstration of a VIPA spectrometer with a frequency comb was performed by Diddams *et al.* (2007) in the visible range, and VIPA spectrometers have been demonstrated in the mid-infrared for more than a decade (Nugent-Glandorf *et al.*, 2012). To the best of my knowledge, the record frequency resolution for a mid-infrared VIPA spectrometer is 190 MHz (Roberts *et al.*, 2020). While VIPA etalons have not yet been demonstrated at longer infrared wavelengths than the 3-5 µm range, dispersive spectrometers using instead an immersion grating have achieved a resolution of 460 MHz in the 8-10 µm region (Iwakuni *et al.*, 2019).

An important work was presented by Fleisher *et al.* (2014) where they used a VIPA spectrometer to perform time-resolved frequency comb spectroscopy (TR-FCS). Their setup consisted of a mid-IR frequency comb centered on 3.8 µm coupled to an enhancement cavity with a 1,250 finesse. They used a dither-lock scheme (Adler *et al.*, 2010). The VIPA spectrometer had a resolution of 1 GHz, with a spectral bandwidth of 65 cm^{-1} limited by the physical dimensions of the camera. The time resolution was 25 µs and the camera acquisition rate was 250 Hz. They reported a NEA^{1s} of $1.1\times$ 10^{-9} cm^{-1} $Hz^{-1/2}$ per spectral element. They could follow the concentration over time of the *trans*-DOCO radical after the laser photolysis of a precursor. They also demonstrated the monitoring of multiple reaction products over time. Their demonstration paved the way for reaction kinetics and branching ratios measurement based on TR-FCS. In a follow-up paper, they determined the rate coefficient of the OD+CO $\rightarrow$ *trans*-DOCO reaction (Bjork *et al.*, 2016).

The main advantages of a VIPA spectrometer is the absence of moving parts and its high time-resolution down to the microsecond timescale. This makes it particularly suitable in reaction kinetics experiments, where it enables the monitoring of the evolving concentrations of multiple chemical species over time. Moreover, VIPA spectrometers are fully compatible with enhancement cavities, typically in the dither-lock scheme previously mentioned, enabling a significant increase in sensitivity. One of the drawbacks of a VIPA spectrometer is the sensitivity of the VIPA etalon to temperature. Under temperature variations it may expand or contract, inducing a change on its FSR and resulting in a change of position of the comb modes on the camera. As the technique heavily relies on calibration ("dark") frames of the camera to extract quantitative information from data, the modes wandering from pixels to pixels due to the changing FSR may tamper with

the calibration. The other drawback of the VIPA spectrometer is the limitation of the spectral bandwidth by the physical dimensions of the camera, typically below 100 cm^{-1}.

1.3.3 Vernier spectrometer

The Vernier spectrometer is another approach to broadband comb light detection. In this case, the comb is filtered using an optical cavity, yielding a much larger repetition rate. The cavity FSR is set so that every m^{th} comb mode is resonant with every n^{th} cavity mode, with $\mathrm{FSR}/f_{rep} = m/n$ the Vernier ratio. The comb transmitted by the cavity then has a repetition rate $m \times f_{rep}$. The successive transmitted comb modes are then sufficiently spaced in frequency to be resolved with a standard grating spectrometer. As the length of the cavity is tuned, using a piezoelectric transducer (PZT), different families of comb modes will successively be in resonance with the cavity modes. It is worth mentioning that the cavity also acts as an enhancement cavity.

The typical performances of a Vernier spectrometer are:

- frequency resolution $\geq$ 1 GHz but comb mode resolution is achievable,
- spectral coverage $\sim$ 200 cm^{-1}, up to 2000 cm^{-1},
- time resolution $\sim$ 10 ms,
- acquisition rate $\sim$ 20 Hz,
- $\mathrm{NEA}^{1s} = 10^{-10}$ cm^{-1} $Hz^{-1/2}$ per spectral element.

The first demonstration of cavity-enhanced spectroscopy with a frequency comb was presented by Gherman & Romanini (2002) in a Vernier approach. Gohle *et al.* (2007) later proposed a setup for a Vernier spectrometer, based on a simple spectrograph and a CCD camera. A tilting mirror was synchronized with the cavity length scan, allowing to streak along the vertical axis of the camera the cavity transmission diffracted by the grating along the horizontal axis. As the cavity length is scanned and different families of comb modes are successively in resonance, they are imaged succesively onto the CCD array. It results in a 2D image that can be reordered into a 1D spectrum, similarly to the VIPA spectrometer. An alternative approach was proposed by Rutkowski & Morville (2014) called Vernier continuous-filtering. The CCD camera and the tilting mirror are replaced by a rotating grating and a photodetector. This approach is detailed below.

With $L_0 = c/f_{rep}$ the perfect match cavity length, the cavity length can be changed to $L_0 + \Delta L$, creating a cavity free-spectral range $\mathrm{FSR} = f_{rep}(1 - \Delta L/L_0)$ and inducing a

relative mismatch between the comb and the cavity $\epsilon = 1 - \mathrm{FSR}/f_{rep} = \Delta L/L_0$. While the cavity length can be set so that every m^{th} comb mode is resonant with every n^{th} cavity mode, a high Vernier ratio (or low value of ϵ) allows comb modes adjacent to the perfect coincidence of the comb-cavity modes to partially resonate with the cavity. This leads to a low resolution Vernier filtering, with each order having a Lorentzian lineshape $\delta\nu_v = c/\Delta\mathcal{F}$ (with $\mathcal{F} = \mathrm{FSR}/\Gamma$ the cavity finesse and Γ the cavity FWHM) and being separated from the next order by the Vernier free-spectral range $\mathrm{FSR}_v = c/\Delta L$.

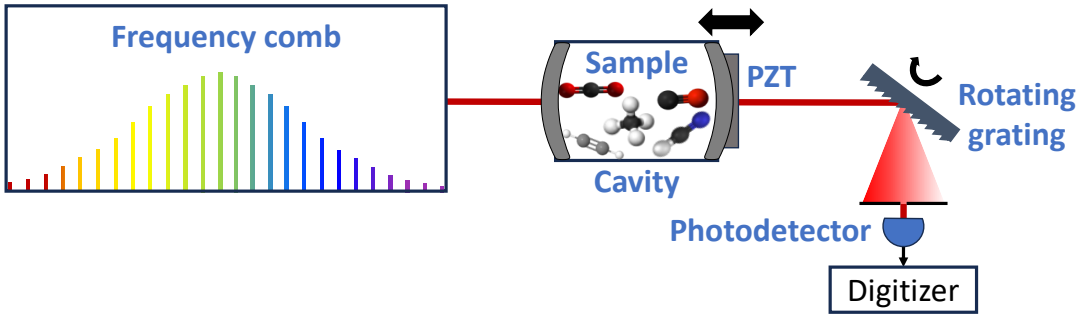

Figure 1.10 : Schematic of a continuous-filtering Vernier spectrometer. The comb is coupled into an optical cavity which acts as a filter and an enhancement cavity. The cavity length is slightly detuned from the comb repetition rate, yielding consecutive orders of Vernier filters. The cavity transmitted light is dispersed onto a grating. Only a fraction of the diffracted light is allowed to pass through an aperture, and recorded with a photodetector. As the cavity is scanned in length, consecutive Vernier orders are transmitted. The grating is synchronously rotated to keep the same beam on the photodetector. In one scan of the cavity, the whole comb spectrum can then be recorded.

The setup they presented is simply described as the one shown on figure 1.10. The cavity is scanned in length with a piezo actuator (PZT) mounted on the back of a cavity mirror, and the grating is synchronously rotated. By adjusting their relative amplitude and phase, the beams diffracted by the grating are quasi stationary in space, whereas the transmitted comb teeth are swept as the cavity length is scanned. This allows to scan the entire comb spectrum in a single diffracted beam. A spatial filter is used to block the other diffracted beams. A record NEA^{1s} of 6×10^{-11} cm^{-1} $\mathrm{Hz}^{-1/2}$ per spectral element was reported, with 10,000 spectral elements recorded in 100 ms, a 1 GHz resolution and a 300-finesse cavity. In a second attempt (Rutkowski & Morville, 2017), they reported a $\mathrm{NEA}^{1s} = 1.1 \times 10^{-10}$ cm^{-1} $\mathrm{Hz}^{-1/2}$, with 31,300 spectral elements acquired in 1s, covering 2000 cm^{-1}. The resolution was 2 GHz and the cavity finesse 3,000.

Khodabakhsh *et al.* (2016) presented a continuous-filtering Vernier setup in the mid-infrared. In a second article (Khodabakhsh *et al.*, 2017), they reported $\mathrm{NEA}^{1s} =$

1.7×10^{-9} cm^{-1} $Hz^{-1/2}$ per spectral element with a 8 GHz resolution and a 25 ms acquisition time.

Although Vernier continuous-filtering is a sensitive technique, its main drawbacks are the precise synchronization of the tilting/rotating mirror/grating and the cavity length sweep, the instrumental function (due to the Lorentzian envelope of a Vernier order) convolved with the cavity transmission, the relative frequency scale calibration based on an etalon and the rather low resolution achievable in a single scan.

1.3.4 Fourier transform spectrometer

Fourier transform spectroscopy has been a major tool for decades for molecular spectroscopy in the infrared (Griffiths *et al.*, 2007), usually referred to as FTIR. It has been mainly used with so-called incoherent thermal souces, typically heated SiC producing a continuum of thermal radiations in the infrared. These sources can be replaced by optical frequency combs, as was demonstrated by Mandon *et al.* (2009). Frequency combs drastically improve Fourier transform spectroscopy compared to an incoherent light source. The significantly higher spectral brightness of frequency combs leads to an increased signal-to-noise ratio for the same acquisition time. Prior to this demonstration, Tillman *et al.* (2005) and Mandon *et al.* (2007) performed Fourier transform spectroscopy with femtosecond modelocked lasers, respectively in the mid and near-infrared. The first demonstration of cavity-enhanced Fourier transform spectroscopy with an OFC was presented by Kassi *et al.* (2010). They coupled a Ti:sapphire comb with a 80 MHz repetition rate to a cavity with twice the FSR. They designed a locking scheme to actively lock the cavity to the comb, using an acousto-optic modulator to generate an error signal. The cavity length was then locked to the comb with a PZT and a PID. Unlike previous demonstrations, they used a continuous scanning FTIR. They reported a $NEA^{1s} = 3\times10^{-7}$ cm^{-1} $Hz^{-1/2}$ with a resolution of 3 GHz.

Figure 1.11(a) shows a typical setup combining a frequency comb and a Fourier transform spectrometer. After passing through the sample, the comb light is coupled into the Michelson interferometer. The beam is separated on a 50/50 beamsplitter, with one "static" arm (red) reflecting off a fixed mirror, while the other reflects off a moving mirror (blue). As the mirror position is scanned, the comb modes are Doppler shifted by $\pm 2v/c$ with v the speed of the mirror and c the celerity of light, and the optical path difference (OPD) between the two arms of the interferometer increases. Both arms recombine on the beamsplitter, yielding two outputs recorded with two photodetectors in a balanced

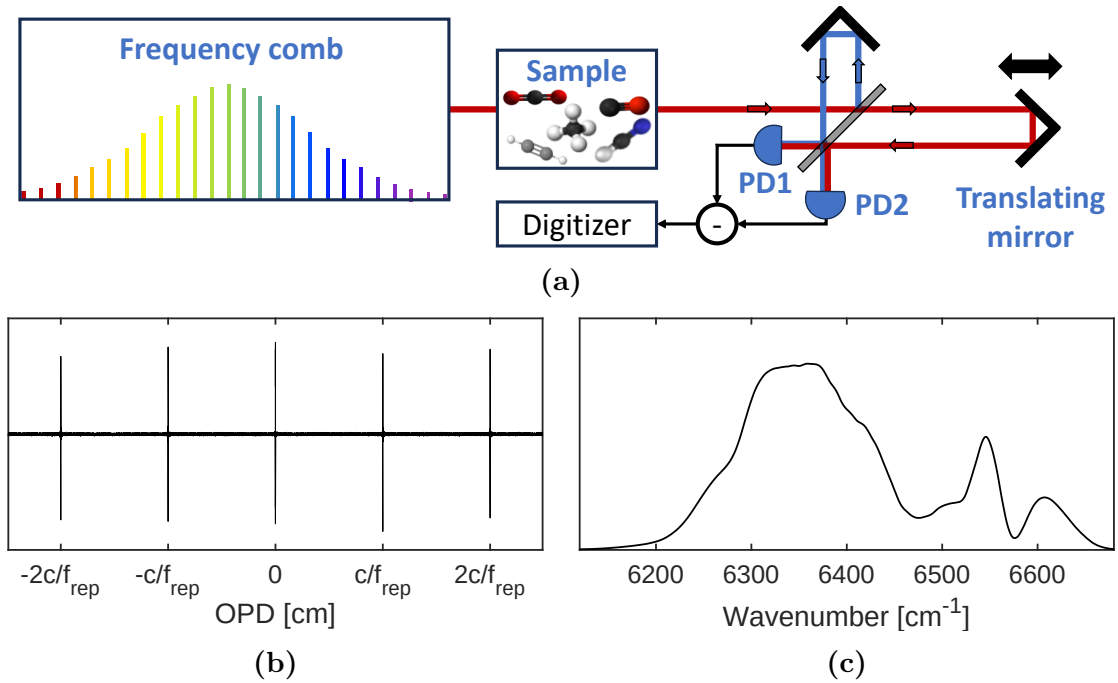

Figure 1.11 : (a) - Schematic of a Fourier transform spectrometer. The comb light is separated with a beamsplitter into two arms of the Michelson inteferometer (transmitted, reflected). Each arm reflects off a corner cube mirror. One mirror is fixed, while the other can translate. The reflected beams recombine on the beamsplitter, and the two outputs of the interferometer are recorded with balanced detection (PD1,2: photodetector). **(b)** - A typical FTS interferogram with a frequency comb, exhibiting bursts spaced by c/f_{rep} in the OPD domain. **(c)** - The spectrum obtained from the FFT of a single-burst interferogram.

detection scheme. The interference pattern thus recorded is called an interferogram. With a frequency comb, the interferogram exhibits bursts evenly spaced by c/f_{rep} in the OPD domain, as seen on figure 1.11(b). These bursts correspond to the OPD values where both arms are in phase. Computing the fast Fourier transform (FFT) of the interferogram then gives the spectrum. Figure 1.11(c) shows the spectrum obtained for a single-burst interferogram. As shown on figure 1.12, the beatnote between the pairs of unshifted (blue) and shifted (red) comb modes interfere and produce a down-converted acoustic comb on the photodetector (black), with a down-conversion factor equal to $2v/c$. While typical FTS exhibit nominal resolution in the tens of MHz, the sub-nominal method enables an achievable resolution equal to the comb modes linewidth (typically on the order of the kHz), as will be detailed in section 1.4.2.

The typical performances of a FTS coupled to an optical frequency comb are:

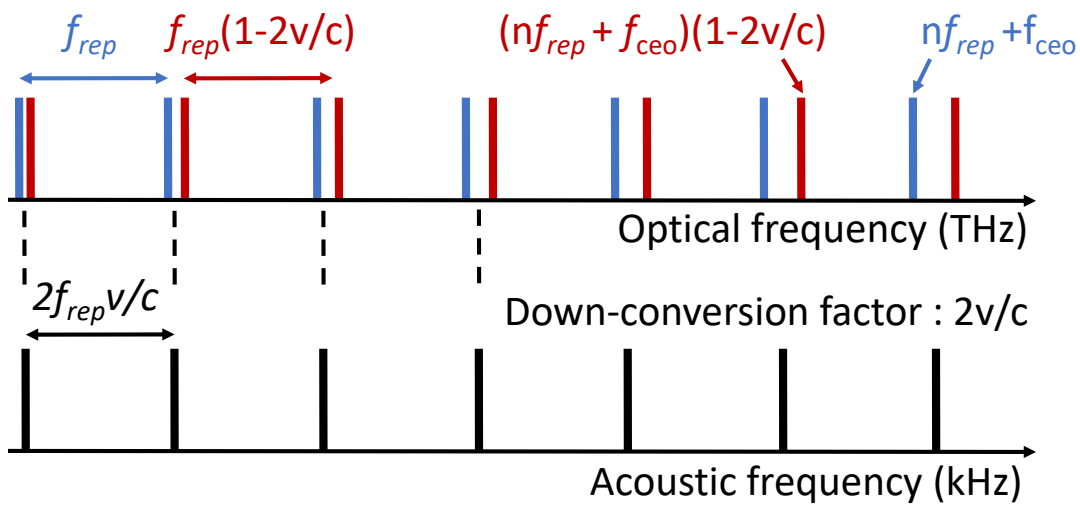

Figure 1.12 : Down-conversion of a frequency comb from optical to acoustic frequencies by a Fourier transform spectrometer. The beatnotes from pairs of fixed (blue) and Doppler-shifted comb modes (red) on the photodetector yield an acoustic comb with a mode spacing $2f_{rep}v/c$. The down-conversion factor is $2v/c$ with v the speed of the interferometer translation stage and c the celerity of light.

- frequency resolution down to the comb modes linewidth ($\sim$ kHz) with the sub-nominal method,
- compatible with enhancement cavities,
- spectral coverage as broad as the spectral range of the beamsplitter,
- acquisition rate $\leq$ Hz, one interferogram every few seconds,
- NEA^{1s} $\sim 10^{-10}$ cm^{-1} Hz $^{-1/2}$ per spectral element.

An important milestone for frequency comb Fourier transform spectroscopy was the work presented by Foltynowicz *et al.* (2011). They locked an Er:fiber comb with a repetition rate of 250 MHz to a 60 cm long cavity, whose finesse was 8,000, using the Pound-Drever-Hall locking scheme (PDH, see section 2.3.1). They used a fast-scanning, twice-folded Michelson interferometer for fast acquisition, and an autobalanced detector (Hobbs, 1997) to reach shot-noise limited sensitivity. They reported a NEA^{1s} = 3.4×10^{-11} cm^{-1} Hz$^{-1/2}$ per spectral element at a resolution of 380 MHz. In a following article, Foltynowicz *et al.* (2013) presented a cavity-enhanced frequency comb Fourier transform spectrometer in the mid-infrared. The comb was locked with a two-point PDH lock to a 3,800 finesse cavity. They retrieved a NEA^{1s} = 6.9×10^{-11} cm^{-1} Hz$^{-1/2}$ per spectral element, with a resolution of 800 MHz.

Nowadays, spectroscopic measurements are routinely conducted in the mid-infrared, in the molecular fingerprint regions at 3-5 µm (Khodabakhsh *et al.*, 2016 ; Sadiek *et al.*, 2020 ; Sadiek *et al.*, 2023 ; Hjältén *et al.*, 2023) and 8 µm (Hjältén *et al.*, 2021).

Using a FTS for frequency comb spectroscopy benefits from its robustness, as the technique has been around for decades. The improvements of fast-scanning FTS and autobalanced detection greatly contributed to increase the sensitivity of the technique, compared to older step-scan FTIRs. A FTS also has the advantage of having the broadest achievable spectral bandwidth, being only limited by the spectral range of the beamsplitter and detector. A FTS can also resolve individual comb modes and provide an absolute frequency axis with the sub-nominal method, which will be covered in section 1.4.2. The main drawback of these spectrometers however, is the reliance on mechanical moving parts. This results in a relative slow acquisition rate, compared to other spectrometers, which makes a FTS less suitable to time-resolved spectroscopy, although it has been performed with an FTIR (Smith & Palmer, 2006).

1.3.5 Dual-comb spectrometer

Dual-comb spectroscopy (DCS) is a form of Fourier transform spectroscopy without the Michelson interferometer, and involves no moving part. Instead of a Doppler-shifted comb by the moving mirror of the interferometer, a second frequency comb (with a slightly different repetition rate than the first comb) is used as a reference to map the first comb modes. This approach was first proposed by Schiller (2002) as a way to measure the transmission and phase properties of a sample. In their proposed setup, one comb interrogates the sample while the second comb acts as a local oscillator to retrieve the change in amplitude and phase that each probe comb mode has undergone. The schematic of a dual-comb spectrometer shown on figure 1.13 is very close to the one they proposed. This is equivalent to the asymmetrical "dispersive" approach in FTIR (Griffiths *et al.*, 2007), on the contrary of the symmetrical approach where both combs probe the sample.

The principle of DCS is shown on figure 1.14. The two combs, of repetition rates f_{rep} (in blue) and $f_{rep} + \delta f_{rep}$ (in red), are detected by the same photodetector. Each pair of comb modes produces a beatnote in the radiofrequency domain. The down-converted radiofrequency comb then has a mode spacing equal to the repetition rate difference δf_{rep}. The down-conversion factor then does not depend on the speed of a moving part of a Michelson inteferometer, but solely on the ratio $\delta f_{rep}/f_{rep}$. The time-domain signals produced by the two combs is analogous to interferograms from Fourier transform spectroscopy, and

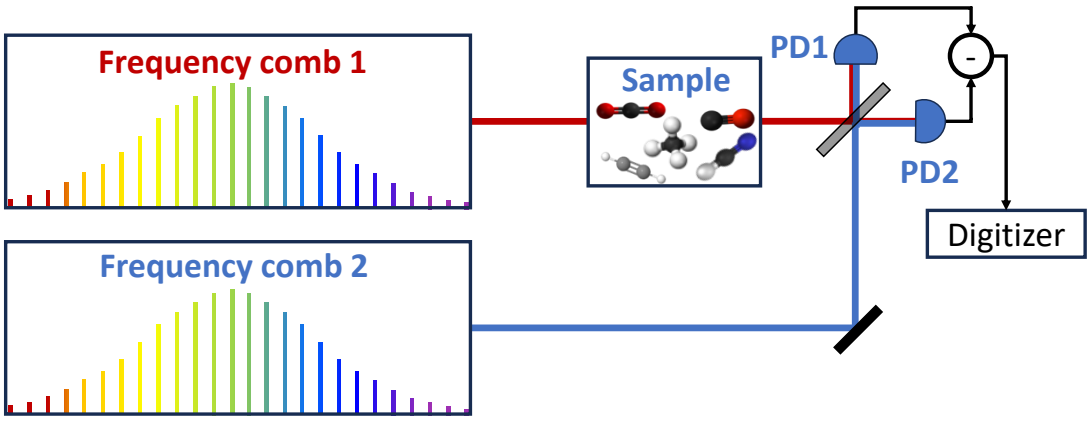

Figure 1.13 : Schematic of a dual-comb spectrometer. The probe comb goes through the sample while the local oscillator comb goes around the cell. Their repetition rates are slightly detuned. They recombine on a beamsplitter, and each output is recorded with photodetectors (PD1,2) in a balanced detection scheme.

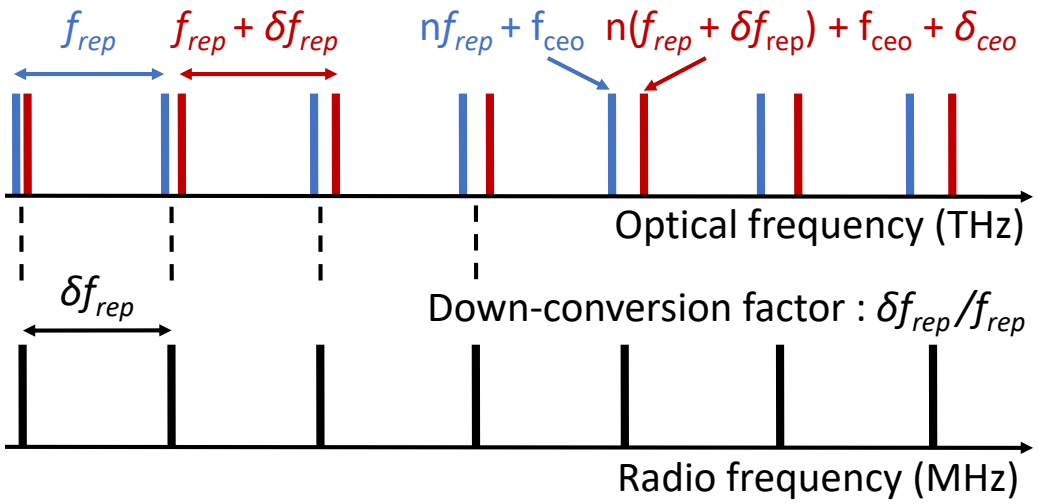

Figure 1.14 : Down-conversion of frequency combs from optical to radiofrequencies by a dual-comb spectrometer. The beatnotes from pairs of modes from the probe comb (red) and the local-oscillator comb (blue) on the photodetector yield a radio comb with a mode spacing δf_{rep}, the relative difference in the two combs repetition rates. The down-conversion factor is $\delta f_{rep}/f_{rep}$.

can be recorded with standard photodetectors whose bandwidths lie in the MHz range. The acquisition time to resolve the radiofrequency comb teeth is $1/\delta f_{rep}$. There is a direct trade-off between acquisition time and spectral coverage. For example, a 100 MHz comb with a million modes can be resolved in a few milliseconds (Coddington *et al.*, 2016). However, it is important to note that single shot spectra have a low SNR and thus requires averaging of successive acquisition. To do so, the two combs need to maintain a relative coherence time longer than the acquisition time. Stabilizing both combs is thus necessary to achieve high SNR. The time coherence of most dual-comb spectrometers is of the order of 1 s. However, Chen *et al.* (2018) presented a phase-stable dual-comb interferometer with a time coherence of 2,000 s. The typical performances of a dual-comb spectrometer are:

- frequency resolution down to the comb modes linewidth ($\sim$ kHz) with fully-referenced combs,
- compatible with enhancement cavities,
- spectral coverage $\sim$ hundreds of cm^{-1},
- time resolution $\sim$ 10 µs,
- acquisition rate set by δf_{rep} typically in the 100 Hz-1 kHz range.

Dual-comb spectroscopy has notably been used in precise spectroscopy measurements. Coddington *et al.* (2008) performed the measurement of the complex spectrum of hydrogen cyanide gas in a cell with a dual-comb spectrometer centered at 1550 nm with a 100 MHz repetition rate, and retrieved 155,000 comb modes in 1s. Both combs were tightly phase locked to common narrow-linewidth cw lasers for coherent averaging of spectra. Bernhardt *et al.* (2010) later demonstrated the first cavity-enhanced dual-comb spectrometer. An ytterbium-doped fiber comb was coupled into a 230 cm long cavity, whose FSR matches the comb repetition rate, and a finesse of 1,200. The comb was locked with PDH to the cavity. The cavity transmitted light was recombined with the free-running local oscillator comb. They reported a $NEA^{1s} = 1.0\times10^{-10}$ cm^{-1} $Hz^{-1/2}$ with a 4.5 GHz resolution and a single spectrum acquisition time of 18 µs.

The main advantages of DCS over dispersive spectrometers is then its relative ease of use, the absence of moving parts and fully-resolved comb modes below the millisecond-timescale. Compared to FTS, the acquisition time of a single spectra is much faster and without any moving parts. However, the noisy nature of single spectra requires coherent averaging to reach high SNR (Roy *et al.*, 2012). Moreover, acquiring two frequency combs

is an expensive feat and their stabilization is complex for cavity-enhanced applications. A major trend nowadays is then the generation of two distinct combs from the same source, using a variety of approaches. This simplifies the stabilization of both combs (Liao *et al.*, 2020).

In the following section, we will described more precisely the implementation of FTS, the approach used throughout this thesis.

1.4 Fourier transform spectroscopy with frequency combs

As frequency combs are pulsed femtosecond lasers, the interferogram obtained in an FTS is a train of bursts separated by an optical path difference of c/f_{rep}. The longer the OPD, the higher the resolution of the final spectrum. The FTS resolution is obtained as

$$f_{\mathrm{FTS}} = \frac{c}{\Delta_{max}}, \tag{1.12}$$

with f_{FTS} the FTS resolution in Hz and Δ_{max} the maximum OPD of the interferogram. Acquiring two or more bursts allows to resolve individual comb modes. However, a FTS exhibits an instrumental lineshape (ILS), which may result in the distortion of narrow absorption features when a single comb mode is absorbed.

1.4.1 Instrumental lineshape

The spectrum obtained with a FTS usually suffers from ILS, due to both the misalignement and divergence of the beams inside the spectrometer and the finite length of the acquired interferogram. In the case of the collimated laser beam, such as with a frequency comb, the ILS mainly originates from the truncation of the interferogram OPD (Griffiths, 1986). The ILS induces a broadening of absorption lines along with a reduction of their intensity by a few percent, and an oscillation ("ringing") on each side of the line (Davis, 2001). Assuming a boxcar function for the interferogram truncation, the ILS in the frequency domain is then a cardinal sine function:

$$f_{\mathrm{ILS}}(\nu, \nu_0) = \frac{\Delta_{max}}{c} \frac{\sin\left[\pi(\nu - \nu_0)\Delta_{max}/c\right]}{\left[\pi(\nu - \nu_0)\Delta_{max}/c\right]}, \tag{1.13}$$

with zero crossings at values of $\nu - \nu_0$ that are integer multiples of c/Δ_{max}. In the frequency domain, the FTS spectrum is thus convolved with the ILS. As the comb modes have

linewidths orders of magnitude narrower than the FTS nominal resolution, they can be approximated as Dirac δ-functions. The convolution then simplifies to a product, and the spectrum after the Fourier transform is obtained as the sum of all the comb mode powers P_n multiplied by their corresponding ILS:

$$S_{\mathrm{FTS}}(\nu) = A \sum_n P_n f_{\mathrm{ILS}}(\nu, \nu_n), \tag{1.14}$$

with A a parameter accounting for the detector gain and responsivity, and ν_n the frequency of the n^{th} comb mode.

Figures 1.15(a) and 1.15(b) display the ILS resulting from the absorption of several comb modes by a broad absorption line, and the absorption of a single comb mode due to an absorption line narrower than the comb repetition rate. The nominal resolution of the

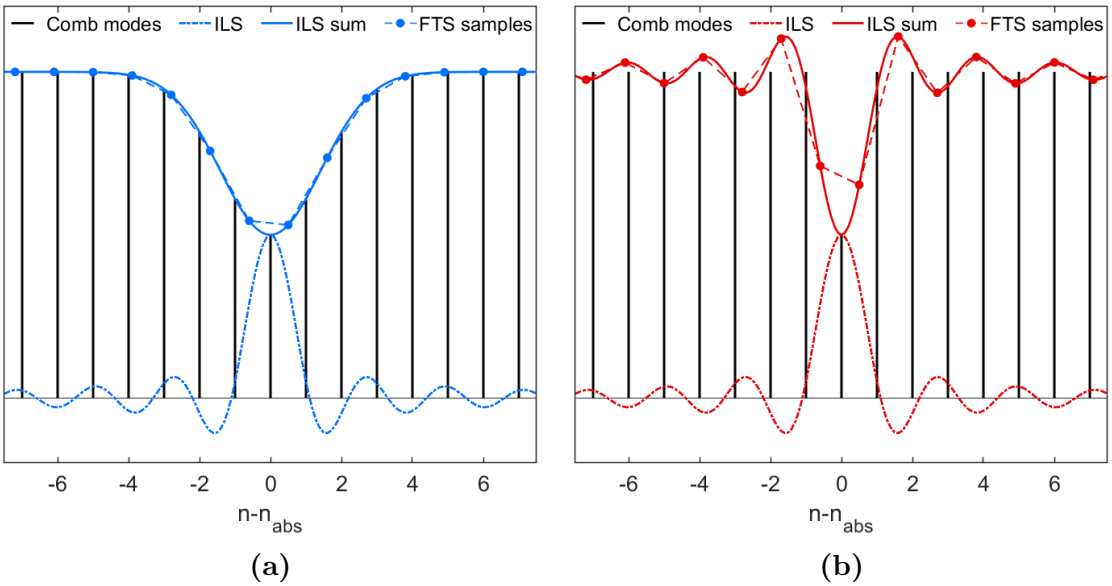

Figure 1.15 : Comparison of ILS for an absorption line **(a)** - broader and **(b)** - narrower than f_{rep} and with a FTS nominal resolution $f_{\mathrm{FTS}} > f_{rep}$. The vertical black lines represent the comb modes, the dashed lines represent the ILS on the most absorbed comb mode of index $\mathrm{n_{abs}}$, the solid lines depict the sum of the ILS for all comb modes and the circular markers show the FTS sampling points, with a dashed trace as a guide to the eye. The x-axis shows the comb mode index centered on $\mathrm{n_{abs}}$. In the case of a broad absorption line spanning several comb modes in **(a)**, no distortion due to ILS is visible and the FTS sampling points map the absorption profile. However, with a narrow line only absorbed by one comb mode in **(b)**, the summed ILS exhibits a strong ringing due to the ILS from the absorbed comb mode. The FTS thus samples the summed ILS, and the retrieved absorption feature is broadened and distorted. The intensity of the absorbed comb mode is not retrieved, due to the contribution of neighboring modes ILS.

FTS is lower than the comb mode spacing, we have $f_{\mathrm{FTS}} > f_{rep}$. In both figures, the black vertical lines represent the comb modes, the dashed-dotted trace corresponds to the ILS at the comb mode central to the absorption line, the solid trace shows the sum of the ILS for all comb modes and the circular markers represent the FTS sampling points. In figure 1.15(a), the absorption profile is sampled by the FTS with no major distortion due to the ILS. However, in figure 1.15(b), the sampled points do not reproduce the absorption of the single comb mode. The broadening and the distortion of the absorption feature is clearly visible. The summed ILS trace exhibits the ILS of the only absorbed comb mode. The absorbed comb mode intensity is not retrieved due to the contribution of the ILS of neighboring comb modes.

The latter case of narrow absorption lines would be common when probing cold gaseous media such as jet expansions. As only one to two comb modes are absorbed per absorption lines, the full absorption profile is not retrieved and suffers from ILS. Measurement of cold, narrow lines with a comb and a FTS thus requires a method called "sub-nominal resolution", allowing to retrieve the intensity of individual comb modes and thus an ILS-free spectrum (*i.e.* reducing the ILS to below the noise level).

1.4.2 Sub-nominal resolution

The sub-nominal method was first introduced by Maslowski *et al.* (2016) while Rutkowski *et al.* (2018) then covered in further details the implementation of the method. The main idea of the sub-nominal method is to match the maximum OPD of a single-burst interferogram to the value of c/f_{rep}. By adjusting the FTS scale of sampled points, it is then possible to retrieve exactly the intensity of individual comb modes.

This is shown on figure 1.16(a), where an interferogram containing several bursts is truncated to a double-sided, single-burst interferogram, with a maximum OPD $\Delta_{max} = c/f_{rep}$. The corresponding FTS sampling is shown on figure 1.16(b). On the contrary of the previous case of figure 1.15(b) where $f_{\mathrm{FTS}} > f_{rep}$, here we have $f_{\mathrm{FTS}} = f_{rep}$. This results in the zero-crossings of the ILS for a given comb mode (dashed-dotted red-trace) to lie on the neighboring comb modes. The individual comb modes are then sampled by the FTS sampling points (red circular markers, with dashed trace for guidance to the eye) and their intensity is retrieved without ILS distortion. The achieved resolution is thus equal to the comb modes width (typically < 1 MHz), with a relatively compact interferometer whose nominal resolution is usually on the order of 100 MHz - 1 GHz.

Sub-nominal resolution can be coupled to the interleaving method, first proposed

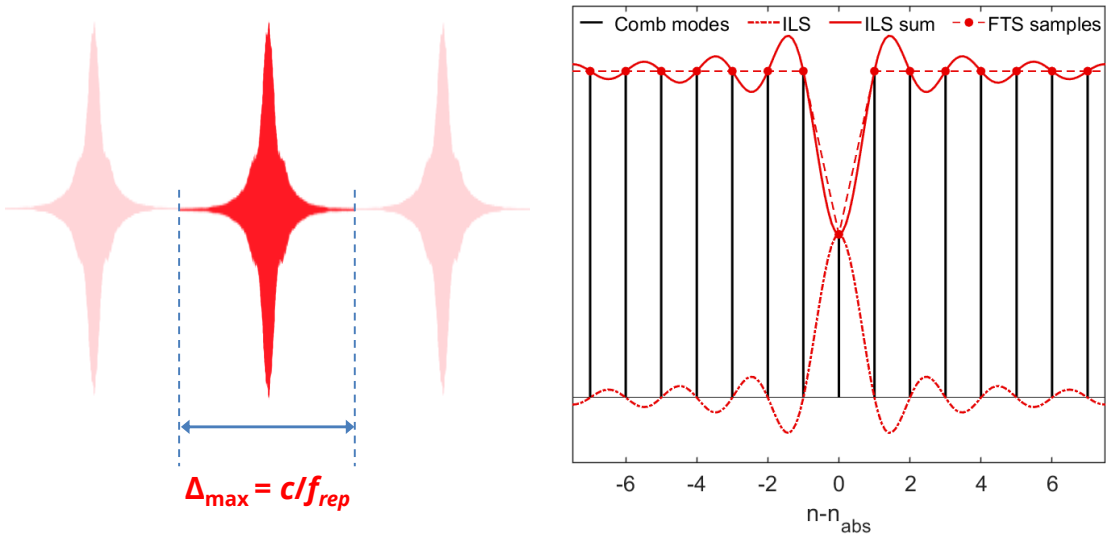

(a) **(b)**

Figure 1.16 : Principles of the sub-nominal method. **(a)** - Interferogram with a train of bursts. Single-burst interferogram is selected with a maximum OPD cut exactly to the value c/f_{rep}. **(b)** - ILS due to an absorption line narrower than the comb mode spacing. The comb modes are shown as the black vertical lines, the dashed-dotted red trace depicts the ILS at the absorbed comb mode of index n_{abs}, the solid red trace shows the sum of the ILS for all the comb modes and the circular markers represent the FTS sampling points. As the maximum OPD of the interferogram is matched to c/f_{rep}, the zero-crossings of the ILS from one comb mode coincide with the neighboring comb modes. The intensity of the absorbed comb mode is retrieved without the contribution of the ILS of other modes.

by Schiller (2002). It offers to acquire spectra at swept values of either f_{rep} or f_{ceo} and interleave them, resulting in an increased density of comb modes in the interleaved spectrum. Coupling the sub-nominal method with interleaving makes it possible to retrieve absorption profiles narrower than the comb mode spacing. These methods have been used in a double-resonance experiment (Foltynowicz *et al.*, 2021) and in the study of cooled large molecules (Changala *et al.*, 2019).

The next subsection will present the fast-scanning FTS setup used during this thesis, and cover the calibration of the OPD axis and the data resampling.

1.4.3 Fast-scanning FTS

A schematic of the fast-scanning FTS is shown on figure 1.17, with a twice-folded interferometer geometry. The comb light transmitted by the cavity is split into two beams that each reflect on retro-reflectors (Newport UBBR2.5-1S) mounted back-to-back on a

translation stage (Thorlabs DDS-300).

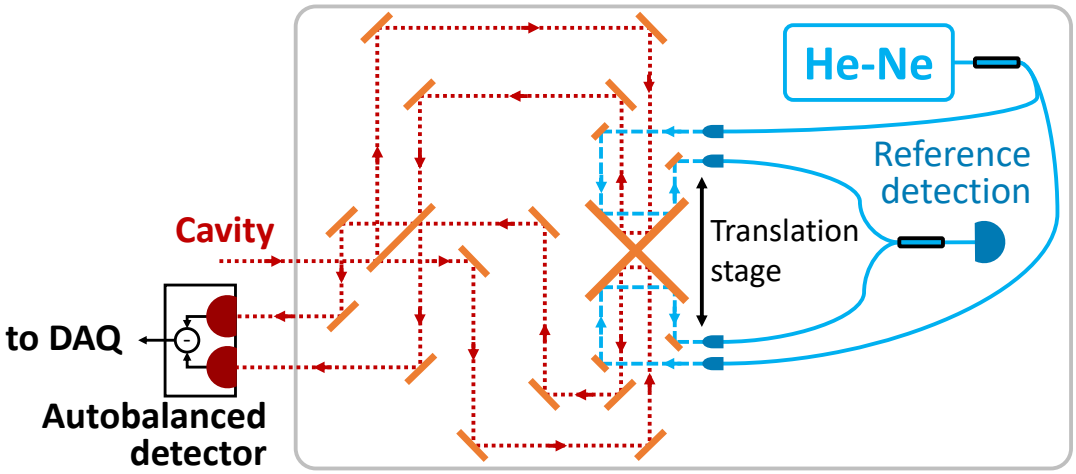

Figure 1.17 : Fourier transform spectrometer. The cavity output (red) is split into two arms with a plate beamsplitter, each arm reflecting on retro-reflectors mounted back-to-back on a translation stage. Both arms recombine on the beamsplitter. An InGaAs autobalanced detector is used to measure both FTS outputs. A frequency-stabilized Helium-Neon laser (blue) is split in half with a fiber splitter, and each arm is coupled to free space where it propagates along the comb towards the retro-reflectors. Both arms are recombined in fiber and the interferogram is measured with a Si photodetector.

These two are detected with a home-built autobalanced detector, based on the JILA design used by Foltynowicz *et al.* (2011), itself based on a design from Hobbs (1997). The detector is optimized to reduce nonlinear effects in the photodiodes. With the autobalancing scheme, the photocurrents from the two photodiodes are subtracted, while the DC offset between them is corrected with a slow feedback loop. This allows to subtract common mode noise, while doubling the interferogram signal since the two FTS outputs are in phase opposition (one path undergoes an even number of reflections while the other undergoes an odd number of reflections). The main difference of this setup compared to literature is the Helium-Neon laser (HeNe, Thorlabs, HRS015B), the frequency-stabilized reference laser to calibrate the OPD as the translation stage is moving, being split in fibers into two arms which reflect off the retro-reflectors in free-space, and are coupled back together in fiber, as shown with the blue path in figure 1.17. The detection of the HeNe interferogram is ensured with a Si photodetector (Thorlabs, PDA36A2). The maximum speed of the translation stage is limited by the bandwidth of both the autobalanced photodetector and the Si photodetector. At 20 dB gain, the latter has a bandwidth of 1 MHz. The translation stage maximum speed was empirically set at 70 mm/s. The total

travel length was set at 270 mm, with data acquisition lasting 4.1 seconds. As data was only acquired on one way of the translation stage, the total acquisition time per spectrum was 10.4 s. The high-speed digitizer was set to acquire 11.6 Mpts at a 2.8 MSample/s acquisition rate, with an alias-free bandwidth of 1.12 MHz.

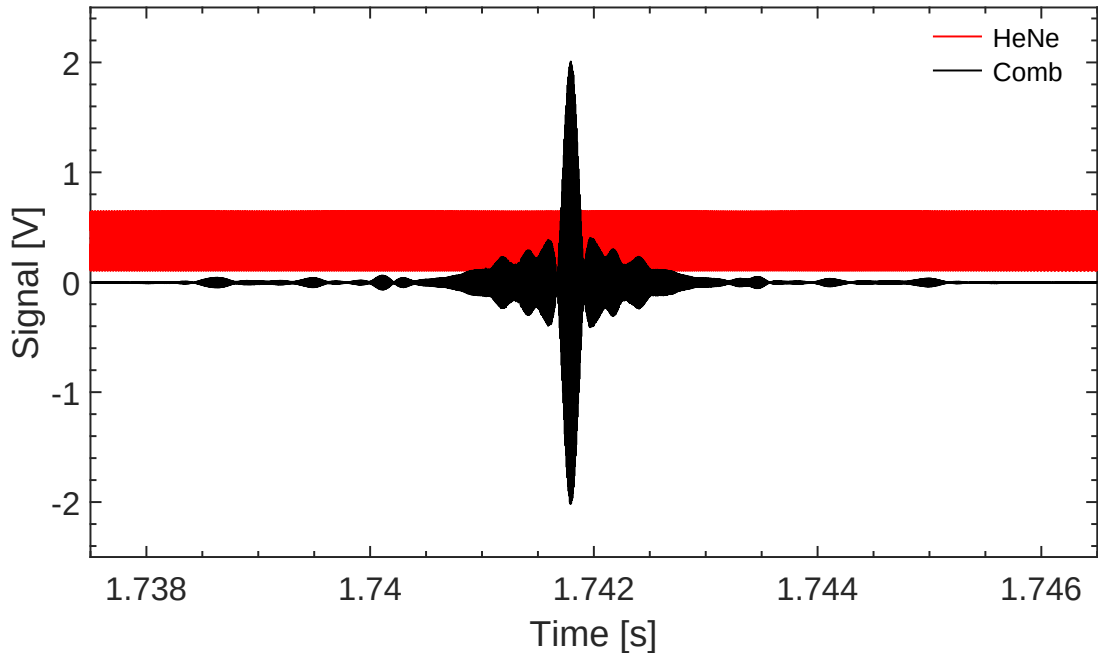

Figure 1.18 : Experimental interferograms zoomed-in on the central burst of the comb interferogram (black trace) with the HeNe interferogram in the background (red trace).

A typical raw output from the FTS is shown on figure 1.18, where the view is zoomed and centered on the burst of the comb interferogram, in the black trace. The HeNe interferogram is visible in red. A close-in view of the burst is displayed on figure 1.19(a), where individual data points are visible for each interferogram. After subtraction of the DC offset on the HeNe signal, the comb interferogram is resampled at the interpolated maxima, minima and zero-crossings of the HeNe interferogram as shown on figure 1.19(b). As the interpolated points are separated by a quarter of the HeNe wavelength λ_{HeNe}, this yields an OPD step $\Delta_{\mathrm{OPD}} = \lambda_{\mathrm{HeNe}}/4$. As both the comb and the HeNe propagate on both arms of the FTS, the maximum OPD is then 4 times the actual displacement of the translation stage. When it moves by λ_{HeNe}, the OPD changes by $4\lambda_{\mathrm{HeNe}}$. The translation stage being 30 cm long, the nominal resolution of the FTS is 250 MHz. However, as was shown in 1.4.2, it is possible to go beyond the nominal resolution of the FTS. This will be necessary to resolve the narrow-linewidth absorption lines of jet-cooled molecules.

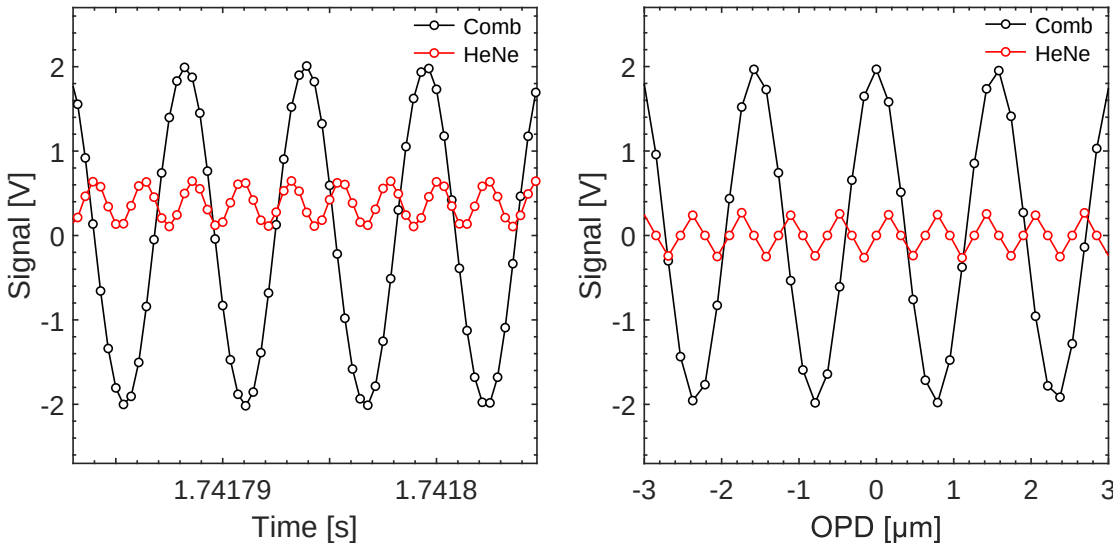

Figure 1.19 : (a) - Zoomed in view of the central burst of the comb raw interferogram (black dotted trace) with the raw HeNe interferogram (red dotted trace). **(b)** - The same part of both interferograms after resampling at the zero-crossings, maxima and minima of the HeNe interferogram.

1.5 Conclusion

In this chapter, we have seen the properties of frequency combs and how they can be exploited for spectroscopy with different spectrometers. In particular, coupling a frequency comb with a Fourier transform spectrometer provides a broadband and versatile spectroscopic measurement tool. Using the sub-nominal and interleaving methods, it is possible to map absorption lines that are narrower than both the comb mode spacing and the FTS nominal resolution.

Fourier transform spectroscopy is then compatible with optical cavities, and allows to cover a significant part of the infrared region with a single instrument. In the next chapter, we will detail the basics of infrared cavity-enhanced spectroscopy.

2 – Infrared spectroscopy with optical cavities

Reaction kinetics aims at measuring the reaction rates and branching ratios of chemical reactions, by monitoring the concentrations of reactants and products over time. To do so, one requires a tool capable of *in situ*, non-invasive and quantitative measurements coupled to known experimental conditions, such as temperature, pressure and the initial concentrations of reactants. Moreover, the chosen tool should provide simultaneous measurement of different chemical species with a single instrument.

Infrared absorption spectroscopy of molecules in the gas phase fulfills several of these requirements. In absorption spectroscopy, one observes the characteristic signature of a given molecule by shining light from a source (whether it is a coherent source such as a laser or an incoherent one) at a molecular sample and measuring the transmitted intensity of light.

The Beer-Lambert law is the relation describing how the intensity from a light source decreases in an absorbing medium. Considering an initial light intensity $I_0(\nu)$ at a given frequency (ν) [Hz], the intensity $I(\nu)$ at a distance l through the medium is:

$$I(\nu) = I_0(\nu)e^{-\alpha(\nu)l}; \tag{2.1}$$

with $\alpha(\nu)$ [cm^{-1}] the absorption coefficient at ν, which describes an absorption per unit length. The absorption coefficient is related to the absorption cross-section $\sigma(\nu)$ [cm^2/molecule], which is the cross-section of the probability of a photon being absorbed by a molecule:

$$\alpha(\nu) = \sigma(\nu)N; \tag{2.2}$$

with N the molecular density, expressed in molecule/cm^3. Measuring $I(\nu)$ while knowing $I_0(\nu)$ after calibration then yields the absorption coefficient. If the light source emits over a broad range of frequencies, or if the source can be tuned in frequency, one then obtain the *spectrum* of the probed medium over a wide range of frequencies. Such spectrum

will present characteristic absorption features corresponding to the molecules present in the medium. In the infrared, molecules absorb light at energies corresponding to their rotational, vibrational and electronic energy levels. Transitions between rotational levels from two different vibrational levels result in absorption lines centered on the transition frequencies. These lines are grouped in vibrational absorption bands. In atmospheric conditions, it is possible to resolve this so-called rovibrational structure of medium-sized molecules (< 10 atoms) in the gas phase. These rovibrational absorption lines observed exhibit specific lineshapes, which depend on the experimental conditions such as temperature and pressure. If these conditions are monitored during the experiment, and the interaction pathlength between the light and the probed sample is known, it is possible to model the spectrum with absorption profiles and *in fine* retrieve the densities of each molecular species present in the sample.

When probing molecules in the gas phase with infrared spectroscopic techniques, an important concern is the achievable sensitivity or signal-to-noise ratio. An increase in sensitivity can be achieved either by lowering the detection noise floor, or by increasing the signal (absorption of light). Following Beer-Lambert's law (equation 2.1), absorption can be enhanced either by:

- increasing $\alpha(\nu)$ by increasing the concentration of molecular gas,
- probing intense absorption lines,
- enhancing the light interaction pathlength L.

The most simple scheme is a single-pass cell with optical windows on each side of the experimental gas cell, as shown on figure 2.1(a). The interaction pathlength is then equal to the gas cell length. One can then increase the interaction pathlength with a multi-pass cell (White, 1942; Herriott *et al.*, 1964), where the windows have been replaced with mirrors. The probe beam is then coupled into the cell, and will be reflected off each mirror many times, as seen on figure 2.1(b). A multi-pass cell can achieve an effective pathlength dozens of times higher than the cell length itself. To further enhance the interaction pathlength, the multi-pass cell can be replaced with an optical cavity/resonator. As displayed on figure 2.1(c), it is made of (at least) two mirrors. With high-reflectivity coatings, optical cavities can reach effective interaction pathlength of several kilometers from a compact setup (see section 2.2.4.2).

An optical cavity made of two mirrors is called a Fabry-Perot resonator, which exhibits evenly-space discrete resonant frequencies. The transmission and reflection of the

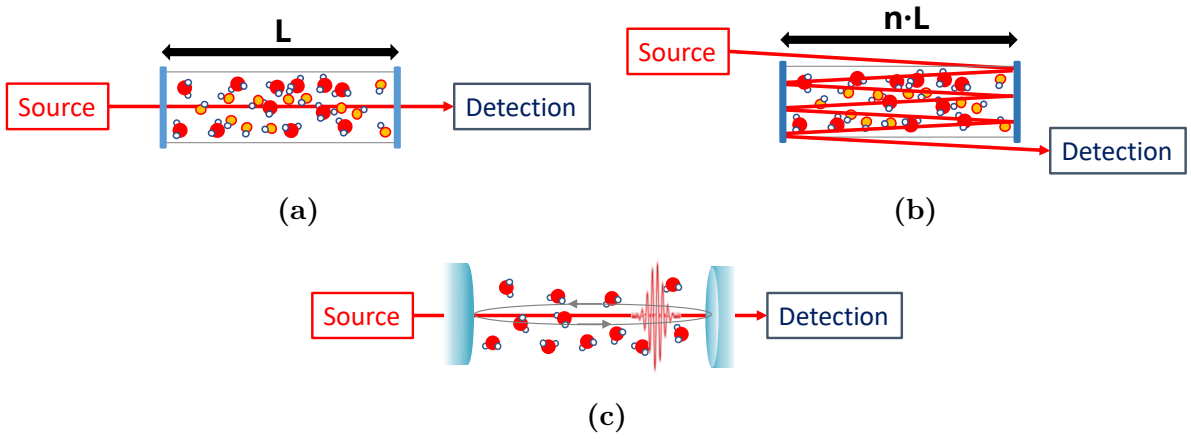

Figure 2.1 : Interaction pathlength enhancement techniques. **(a)** - Single-pass cell absorption. **(b)** - Multi-pass cell absorption. **(c)** - Cell enclosed with high reflectivity mirrors constituting an optical cavity.

resonator can be modelled with the cavity transfer functions, which depend on the cavity length and the reflectivity of the mirrors. When conducting spectroscopic measurements with an intracavity absorber, the transmission of the cavity thus has to be modelled with the transmission function instead of the Beer-Lambert law.

In this chapter, we will cover the spectroscopy of molecules in the infrared, the origin of the absorption coefficient, the absorption lineshapes used to model molecular absorption spectra, the Fabry-Perot cavity and its applications to gas phase spectroscopy, and finally, the methods allowing to lock a laser to a cavity and stabilize the cavity length.

2.1 Infrared spectroscopy

2.1.1 Rotational, vibrational and electronic spectroscopy

Molecules present absorption features in different parts of the electromagnetic spectrum. These features are unambiguous identifiers of the associated molecule. Since molecules have rotational and vibrational degrees of freedom, there exists different rotational and vibrational energy levels. Pure rotational transitions between two rotational levels correspond to frequencies in the microwave region, while vibrational transitions occur in the infrared. The coupling of rotation and vibration allows rovibrational transitions, inducing discrete absorption lines grouped together in absorption bands in all infrared regions. Transitions between different electronic levels of the molecule may also occur, with fre-

quencies typically in the UV, visible and near-infrared ranges. As electronic levels are more widely spaced than vibrational and rotational levels, there are rovibrational transitions within an electronic absorption band, also referred to as rovibronic transitions.

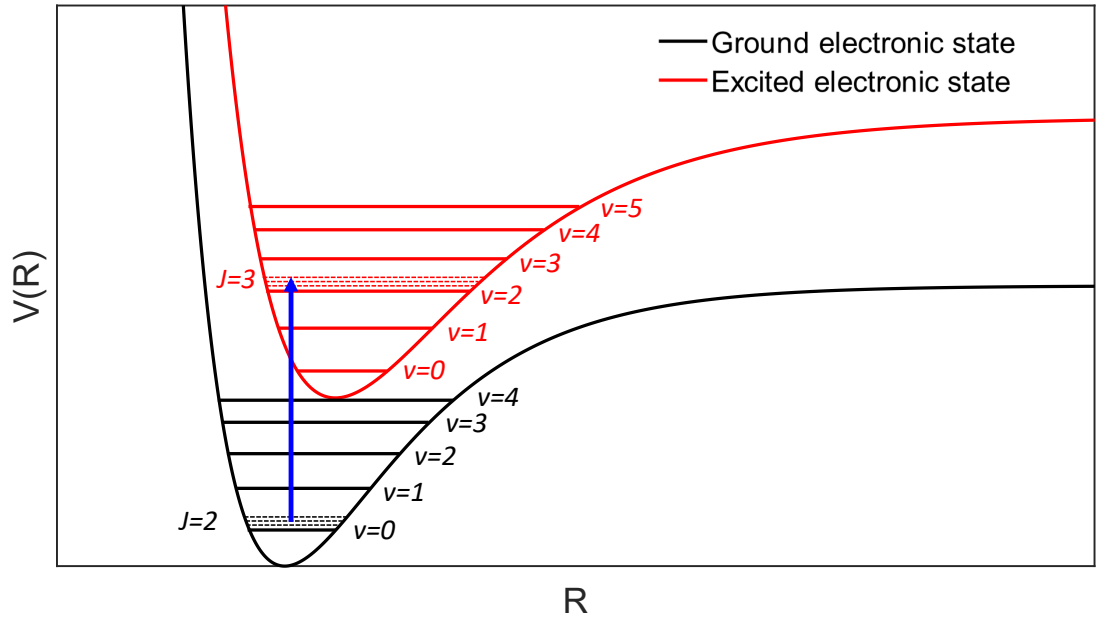

Figure 2.2 : The potential energy curve as a function of internuclear distance is shown for two electronic states of a diatomic molecule, the ground state (black) and an upper excited state (red). The blue arrow represents a rovibronic transition between the two electronic states with $v" = 0 \rightarrow v' = 2$ and $J" = 2 \rightarrow J' = 3$. The vibrational levels are represented as solid horizontal lines, while the rotational levels of the two vibrational levels involved in the transition, as dashed horizontal lines.

A rovibronic transition is shown on figure 2.2. It displays the potential energy curves of two electronic states, in black the ground state and in red an upper excited state. The vibrational levels of each electronic state are represented as horizontal solid lines. The rotational levels are represented as horizontal dotted lines, for the two vibrational levels involved in the transition. The rovibronic transition is shown by the blue vertical arrow. Here, J is the rotational quantum number associated with the rotational level, and v is the vibrational quantum number associated with the vibrational level. The population of rotational, vibrational and electronic levels follows a Boltzmann distribution in the case of local thermodynamic equilibrium (LTE). In such case, we have $T_{rot} = T_{vib} = T_{elec}$.

2.1.1.1 Rotational spectroscopy

Molecules exhibit rotational levels, with transitions between levels corresponding to the microwave region. Lines are spaced by the molecules rotational constant, which depends on both the size of the molecule and its dipole moment. Typical values of the rotational constant are in the range ∼0.1-10 cm^{-1}. For example, CO has a rotational constant of 1.93 cm^{-1}. Pure rotational transitions may only occur from J" to $J' + 1$ (absorption) or J' to J" $- 1$ (emission), following the selection rule $\Delta J = \pm 1$.

2.1.1.2 Vibrational spectroscopy

Molecules also exhibit vibrational motion, with different levels of freedom. The number of vibrational levels of freedom, or vibrational modes of a molecule, depends on how many atoms it possesses and its geometry:

- for a linear molecule with N atoms, there are $3N - 5$ vibrational modes,
- for a non-linear molecule with N atoms, there are $3N - 6$ vibrational modes.

A diatomic molecule then has only 1 vibrational mode. However, not all modes are excited by infrared radiation. The vibration has to induce a change in the dipolar moment of the molecule as atoms move relative to one another, for the mode to be called "IR-active". As an example, figure 2.3(a) displays the vibrational symmetric stretching mode of CO_2. As both oxygen atoms oscillate towards the carbon atom, in opposite directions, no change in the dipole moment is induced. The mode is "IR-inactive". On the contrary, the antisymmetric strecth on figure 2.3(b) and the bending mode on figure 2.3(c) are IR-active, with vibrational frequencies of 2349 cm^{-1} and 667 cm^{-1} respectively. In the case of diatomics, only heteronuclear molecules exhibit an IR-active mode. For most molecules, their fundamental bands lie in the 400-4,000 cm^{-1} range, which corresponds to the mid-infrared (mid-IR) region of the electromagnetic spectrum. This range is often referred to as the molecular fingerprint region.

It is noteworthy that molecules exhibit more bands than only the fundamental ones:

- overtone bands that are weaker than the fundamental band, with $\Delta v = \pm 2, \pm 3, ...$ and the first overtone more intense than the second, the second more intense than the third, and so on,
- combination and difference bands for polyatomic molecules, when two or more bands interact and the resulting vibrational frequency is the sum or the difference of their respective frequencies,

- *hot bands*, when the initial vibrational state of the transition is an excited state.

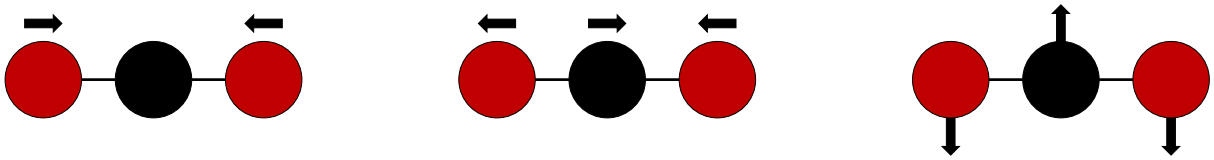

(a) **(b)** **(c)**

Figure 2.3 : Vibrational modes of CO_2, with the carbon atom in black and the oxygen atoms in red. **(a)** - Symmetric streching vibrational mode of CO_2, which induces no change on the dipole moment of the molecule and thus is IR-inactive. **(b)** Antisymmetric streching vibrational mode of CO_2, which is IR-active. **(c)** In-plane bending vibrational mode of CO_2, which is also IR-active.

2.1.1.3 Rovibrational spectroscopy

In the infrared, rotational transitions happen at the same time as vibrational transitions. Infrared spectra then exhibit absorption bands made of several rovibrational lines, corresponding to the different rotational transitions.

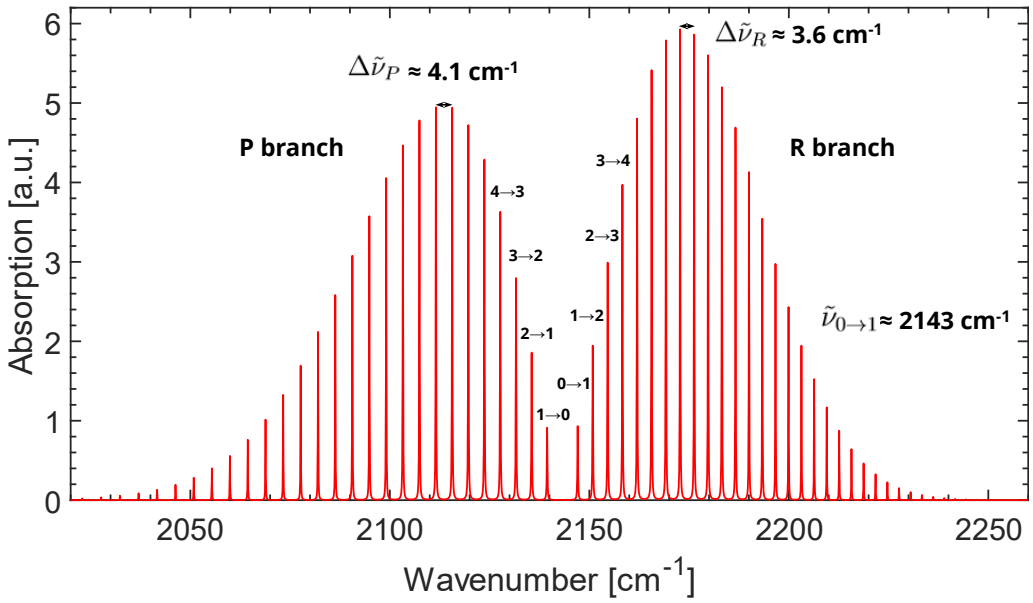

Figure 2.4 : rovibrational spectrum of the fundamental vibrational band v_1 of 0.1 % of $^{12}C^{16}O$ near 2143 cm^{-1} at 1 atm and 296 K. The initial and final rotational quantum numbers are labeled for transitions $J" = 1 - 4$ and $J" = 0 - 3$ for the P and R branches respectively.

Rovibrational lines are seen in 2 groups for a given absorption band: the P and R branches. The P branch corresponds to transitions $J" \rightarrow J' - 1$ ($\Delta J = -1$) and the R branch to transitions $J" \rightarrow J' + 1$ ($\Delta J = +1$). In the case of diatomic molecules with non-zero electronic angular momentum, there exists a Q branch with $\Delta J = 0$. Figure 2.4 displays the spectrum of the fundamental band of CO centered at 2143 cm^{-1}, with a concentration of CO in air [CO] = 0.1 %, a pressure of 1 atm and a temperature of 296 K. The P and R branches are easily identifiable, whereas no Q branch is visible as CO does not exhibit an electronic angular momentum. We remark that as J increases, the spacing between lines in the P branch increases whereas it decreases in the R branch. In other words, the R lines converge while P lines diverge.

2.1.2 Absorption and dispersion coefficients

Absorption lines due to rotational, rovibrational or rovibronic transitions exhibit an absorption profile, centered on the frequency of the transition. This profile, or lineshape, depends on the experimental conditions such as the pressure or the temperature of the studied gas. When measuring absorption spectra, it is important to account precisely for this lineshape to retrieve precise density values. Thus, with the appropriate model of absorption profiles, one can fit absorption spectra and retrieve experimental parameters.

This subsection will first cover the absorption and dispersion of light by molecules, the following subsection will focus on the lineshape function and the different line broadening mechanisms, and the third subsection will concentrate on the absorption profiles commonly employed to model molecular spectra.

2.1.2.1 Complex refractive index

In the vicinity of a molecular transition, the complex refractive index of a molecular gas at a given wavenumber $\tilde{\nu}$ can be expressed as:

$$n(\tilde{\nu}) = n'(\tilde{\nu}) - i\kappa(\tilde{\nu}), \tag{2.3}$$

where $n'(\tilde{\nu})$ and $\kappa(\tilde{\nu})$ are the real and imaginary resonant components, connected by the Kramers-Kronig relations (Demtröder, 2014).

An electromagnetic (EM) wave $E = E_0 e^{i(\omega_0 t - k_0 z)}$ of angular frequency $\omega_0 = 2\pi\tilde{\nu}_0 c$ and wave vector $k_0 = 2\pi\tilde{\nu}_0$ with $\tilde{\nu}_0$ the frequency expressed in wavenumbers, propagates in the z direction through a sample with refractive index $n(\tilde{\nu}_0) = n$ at $\tilde{\nu}_0$. Its angular frequency

is then $\omega_n = \omega_0$ and its wave vector $k_n = k_0 n$. We have:

$$\begin{aligned} E &= E_0 \exp\Big[i(\omega_n t - k_n z)\Big], \\ E &= E_0 \exp\Big[i(\omega_0 t - k_0 n' z + k_0 i\kappa z)\Big], \\ E &= E_0 \exp(-k_0\kappa z) \exp\Big[i(\omega_0 t - k_0 n' z)\Big], \\ E &= E_0 \exp(-2\pi\tilde{\nu}_0\kappa z) \exp\Big[ik_0(ct - n' z)\Big], \end{aligned} \tag{2.4}$$

with $k_0 c = \omega_0$. This equation therefore shows that the imaginary part of the complex refractive index κ is responsible for the **absorption** of the EM wave. After propagating from $z = 0$ to $z = 1/\Big(2\pi\tilde{\nu}_0\kappa\Big)$, the EM wave amplitude has been reduced to $1/e$ of the original amplitude E_0. The real part of the complex refractive index n' is responsible for the **dispersion** of the EM wave, implying its phase velocity $v = c/n'$ is dependent on the frequency. The intensity of the EM wave is $I \propto EE^*$, which diminishes as:

$$I = I_0 e^{-2k_0\kappa z}. \tag{2.5}$$

We can then define general formulas for absorption coefficient $\alpha(\tilde{\nu})$ and the dispersion coefficient $\phi(\tilde{\nu})$ at a wavenumber $\tilde{\nu}$ as:

$$\alpha(\tilde{\nu}) = 2k_0\kappa(\tilde{\nu}), \tag{2.6a}$$

$$\phi(\tilde{\nu}) = 2k_0 n'(\tilde{\nu}). \tag{2.6b}$$

The absorption and dispersions coefficients are then obtained from the complex lineshape function.

2.1.3 Complex lineshape function and lineshape broadening

For a given transition from lower energy level i of energy E_i [cm^{-1}] to upper level j of energy E_j [cm^{-1}] with associated wavenumber $\tilde{\nu}_{ij} = E_j - E_i$, the absorption and dispersion coefficients are obtained from the real and imaginary parts of a complex lineshape function $\chi_{ij}(\tilde{\nu})$ [cm]:

$$\begin{aligned} \alpha_{ij}(\tilde{\nu}) &= S^*_{ij}\, N\, \mathrm{Re}\Big(\chi_{ij}(\tilde{\nu})\Big), \\ \phi_{ij}(\tilde{\nu}) &= S^*_{ij}\, N\, \mathrm{Im}\Big(\chi_{ij}(\tilde{\nu})\Big). \end{aligned} \tag{2.7}$$

with S^*_{ij} [cm^{-1}/(molecule·cm^{-2})] the linestrength of the transition, given here in wavenumbers per column density, and N [molecule/cm^3] the molecular density. The complex lineshape function is normalized, so that the integral of its real part over the absorption

line is equal to unity:

$$\int_{line} \mathrm{Re}\Big(\chi_{ij}(\tilde{\nu})\Big) d\tilde{\nu} = 1. \tag{2.8}$$

The lineshape function thus represents the probability of a photon to be absorbed versus frequency. The area under the absorption line then corresponds to the integrated absorption [cm^{-2}] $S_{ij} = S^*_{ij}\, N$, as seen on figure 2.5 with the red area under the absorption coefficient curve.

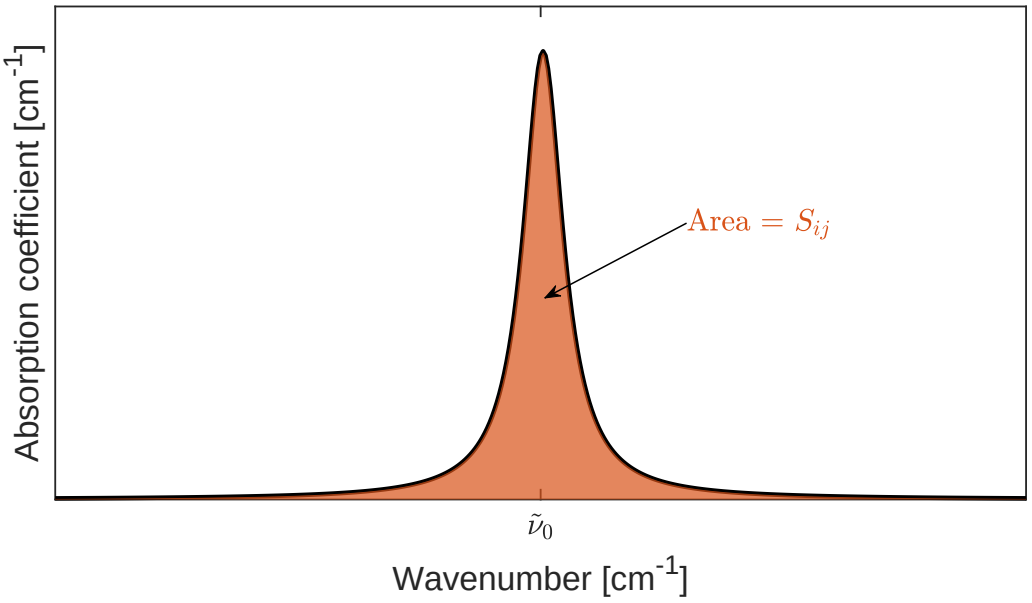

Figure 2.5 : Absorption lineshape of a rovibrational line, in termes of the absorption coefficient over frequency in wavenumbers. The filled orange area below the curve corresponds to S_{ij} the integrated absorption.

The linestrength is dependent on the temperature, therefore on the population of the lower and upper levels i and j. S^*_{ij} can be obtained at any temperature T from its value at a temperature of reference, for example $T_{ref} = 296$ K in the HITRAN2020 database (Gordon *et al.*, 2022):

$$S^*_{ij}(T) = S^*_{ij}(T_{ref}) \frac{Q(T_{ref})}{Q(T)} \frac{\exp(-c_2 E_i/T)}{\exp(-c_2 E_i/T_{ref})} \frac{[1-\exp(-c_2\tilde{\nu}_{ij}/T)]}{[1-\exp(-c_2\tilde{\nu}_{ij}/T_{ref})]}, \tag{2.9}$$

with $Q(T)$ the total internal partition function of the molecule at temperature T and c_2 [cm·K] the second radiation constant, defined as $c_2 = hc/k_B$.

The complex lineshape function takes into account the natural, thermal and pressure broadening effects determining the lineshape of an absorption line.

2.1.3.1 Natural broadening

The natural broadening is due to the finite radiative lifetime of the upper level of the transition. The Heisenberg uncertainty principle states that the uncertainty in energy ΔE times the uncertainty in time Δt is greater or equal than the reduced Planck constant:

$$\Delta E \Delta t \geq \hbar. \tag{2.10}$$

It yields an uncertainty in frequency $\Delta\nu$:

$$\Delta\nu_N = \frac{1}{2\pi\tau_{rad}}; \tag{2.11}$$

with τ_{rad} the radiative lifetime of the upper level. The shorter the lifetime, the larger the frequency uncertainty. For a rovibrational transition, the lifetime is typically of a few milliseconds, which corresponds to $\Delta\nu_N$ ∼10-100 Hz, or equivalently in wavenumbers $\Delta\tilde{\nu}_N$ ∼10^{-10}-10^{-9} cm^{-1}.

The natural broadening gives a Lorentzian lineshape, and its associated complex lineshape function is:

$$\chi_N(\tilde{\nu}) = \frac{1}{\pi}\frac{\Delta\tilde{\nu}_N/2}{(\tilde{\nu}-\tilde{\nu}_{ij})^2 + (\Delta\tilde{\nu}_N/2)^2}, \tag{2.12}$$

with $\Delta\tilde{\nu}_N$ the FWHM and $\tilde{\nu}_{ij}$ [cm^{-1}] the wavenumber of the transition. An absorption line is then always broader than the transition central frequency. Natural broadening is however negligible in front of thermal and pressure broadenings.

2.1.3.2 Thermal broadening

Thermal broadening comes from the speed of the molecules relative to the probe light beam. Due to the Doppler effect, molecules moving towards the light source see blue-shifted photons while molecules moving away see red-shifted photons. This results in a broadening of the absorption lineshape. Thermal broadening is then referred to as Doppler broadening. Since the velocity distribution of molecules in a gas at thermal equilibrium follows a Maxwell law, the associated lineshape function is a Gaussian:

$$\chi_D(\tilde{\nu}) = \sqrt{\frac{4\ln(2)}{\pi\Gamma_D^2}}\exp\left[\frac{-4\ln(2)(\tilde{\nu}-\tilde{\nu}_{ij})}{\Gamma_D^2}\right] \tag{2.13}$$

with Γ_D the FWHM of the Gaussian profile, also named the Doppler width. It is defined as:

$$\Gamma_D = 2\sqrt{\frac{2\,\ln(2)\,k_B T N_A}{M}}\tilde{\nu}_{ij} \tag{2.14}$$

where k_B is the Boltzmann constant, T is the temperature [K], N_A is the Avogadro constant [mol^{-1}], $\tilde{\nu}_{ij}$ the transition wavenumber [cm^{-1}] and M is the molar mass of the molecule [g/mol]. As an example, at an ambient temperature $T = 296$ K, the Doppler width of the P(6) line of the second overtone band (v" $= 0 \rightarrow v' = 3$) of CO is 0.015 cm^{-1} (441 MHz), orders of magnitude higher than the natural linewidth of a rovibrational transition. Doppler broadening is the dominant effect at high temperatures and low pressures ($<<$ 1 Torr). As pressure increases however, it is the pressure broadening that starts dominating.

2.1.3.3 Pressure broadening

Pressure broadening comes from intermolecular collisions, which induce energy exchanges between the colliding molecules. This in turn broadens the absorption lines. The broadening depends on the mean time between collisions τ_C:

$$\Delta\nu_C = \frac{1}{2\pi\tau_C}. \tag{2.15}$$

The higher the pressure, the more probable a collision is to happen, and the smaller τ_C. The broadening then increases linearly with the pressure. We have $\Gamma_C = \Delta\nu_C/c$ the pressure broadening coefficient in cm^{-1}. Similarly to natural broadening, pressure broadening yields a Lorentzian lineshape:

$$\chi_C(\tilde{\nu}) = \frac{1}{\pi}\frac{\Gamma_C/2}{(\tilde{\nu}-\tilde{\nu}_{ij})^2 + (\Gamma_C/2)^2}, \tag{2.16}$$

where Γ_C is the FWHM of the lineshape. The pressure broadening coefficient is often expressed as γ_C, its normalized form relative to pressure in cm^{-1}·atm^{-1}. In air and at ambient temperature, many molecules have collision-broadening around 0.1 cm^{-1}atm^{-1}, yielding a linewidth of 3 GHz (0.1 cm^{-1}) at atmospheric pressure. It is noteworthy to mention that collisions also perturbate the energy levels of molecules, inducing a frequency shift on absorption lines. This pressure shift is also expressed in cm^{-1}·atm^{-1}.

2.1.4 Absorption profiles in atmopsheric conditions

The Gaussian profile due to Doppler broadening is only true at high temperatures and low pressures, while the Lorentzian profile due to pressure broadening is valid at low temperatures and high pressures. In any other case, both effects are usually accounted for with the Voigt profile.

2.1.4.1 Voigt profile

The Voigt profile is the convolution of the Gaussian and Lorentzian profiles aforementionned. The Voigt profile can be approximated with the complex error function, also called the Faddeeva function (Schreier, 1992).

Figure 2.6 compares the normalized absorption profiles of the P(6) line from the second overtone of 0.1 % of CO in argon, at increasing pressures of 1, 100 and 500 Torr. In blue at 1 Torr, the profile is dominated by Doppler broadening and the lineshape is close to a Gaussian. At 100 and 500 Torr, the Lorentzian component from pressure broadening becomes prominent, clearly visible as the Lorentzian function goes to zero on the wings at a slower pace than the Gaussian. The pressure induced frequency shift is also visible as the pressure increases, the peaks are displaced to lower frequencies.

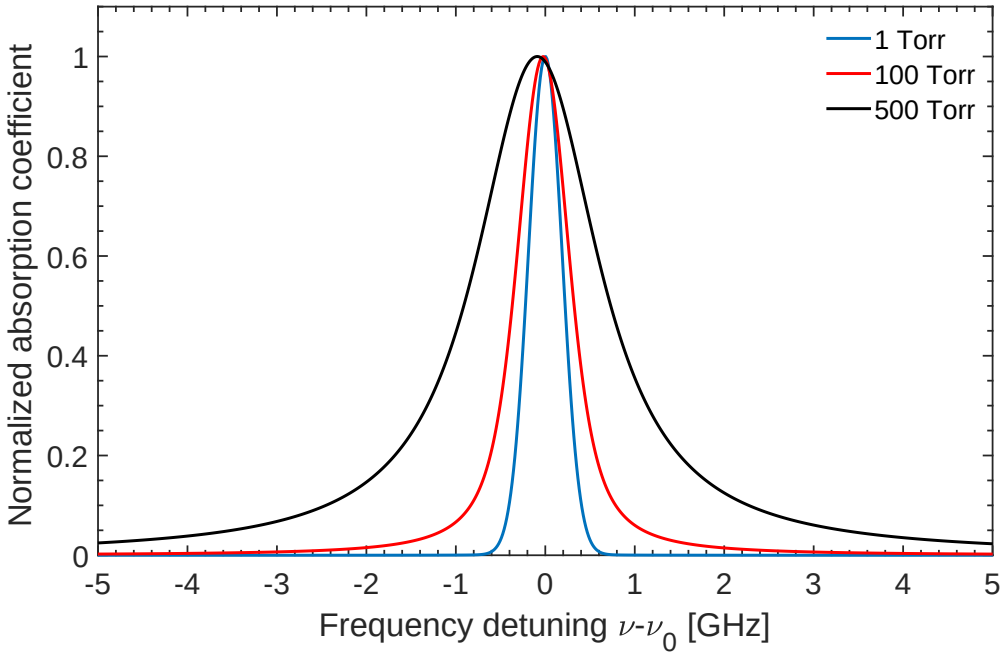

Figure 2.6 : Voigt profiles with normalized absorption coefficient computed for the P(6) line from the second overtone of CO, with 0.1 % of CO in argon at 296 K and with increasing pressures. At 1 Torr (blue), Doppler broadening is dominant and the profile resembles a Gaussian. At 100 and 500 Torr (red and black), collision-broadening becomes dominant and the profiles are closer to a Lorentzian, with the wings decreasing to zero at a slower pace than a Gaussian. As pressure increases, the pressure shift becomes more apparent.

However, the Voigt profile cannot perfectly reproduce spectra at low to moderate pressures, as it does not take into account other second-order lineshape narrowing effects

such as the collisional narrowing (or Dicke narrowing) due to velocity-changing collisions (Dicke, 1953) and the speed-dependence of the relaxation rate (Rohart *et al.*, 1997). This can lead to significant discrepancies between experimental absorption lines and a model based on Voigt profiles for fitting. These discrepancies are noticeable when subtracting the fitted model from the experimental data, as sensitivity of the instruments increases (Bui *et al.*, 2014). There are other line profiles, such as the Galatry profile (GP, or equivalently the Rautian profile) and the Nelkin-Ghatak (NGP) which take into account velocity-changing collisions (Dicke narrowing), with a soft-collision model for the GP and a hard-collision one for the NGP. There also exists speed-dependent version of these models, referred to as speed-dependent Voigt profile (SDVP), speed-dependent Galatry (SDGP) and speed-dependent Nelkin-Ghatak (SDNGP) (Hartmann *et al.*, 2008).

2.1.4.2 Hartmann-Tran profile

Another profile referred to as the partially-correlated quadratic speed-dependent hard-collision profile (pCqSDHCP) or the partially-correlated quadratic speed-dependent Nelkin-Ghatak profile (pCqSDNGP) had been used to model ultra-high accuracy experimental data (Joubert *et al.*, 1999 ; Ciuryło *et al.*, 2001). Its latest formulation was proposed by Ngo *et al.* (2013), and Tran *et al.* (2013) showed it could be efficiently computed with high accuracy. It is now commonly referred to as the Hartmann-Tran profile (HTP). The HTP is now the recommended line profile for the modelling of molecular absorption spectra (Tennyson *et al.*, 2014).

The HTP has seven parameters:

- Doppler broadening Γ_D [cm^{-1}],
- the pressure broadening averaged over all speeds Γ_0 [cm^{-1}],
- the pressure shift averaged over all speeds Δ_0 [cm^{-1}],
- the speed-dependent pressure broadening Γ_2 [cm^{-1}],
- the speed-dependent pressure shift Δ_2 [cm^{-1}],
- the frequency of velocity-changing collisions $\tilde{\nu}_{VC}$ [cm^{-1}],
- the correlation parameter η.

The correlation parameter η is dimensionless. The HTP lineshape function can be defined as:

$$\chi_{\mathrm{HTP}}(\tilde{\nu}) = \frac{1}{\pi} \frac{A(\tilde{\nu})}{1 - \left[\tilde{\nu}_{VC} - \eta(C_0 - 3C_2/2)\right] A(\tilde{\nu}) + \eta C_2 / v_{a0}^2 B(\tilde{\nu})}, \tag{2.17}$$

with $C_k = \Gamma_k + i\Delta_k$ (with $k = [0, 2]$), $A(\tilde{\nu})$ and $B(\tilde{\nu})$ two parameters obtained from the Faddeeva function, and the most probable speed v_{a0}:

$$v_{a0}^2 = \frac{c}{\sqrt{\ln 2}\tilde{\nu}_{ij}}\Gamma_D. \tag{2.18}$$

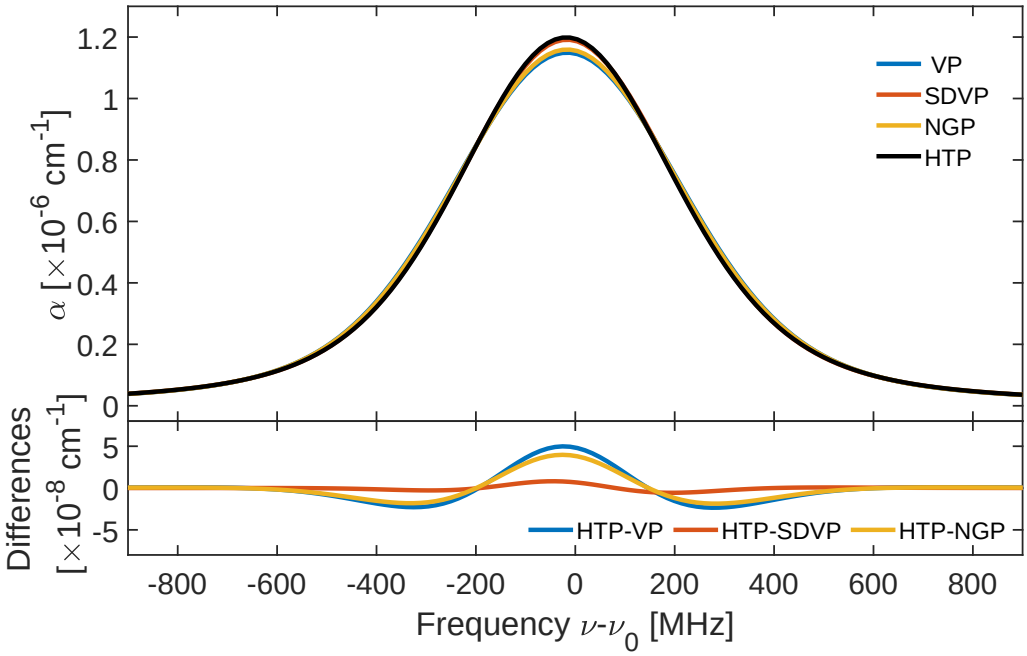

Figure 2.7 : Voigt, speed-dependent Voigt, Nelkin-Ghatak and Hartmann-Tran profiles computed for the P(6) line from the second overtone of CO, with 0.1 % of CO in argon at 296 K and a pressure of 50 Torr.

A comparison of the previously mentioned line profiles is shown on figure 2.7. The top panel shows the absorption profile as the absorption coefficient versus the detuning frequency from the center of the P(6) line from the $3 \leftarrow 0$ band of CO, with 0.1 % of CO diluted in argon at 296 K and a pressure of 50 Torr. The blue trace corresponds to the VP, the red trace to the SDVP, the yellow trace to the NGP and the black trace to the HTP. The bottom panel displays the differences of the VP, the SDVP and the NGP relative to the HTP as blue, red and yellow traces respectively. It is clear from both panels that the VP and the NGP overestimate the wings of the profile and underestimate its height. Taking into account speed-dependent effects, the SDVP is much closer to the HTP. This higlights the importance of the chosen absorption profile when modelling absorption spectra. The profile should be matched to the experimental conditions of pressure and temperature and be chosen relative to the achieved signal-to-noise ratio. As a more so-

phisticated profile like the HTP has more parameters than the simpler Voigt, using it to model low SNR data could lead to overfitting, meaning that fitted values for the model parameters do not necessarilly have a physical interpretation.

The goal of fitting experimental spectra with absorption profiles is to reproduce experimental data with the model in the best way possible. To assess the quality of the fit, the differences between the data and the model are computed, yielding the fit residuals (or fit residuum). The fitting procedure is usually conducted with least-square reduction algorithm. In such a case, the algorithm aims at minimizing the value $\chi^2 = (data - model)^2$. Flat residuals containing only statistical noise (typically white noise) indicate a trustworthy fit of the data. Uncertainties can then be evaluated.

We have seen that precision spectroscopy in the infrared requires high sensitivity, high resolution and a broad spectral coverage. The next section will cover Fabry-Perot optical cavities as a mean to enhance sensitivity.

2.2 Fabry-Perot cavity

A Fabry-Perot cavity or resonator is a linear optical cavity made of two reflecting surfaces facing each other, typically mirrors. The separation between the two mirrors is the cavity length L. The cavity confines light along its direction of propagation. Different configurations of Fabry-Perot cavities are possible and depend on the radius of curvature of each mirror R_1 and R_2 and the cavity length:

- plane-plane when $R_1 = R_2 = \infty$,
- concentric when $R_1 = R_2 = L/2$,
- semi-confocal when $R_1 = L/2$ and $R_2 = \infty$,
- confocal when $R_1 = R_2 = L$,

with each case depicted on figure 2.8(a) to 2.8(d). An optical resonator is stable if the light stays confined between the mirrors, as the number of light round-trips within the cavity goes up to infinity. The stability then depends on the cavity length and the curvature of the mirrors. A Fabry-Perot cavity is stable if it verifies the following condition:

$$0 \leq g_1 g_2 \leq 1 \tag{2.19}$$

with

$$g_j = 1 - \frac{L}{R_j} \tag{2.20}$$

with $j = [1,2]$ and R_j the radius of curvature of the j^{th} mirror. This condition implies that for a light beam to be resonant within the cavity, its wavefront curvature has to match the mirrors radius of curvature at the mirrors positions.

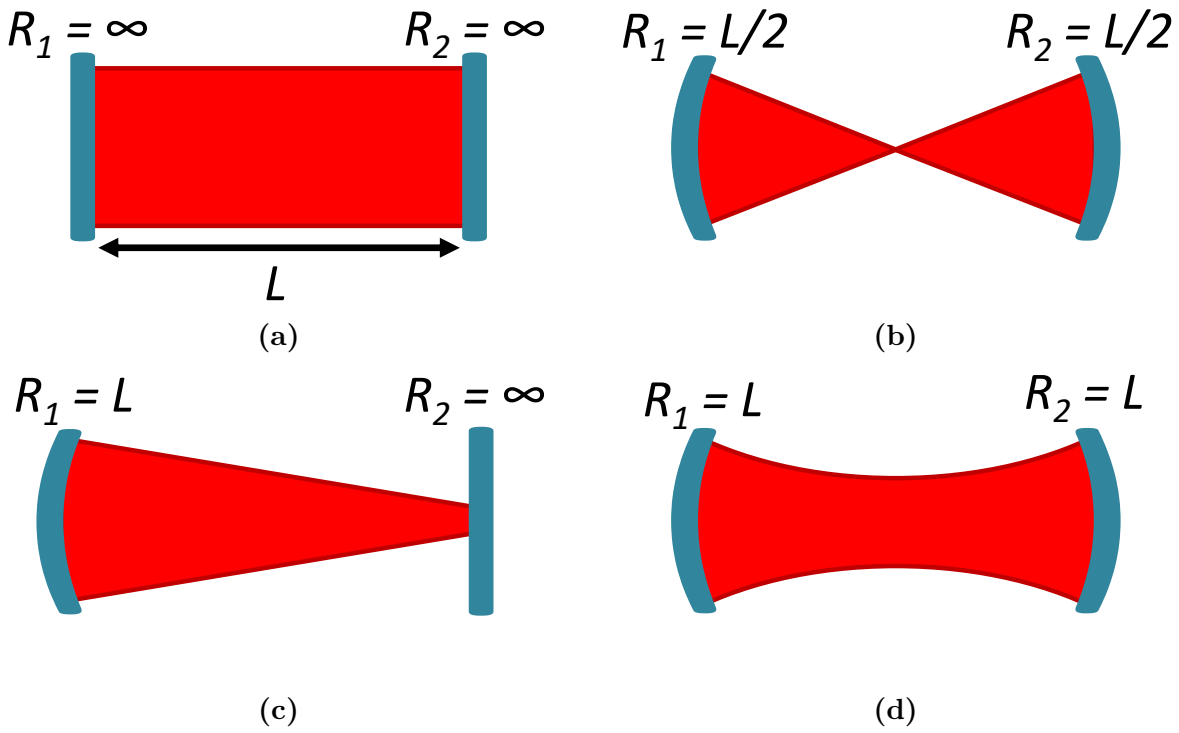

Figure 2.8 : Cavity geometries. **(a)** - Plane-plane cavity. **(b)** - Concentric cavity. **(c)** - Semi-concentric cavity. **(d)** - Confocal cavity.

Optical cavities exhibit different spatial resonant modes, with different spatial intensity distributions. These are called the transverse modes of the cavity.

2.2.1 Cavity spatial modes

The transverse modes of a cavity are also called the Hermite-Gauss modes, and are obtained from the product of a Gaussian beam and Hermite polynomials. To determine the intensity distributions of transverse modes, we first have to cover Gaussian beams.

2.2.1.1 Gaussian beams

Gaussian beams have an intensity profile that follows a Gaussian distribution. Figure 2.9(a) displays the intensity profile of a monochromatic Gaussian beam with wavelength

λ =1550 nm propagating along the z-axis, as a function of the z position and the radial position, the distance from the beam axis. The beam converges to the focus or beam waist, where the beam radius is minimal. The beam radius, $w(z)$ is defined as the distance from the beam axis where the intensity is reduced to $1/e^2$ ($\sim$13.5%) of its maximum value. It varies along the axis of propagation. The corresponding figure 2.9(b) shows the beam diameter as a function of z. At the beam waist, we have the minimum beam radius $w(0) = w_0$, displayed in blue on the figure. The Rayleigh range z_R is also shown in red in the figure. It is defined as:

$$z_R = \frac{\pi w_0^2}{\lambda}. \tag{2.21}$$

At z_R the beam radius is $w(z_R) = \sqrt{2}w_0$. The beam radius is obtained at any z value as:

$$w(z) = w_0\sqrt{1 + \left(\frac{z}{z_R}\right)^2}. \tag{2.22}$$

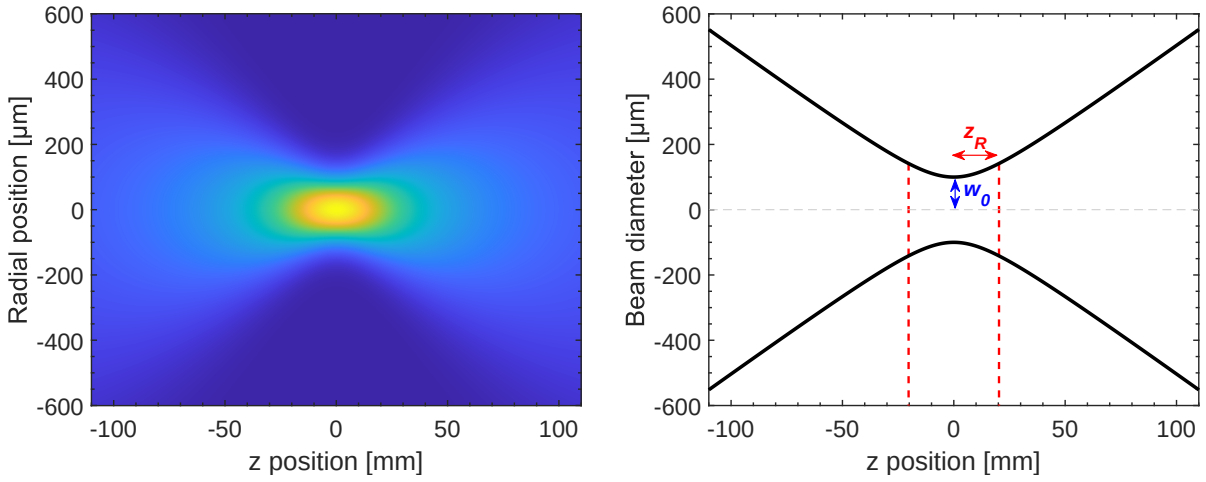

Figure 2.9 : Gaussian beam intensity distribution and beam diameter.**(a)** - Radial intensity distribution of a Gaussian beam propagating along the z-axis. The warmer the color, the higher the intensity. The intensity is at a maximum at the waist position of the beam in the center of the figure. The intensity decreases as the beam diverges away from the waist position. **(b)** - The beam diameter along the z-axis. At the waist there is the minimum beam radius w_0, shown in blue. The red-dotted lines show the Rayleigh range of the beam z_R, shown in red.

The electric field of a Gaussian beam propagating along the z-axis and radial position

r is defined as:

$$E(r,z) = E_0 \frac{w_0}{w(z)} \exp\left(-\frac{r^2}{w(z)^2}\right) \exp\left(i\left[kz - \arctan\left(\frac{z}{z_R}\right) + \frac{kr^2}{2R(z)}\right]\right) \tag{2.23}$$

with the wave-vector $k = \frac{2\pi}{\lambda}$, the Gouy phase $\psi = \arctan\left(\frac{z}{z_R}\right)$ and the radius of curvature of the wavefront $R(z)$:

$$R(z) = z\left[1 + \left(\frac{z_R}{z}\right)^2\right]. \tag{2.24}$$

The wavefront is flat at the waist and far from the waist, we have $R(z) \to \infty$. We can then define the complex beam parameter $q(z)$ as:

$$\frac{1}{q(z)} = \frac{1}{z + iz_R} = \frac{1}{R(z)} - i\frac{\lambda}{\pi w(z)^2}. \tag{2.25}$$

The complex beam parameter of a Gaussian beam is modified after propagating through an optical element as:

$$q' = \frac{Aq + B}{Cq + D} \tag{2.26}$$

with A, B, C and D the components of the ABCD matrix of the optical element. It should be noted that an ABCD matrix verify that $AD - BC = 1$.

2.2.1.2 Transverse modes

With a cavity aligned along the z-axis, the electric field associated with the transverse mode of order (m,n) at z in the xy-plane is given by:

$$\begin{aligned} E_{mn}(x,y,z) = E_0 \frac{w(z)}{w_0} \cdot H_m\left(\sqrt{2}\frac{x}{w(z)}\right) \exp\left(\frac{-x^2}{w(z)^2}\right) \cdot H_n\left(\sqrt{2}\frac{y}{w(z)}\right) \exp\left(\frac{-y^2}{w(z)^2}\right) \\ \exp\left(-i\left[kz - (1+m+n)\arctan\left(\frac{z}{z_R}\right) + \frac{k(x^2+y^2)}{2R(z)}\right]\right), \end{aligned} \tag{2.27}$$

with $H_{m,n}$ the Hermite polynomial of order (m,n). The intensity for each mode is then obtained as $I_{mn}(x,y,z) = E^*_{mn}(x,y,z)E_{mn}(x,y,z)$. The intensity distributions of the transverse modes up to order $m = n = 3$ are displayed on figure 2.10. The modes are referred to as transverse electro-magnetic modes of order m,n (TEM_{mn}). The TEM_{00} mode is the fundamental mode of the cavity, and exhibits a Gaussian profile.

In the next subsection, we will cover the transfer functions of a cavity and its frequency modes.

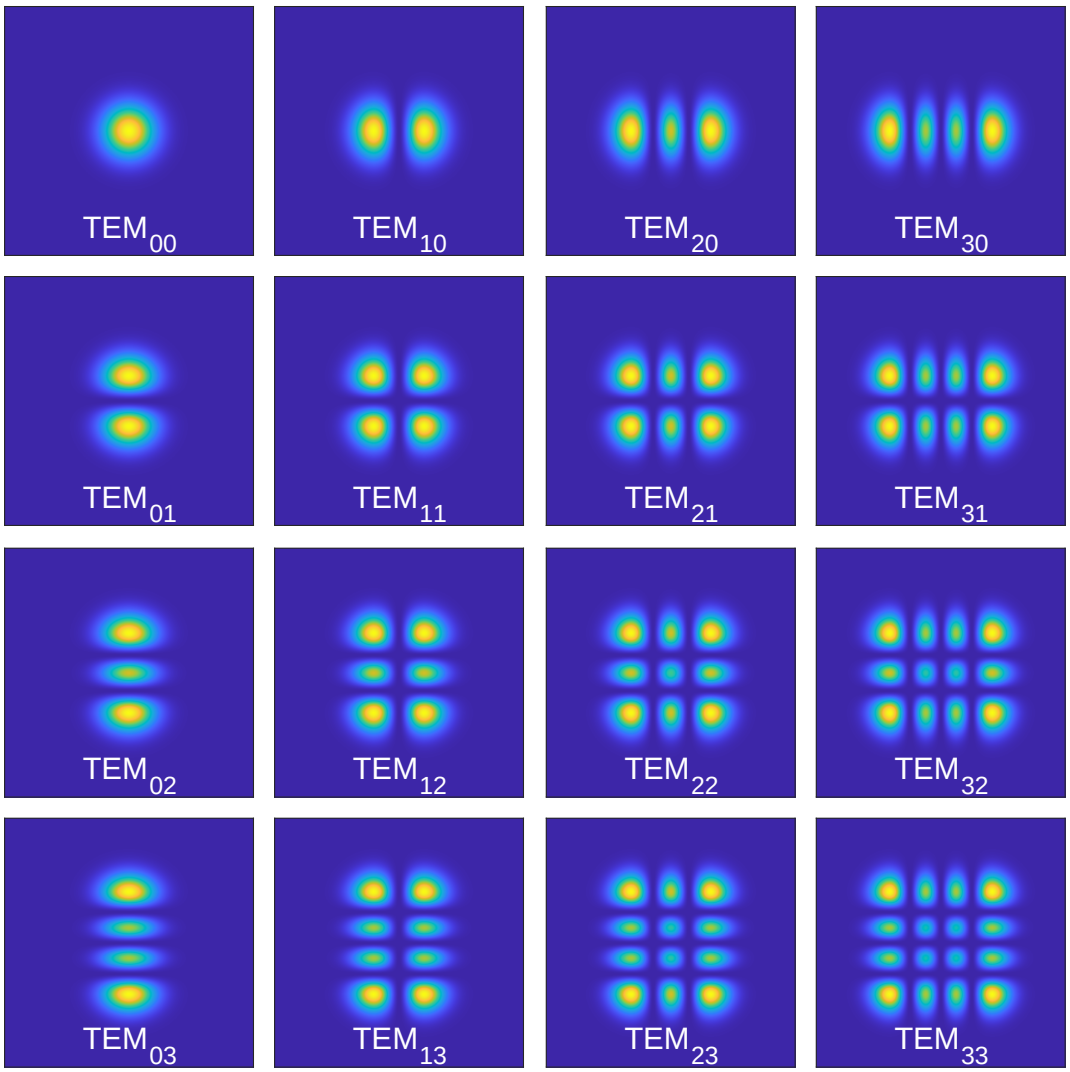

Figure 2.10 : Intensity profiles of transverse modes of an optical cavity. The TEM_{00} mode is a Gaussian mode, and is called the fundamental mode of the cavity.

2.2.2 Stationary transfer functions in the frequency domain

2.2.2.1 In transmission

Let us consider a cavity made of two mirrors M_1 and M_2 with electric field reflection and transmission coefficients r_j and t_j, with j =[1,2]. We assume a cavity without losses. We define the round-trip time of flight within the cavity as:

$$\tau_{rt} = 2Ln_r/c, \tag{2.28}$$

with n_r the refractive index of the intracavity medium. The electric field of light coupled into the cavity undergoes a phase-shift $\phi(\nu)$ at each round-trip, depending on the light frequency ν:

$$\phi(\nu) = 2\pi\nu\tau_{rt}. \tag{2.29}$$

Frequencies satisfying the condition $\phi(\nu_k) = 2k\pi$ with k an integer, interfere constructively with themselves and are resonant within the cavity. Thus we have $\nu_k = k/\tau_{rt}$.

As seen on figure 2.11, radiation with electric field $E_{inc}(t)$ incoming onto the cavity is first transmitted by the input mirror M_1 and undergoes n round-trips with $n = 0, 1, 2, 3, 4...$ to infinity. For each round trip, the field is retarded by τ_{rt} and its magnitude is reduced by a factor $r_1 r_2$. After n round-trips, the field has been retarded as $n\tau_{rt}$ and the magnitude has thus been reduced by $(r_1 r_2)^n$. At each round-trip, the field is partially transmitted by the output mirror M_2 and the magnitude is reduced by t_2. It corresponds to n and a half round-trip within the cavity, therefore the field is retarded by $(n+1/2)\tau_{rt}$. The total transmitted electric field $E_{trans}(t)$ is thus the superposition of an infinity of transmitted fields which underwent n round-trips within the cavity:

$$E_{trans}(t) = \sum_{n=0}^{\infty} t_1 t_2 (r_1 r_2)^n E_{inc}\Big(t - (n + \frac{1}{2})\tau_{rt}\Big). \tag{2.30}$$

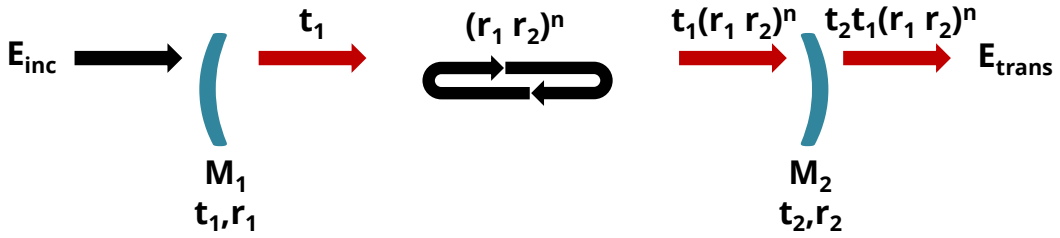

Figure 2.11 : Schematized transmission of an optical cavity. An incoming electric field E_{inc} is transmitted by the input mirror M_1, and undergoes consecutive round-trips between the two cavity mirrors. It is partially transmitted at each round-trip by output mirror M_2. The transmtted electric field E_{trans} is then the sum of all electric fields partially transmitted after n round-trips, with n going from 0 to infinity. The magnitude of each resonant field has been reduced by a factor $t_2 t_1 (r_1 r_2)^n$.

We then obtain the transmitted electric field in the frequency domain $\hat{E}_{trans}(\nu)$ after a Fourier transform:

$$\widehat{E}_{trans}(\nu) = \frac{1}{\sqrt{2\pi}} \int E_{trans}(t) \exp(-i2\pi\nu t) dt,$$

$$= \sum_{n=0}^{\infty} t_1 t_2 (r_1 r_2)^n \exp\Big[-i(n+\frac{1}{2})2\pi\nu\tau_{rt}\Big]\widehat{E}_{inc}(\nu),$$

$$= t_1 t_2 \exp\Big(-\frac{i}{2}\phi(\nu)\Big)\widehat{E}_{inc}(\nu)\sum_{n=0}^{\infty}\Big[r_1 r_2 \exp\Big(-i\phi(\nu)\Big)\Big]^n, \tag{2.31}$$

and with $r_1 r_2 exp\Big(-i\phi(\nu)\Big) < 1$ we can write:

$$\widehat{E}_{trans}(\nu) = \frac{t_1 t_2 \exp\Big(-\frac{i}{2}\phi(\nu)\Big)}{1 - r_1 r_2 \exp\Big(-i\phi(\nu)\Big)}\widehat{E}_{inc}(\nu).$$

Hence the transmission transfer function, if we consider the mirrors to be identical with $r_1 = r_2 = r$ and $t_1 = t_2 = t$:

$$\mathcal{H}_{trans}(\nu) = \frac{t^2 \exp\Big(-\frac{i}{2}\phi(\nu)\Big)}{1 - r^2 \exp\Big(-i\phi(\nu)\Big)} \tag{2.32}$$

The intensity transmission transfer function is then obtained as the square of the electric field transmission function:

$$H_{trans}(\nu) = |\mathcal{H}_{trans}(\nu)|^2 = \frac{T^2}{(1-R)^2 + 4R\sin^2\Big(\frac{1}{2}\phi(\nu)\Big)}, \tag{2.33}$$

with $T = |t|^2$ and $R = |r|^2$ the mirrors intensity transmission and reflection coefficients respectively. It should be noted that r, t, R and T are dependent on frequency.

This transfer function translates into narrow transmission modes in the frequency domain, as shown on figure 2.12(a). The modes are separated by the cavity free spectral range (FSR) defined as the inverse of the round-trip time:

$$\nu_{\text{FSR}} = \frac{1}{\tau_{rt}} = \frac{c}{2Ln_r}. \tag{2.34}$$

For practical reasons, we consider the FSR as constant for the moment. To the fundamental TEM_{00} mode then correspond k longitudinal modes separated in frequency by ν_{FSR}. For the higher order TEM_{mn} modes, the corresponding resonant frequencies are:

$$\nu_{mnk} = \frac{c}{2Ln_r}\left(k + \frac{1}{\pi}(m+n+1)\arccos(g_1 g_2)\right). \tag{2.35}$$

depending on the transverse order (mn). Each higher order transverse mode of frequency ν_{mnk} is thus associated to the k^{th} longitudinal mode. With only the TEM_{00} mode excited, we have:

$$\nu_{00k} = \nu_k = \frac{c}{2Ln_r}\left(k + \frac{1}{\pi}\arccos(g_1 g_2)\right) \tag{2.36}$$

the frequency of the k^{th} longitudinal mode.

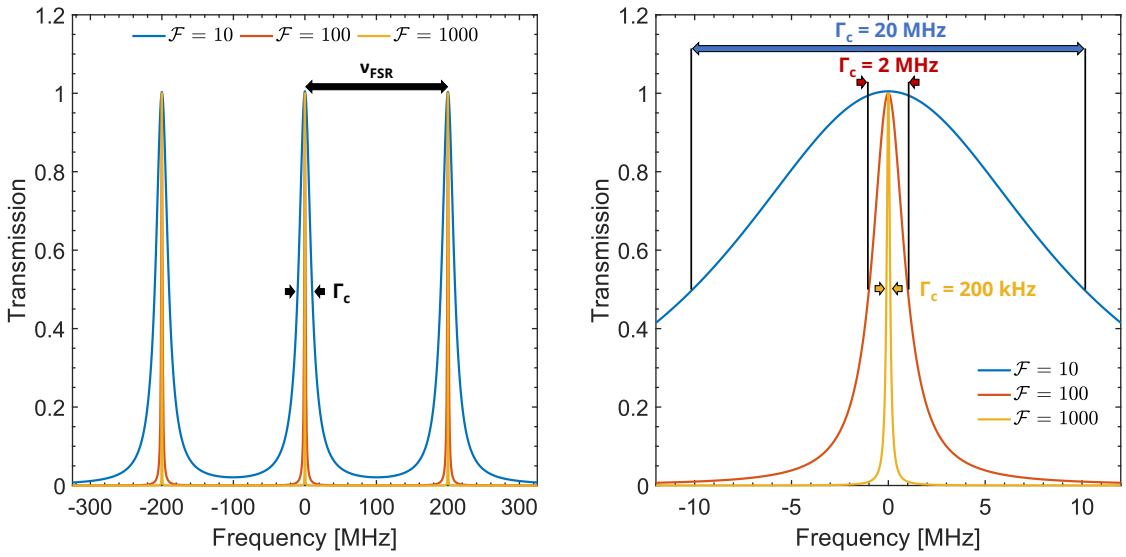

Figure 2.12 : Comparison of longitudinal modes for cavities with increasing finesse values. **(a)** - Longitudinal modes in frequency space for a cavity with a free-spectral range of 200 MHz and a finesse $\mathcal{F} = 10$ (blue trace), $\mathcal{F} = 100$ (red trace) and $\mathcal{F} = 1000$ (yellow trace). **(b)** - Zoomed-in view on one cavity mode. An increase of the finesse by a factor of ten directly translates in a decrease of the modes linewidth by tenfold.

Since the cavity has loss mechanisms, whether it is due to the transmission of the mirrors, their intrinsic losses or the absorption of light by the intracavity medium, the cavity mirrors can not be considered to have reflectivities equal to one. Assuming both mirrors to be identical, we have the intensity reflection, transmission and absorbance coefficients R, T and A, which are dimensionless, sum up to unity for each mirror. We have:

$$R + T + A = 1. \tag{2.37}$$

Due to these loss mechanisms, the cavity modes are not Dirac function at frequencies ν_k, but rather have a Lorentzian spectral lineshape $\gamma_{k,L}$ defined as:

$$\gamma_{k,L}(\nu) = \frac{\Gamma_c^2}{\Gamma_c^2 + 4(\nu - \nu_k)^2}, \tag{2.38}$$

with Γ_c the FWHM of the longitudinal mode, also referred to as the mode linewidth. Here the peak of each mode is normalized to unity.

The cavity finesse is a metric used to assess the frequency selectivity of cavity modes.

It is defined as the ratio of the FSR and the cavity mode linewidth:

$$\mathcal{F} = \frac{\nu_{\text{FSR}}}{\Gamma_c}. \tag{2.39}$$

For a cavity composed of mirrors with different intensity reflection coefficients R_1 and R_2, the finesse may also be expressed as:

$$\mathcal{F} = \frac{\pi \left(R_1 R_2\right)^{\frac{1}{4}}}{1 - \sqrt{R_1 R_2}}, \tag{2.40}$$

which simplifies, if we consider the mirrors as identical with $R_1 = R_2 = R$, to:

$$\mathcal{F} = \frac{\pi\sqrt{R}}{1 - R}. \tag{2.41}$$

The finesse depends only on the mirrors reflectivities and is therefore constant for a given cavity, whereas the FSR and the mode linewidth both vary with the cavity length. Figures 2.12(a) and 2.12(b) compare the spectral signatures of cavities with the same FSR of 200 MHz (L = 75 cm) with increasing finesses of 10, 100 and 1000 shown as the blue, red and yellow traces respectively. A tenfold increase in finesse directly translates as a tenfold decrease in the mode linewidth. The higher the finesse, the narrower the cavity modes and the more selective they are.

2.2.2.2 In reflection

Similarly, we can define the reflected electric field at a time t, $E_{ref}(t)$, as the sum of the incoming electric field reflected by M_1 and the resonant fields transmitted by M_1 after n round-trips, as shown on figure 2.13. We can write:

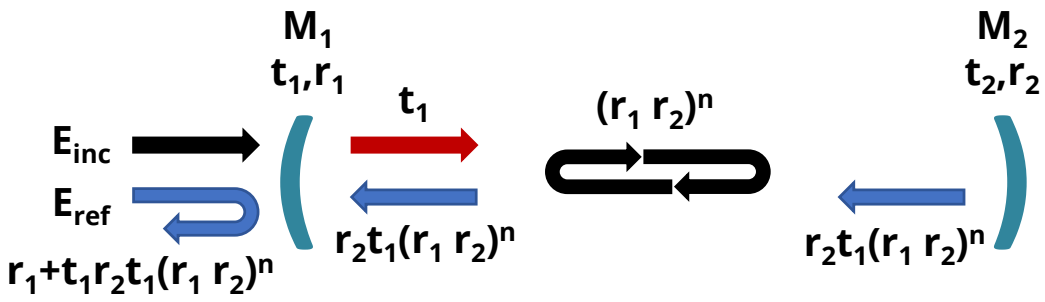

Figure 2.13 : Schematized reflection of an optical cavity. The electric field reflected by the cavity E_{ref} is the superposition of the reflected part of the incoming field E_inc and resonant fields transmitted by the input mirror M_1 after n round-trips.

$$E_{ref}(t) = r_1 E_{inc}(t) - t_1 r_2 t_1 \sum_{n=0}^{\infty} (r_1 r_2)^n E_{inc}\Big(t - (n+1)\tau_{rt}\Big). \tag{2.42}$$

Hence in the frequency domain:

$$\widehat{E}_{ref}(\nu) = \left[r_1 - \frac{t_1 r_2 t_1 \exp\Big(-i\phi(\nu)\Big)}{1 - r_1 r_2 \exp\Big(-i\phi(\nu)\Big)} \right] \widehat{E}_{inc}(\nu) \tag{2.43}$$

and the reflection transfer function:

$$\mathcal{H}_{ref}(\nu) = r_1 - \frac{t_1 r_2 t_1 \exp\Big(-i\phi(\nu)\Big)}{1 - r_1 r_2 \exp\Big(-i\phi(\nu)\Big)}. \tag{2.44}$$

Assuming the mirrors as identical with $r_1 = r_2 = r$ and $t_1 = t_2 = t$ and $R + T = 1$, we can write:

$$\mathcal{H}_{ref}(\nu) = r - \frac{t^2 r \exp\Big(-i\phi(\nu)\Big)}{1 - r^2 \exp\Big(-i\phi(\nu)\Big)} = \frac{r\Big(1 - \exp\Big(-i\phi(\nu)\Big)\Big)}{1 - r^2 \exp\Big(-i\phi(\nu)\Big)} \tag{2.45}$$

Assuming a lossless cavity, the intensity reflection transfer function verifies that:

$$H_{trans}(\nu) + H_{ref}(\nu) = 1. \tag{2.46}$$

The figure 2.14(a) displays $H_{ref}(\nu)$ versus frequency. The cavity FSR is 200 MHz and

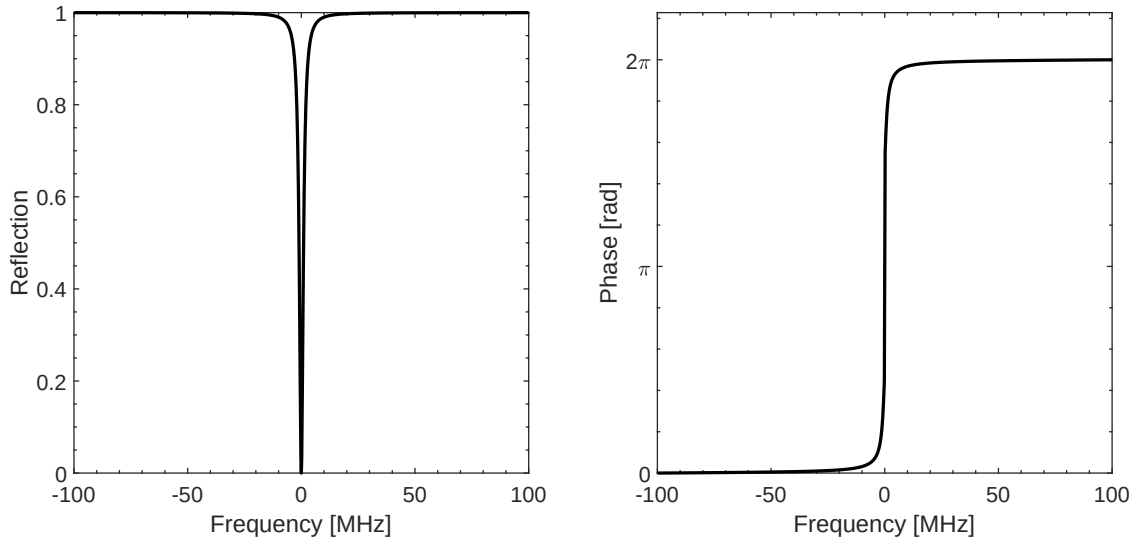

(a) **(b)**

Figure 2.14 : Amplitude and cumulated phase of the cavity reflection transfer function for a 100 finesse cavity and FSR of 200 MHz. **(a)** - Amplitude of the reflection transfer function, which goes down to zero on resonance. **(b)** - Cumulated phase of the reflection transfer function. On resonance the phase is shifted by π.

its finesse of 100. On resonance (at 0 MHz on the relative frequency axis), the reflected intensity decreases down to zero. We observe that equation 2.46 is verified, when comparing to the transmission transfer function previously displayed on figure 2.12(a). The phase associated to the reflected electric field is shown on figure 2.14(b). On resonance, the phase shift is equal to π. After the resonance, the phase increases to 2π. Looking at the slope of the phase, it is possible to determine on which side of the resonance we are. This is exploited by the Pound-Drever-Hall locking scheme to lock a laser to a cavity, which will be covered in section 2.3.

2.2.2.3 Cavity-enhanced absorption spectroscopy

In the case of an intracavity absorber, the electric field transmission transfer function of the cavity can be expressed as (Gianfrani *et al.*, 1999):

$$\mathcal{H}^{abs}_{trans}(\nu) = \frac{t^2\, e^{-\alpha(\nu)L/2}\, e^{-i\varphi(\nu)L/2 - i\phi(\nu)/2 - i\psi(\nu)/2}}{1 - r^2\, e^{-\alpha(\nu)L}\, e^{-i\varphi(\nu)L - i\phi(\nu) - i\psi(\nu)}} \tag{2.47}$$

with t and r the frequency-dependent electric field transmission and reflection coefficient of the cavity mirrors, $\alpha(\nu)$ and $\varphi(\nu)$ the intracavity medium absorption and dispersion coefficients, L the cavity length, $\phi(\nu)$ the round trip phase shift and $\psi(\nu)$ the intracavity dispersion due to the mirror coatings. The intensity transmission function is then obtained as follows:

$$\begin{gathered} H^{abs}_{trans}(\nu) = |\mathcal{H}_{trans}(\nu)|^2, \\ H^{abs}_{trans}(\nu) = \frac{T^2 e^{-\alpha(\nu)L}}{(1 - R\, e^{-\alpha(\nu)L})^2 + 4\, R\, e^{-\alpha(\nu)L} \sin^2\Big(\varphi(\nu)L/2 + \phi(\nu)/2 + \psi(\nu)/2\Big)}. \end{gathered} \tag{2.48}$$

The expressions from equations 2.47 and 2.48 can be used to model normalized experimental transmission spectra, and retrieve the absorption and dispersion coefficients of the intracavity medium. One then measures the intensity transmitted by the cavity, in a spectroscopic technique named cavity-enhanced absorption spectroscopy (CEAS), which has been extensively used in molecular spectroscopy. The main advantage of the technique is its sensitivity increased by the high reflectivity of the mirrors, which enables long interaction pathlength between the intracavity light and sample.

CEAS has been implemented with optical frequency combs (Foltynowicz *et al.*, 2011) in the form of direct frequency comb spectroscopy. The comb can either be tightly locked to the cavity, using the Pound-Drever-Hall locking scheme (see section 2.3), or be dither-locked (Adler *et al.*, 2010). In the former case, a two-point locking scheme can be

used to lock the two comb parameters to the cavity, namely f_{rep} and f_{ceo} (Foltynowicz *et al.*, 2013). It has been shown that the effective pathlength, and thus the sensitivity, are increased by a factor $\sim 2\mathcal{F}/\pi$ in the case of tight locking to the cavity and small absorption (Thorpe & Ye, 2008). With typical mirror reflectivities of 99.9% and a cavity length of $L = 1$ m, the finesse is $\mathcal{F} \sim 3{,}000$ and the effective pathlength is $L_{eff} \sim L \times 2\mathcal{F}/\pi \simeq 2,000$.

To ensure precise and accurate measurements, the cavity length is also stabilized using a PZT mounted on the back of one mirror (Foltynowicz *et al.*, 2013). The cavity transmission is then analyzed using either a dispersive spectrometer or a FTS (Adler *et al.*, 2010). The main source of noise in CEAS with combs is the frequency-to-amplitude noise conversion, due to the remaining frequency jitter of the comb modes relative to the cavity modes. The intensity transmitted by the cavity is therefore not constant, but noisy. Frequency modulation techniques exist to overcome this issue, namely NICE-OHMS (Khodabakhsh *et al.*, 2014).

2.2.3 Mode-matching

2.2.3.1 Spatial mode-matching

When coupling a laser beam into an optical cavity, the aim is to mode-match the laser beam to the cavity fundamental TEM_{00} mode. To do so, two aspects have to be taken into consideration. Firstly, the complex beam parameter at the laser waist q_{las} has to be matched to the complex beam parameter of the cavity TEM_{00} waist q'_{cav}. This can be done with a single lens of focal length f, as shown on figure 2.15. The lengths d_1 between the laser waist and the lens, and d_2 between the lens and the cavity waist, have to be determined.

Using ABCD matrix formalism we have:

$$q'_{cav} = \frac{Aq_{las} + B}{Cq_{las} + D}. \tag{2.49}$$

where the equivalent ABCD matrix of the system is the matrix product of each component in inverse order. For a propagation over distance d we have the matrix:

$$\begin{pmatrix} A & B \\ C & D \end{pmatrix} = \begin{pmatrix} 1 & d \\ 0 & 1 \end{pmatrix}, \tag{2.50}$$

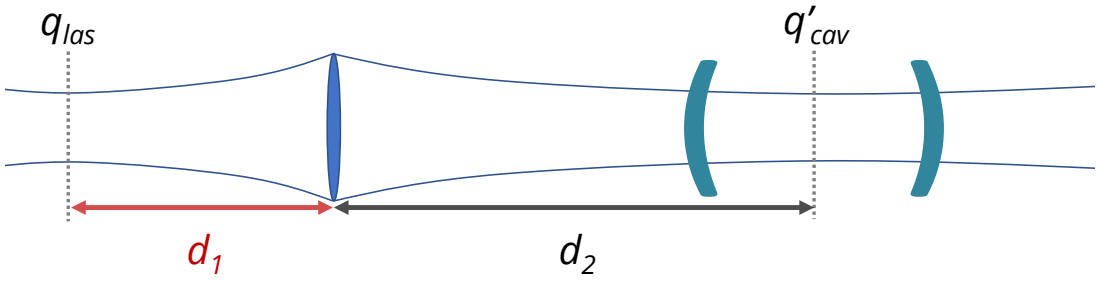

Figure 2.15 : Spatial mode-matching between a laser beam and the fundamental cavity mode using a single lens of focal length f. The complex beam parameter of the laser at its waist, q_{las} has to be matched to the complex beam of the cavity at its waist, q'_{cav}. For a cavity of length L composed of two identical concave mirrors, the waist is located in the middle of the cavity. The distance between the laser beam waist and the lens, d_1, and the distance between the lens and the cavity waist, d_2, can be obtained with the ABCD matrix formalism.

and for a lens of focal length f we have:

$$\begin{pmatrix} A & B \\ C & D \end{pmatrix} = \begin{pmatrix} 1 & 0 \\ -\frac{1}{f} & 1 \end{pmatrix}. \tag{2.51}$$

We then have for the whole system:

$$\begin{pmatrix} A & B \\ C & D \end{pmatrix} = \begin{pmatrix} 1 & d_2 \\ 0 & 1 \end{pmatrix} \begin{pmatrix} 1 & 0 \\ -\frac{1}{f} & 1 \end{pmatrix} \begin{pmatrix} 1 & d_1 \\ 0 & 1 \end{pmatrix} = \begin{pmatrix} 1 - \frac{d_2}{f} & d_1 + d_2 - \frac{d_1 d_2}{f} \\ -\frac{1}{f} & 1 - \frac{d_1}{f}. \end{pmatrix} \tag{2.52}$$

The wavefront curvature at the laser beam waist tends to infinity, thus q_{las} is a pure imaginary number as $q_{las} = iz_{las}$ with z_{las} the Rayleigh range of the laser beam. It can be determined experimentally prior to the laser-cavity coupling. Similarly, q'_{cav} is also a pure imaginary number as $q'_{cav} = iz'_{cav}$ with z'_{cav} the Rayleigh range of the cavity TEM_{00} mode, which can be determined with equation 2.24 at $z = L/2$, the output mirror position. Assuming that the wavefront curvature $R(z)$ at $z = L/2$ is equal to R, the radius of curvature of the cavity mirrors, we have $z'_{cav} = \sqrt{(R - \frac{L}{2})\frac{L}{2}}$. We may then write:

$$iz'_{cav} = \frac{ACz_{las}^2 - BCiz_{las} + ADiz_{las} + BD}{C^2 z_{las}^2 + D^2} = \frac{ACz_{las}^2 + BD + iz_{las}}{C^2 z_{las}^2 + D^2}. \tag{2.53}$$

Separating the real and imaginary parts yield:

$$ACz_{las}^2 + BD = 0, \tag{2.54}$$

$$z_{\prime cav} = \frac{z_{las}}{C^2 z_{las}^2 + D^2} \rightarrow C^2 z_{las}^2 + D^2 = \frac{z_{las}}{z_{\prime cav}}. \tag{2.55}$$

We then have two equations:

$$\begin{cases} z_{las}^2(d_2 - f) + \Big[f(d_1 + d_2) - d_1 d_2\Big](f - d_1) & = 0, \\ z_{las}^2 + (f - d_1)^2 - f^2 \frac{z_{las}}{z'_{cav}} & = 0. \end{cases} \tag{2.56}$$

Solving these two equations give d_1 and d_2:

$$\begin{cases} d_2 = \frac{f(d_1^2 - f d_1 + z_{las}^2)}{(d_1 - f)^2 + z_{las}^2}, \\ \\ d_1 = f + \sqrt{z_{las}\left(\frac{f^2}{z'_{cav}} - z_{las}\right)}. \end{cases} \tag{2.57}$$

Knowing the cavity length, the mirrors radius of curvature, the focal length of the lens and the laser beam Rayleigh range, we can then precisely position the lens for the spatial mode-matching. The lens is usually mounted on a translation stage for fine tuning.

Secondly, the alignment of the laser beam with the cavity optical axis has to be optimized with the injection mirrors and the angles of the cavity mirrors, to ensure an optimal coupling of the laser light into the TEM_{00} mode and maximize cavity transmission.

2.2.3.2 Frequency mode-matching with an OFC

Coupling an optical frequency comb into a Fabry-Perot cavity requires a frequency mode matching. Indeed, the equidistant comb teeth of the OFC nees to be superimposed on the cavity modes to ensure a broad spectral transmission. To do so, the comb repetition rate f_{rep} has to be matched to the cavity FSR. Moreover, the comb offset frequency has to be tuned so that the comb modes are centered on the cavity modes, to maximize the transmitted intensity. However, the cavity FSR is not constant but rather have a dependence on frequency. This is due to both the dispersion of the cavity mirrors, and the dispersion from the intracavity medium. Near a molecular transition, the cavity modes are broadened and shifted in frequency (Cygan *et al.*, 2013).

This results in an effective local mode-matching, as shown on figure 2.16. The perfect match is achieved for a "central" comb mode. The neighboring modes are also transmitted by their respective cavity modes. However, the further away from the perfect match, the more the comb modes drift out of resonance with the cavity modes. This limits the spectral bandwidth transmitted by the cavity. The higher the cavity finesse, the narrower the cavity modes and the sooner the comb modes are off the resonance, resulting in a narrower transmitted spectrum.

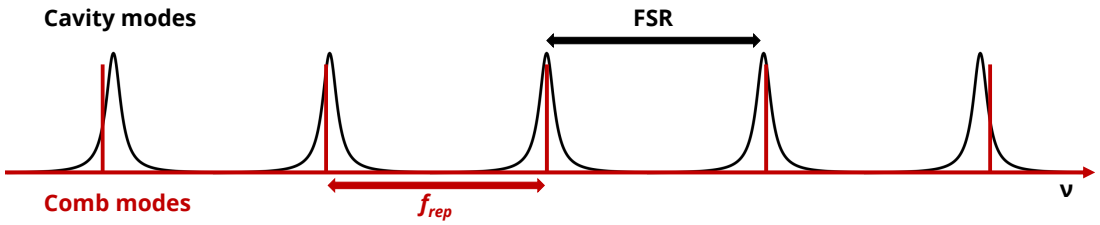

Figure 2.16 : Frequency mode-matching between an optical frequency comb (modes in red) and a Fabry-Perot cavity (modes in black) seen in the frequency domain. As the cavity FSR is dependent on frequency, due to dispersion from the cavity mirrors and the intracavity medium, the comb modes can only be matched locally to the cavity modes. Far from the agreement, the comb modes are not resonant with the cavity modes. This in turn limits the spectral bandwidth that is transmitted by the cavity. The more reflective the mirrors are, the higher the cavity finesse, resulting in narrower cavity modes. The transmitted spectral bandwidth of the comb thus decreases when the finesse increases.

2.2.4 Cavity transient response

Let us now determine the time-dependent cavity response in transmission after the incoming light source coupled into the cavity is shut off, in the case of an intracavity absorber. We need to take the inverse Fourier transform of the frequency-dependent electric field we described in equation 2.47, where $\hat{E}^{abs}_{trans}(\nu) = \mathcal{H}^{abs}_{trans}(\nu)\hat{E}_{inc}(\nu)$. We have in the time domain:

$$E^{abs}_{trans}(t) = \int h(t-t')E_{inc}(t')dt' \tag{2.58}$$

with $h(t-t')$ the cavity temporal response obtained as:

$$h(t) = \frac{1}{2\pi}\int \frac{t^2\, e^{-\alpha(\nu)L/2}\, e^{-i\varphi(\nu)L/2 - i\phi(\nu)/2 - i\psi(\nu)/2}}{1 - r^2\, e^{-\alpha(\nu)L}\, e^{-i\varphi(\nu)L - i\phi(\nu) - i\psi(\nu)}} e^{i2\pi\nu t} d\nu. \tag{2.59}$$

From there, it can be shown that the decay of the light stored in a cavity mode follows a decaying exponential law and $h(t)$ can be written as (Lehmann & Romanini, 1996):

$$h(t) = \frac{1}{\sqrt{2\pi}}\sum_q A(\nu_q)\exp\left(-\frac{t-\tau_{rt}/2}{2\tau_{rd}(\nu_q)}\right)\exp\left[i2\pi\nu_q(t-\tau_{rt}/2)\right]\Theta(t-\tau_{rt}/2) \tag{2.60}$$

with ν_q the frequency of the q^{th} cavity mode and $\Theta(t)$ the Heavyside function, with:

$$\Theta(t) = \begin{cases} 0 & t < 0, \\ 1 & t > 0, \end{cases} \tag{2.61}$$

and

$$\tau_{rd}(\nu_q) = \frac{\tau_{rt}\, r^2 \exp(-\alpha(\nu_q)L)}{2\Big(1 - r^2 \exp(-\alpha(\nu_q)L)\Big)}, \tag{2.62}$$

$$A(\nu_q) = \sqrt{2\pi}\, \frac{t^2 \exp(-\alpha(\nu_q)L/2)}{\tau_{rt} r^2 \exp(-\alpha(\nu_q)L)}. \tag{2.63}$$

The decay of the intensity of light coupled into a cavity mode and shut off at time t is taken as:

$$I^{abs}_{trans}(t) = |E^{abs}_{trans}(t)|^2 = \frac{1}{2\pi} A^2(\nu_q) \exp\left(-\frac{t - \tau_{rt}/2}{\tau_{rd}(\nu_q)}\right) \tag{2.64}$$

2.2.4.1 Ring-down time

The value $\tau_{rd}(\nu_q)$ is the ring-down time of the cavity at ν_q. It characterizes when the intensity transmitted by the cavity drops down to $1/e$ of its original value, before the incoming light source was shut off. It depends on both the intracavity absorption and the mirrors reflectivity. In the case of weak absorption and high mirror reflectivity (close to unity), the inverse of the ring-down time is linear with absorption and the mirror intensity reflection coefficient:

$$\frac{1}{\tau_{rd}(\nu)} = \frac{\Big(1 - R + \alpha(\nu)L\Big)c}{L} \tag{2.65}$$

therefore the absorption coefficient can be retrieved as:

$$\alpha(\nu) = \frac{1}{c\tau_{rd}(\nu)} - \frac{1}{c\tau_0(\nu)} \tag{2.66}$$

where $\tau_0(\nu)$ is the empty cavity ring-down time, given by $\tau_0 = \frac{L}{c(1-R)}$, which characterizes the intrinsic losses of the cavity.

It comes that in the presence of an intracavity absorber, for example molecular species in the gas phase, the ring-down time decreases with absorption, we have $\tau_{rd} < \tau_0$. Measuring $\tau_{rd}(\nu)$ then yields directly the absorption coefficient at frequency ν. The ring-down time is obtained by fitting a decaying exponential model to the measured cavity light decay, when the light source is shut off. This is exploited in cavity ring-down spectroscopy or CRDS.

2.2.4.2 Cavity ring-down spectroscopy

CRDS was first implemented by O'Keefe & Deacon (1988) with a pulsed laser. Lehmann & Romanini (1996) then set the theoretical fundamentals of the technique, and showed

that to retrieve single exponential decays, the laser coupled into the cavity needs to be narrower than the cavity FSR, in order to excite only one cavity mode. However, pulse lasers exhibit broad emission, with FWHM on the same order as the cavity FSR. They proposed to use continuous-wave (cw) lasers instead, which at the time of their publication could reach linewidth below 5 MHz. The first implementation of cw-CRDS was presented by Romanini *et al.* (1997) with an AOM to shut off the laser light and a high-finesse cavity ($\mathcal{F} \sim 30,000$). The AOM was triggered when the cavity transmission would cross a threshold value. The cavity length was modulated using a PZT mounted on one of the mirrors, to ensure the laser would be coupled into the cavity twice by modulation period. To record a full spectrum, the laser frequency was tuned by changing the length of the laser cavity.

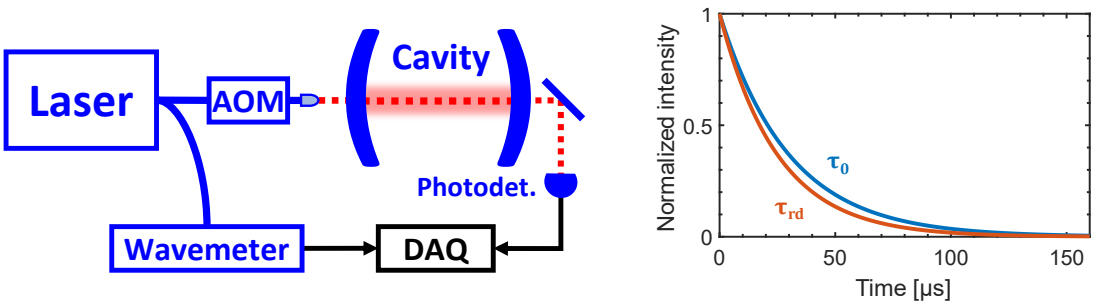

(a) **(b)**

Figure 2.17 : Typical CRDS setup and ring-down. **(a)** - Basic cw-CRDS setup. The laser, typically a DFB or ECDL, is coupled into a very-high finesse cavity ($\mathcal{F} >$ 100,000). The AOM acts as the fast optical switch to trigger ring-down events, which are recorded on the photodiode at the cavity output. A wavemeter is used to monitor the laser frequency, which is tuned by changing either the temperature or the pump current. **(b)** - Exponental decays recorded for an empty cavity (blue trace) with the associated ring-down time τ_0 and for an intracavity absorber (red trace) with ring-down time τ_{rd}. The difference of the two ring-down times is proportional to the absorption coefficient of the intracavity medium at this particular frequency.

Figure 2.17(a) shows a basic setup of cw-CRDS. The laser is a cw narrowband laser, usually a DFB or an ECDL, and is coupled to a very-high finesse cavity. In the near-infrared, cavity finesses exceed 100,000. The laser is fibered to an AOM which acts as the fast optical switch. The laser frequency is tuned by changing the pump current, its temperature or the cavity length, and monitored with a wavemeter. The cavity transmission is measured with a photodetector whose bandwidth has to be matched to the anticipated

decay duration. When the measured intensity crosses a set threshold, the AOM shuts off the laser light and a decay is recorded, along with the frequency of the laser. Figure 2.17(b) shows the expected shorter ring-down time τ_{rd} in the presense of a molecular sample in the cavity, in red, compared to the empty cavity ring-down time τ_0 in blue.

Since its first demonstration, cw-CRDS has become one of the most used spectroscopic technique, able to reach very high sensitivity with rather simple and robust setups. It has reached a record absorption sensitivity of 5×10^{-13}cm^{-1} (Kassi & Campargue, 2012). Its robustness has allowed compact, portable setups to be used in extreme conditions, such as close to volcanoes (Kassi *et al.*, 2006) or airborne measurements (Chen *et al.*, 2010). More recently, CRDS was taken to sub-MHz accuracy and its sensitivity improved by locking the cavity to the cw laser using the Pound-Drever-Hall scheme (see section 2.3) and referencing the laser to an optical frequency comb (Cygan *et al.*, 2011 ; Long *et al.*, 2012). To increase the acquisition rate of CRDS, frequency-agile techniques have also been developed (Truong *et al.*, 2013 ; Long *et al.*, 2014). While most CRDS experiments are performed in the visible and near-infrared regions, where the highest reflective mirror coatings are available, CRDS has also been taken to the mid-infrared (Paldus *et al.*, 2000 ; Long *et al.*, 2016).

Nowadays, CRDS cavities have finesses in the hundreds of thousands. The enhancement factor of CRDS is $\sim \mathcal{F}/\pi$, yielding effective interaction pathlengths of tens of kilometers with one meter-long optical cavities. It should be noted that the enhancement factor of CRDS is half the enhancement factor of CEAS. This is because in CRDS, light leaks out of both mirrors, whereas for CEAS, the steady input beam suppresses the decay at the input mirror. CEAS is then twice as sensitive to intracavity absorption than CRDS, given the same cavity is used (Thorpe & Ye, 2008).

2.3 Stabilization methods

2.3.1 Pound-Drever-Hall

To efficiently lock a laser to an optical cavity and ensure it is continuously transmitted, one can use the Pound-Drever-Hall (PDH) locking scheme (Drever *et al.*, 1983). The idea behind the technique is to provide information on relative frequency difference between a laser and the nearest cavity mode. To do so, the laser is phase-modulated at a frequency f_{PDH} to induce sidebands on each side of the laser frequency. For simplicity,

we will instead consider the angular frequency of the modulation $\omega_m = 2\pi f_{\mathrm{PDH}}$ for the following development. The modulation frequency ω_m should greatly exceed the cavity mode linewidth to ensure the sidebands are reflected by the cavity.

Let us consider the modulated laser electric field E_i as:

$$E_i = E_0 e^{i(\omega t + \beta \sin(\omega_m t))}, \tag{2.67}$$

with E_0 the laser amplitude and β the modulation amplitude. Considering $\beta \sin(\omega_m t)) << 1$, equation 2.67 can be series expanded as:

$$\begin{aligned} E_i &\approx E_0 e^{i\omega t}\Big[1 + i\beta \sin(\omega_m t)\Big], \\ E_i &= E_0 e^{i\omega t}\left(1 + \frac{\beta}{2} e^{i\omega_m t} - \frac{\beta}{2} e^{-i\omega_m t}\right). \end{aligned} \tag{2.68}$$

We have the laser carrier surrounded by two sidebands at $-\omega_m$ and ω_m. Considering the cavity reflection transfer function from equation 2.45, we can express the reflected electric field as:

$$\begin{aligned} E_{ref} = E_0\Big[&\mathcal{H}_{ref}(\omega) e^{i\omega t} + \mathcal{H}_{ref}(\omega + \omega_m) e^{i(\omega+\omega_m)t} \\ &+ \mathcal{H}_{ref}(\omega + \omega_m)\frac{\beta}{2} e^{i(\omega+\omega_m)t} - H_{ref}(\omega - \omega_m)\frac{\beta}{2} e^{i(\omega-\omega_m)t}\Big]. \end{aligned} \tag{2.69}$$

The reflected intensity is obtained as:

$$I_{ref} = E^*_{ref} E_{ref} \tag{2.70}$$

$$\begin{aligned} I_{ref} = &I_0 \left|H_{ref}(\omega)\right|^2 + I_0 \frac{\beta^2}{4}\left[\left|H_{ref}(\omega + \omega_m)\right|^2 + \left|H_{ref}(\omega - \omega_m)\right|^2\right] \\ &+ I_0\beta\Big(Re\Big[H_{ref}(\omega)H^*_{ref}(\omega + \omega_m) - H^*_{ref}(\omega)H_{ref}(\omega - \omega_m)\Big]\, cos(\omega_m t) \\ &+ Im\Big[H_{ref}(\omega)H^*_{ref}(\omega + \omega_m) - H^*_{ref}(\omega)H_{ref}(\omega - \omega_m)\Big]\, \sin(\omega_m t)\Big) \\ &+ (2\omega_m \text{ terms}). \end{aligned} \tag{2.71}$$

The component $Im\Big[H_{ref}(\omega)H^*_{ref}(\omega+\omega_m) - H^*_{ref}(\omega)H_{ref}(\omega-\omega_m)\Big]\, \sin(\omega_m t)$ can be retrieved by measuring the reflected intensity with a photodetector, which is bandpass filtered at ω_m. The filtered signal is then demodulated at ω_m with the phase-adjusted output of the modulation source.

Adjusting the phase of the modulation source for the demodulation allows to only retrieve the *sine* component of equation 2.71 without the *cosine* component. The result of the demodulation is shown on figure 2.18, which is the PDH error signal. It exhibits a very steep slope on resonance, enabling precise locking of the laser to the cavity resonance.

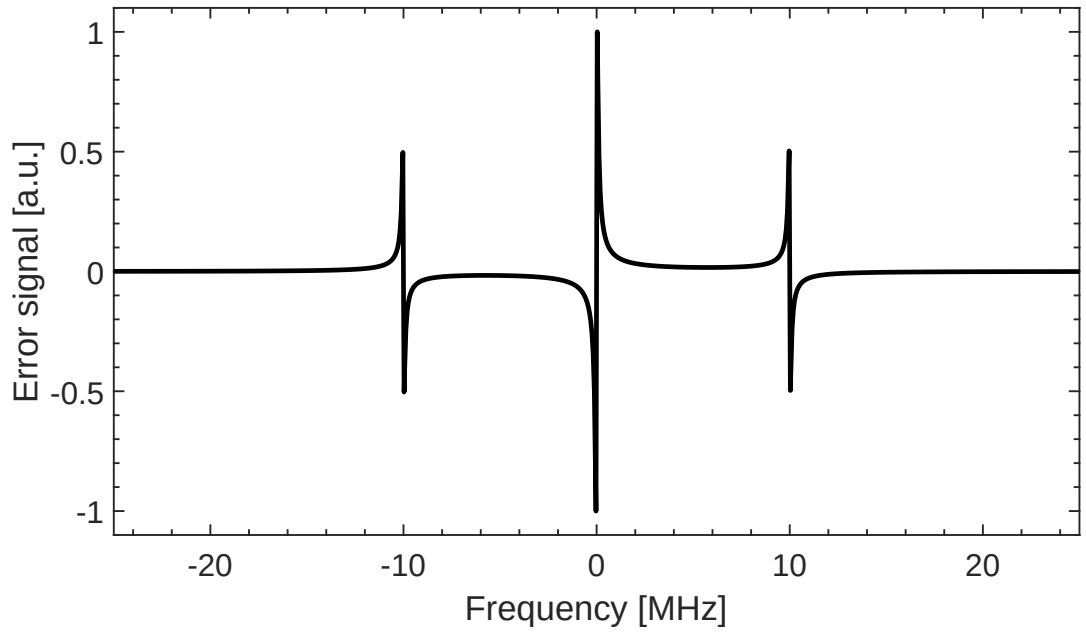

Figure 2.18 : Theoretical PDH error signal obtained after filtering the demodulated signal, with a modulation frequency $f_{\mathrm{PDH}} = 10$ MHz.

Figure 2.19 shows a typical PDH setup to lock a laser, such as a frequency comb, to an optical cavity. The laser is phase-modulated with an EOM to induce sidebands. The EOM is driven by a frequency reference at f_{PDH}. In free-space, it is linearly polarized with a half-wave plate ($\lambda/2$) and propagates through a polarized beam-splitter (PBS). The laser light is then circularly polarized with a quarter-wave plate ($\lambda/4$). After reflection on the cavity input mirror, the reflected light has been shifted by *pi* and is now circularly polarized in the opposite direction. After propagating through the $\lambda/4$, the reflected beam polarization is linear, though orthogonal compared to the incoming laser beam. It is then reflected by the PBS. The angles of the $\lambda/2$ and $\lambda/4$ are optimized to maximize the input beam intensity. These three components ($\lambda/2$, PBS and $\lambda/4$) also act as an optical isolator, preventing any light feedback into the laser.

Here, in the case of a frequency comb, the retrieved reflected beam is then dispersed onto a diffraction grating and filtered through a pinhole or a slit to let through a narrow part of the laser spectrum. With a narrow band laser, the grating and slit are not necessary. The reflected light intensity is then measured with a photodetector, whose bandwidth is required to exceed the EOM modulation frequency for proper detection of the modulated reflected light. The photodetector output is bandpass-filtered centered on the modulation frequency, and demodulated with the phase-optimized f_{PDH} signal in a double-balanced

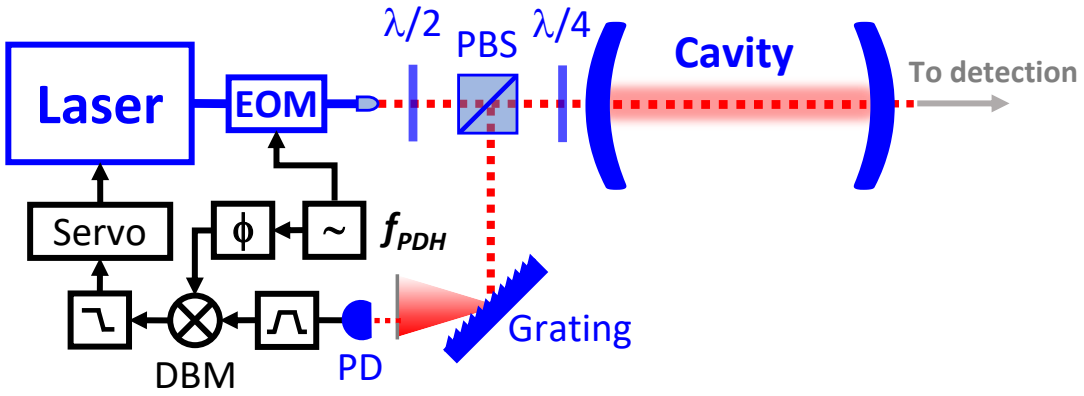

Figure 2.19 : Setup of a Pound-Drever-Hall scheme to lock a laser to an optical cavity. The laser is phase-modulated with an EOM at a frequency f_{PDH}, and the laser light reflected by the cavity is retrieved with a λ/2, a PBS and a λ/4. The reflected signal is measured with a photodetector (PD), whose output is bandpass-filtered and demodulated in a DBM with the phase-matched f_{PDH}. The DBM output is lowpass filtered, yielding the PDH error signal. This error signal is fed to a servo-controller, that can act on the laser actuator(s) to maintain the laser locked to the cavity and ensure continuous transmission.

mixer (DBM). Its output yields the PDH error signal after a lowpass filter to prevent high frequency noise. The obtained error signal may then be fed into a servo-controller to have feedback on an actuator of the laser.

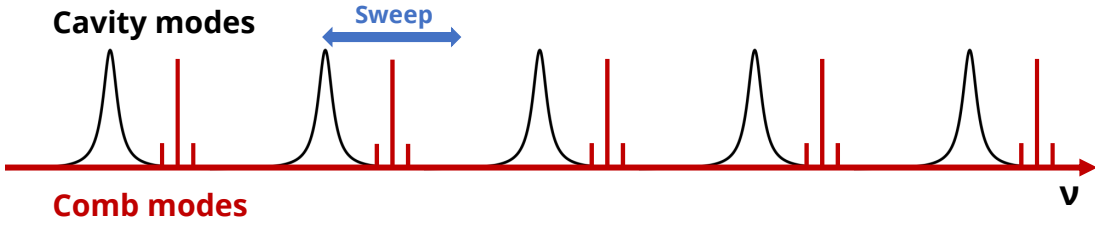

Figure 2.20 : Schematized sweep of the cavity length with an EOM-modulated frequency comb. To each comb mode is associated two sidebands at $\pm f_{\mathrm{PDH}}$. When the cavity length is modulated, the cavity modes sweep back and forth. The "lower" sidebands (at -f_{PDH} from their respective comb modes), the comb modes and the "upper" sidebands (at +f_{PDH} from their respective comb modes) are in turn transmitted by the cavity.

Before locking, the cavity length can be swept to visualize and optimize the PDH error signal. In the case of a frequency comb, as shown on figure 2.20, each comb mode is surrounded by two sidebands. When the cavity length modulated by more than f_{PDH}, the cavity FSR will successively increase and decrease, resulting in a sweep of the cavity modes. The lower frequency sidebands, the comb modes and the upper sidebands will

be successively on resonance. This is presented on figure 2.21, which shows the cavity transmission of an EOM-modulated frequency comb (offset by 0.5 V for clarity) and the associated PDH error signal when the cavity length is modulated by one FSR. The blue trace corresponds to the cavity transmission, with the central carrier of the laser along the sidebands at $\pm f_{\mathrm{PDH}}$. The associated PDH error signal is displayed below in the red trace, which resembles the one shown previously on figure 2.18. We recognize the steep slope of the error signal centered on the peak cavity transmission, where the comb modes are on resonance with their respective cavity modes.

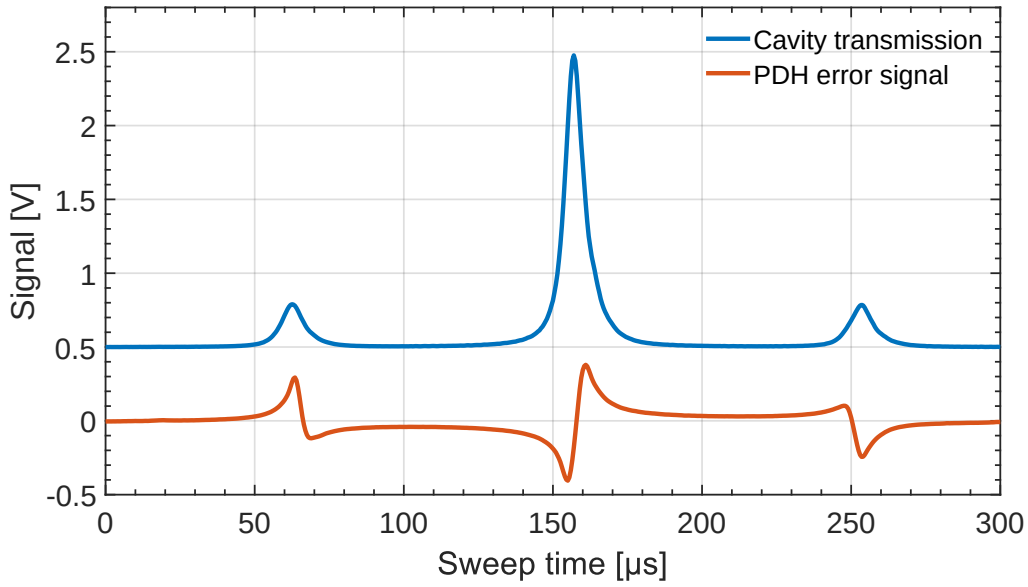

Figure 2.21 : Experimental data showing the transmission of a frequency comb by an optical cavity (blue trace, offset by 0.5 V for clarity) and associated PDH error signal (red trace) when the cavity length is modulated by one FSR. The sidebands are located at $\pm f_{\mathrm{PDH}}$ on each side of the laser central carrier. We recognize the steep slope of the error signal where the comb modes are on resonance with their respective cavity modes.

2.3.2 Radiofrequency stabilization

When performing frequency comb spectroscopy, one key aspect of the measurement is the stabilization of the laser repetition rate f_{rep}. Indeed, the repetition rate must be stabilized for the frequency comb to provide high spectral resolution and a direct frequency axis calibration.

In cavity-enhanced measurements, one benefits from the locking of the frequency comb to the optical cavity. As the comb repetition rate is maintained equal to the cavity FSR,

one may then act on the cavity length to in turn stabilize f_{rep} to a given value. Such a setup is described on figure 2.22. A frequency comb is locked to an optical cavity with the PDH scheme previously covered in section 2.3.1. The PDH electronic components are not detailed on the figure and summarized by the black box "PDH electronics". After locking, the f_{rep} value is monitored and fed to a phase detector (PDT) where it is compared to the signal from an arbitrary waveform generator, itself referenced to a SI frequency reference such as a GPS-disciplined atomic clock or an hydrogen maser. The phase detector compares the phase difference between the two frequencies and outputs a signal whose frequency is the difference between f_{rep} and the AWG frequency. This error signal is fed to a servo-controller which acts on a piezo-electric transducer (PZT) mounted on the back of one cavity mirror. The PZT is then used to stabilize the cavity length, and in turn the comb repetition rate. As the AWG output frequency can be tuned, it is possible to lock f_{rep} to a desired radiofrequency (RF) value while the comb is still locked to the cavity.

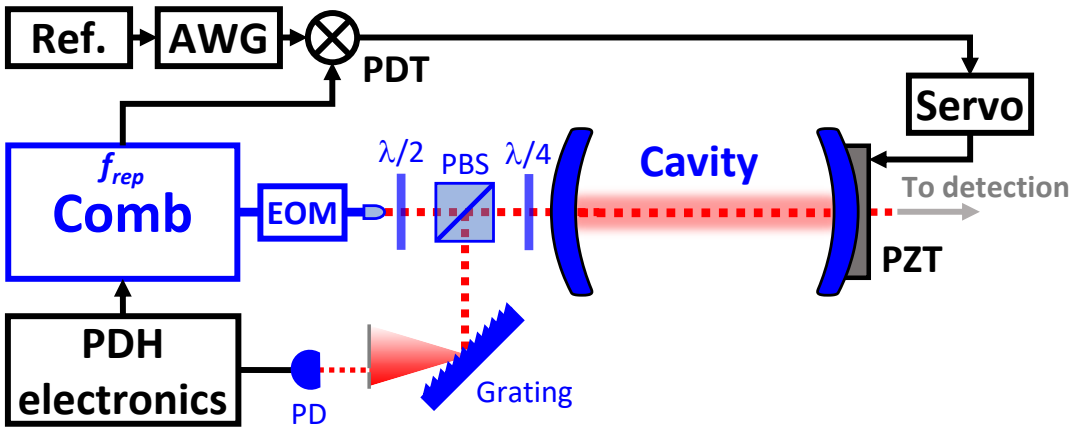

Figure 2.22 : Basic setup to stabilize the comb repetition rate by acting on the cavity length. Ref.: frequency reference. AWG: arbitraty waveform generator. PDT: phase detector. After locking the comb to the cavity with PDH, f_{rep} is compared in a phase detector to a reference frequency provided by an AWG, itself referenced to a SI reference frequency. The phase detector output is the frequency difference between f_{rep} and the reference frequency. This output is then used as an error signal and fed to a servo-controller, which acts on a PZT mounted on the back of one cavity mirror to stabilize the cavity length. Thus f_{rep} is locked to the reference frequency from the AWG, and can be tuned.

This tunability of f_{rep} while the comb is locked to the cavity enables the use of the interleaving method. By acquiring spectra at different values of f_{rep}, one can map absorption lines that are narrower than f_{rep} (see section 1.4.2).

2.4 Conclusion

In a first part, we have seen how molecules absorb light at certain frequencies and how the study of absorption spectra of molecules in the infrared yield absorption lines gathered in rovibrational bands, we covered the different mechanisms that shape the profile of these absorption lines and which absorption profiles are commonly used to model experimental spectra. In a second part, we covered the properties of optical cavities and how they can be used to enhance the interaction pathlength between light and a probed sample, namely CEAS and CRDS. Finally, we saw the PDH scheme to lock a laser to a cavity, and the RF stabilization scheme allowing to stabilize a frequency comb repetition rate to a RF frequency.

From these concepts, the next chapter will cover the first implementation of a broadband CRDS technique, coupling a frequency comb and a time-resolved Fourier transform spectrometer.

3 – Optical frequency comb Fourier transform cavity ring-down spectroscopy

3.1 Broadband cavity ring-down spectroscopy

Cavity ring-down spectroscopy (CRDS) is one of the most sensitive spectroscopic technique, with the advantages of being calibration-free and immune to the light source intensity fluctuations as explained in section 2.2.4.2. Nowadays CRDS is mainly performed with continuous wave lasers, which provide high spectral density and resolution, but suffers from slow tuning speed. Recent techniques have been developed to drastically increases the acquisition rate up to 1 THz/s, using electro-optic-modulators (Long *et al.*, 2014, Long *et al.*, 2015), Mach-Zehnder modulators (Burkart *et al.*, 2015) or frequency-swept synthesizers (Gotti *et al.*, 2020). However, the spectral elements are still acquired in a sequential fashion, and the frequency axis is calibrated with an optical frequency comb. When experimental conditions are subject to change over time, there is a strong interest in obtaining multiplexed spectra where the spectral elements are measured simultaneously with a broadband light source.

Such a broadband CRDS technique was first demonstrated with a pulsed dye laser and a step-scan time-resolved Fourier transform spectrometer by Engeln & Meijer (1996). Cavity light decays were recorded at each step of the spectrometer translation stage, which yielded a time-resolved interferogram after data was rearranged. They used a pulsed dye laser emitting near 763 nm with a 400 cm^{-1} bandwidth and a 4,000 finesse cavity to measure the (0,0) band of the O_2 $b^1\Sigma_g^+ \leftarrow X^3\Sigma_g^-$ transition. The data consisted of 3260 discrete mirror positions averaged over 200 laser shots, for a total acquisition time of 4h. They reported a noise-equivalent absorption of 2.5×10^{-7} cm^{-1} with a resolution of 0.4 cm^{-1}, which, along with the measurement duration, was quite limiting for applications.

A second technique was proposed by Scherer (1998) with a CCD camera, diffraction grating and a high-speed rotating mirror called ringdown spectral photography (RSP). The decaying cavity light was dispersed in wavelength by the grating onto the x-axis of the camera while the rotating mirror allowed time resolution along the y-axis. Time resolution of the measurement depends on the mirror rotating speed. Scherer first measured the overtone band of propane near 635 nm with a narrow-band light source he would shift in frequency. In a follow-up paper (Scherer *et al.*, 2001), a broadband light source was used to probe propane near 635 nm and the O_2 rovibronic band near 690 nm. However, the best resolution of 1.5 cm^{-1} (limited by the diffraction grating) was the limiting factor to resolve individual lines. No sensitivity analysis was performed.

Czyżewski *et al.* (2001) used a pulsed dye laser with a spectrograph and a gated image intensifier CCD camera. Time-dependent spectra were acquired by triggering the camera at consecutive delays relative to consecutive laser pulses. This implies sensitivity of the final decay to pulse-to-pulse intensity fluctuations. The FWHM of the laser was 15 nm near 430 nm. The cavity ($\mathcal{F}$ = 1,500 at 410 nm) was filled with 10 ppm NO_2. No information was given on the spectrograph resolution or the sensitivity. In their review, Ball & Jones (2003) estimated the sensitivity to as low as $10^{-5}cm^{-1}$. A similar setup was developed by Ball *et al.* (2001) with a clocked two-dimensionnal CCD.

Thorpe *et al.* (2006) presented the first demonstration of broadband CRDS using an optical frequency comb as the light source. They combined a CCD camera, a grating monochromator and a rotating mirror for multiplex acquisition of the comb spectrum, with the same approach as (Scherer *et al.*, 2001). They reported an acquisition time of 1.4 ms for a single spectrum, along with a resolution of 0.8 cm^{-1}, limited by the resolution power of the dispersion grating (no sensitivity was extracted from the final spectrum).

More recently, Lisak *et al.* (2022) performed dual-comb CRDS with electro-optics combs pumped from the same oscillator. The high acquisition speed of a single time-resolved interferogram (5 µs) allowed several interferograms to be recorded during a single cavity decay to yield the decay time-dependence. This setup demonstrated a sensitivity of 3×10^{-8} cm^{-1} for an acquisition time of 1 s and a cavity finesse around 19,800.

The table 3.1 summarizes the main characteristics of each approach to broadband CRDS.

Table 3.1 : Summmary of performances of previous broadband CRDS setups. The integration time for sensitivities is displayed in parentheses.

Implementation	Engeln & Meijer (1996)	Scherer *et al.* (2001)	Czyżewski *et al.* (2001)
Light source	Pulsed dye laser	Pulsed dye laser	Pulsed dye laser
Wavelength	763 nm	630 nm	425 nm
Bandwidth	400 cm^{-1}	350 cm^{-1}	840 cm^{-1}
Finesse	4,000	31,000	1,500
Sensitivity	2.5×10^{-7} cm^{-1} (4h)	2.0×10^{-8} cm^{-1} (40µs)	10^{-5} cm^{-1} (1.5µs)
Resolution	0.4 cm^{-1}	1.5 cm^{-1}	-
Acquisition time	4h	40 µs (single shot)	1.5 µs (single shot)
NEA^{1s}	9.5×10^{-7} $cm^{-1}Hz^{-1/2}$	1.6×10^{-7} $cm^{-1}Hz^{-1/2}$	-
Implementation	Thorpe *et al.* (2006)	Lisak *et al.* (2022)	
Light source	Ti:Sa frequency comb	Electro-optics combs	
Wavelength	800 nm	1564 nm	
Bandwidth	200 cm^{-1}	0.8 cm^{-1}	
Finesse	4,500	19,800	
Sensitivity	6.4×10^{-7} cm^{-1} (1.4 ms)	1.5×10^{-7} cm^{-1} (1 s)	
Resolution	0.8 cm^{-1}	0.033 cm^{-1}	
Acquisition time	1.4 ms	5 μs	
NEA^{1s}	1.5×10^{-9} $cm^{-1}Hz^{-1/2}$	3.0×10^{-8} $cm^{-1}Hz^{-1/2}$	

3.2 First implementation of frequency comb based FT-CRDS

We developed a new broadband CRDS technique, pairing a near-infrared frequency comb and a fast-scan time-resolved Fourier transform spectrometer (FTS). This new approach combines the multiplex measurement of a FTS and the sensitivity and frequency precision of a frequency comb.

3.2.1 Experimental setup

The schematic of the experimental setup is shown on figure 3.1(a). The laser is an Erbium fiber comb with a repetition rate $f_{rep} = 100$ MHz, delivering 100 mW of output power. The emitted light goes through a fibered AOM (G&H, SFO1814-T-M080-0.4C2J-3-F2P-03), which shift the laser frequency by 80 MHz. It is used as an ultrafast optical switch with a rise/fall time of 35 ns to shut off the comb light and induce cavity light decays. The comb light then propagates to free-space to be mode-matched to the measurement cavity. The cavity mirrors (Layertec, coating A0612015, 99.88 % reflectivity, radius of curvature = 1 m) are separated by 75 cm (FSR = 200 MHz). This yields a theoretical empty-cavity ring-down time of 2.1 µs. The cavity is opened to air and not enclosed in a gas cell. Therefore, measurements will be conducted at atmospheric pressure and ambient temperature on atmospheric species, mainly CO_2 and H_2O.

The comb is PDH locked to the cavity to ensure quasi-continuous transmission at the cavity output (see section 2.3.1). The PDH error signal, obtained as described in section 2.3.1, is fed to two high-speed servo-controllers (NewFocus LB1005-S). These servos outputs are connected to the EOM located inside the comb oscillator cavity and to the slow PZT fiber-stretcher, acting as fast and slow actuators respectively. The transmitted cavity light then propagates to a fast-scanning FTS, whose design is similar to the one described in section 1.4.3. The main difference resides in that both FTS outputs are recorded with independent photodetectors (Thorlabs, PDA10CS2, PD1 and PD2 on figures 3.1(a) and 3.1(b)) with a bandwidth of 13 MHz. The optical path difference is calibrated with the frequency stabilized HeNe laser, which propagates in one arm of the interferometer. The reason for this design is covered in the next subsection 3.2.2 concerning data acquisition. It is coupled in fiber and split with a 50:50 splitter. Half of the light is coupled to free-space, reflected off the retro-reflector and coupled back in fiber, to be recombined with the other

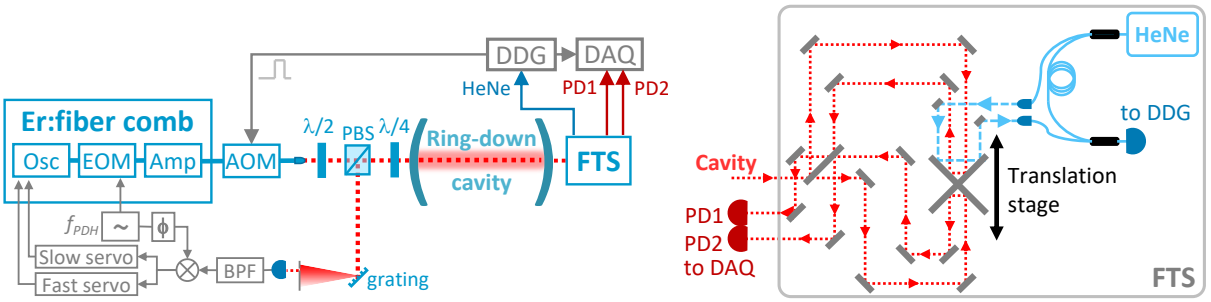

Figure 3.1 : (a) - Experimental setup. EOM: Electro-optic modulator. AOM: Acousto-optic modulator. λ/2: half-wave plate. λ/4: quarter-wave plate. PBS: Polarizing beam-splitter. BPF: Band-pass filter. DDG: Digital delay generator. DAQ: Acquisition board. FTS: Fourier transform spectrometer. PD1,2: photodetectors. **(b)** - Fourier transform spectrometer. The geometry is a twice-folded Michelson interferometer. Both outputs are measured on independent photodetectors (PD1 and PD2) and acquired by DAQ. A stabilized HeNe laser propagates along the comb on one arm of the FTS, to calibrate the optical path difference (OPD). Note that the OPD varies twice as fast for the comb interferogram compared to the HeNe interferogram, for a given translation stage displacement.

half of the light that stayed in fiber after the first splitter. The sinewave interferogram it produces is recorded on a photodetector (Thorlabs, PDA36A2) and used as reference signal for a digital delay generator (DDG, Berkeley Nucleonics Corp 745T). When the translation stage moves by half a HeNe wavelength (λ_{HeNe}), the DDG generates a boxcar signal which is used to trigger the AOM and shut off the comb light. The same boxcar signal is used to trigger the data acquisition board (National Instruments, NI-PC1 5922, 256 MB/channel memory). The signals from PD1 and PD2 are acquired simultaneously at 15 MSamples/s with 16 bits resolution and an alias-free bandwidth of 6 MHz. In total, 440,000 decay events are acquired, each event containing 180 points. This yields a total of 50.6 cm OPD for both comb interferograms. The data acquisition will be discussed with more details in the next section.

3.2.2 Data acquisition

To ensure an efficient data acquisition, the cavity light decay events are synchronously triggered by the AOM and recorded by the acquisition board, which are simultaneously controlled by the DDG. The DDG burst duration is set to 12 µs to acquire the whole decay. As the DDG burst is triggered by the HeNe interferogram, how often the triggers

happen depends on the translation stage speed. If the HeNe laser beam were propagating on both sides of the FTS (as in the case of the FTS described in section 1.4.3), a trigger would occur everytime the translation stage moved by $\lambda_{\mathrm{HeNe}}/4$. Since consecutive triggers of the DDG should be spaced by 4 times the burst duration to ensure that no event is missed, the translation stage would have to move by $\lambda_{\mathrm{HeNe}}/4$ every 48 µs, yielding a constant speed of 3.3 mm/s. However, the cart movement is not perfectly continuous at low speeds below 3-4 mm/s but rather erratic. The choice was then to propagate the HeNe laser beam along one FTS arm only, with triggers happening when the cart moves by $\lambda_{\mathrm{HeNe}}/2$. This allowed to use a higher speed of 5 mm/s with a steady translation stage movement.

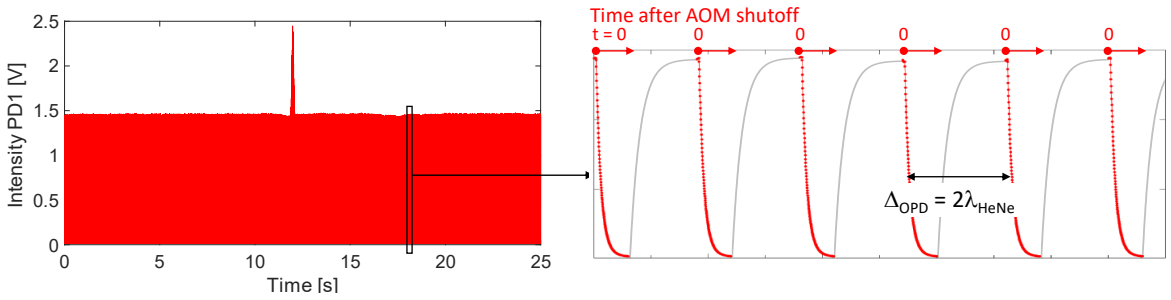

(a) **(b)**

Figure 3.2 : (a) - Raw data from PD1. The central burst of the interferogram is clearly visible at t = 12 s. **(b)** - Zoom-in on raw data. The red-dotted lines corresponds to the cavity light decays that are acquired. The solid grey lines corresponds to cavity build-ups, which are not acquired on the acquisition board. The AOM and the board are triggered every time the cart moves by $\lambda_{\mathrm{HeNe}}/2$ and the corresponding light decay is acquired. The AOM is then switched back on, light build up in cavity until next trigger. Every n^{th} decay points are separated by the OPD step $\Delta_{\mathrm{OPD}} = 2\lambda_{\mathrm{HeNe}}$.

Figure 3.2(a) displays raw data acquired from PD1, corresponding to the decays set off when the FTS translation stage moves by $\Delta_{\mathrm{OPD}} = 2\lambda_{\mathrm{HeNe}}$. The center burst is clearly visible at t = 12 s, corresponding to the zero OPD value. Figure 3.2(b) shows successive decays: the red-dotted traces correspond to the acquired decay events while the solid grey lines show the cavity build-ups, which are not recorded. Each decay here is a multi-exponential function, corresponding to the sum of the transmitted comb modes decaying simultaneously. It is worth mentioning here that the AOM when triggered also shuts off the PDH error signal. The servo parameters were adjusted to minimize the impact on the locks. This ensures cavity build-ups, when the AOM is switched off and the comb light is injected again in the cavity. The upper scales depicts the time scale of each decay. The

decay data points are separated in the time domain by $1/f_{acq}$, with f_{acq} the acquisition rate. The translation stage is continuously moving as the data is acquired (compared to Engeln & Meijer (1996) where data is acquired at each discrete step of the stage), though it does not prevent interferogram calibration at any given time after shut-off (considering every n^{th} point of each decay). The OPD step remains equal to $2\lambda_{HeNe}$ at any given delay, whereas the absolute OPD scale is shifted from one delay to the next. This induces a slight phase shift of the interferograms as the delay after shut-off increases, without noticeable impact on the spectrum.

When the acquisition board is triggered, it records a sample (a single decay event) which is stored on its onboard memory. While the acquisition is in progress, the memory is emptied by groups of 4,000 decays, which are then copied on the computer drive as a single file. We noticed a timing jitter between the DAQ internal clock and the AOM shutoff. This comes from the nature of the board acquisition scheme: data points are continuously measured at 15 MS/s, the trigger only indicates when to fetch data. The acquisition rate $f_{acq} = 15$ MS/s then yields a $1/f_{acq} = 67$ ns uncertainty on acquisition start after the DDG trigger.

3.2.3 Data processing

The raw data from both photodetectors PD1 and PD2 are rearranged by time delay relative to the AOM shutoff. This yields a 3D time-resolved interferogram displayed on figure 3.3(a), zoomed in on the central burst at zero optical path difference (OPD). The solid red trace corresponds to a decay event at a given OPD. Two orthogonal axis display the OPD and time delay. Continuous intensity points at $t < 0$ µs were acquired, though not useful and deleted for further data processing. Figure 3.3(b) displays the interferograms at $t = 0$ µs of PD1 (blue trace) and PD2 (red trace). There is a strong intensity noise due to the conversion of the comb-cavity frequency noise to amplitude, added to the timing jitter of the DAQ internal clock relative to the AOM shutoff. From the figure, it is clear that intensity noise is common to both interferograms. One can cancel it by using a numerical balancing approach. Since the two outputs of a Michelson interferometer are in phase opposition, subtracting one from the other cancels out common noise while doubling the interferogram peak-to-peak value (Foltynowicz *et al.*, 2011). Due to imperfect alignment and gain differences between PD1 and PD2, differences in the two outputs DC levels are to be expected. Therefore, these differences have to be compensated for an efficient noise cancellation.

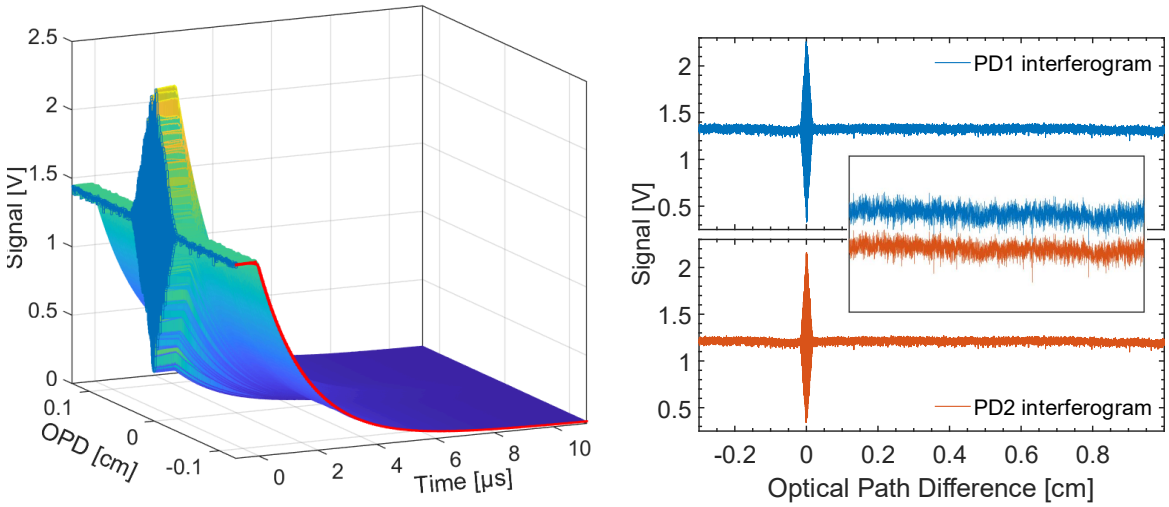

(a) **(b)**

Figure 3.3 : (a) - Rearranged data from PD1 as a 3D decaying interferogram centered on the burst at zero OPD. The solid red trace corresponds to a single decay event. **(b)** - Interferograms from PD1 (blue trace) and PD2 (red trace) at t = 0 μs together with a zoomed-in view on both baselines.

The balancing procedure is as follows. At each time delay, interferograms from PD1 and PD2 are divided by one another (in our case PD1/PD2) and a third order polynomial function $poly_{correction}$ is fitted to the division. The denominator interferogram PD2 is multiplied by this function to match the numerator interferogram PD1 DC value as $PD2_{corrected} = PD2 \times poly_{correction}$. The PD1-$PD2_{corrected}$ subtraction at each time delay yields the balanced 3D interferogram shown on figure 3.4(a). Another balancing method consists of separating the interferograms from PD1 and PD2 at each time delay in a given number of samples. The mean of each sample is then computed. Finally, for any pair of samples from the PD1 and PD2 interferograms at each time delay, the ratio of their mean values is used as the correction factor. For both methods, the computation time and the root mean square (RMS) value of the interferograms baseline on the right side of the central burst were compared. For a 440,000 by 167 array, the polynomial balancing took 4.4 s to complete while the mean sample method took 0.56 s. The RMS values were 1.09 mV and 730 µV for the polynomial and mean sample methods respectively, with the detector noise at the selected gain value being 264 µV. For future measurements, the mean sample method will be preferred.

The interferogram mean value is now zero, and the peak-to-peak value is doubled. The interferogram at t = 0 µs is represented by the solid blue trace in the red square, and

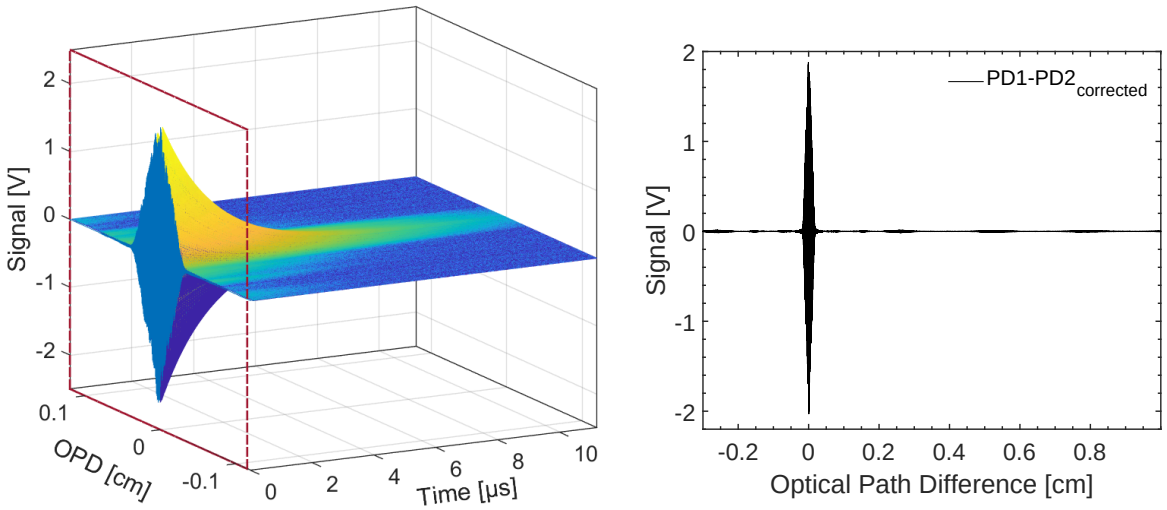

(a) **(b)**

Figure 3.4 : (a) - A 3D view of the balanced interferogram centered on the burst at zero OPD. The solid blue trace at t = 0 µs represents the interferogram right after the AOM shutoff. **(b)** - Balanced interferogramm at $t = 0\,\mu s$.

shown on the 2D graph of figure 3.4(b). The signal-to-noise ratio (SNR, defined as the maximum value divided by the standard deviation of the baseline) is increased thirtyfold for this balanced interferogram relative to raw data from figure 3.3(b).

From the 3D balanced interferogram, the next step is obtaining the FFT of each 2D interferogram at any time delay. Computing the absolute values of the FFT yields the 3D spectrum shown on figure 3.5(a). At every spectral element of the wavenumber axis corresponds a single exponential decay along the time axis. The solid blue trace at zero delay shows the transmission CEAS spectrum, where absorption features are visible. Isolating data points at a given spectral element along the time axis yields the cavity ring-down at this wavenumber, as displayed on figure 3.5(b) for the spectral element at 6325 cm^{-1}.

In the upper panel, the data in black circles was fitted with a single exponential decay model (solid red trace) of the form:

$$I(t) = I_0\, e^{-t/\tau_{rd}} + y_0 \tag{3.1}$$

with I_0 the magnitude, t the time in µs, τ_{rd} the ring-down time in µs and y_0 the offset. The offset comes from taking the absolute value of the FFT and is always positive. It has no physical meaning, unlike the DC offset of the detector with cw-CRDS. This non-linear

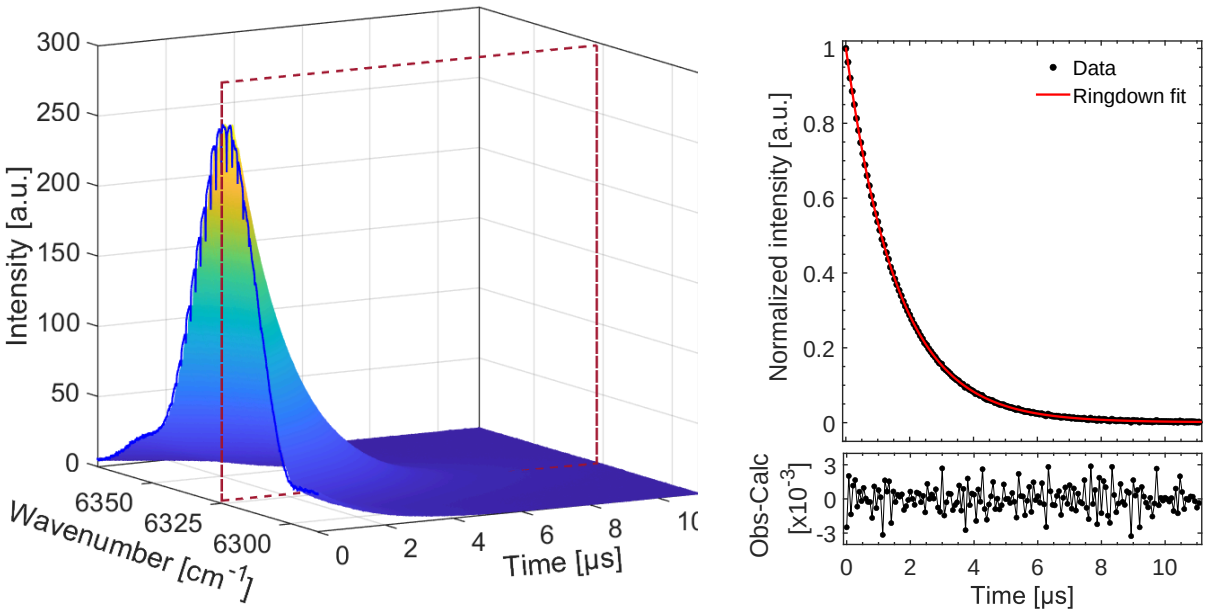

(a) **(b)**

Figure 3.5 : (a) - 3D spectrum computed from the absolute value of the FFT of the 2D interferogram at each time delay, along the OPD axis. At each spectral element corresponds a single exponential ring-down. The solid blue trace at t = 0 µs represents the transmission spectrum with visible CO_2 absorption features. **(b)** - Ring-down at 6325 cm $^{-1}$. Upper panel - normalized ring-down data (black circular markers) fitted with a decaying exponential model (solid red trace). Lower panel - fit residuals.

fit was performed with a function built on the fminsearch function from MATLAB, which is based on the Nelder-Mead simplex method (Lagarias *et al.*, 1998). A comparison was made with the fit function from MATLAB with a Trust-Region algorithm (Coleman & Li, 1996). Both algorithm agreed on the ring-down time down to 10^{-11} s. The lower panel shows the fit residuum, which is flat and without remaining structure. The SNR is over 783, defined as the maximum of the decay (equal to unity since the decay is normalized) divided by the root-mean-square (RMS) value of the residuals (1.28×10^{-2}).

Repeating this procedure at every given spectral element yields the spectral variation of the ring-down time. As we saw in section 2.2.4.2,

$$\frac{1}{c\tau_{rd}(\nu)} = \frac{1}{c\tau_0(\nu)} + \alpha(\nu) \tag{3.2}$$

with c the celerity of light in vacuum in cm.s^{-1}, ν the wavenumber, $\tau_{rd}(\nu)$ the ring-down time with an intracavity sample at ν in microseconds, $\tau_0(\nu)$ the empty cavity ring-down time at ν and $\alpha(\nu)$ the molecular absorption coefficient in cm^{-1}. Figure 3.6 displays

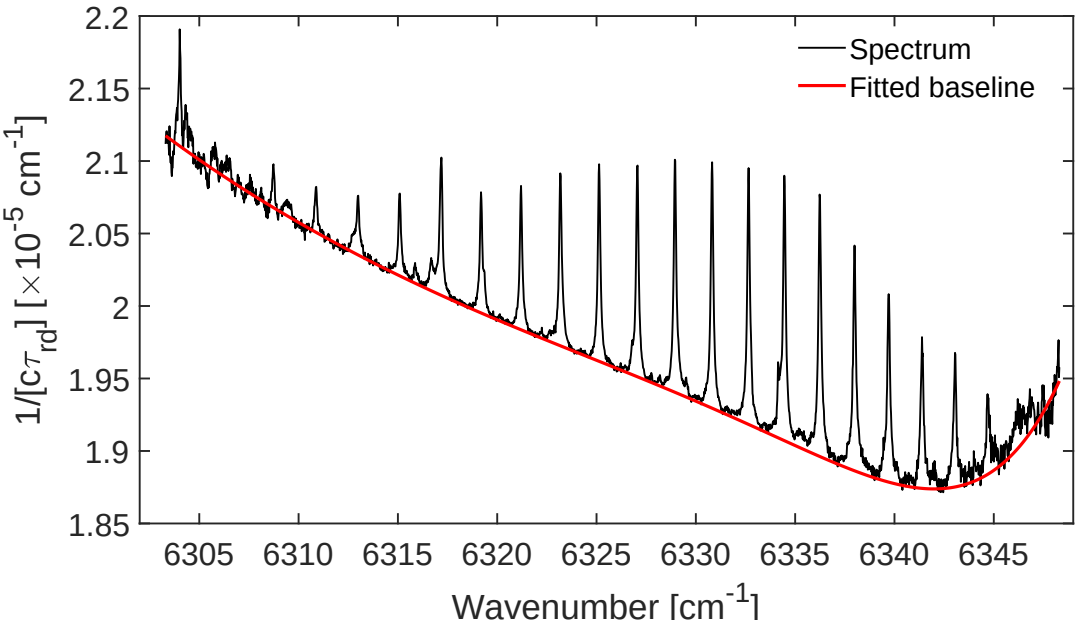

Figure 3.6 : CRDS spectrum obtained after fitting decaying exponential model at each spectral element (black trace). The fitted baseline (red trace) corresponds to $1/c\tau_0$, with τ_0 the empty cavity ring-down time.

the experimental data in black as $[c\tau_{rd}(\nu)]^{-1}$ over the whole range where the comb was transmitted by the cavity. The wavenumber axis was calibrated with the HeNe wavelength value and one molecular transition frequency from the HITRAN database (Gordon *et al.*, 2022). The red trace represents the fitted baseline and corresponds to $[c\tau_0]^{-1}$, from which the cavity mirror reflectivity can be obtained according to:

$$\tau_0 = \frac{L}{c(1-R+A)} \tag{3.3}$$

with L the cavity length, c the velocity of light, R the mirror reflectivity and A representing the cavity optical losses. The baseline is subtracted from the spectrum during the fitting process for ambient air analysis.

3.2.4 Ambient air measurement

As the cavity was in open air, we aimed at measuring CO_2 and H_2O concentrations in the laboratory air. A model of the absorption lines was computed as Voigt profiles with lineshape parameters from the HITRAN2020 database to compare with experimental data. The CO_2 and H_2O concentrations were the only fitted lineshape parameters. As

the concentrations are linear parameters, a matrix multivariate linear regression (MLR) was used to linearly fit the model to the data. This also allowed to simultaneously fit the molecular spectrum and the baseline as a seven-order polynomial, which was then removed from the spectrum to isolate the molecular transitions. The room temperature was 20°C with an uncertainty of 10%, the pressure was estimated at 1 atm with an uncertainty of 1% while CO_2 and H_2O concentrations were assumed at 400 ppm and 1% respectively as fit initial values.

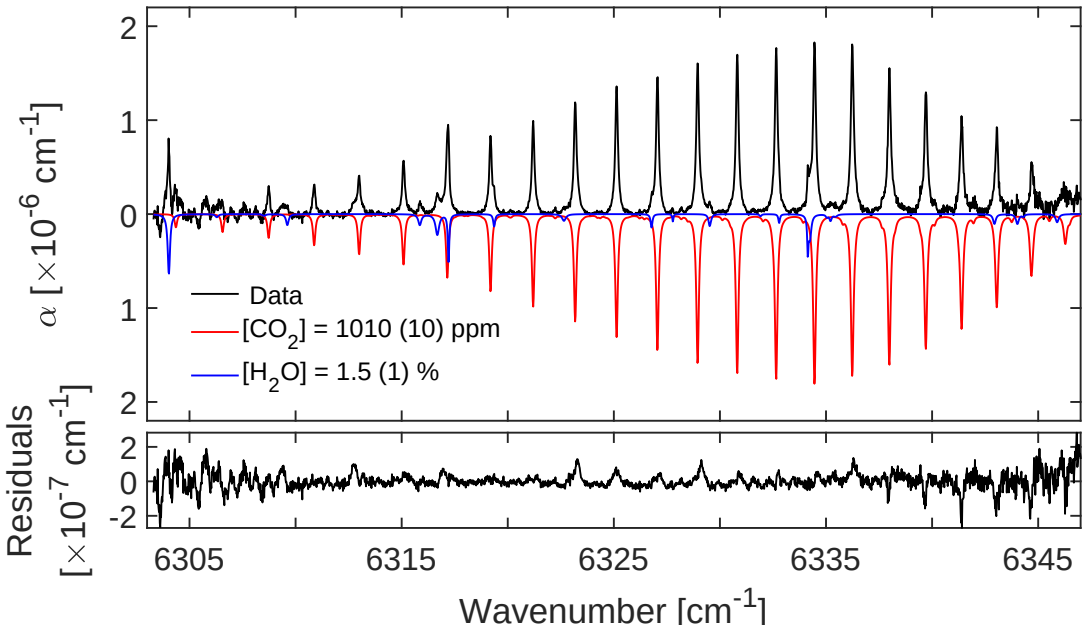

Figure 3.7 : Fitted spectrum with HITRAN parameters and Voigt profile. Black trace: experimental data. Models of H_2O (blue trace, inverted for clarity) and CO_2 (red trace, inverted for clarity).

Figure 3.7 presents the fitting results. In the top panel, the baseline-free spectrum is visible in black whereas the red and blue traces corresponds to the fitted absorption coefficient spectra of CO_2 and H_2O respectively (the model is inverted for clarity). The retrieved concentrations were $[CO_2]$ = 1010(10) ppm and $[H_2O]$ = 1.5(1)%, which are consistent with the conditions of a closed laboratory. Refitting the data with upper and lower bound values for the temperature and the pressure yielded bound values for the concentrations, which where translated to the uncertainty values. The noise equivalent absorption (NEA) is 5.2×10^{-8} cm $^{-1}$, computed from the RMS value of the residuals. It describes the minimum detectable absorption at 1σ. The resulting SNR is 36 for 0.02 cm^{-1} resolution (600 MHz). The total acquisition time was 25.3 s for a single spectrum

containing 2279 spectral elements. This yields a noise equivalent absorption at 1s averaging time (NEA^{1s}, defined in equation 1.11) of 5.5×10^{-9} cm $^{-1}$Hz$^{-1/2}$ per spectral element The residuals demonstrate distortions for some lines in the center of the range, whose linestrength seem to be uncorrelated to the distortions magnitude. We assume this remaining structure comes from the lack of cavity stabilization (translating in a drift of f_{rep} and f_{ceo}) combined with the irregular scan speed of the FTS translation stage. As the OPD calibration depends on triggering the AOM and the DAQ on consecutive events from the HeNe interferogram, the constant speed of the cart is critical in order not to miss events.

3.2.5 Comparison with cavity-enhanced absorption spectroscopy (CEAS)

To compare with the CRDS analysis, the spectrum at t = 0 µs from figure 3.5(a) is processed to obtain the cavity-enhanced absorption spectrum. A MLR is used to fit simultaneously the baseline and a model of the cavity transmission. The fitted CEAS spectrum is shown on figure 3.8 in the black trace. The fitted cavity transmission model is displayed in red. Lines are clearly distorted due to molecular dispersion (see subsection 2.1.2).

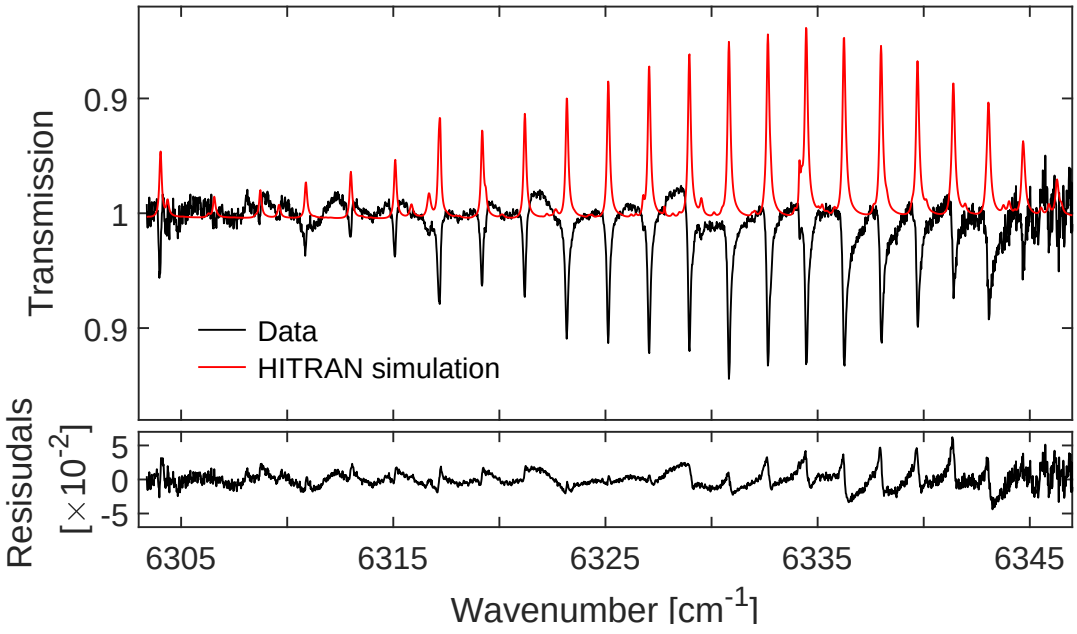

Figure 3.8 : CEAS spectrum (black trace) compared to a cavity transmission model simulated with HITRAN parameters (red trace, inverted for clarity).

Compared to the CRDS spectrum, the CEAS approach needs to account for molecular

dispersion, and requires a calibration of the cavity finesse and length. However, a single CEAS measurement is much faster, with a measurement time on the order of a second.

3.2.6 Limitations and outlook

This proof-of-concept experiment implemented CRDS with a frequency comb and an FTS. Quantitative measurement of CO_2 and H_2O concentrations in the laboratory air were performed. Four limitations to the setup were then identified:

- the AOM shutting off the PDH error signal limits how high the cavity finesse can be. The higher the finesse, the longer the decay and the longer the error signal will be off. At some point (unknown to us) we assume that the locking electronics wouldn't be able to relock and ensure the cavity light build-up until the next decay.
- the cart speed has to be kept constant during measurement. The higher the finesse, the slower the cart will need to move while maintaining steady movement. Our translating stage moves erratically below a few mm/s.
- the cavity length needs to be stabilized in order to stabilize the comb repetition rate and offset.
- the cavity should be enclosed in a gas cell in order to control the measured samples conditions and allow precise quantitative measurements.

This proof-of-concept was published in an article describing the apparatus and workflow (Dubroeucq & Rutkowski, 2022).

3.3 Improving FT-CRDS

To further develop the FT-CRDS technique and improve its performances, we collaborated with Piotr Masłowski and Dominik Charczun from Nicolaus Copernicus University in Toruń, Poland. The objectives of this collaboration were: a higher cavity finesse for enhanced sensitivity, a controlled environment and stabilization of the cavity length.

3.3.1 High-finesse cavity setup

The main objective of the new FT-CRDS setup was to increase the cavity finesse, translating into an increased sensitivity. This requires to decouple the comb and the PDH error

signal, allowing the AOM to shut off light without impacting the locking scheme. Indeed, in the first setup of FT-CRDS previously described, the cavity reflected comb light was retrieved to generate the PDH error signal. The AOM would then shut off the comb light to trigger decay events, while simultaneously shutting off the error signal. This in turn limited the AOM shut-off duration (to maintain the comb locked to the cavity), which was determined by the cavity ring-down time depending on the finesse. Greatly increasing the cavity finesse thus requires to decouple the comb light and the PDH error signal. The solution was to use a cw laser as an intermediate locking point between the comb and the cavity. The cw laser is locked to the cavity with PDH, and stays locked during the whole measurement, while the comb is locked to the cw laser and transmitted by the cavity. The comb light can then be shut off at will with the AOM, without impact on the cw PDH lock.

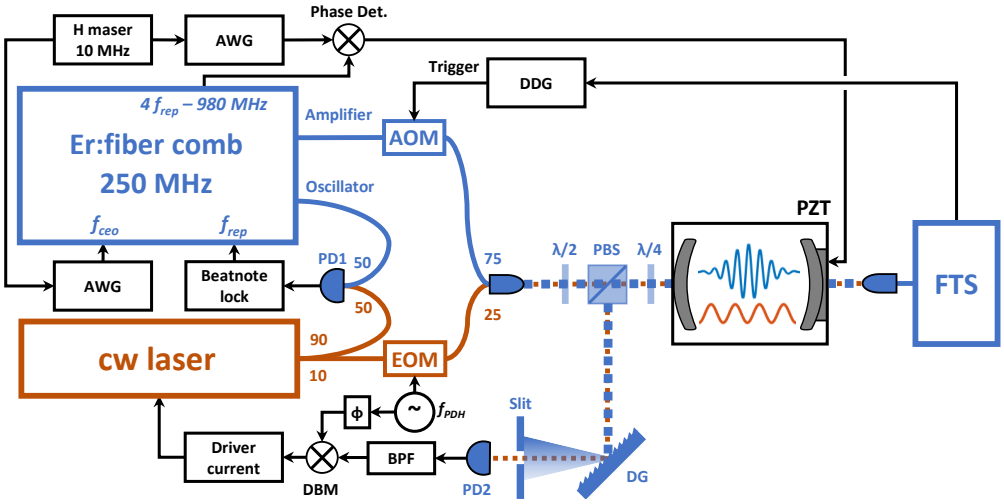

Figure 3.9 : Exprimental setup developed in Toruń. A cw laser is locked with PDH to the optical cavity. The comb offset frequency f_{ceo} is locked relative to a H maser reference. Light from the comb oscillator is beat against the cw laser on a fast photodetector. The obtained beatnote at 50 MHz is used to lock the comb to the cw, and thus to the cavity. Both lasers are coupled into the cavity. The comb AOM can be switched on and off withtout impacting the PDH error signal. AWG: arbitrary waveform generator. AOM: acousto-optic modulator. EOM: electro-optic modulator. PD1,2: photodetectors. $\lambda/2$: half-wave plate. $\lambda/4$: quarter-wave plate. PBS: polarizing beam-splitter. DG: diffraction grating. BPF: band-pass filter. DBM: double balanced mixer. PZT: piezo-electric transducer. FTS: Fourier transform spectrometer.

This new setup is described on figure 3.9. The comb was an Er:fiber from Menlo Systems with a repetition rate of 250 MHz and an amplified output power of 250 mW.

The cw laser was a RIO ECDL emitting at 1545 nm (6472 cm^{-1}). Both lasers were coupled into a high finesse cavity (measured as 21,400(60) at 6472 cm^{-1} with a CRDS measurement using the RIO laser) with a length of 60 cm and a free spectral range FSR = 250 MHz, yielding a theoretical cavity ring-down time of 12.7 µs. The cavity output is transmitted to the twice-folded FTS whose travel range is 120 cm, yielding a maxiumum resolution of 62 MHz. Both FTS outputs are measured with two Newport Model 2053-FS photodetectors.

The comb frequency offset f_{ceo} is compared with a phase detector to the frequency of an AWG referenced to a 10 MHz hydrogen maser. The phase detector output is fed to a PI servo-controller (NewFocus LB-1005S) which acts on the comb pump current to lock f_{ceo} to the frequency of the AWG. The cw laser is fibered to a 90:10 fiber splitter. The 10% branch is fibered to an EOM, inducing sidebands on the laser mode which are necessary to retrieve the PDH error signal. The EOM is modulated at 10 MHz provided by a H-maser. The 90% branch goes to a 50:50 fiber coupler along the light from the comb oscillator. Both beams go to free space after the splitter, and propagate to a fast photodetector (PD1). This yields a beatnote between the cw laser and the nearest comb mode, f_{beat} on figure 3.10.

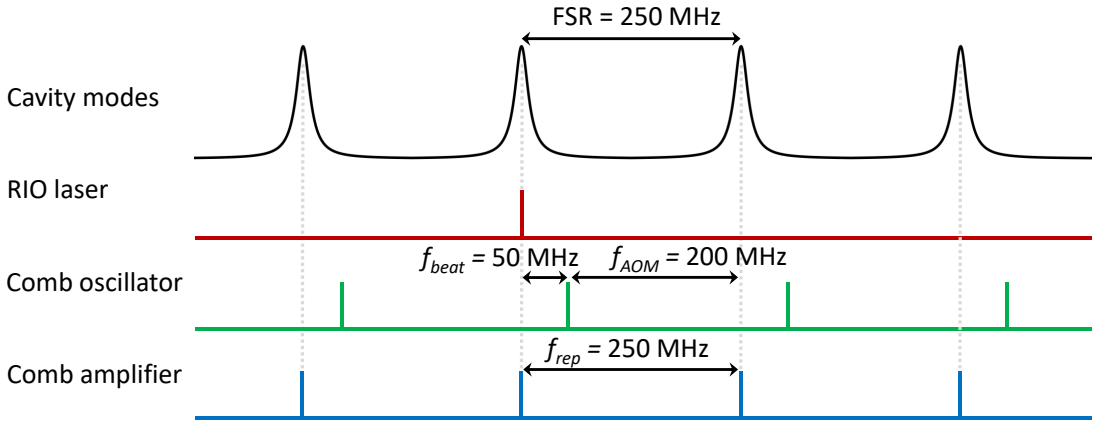

Figure 3.10 : Schematic of the locking scheme in the frequency domain. The RIO is locked with PDH to the measure cavity whose FSR is 250 MHz. The beatnote between the RIO and the comb oscillator allows to lock the latter at f_{beat} = 50 MHz from the former. The comb amplifier is shifted with an AOM at f_{AOM} = 200 MHz from the oscillator, hence it is also transmitted by the cavity modes. Finally, the cavity length, and thus its FSR, is corrected to maintain a constant f_{rep} value.

The comb amplifier output is fibered to an AOM operated at 200 MHz with a direct digital synthesizer (DDS). The amplifier is thus shifted by 200 MHz relative to the oscillator, f_{AOM} on figure 3.10. The AOM output is fibered to the 75% fiber of a 75:25

fiber coupler. The 25% branch comes from the output of the cw laser EOM. The comb amplifier and the cw laser then propagate in free space and are coupled into the optical cavity which is enclosed in a gas cell. The cell can be emptied and filled with a gas mixture at a controlled pressure. The cavity reflected beam is dispersed on a diffraction grating, and filtered to a slit to block as much light from the comb as possible. The light from the modulated cw laser is sent on a fast photodetector (PD2) whose output is band-pass filtered and demodulated with the H maser reference. The obtained PDH error signal is processed to lock the cw laser to the optical cavity, with a servo-controller acting on the laser driver current. Thereafter, the comb repetition rate is locked to the beatnote between the oscillator and the cw laser. With this beatnote set at 50 MHz, light from the comb amplifier is continuously transmitted by the optical cavity (since the comb is shifted by 200 MHz by the AOM and the cavity FSR is 250 MHz). The cw laser here acts as an intermediate locking point between the comb and the cavity. To stabilize the cavity length, the downconverted f_{rep} value ($4f_{rep}$ - 980 MHz) is demodulated with a reference frequency from an AWG (referenced to the H-maser) in a phase detector. The phase detector output is fed to an integrator servo-controller (NewFocus LB-1005S) which acts on a PZT mounted on the back of one cavity mirror, to control and stabilize its length. Figure 3.10 summarizes the locking scheme between the comb, the RIO and the cavity:

- the RIO cw laser is locked with PDH to a given cavity mode and follows it
- the comb oscillator is locked at a frequency $f_{beat} = 50$ MHz away from the RIO ; the comb modes follow the RIO
- the comb amplifier modes are shifted by $f_{AOM} = 200$ MHz from the oscillator modes
- as FSR $= f_{beat} + f_{AOM} = f_{rep}$, the comb amplifier modes are transmitted by the cavity modes
- the cavity length is corrected so that f_{rep} remains constant
- not shown on the figure: f_{ceo} is locked to an external reference.

The cavity transmitted light is coupled into fiber and fed into the FTS. The schematic is the same as described in section 3.2.1, with the exception of the HeNe laser propagating along the comb on both sides of the interferometer. The translation stage is 120 cm long (Aerotech ACT165DL-1200) and can be operated as slow as 0.1 mm/s. The data acquisition procedure with the DDG triggering simultaneously the data acquisition board and the comb AOM is the same as described in section 3.2.2. The data processing follows the

same balancing procedure as described in section 3.2.3. A typical interferogram obtained after data processing is shown on figure 3.11, with an inset zoom on the central burst.

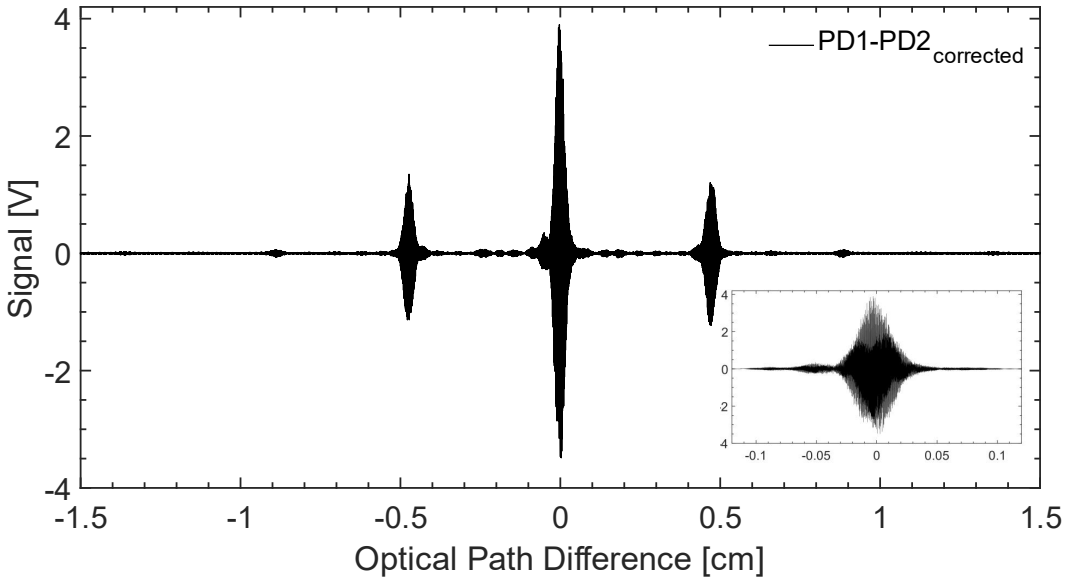

Figure 3.11 : Zoomed-in view of the interferogram obtained after the balancing procedure. The two bursts on each side of the central burst are caused by optical etalons. The inset on the bottom right corner shows a zoom on the central burst.

There is a notable difference in the data processing regarding the ring-down fitting compared to subsection 3.2.3. The acquired datasets are averaged after FFT in the frequency domain. However, computing the absolute value of the FFT of each interferogram results in a positive offset on the last points of the ring-down, when there is no light and noise is dominating. This can in turn offset the fitted ring-down time. To avoid this bias, the number of points in each ring-down is adjusted depending on the ring-down time and the SNR. At first, the natural logarithm (ln) of each ring-down is computed and roughly adjusted with a linear regression. As a ring-down is an exponential decay, its ln value is a decreasing linear function of time. When the ring-down becomes non-exponential due to the aforementioned bias, its ln value becomes non-linear. The slope coefficient from the linear regression then yields a first estimate of the ring-down time τ_{estimate}. The root-mean-square value of the linear regression residuals gives an estimate of the SNR of the given ring-down data. The length of each ring-down is then reduced to 2 to 4 times τ_{estimate}, depending on the SNR value. This is depicted on figure 3.12(a), where we see the natural logarithm of the ring-down at 6325 cm^{-1} (in blue circles) with the linear regression (red

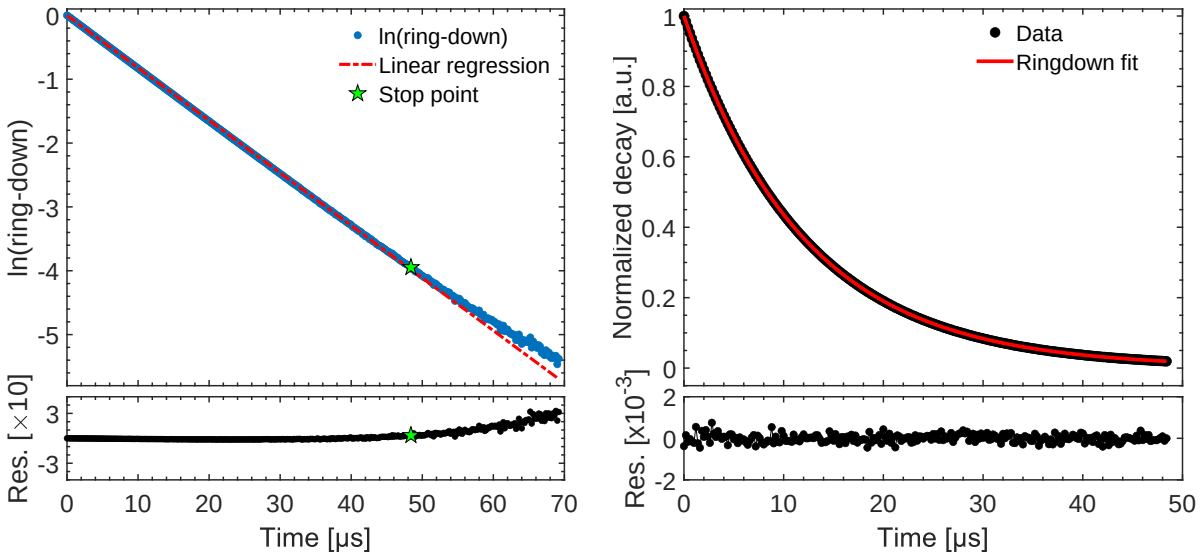

(a) (b)

Figure 3.12 : (a) - Logarithm of the ringdown at 6325 cm^{-1} (blue circles) with best linear fit (red dashed line) in the top panel. The lower panels shows the residuals from the fit. The green stars in both panels represent the point where noise starts dominating. **(b) -** Cropped ring-down data points from (a) (black circles) with fitted decaying exponential model (red solid line). Lower panel shows the fit residuals, which present no remaining structure. The associated SNR is 5278.

dashed line). The green star marks the cropping point of the data, where the ln value becomes non-linear and noise dominates. The cropped ring-down is then fitted with a decaying exponential model as described in subsection 3.2.3, as shown on figure 3.12(b). The fit residuals in the lower panel present no structure, and the SNR (computed as the inverse of the RMS value of the residuals) is 5278. This new procedure reduces the impact of the offset from the absolute value of the FFT on the fitted value τ_{rd}.

3.3.2 CO in gas cell measurement

The high-finesse setup was used to probe $^{12}C^{16}O$ in argon. The following paragraph describes the gas mixture, the stability of all frequencies kept locked during the measurements and the data acquisition parameters.

3.3.2.1 Measurement conditions

Table 3.2 summarizes the gas parameters, the rms fluctuations of the locked frequencies and the data acquisition parameters. A gas bottle containing 1023±20 ppm of $^{12}C^{16}O$ in argon was diluted 4 times in the gas cell enclosing the cavity, to yield a mixture of 250 ppm of CO in argon at 534(2) Torr (703 mbar). The pressure was measured with a 1000 Torr MKS Baratron with a resolution of 10 mTorr and an uncertainty of 0.25% of the measured value. The photo-detectors bandwidth was set at 5 MHz while the acquisition board sample rate was set at 5 MSample/s with an alias-free bandwidth of 2 MHz. A total of 15 spectra was acquired in 79 min (5 min 16 s per spectrum) in two distinct sets of data containing 7 and 8 spectra each. For each spectrum, a total of 2 million decay events were acquired, each decay event containing 350 sampling points.

Table 3.2 : Experimental conditions for the FT-CRDS measurement of $^{12}C^{16}O$ in argon.

Gas mixture		**Data acquisition**	
Gas mixture	$^{12}C^{16}O$ in argon	Acquired datasets	15
CO concentration	1023±20 ppm	Cart travel speed	1 mm/s
Dilution	4 times in pure argon	Cart travel length	1,270 mm
Pressure in cell	534(2) Torr	Resolution	250.27 MHz
Pressure uncertainty	0.25% of measure	Acq. time per dataset	5 min 16 s
Pressure resolution	10 mTorr	Total acquisition time	79 minutes
Lock frequencies		Photodetectors bandwidth	5 MHz
f_{rep} RMS value	6.9 $\times 10^{-3}$ Hz	DAQ sample rate	5 MSamples/s
f_{ceo} RMS value	1.3 Hz	DAQ alias-free bandwidth	2 MHz
f_{beat} RMS value	6.9 Hz	Data points per decay	350

During measurement, f_{rep}, f_{ceo} and the comb oscillator - cw laser beatnote f_{beat} were acquired with a frequency counter at 1 Hz. The monitored values for the second dataset are displayed on figure 3.13 minus their mean values. For f_{rep} in blue in the top panel, the RMS value is 6.9 $\times 10^{-3}$ Hz. This converts into 5.2 kHz uncertainty into the optical domain. The RMS value for f_{ceo} (middle panel, red) is 1.3 Hz. For f_{beat}, the RMS value is 6.9 Hz. The combined uncertainty for a given comb mode is then 5.2 kHz in the optical domain, which is the frequency precision of the measurement.

The next subsection will cover the fit procedure and the results obtained from the fitted spectrum.

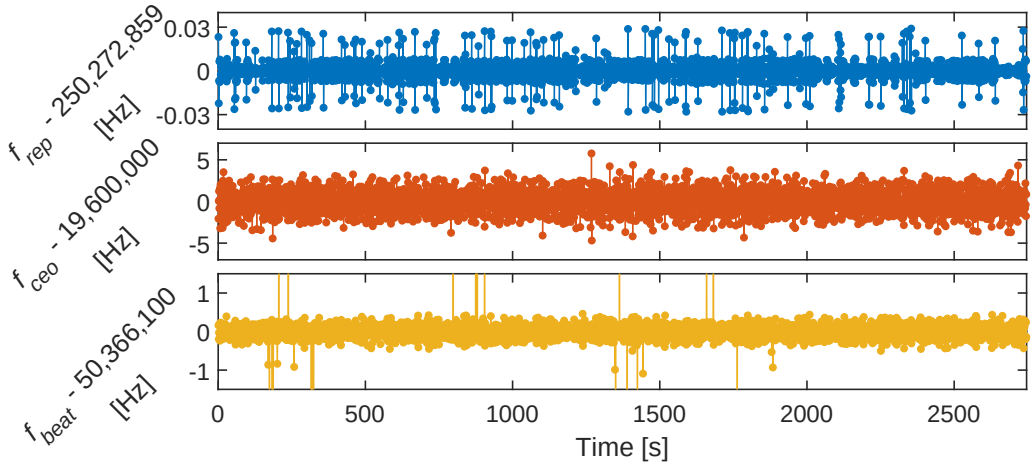

Figure 3.13 : Measured values of: f_{rep} (top panel), f_{ceo} (middle pannel) and f_{beat} (bottom panel). The mean values were subtracted. The measurement was made at 1 Hz.

3.3.2.2 Fit results

The averaged, processed and fitted data are displayed on figure 3.14. The experimental spectrum in absorption coefficient per unit length is shown in black. The baseline was subtracted in a similar fashion to section 3.2.4 with a matrix linear regression. The spectrum without baseline is then fitted with a non-linear least squares algorithm. The model computes lineshapes with Voigt profiles. The fitted parameters for each line are:

- the pressure broadening with argon γ_{Ar},
- the frequency shift f_{shift}.

The temperature and the CO concentration were also fitted as global parameters. The other line parameters such as the central frequency, the linestrength, the self pressure broadening and the pressure frequency shift are fixed to the values from the HITRAN2020 database (Gordon *et al.*, 2022). The red trace represents the fitted model of the P-branch lines from the CO second overtone (from the P(1) to the P(12) line), inverted for clarity. The RMS value of the residuals is 5.9 $\times 10^{-9}$ cm^{-1}, yielding a NEA^{1s} of 5.1 $\times 10^{-9}$ cm^{-1}Hz$^{-1/2}$ per spectral element, for 6401 spectral elements and a total acquisition time of 79 min. In the centermost part of the spectrum between 6315 and 6335 cm^{-1}, the RMS value of the residuals is 1.1 $\times 10^{-9}$ cm^{-1} with a NEA^{1s} of 9.6 $\times 10^{-10}$ cm^{-1}Hz$^{-1/2}$ per spectral element, which is a clear improvement over the previous setup performances even when taking into account the 15 averaged spectra and the higher spectral resolution.

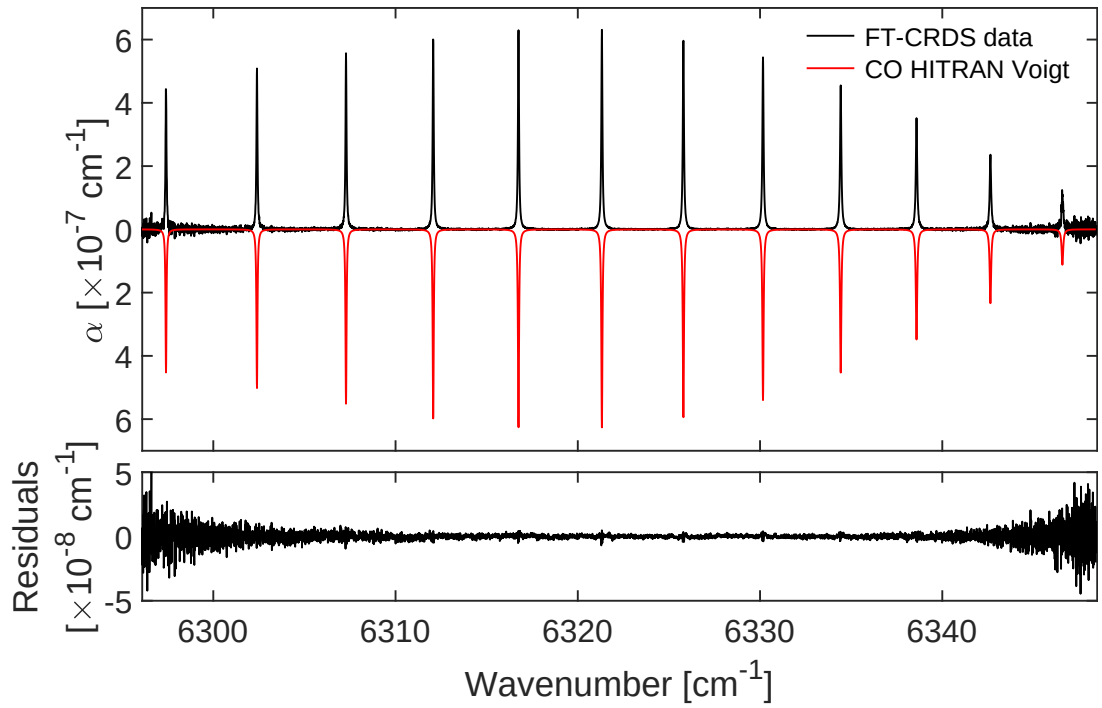

Figure 3.14 : CO experimental data (black trace) compared to the line-by-line fitted model (red trace) with Voigt profiles and HITRAN database parameters. The lower panel depicts the fit residuals. The residuals are quite tight in the center of the spectrum, with remaining intensity discrepancies in the middle of each line.

A good agreement between the experimental spectrum and the fitted model is observed. However, remaining structure in the residuals is visible at each line position in the center of the spectrum, where the SNR is the highest. This discrepancy with the Voigt profile is investigated in section 3.3.2.4.

Table 3.3 summarizes the pressure broadenings of CO in argon and the frequency shifts obtained for each line, the global temperature and the CO concentration.

3.3.2.3 Uncertainty budget

The total uncertainties, displayed in table 3.3 between parenthesis, were obtained as the square root of the sum of squared type A and B uncertainties.

Type A (statistical) uncertainty values were obtained from the estimated Jacobian matrix J of the parameters. The covariance matrix Cov was then estimated with:

$$Cov = \mathrm{inv}(J^T J). \tag{3.4}$$

Table 3.3 : Pressure broadening coefficients relative to argon, temperature and CO concentration fitted values and their respective uncertainties.

Lines	P(12)	P(11)	P(10)	P(9)	P(8)	P(7)
γ_{Ar}[$\times$ 10^{-3} $cm^{-1} \cdot atm^{-1}$]	42.5(5)	44.5(5)	46.0(4)	46.5(4)	47.5(4)	49.0(4)
f_{shift} [$\times$ 10^{-3} cm^{-1}]	-6.9(4)	-7.1(4)	-7.6(3)	-6.9(3)	-6.7(3)	-7.0(3)
Lines	P(6)	P(5)	P(4)	P(3)	P(2)	P(1)
γ_{Ar}[$\times$ 10^{-3} $cm^{-1} \cdot atm^{-1}$]	50.8(5)	53.2(5)	56.4(6)	60.5(7)	64.3(10)	71.1(19)
f_{shift} [$\times$ 10^{-3} cm^{-1}]	-7.2(3)	-7.1(4)	-6.4(4)	-5.5(6)	-5.3(9)	-4.6(18)
T [K]	295.2(15)					
CO concentration [ppm]	244.6(21)					

The root mean square error RMSE is then defined as:

$$\text{RMSE} = \sqrt{\frac{\Sigma(data - model)^2}{N - k}} \tag{3.5}$$

where N is the number of data points in the absorption line and k is the number of fitted parameters. $N - k$ represents the degrees of freedom. The standard errors SE for each parameter is obtained with:

$$\text{SE} = \text{RMSE} \times \sqrt{\text{diag}(Cov)}. \tag{3.6}$$

Type B (other) uncertainties come from the error of the measured pressure in the cell. The fitting procedure was performed with a pressure of 534 Torr. The pressure uncertainty being 2 Torr, the spectrum was also fitted at 532 and 536 Torr. The type B uncertainties for each fit parameter were then obtained as the total absolute variation for the parameters relative to their 534 Torr fit values. The contributions of type A and type B uncertainties are displayed on table 3.4. From the table, we see that type A uncertainties are more prominent than type B uncertainties.

Table 3.4 : Uncertainty budget of the Voigt profile fitted parameters.

	Lines	P(12)	P(11)	P(10)	P(9)	P(8)	P(7)
γ_{Ar}[$\times$ 10^{-4} cm^{-1} $\cdot$ atm^{-1}]	Type A	3.9	3.5	3.2	2.9	2.8	2.8
	Type B	2.4	2.4	2.3	2.4	2.4	2.6
f_{shift} [$\times$ 10^{-4} cm^{-1}]	Type A	3.4	3.1	2.9	2.7	2.6	2.6
	Type B	0.31	0.10	0.03	0.11	0.21	0.22
	Lines	P(6)	P(5)	P(4)	P(3)	P(2)	P(1)
γ_{Ar}[$\times$ 10^{-4} cm^{-1} $\cdot$ atm^{-1}]	Type A	3.1	3.5	4.2	5.6	8.3	18
	Type B	2.7	2.8	3.2	3.3	4.1	5.5
f_{shift} [$\times$ 10^{-4} cm^{-1}]	Type A	2.8	3.2	3.9	5.2	8.0	17
	Type B	0.09	0.08	0.65	2.18	1.31	3.00
T [K]	Type A			1.41			
	Type B			0.48			
CO concentration [ppm]	Type A			1.65			
	Type B			1.18			

3.3.2.4 Comparison with Hartmann-Tran profile

As structure remains in the center of the lines in the residuals of the Voigt profile fit, a comparison with the Hartmann-Tran profile was conducted (Ngo *et al.*, 2013). The HTP takes into account more lineshape parameters than the VP (namely speed-dependent effects and velocity-changing collisions). Comparing how well each profile fits the experimental data may tell if the technique is sensitive enough to detect these beyond-Voigt features in the absorption lineshapes. The comparison was done on the P(9), P(6), P(4) and P(2) which were previously studied in a comb-assisted CRDS experiment (Kowzan *et al.*, 2017). The HTP parameters are described in section 2.1.4. Their associated values for CO in argon were taken from Kowzan *et al.* (ibid.).

The fit parameters were the CO concentration and the temperature, globally fitted for all lines simultaneously. The comparison of both line profiles is displayed on figure 3.15. The top panel shows the experimental data (black circles) fitted with the HTP (blue solid line). The residuals from the previous VP fit and from the HTP fit are shown on the middle and bottom panel respectively. For comparison, a quality factor for the fit, QF

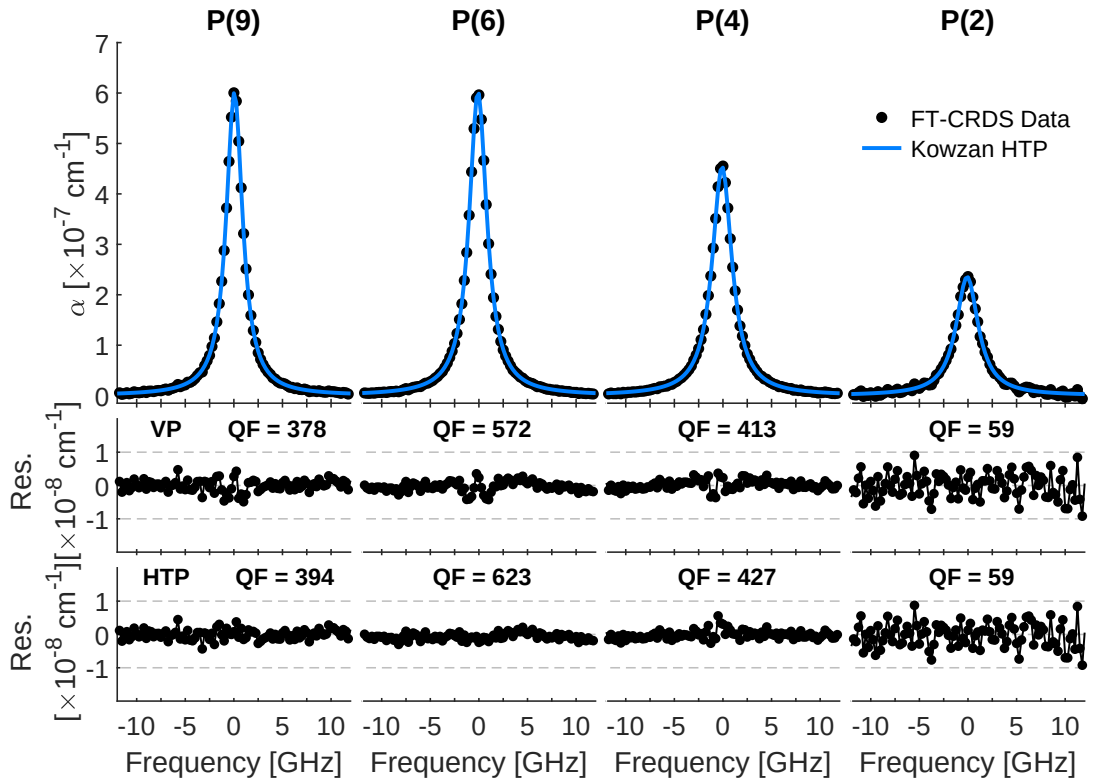

Figure 3.15 : The P(9), P(6), P(4) and P(2) lines fitted with Hartmann-Tran profiles and parameters from a previous study. The top panel shows experimental data points (black circular markers) with the fitted model (blue solid trace). The lower panel depicts the residuals from the HTP fit and the quality factors for each line. The middle panel shows the residuals for the previous Voigt profile fit of these lines, and the corresponding quality factors. There is good agreement between the VP and the HTP. The comparison shows an improvement in the quality factors for the P(9), P(6) and P(4) lines with the HTP. The most significant improvement is for the P(6) line, where the SNR is the highest.

(Cygan *et al.*, 2012, Bui *et al.*, 2014) is computed for each absorption line with both line profiles. QF is defined as the ratio of the maximum absorption of the line, α_{max}, divided by the root mean square error of the residuals RMSE defined in eq. 3.5:

$$\mathrm{QF} = \frac{\alpha_{max}}{\mathrm{RMSE}} \tag{3.7}$$

The VP residuals display a discrepancy between the data and the VP model at the line center for the P(9), P(6) and P(4) lines, which belong to the highest SNR part of the spectrum, whereas the HTP residuals for these lines show a better agreement with data. The signal-to-noise ratio is therefore high enough to detect speed-dependent effects and/or collisional narrowing. This correlates with an appreciable improvement of QF for the P(9),

P(6) and P(4) lines with the HTP relative to the VP. There is no improvement for the P(2) line due to its lower SNR. The retrieved parameters with HTP are $[CO]_{HTP}$ = 242.8(15) ppm and T_{HTP} = 292.6(9) K. These values and the ones obtained from the Voigt fit lie in the error bars of one another, with $[CO]_{VP}$ = 244.6(21) ppm and T_{VP} = 295.2(15) K. However there is still a significant discrepancy between the two temperatures.

3.4 Conclusion

To conclude, a first proof-of-concept setup demonstrated the feasibility of OFC-based FT-CRDS and its use for quantitative spectroscopy measurement. A second setup was developed to push further the performances of the technique. Using a cw laser as a locking proxy between the comb and the cavity, the technique was applied to a high finesse cavity to probe the P-branch of the second overtone band of CO in argon. Precise lineshapes were retrieved in a non-linear fitting procedure and compared to previous measurement, showing a high enough sensitivity to resolve features beyond the Voigt profile.

OFC-based FT-CRDS is a sensitive, multiplexed spectroscopic technique which benefits from both the frequency precision of frequency combs and the sensitivity, calibration-free advantages of CRDS. Currently, the technique is limited by the acquisition time it requires, which increases linearly with the cavity finesse. Faster acquisition implies either a lower cavity finesse, or undersampling the interferograms allowing to set a higher speed on the FTS translation stage. Also, it is noteworthy to mention that in its current state, the high-finesse setup is subject to noise due to the cw laser - comb locking.

The next step for FT-CRDS is single comb mode resolution and the application of the sub-nominal and interleaving methods (see section 1.4.2). This would allow to measure absorption lines narrower than the comb mode spacing. Moreover, the acquisition procedure of this technique was also designed for monitoring over time the concentrations of reactants, transient species and products in reaction kinetics experiments.

4 – Probing cold supersonic jets with optical frequency combs

Cooling down translational, rotational and vibrational degrees of freedom of molecules has been of great interest to study molecular structure and dynamics, from high resolution molecular spectroscopy (Levy, 1980) to cold chemistry, reaction kinetics and laboratory astrophysics (Smith & Rowe, 2000). It is of particular interest when studying large polyatomic molecules, which exhibit congested spectra at room temperature due to the very high number of ro-vibrational states populated. For instance, figure 4.1(b) shows the congested spectrum of buckminsterfullerene (C_{60}) in warm conditions as the red trace, as opposed to its cold rotationally-resolved counterpart in the blue trace. Two main cooling techniques have been used in the past decades: buffer gas cooling cells and supersonic jet expansions (also called free jets or molecular beams), with the latter being decades older than the former.

Buffer gas cooling cells consists of a vacuum chamber whose walls are cooled down to cryogenic temperatures with a liquid-helium cryostat. The molecular gas sample is introduced in the chamber mixed with a cooled inert gas, typically helium. The gas sample internal degrees of freedom are relaxed through collisions with the buffer gas, and its translational and internal temperatures are taken down to equilibrium with the chamber walls temperature. Such apparatus have been extensively used with different spectroscopic techniques, for example microwave spectroscopy (Messer & De Lucia, 1984) or laser-induced fluorescence (LIF), with Patterson *et al.* (2010) reporting translational and rotational temperatures of 6 K for naphtalene cooled with helium. In a later work, Patterson & Doyle (2012) produced gas phase benzonitrile, acetone, 1-2 propanediol, fluorobenzene and anisole molecules at a temperature of 8 K in a helium buffer gas cell and detected them with Fourier transform microwave spectroscopy. They retrieved helium–molecule low temperature rotational and vibrational relaxation cross-sections, thanks to the efficient vibrational cooling of buffer gas cooling cells through collisions.

Laser based buffer cell experiments have also been conducted in the infrared region, notably with optical frequency combs. Spaun *et al.* (2016) reported a cavity-enhanced frequency comb Fourier transform spectroscopy setup to probe a helium-cooled buffer gas cell in the mid-infrared. They used an ytterbium-pumped optical parametric oscillator (OPO) emitting between 2.8 and 4.8 µm (in the molecular fingerprint region corresponding to the C-H bond stretching region) with a 6,000 finesse to enhance sensitivity. With this setup, they recorded spectra of nitromethane (CH_3NO_2), naphthalene ($C_{10}H_8$), adamantane ($C_{10}H_{16}$) and hexamethylenetetramine ($C_6N_4H_{12}$) with translational and rotational temperatures of ~ 10 K. They showed that large molecules could be rovibrationally resolved by efficient cooling of their internal degrees of freedom. Changala *et al.* (2016) used the same cell with either a PDH locked comb/cavity and FTS scheme or a swept-cavity with a VIPA spectrometer, and compared the sensitivity of both setup. The PDH/FTS scheme reached a noise-equivalent absorption sensitivity of 7.6×10^{-10} $cm^{-1}Hz^{-1/2}$ per spectral element, which was an order of magnitude lower than the state-of-art at the time. For the swep-cavity/VIPA measurements, the sensitivity was reported as 10 times higher than the FTS value. With either of the two setups, they probed vinyl bromide, adamantane and diamantane and compared the spectra of the two latter. As adamantane was rovibrationally resolved whereas diamantane wasn't, they observed that the latter had a total density of vibrational states an order of magnitude higher than the former in the 3000 cm^{-1} region. They concluded that, to obtain high-resolution rovibrational spectra of large molecules, measurements should be performed at longer wavelengths, beyond 5 µm. Following this study, the setup was modified to probe the 8.5 µm region using a DFG frequency comb (Changala *et al.*, 2019). With this setup, they measured the first rovibrationally resolved spectrum of C_{60} by cooling it down with argon as the buffer gas. The experimental setup is viewed on figure 4.1(a), with the oven inside which the solid sample of C_{60} was heated up to 1000 K to produce sublimated vapor, which then entered the cryogenic cell through the inlet plate along with argon molecules. The cavity mirrors are mounted on either side of the cell. The spectrum they obtained is shown on figure 4.1(b) as the blue trace, with the Q and R branches easily identifiable after comparison with the simulated spectrum in black. They reported a rotational temperature of 150 K, close to the cell walls temperature of 135 K. The cooling process was limited by the condensation temperature of argon at 87 K.

The other, much older cooling technique consists of adiabatically expanding a gas from a high pressure reservoir through a nozzle into a vacuum chamber. The gas stagnation

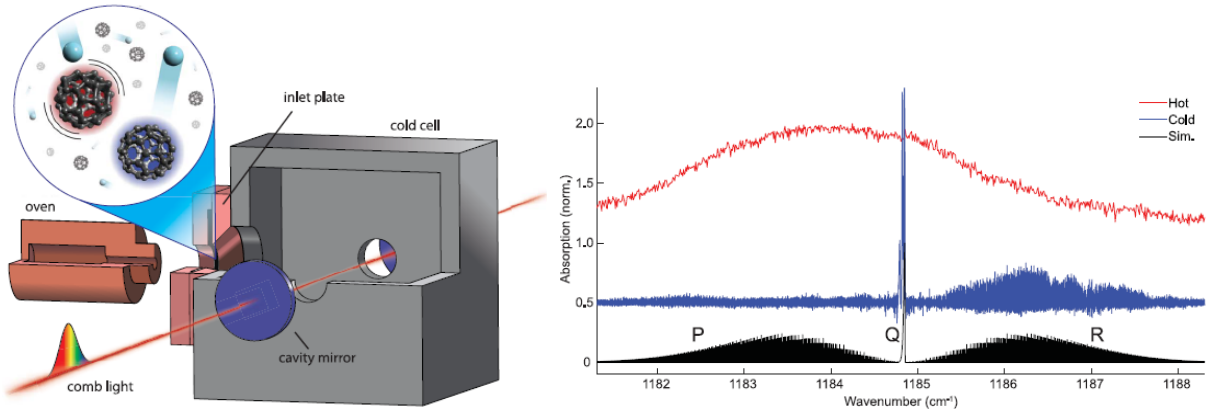

(a) **(b)**

Figure 4.1 : (a) - Experimental setup designed for probing large hydrocarbons with cavity-enhanced comb spectroscopy. The molecules are heated inside an oven, and the resulting sublimated vapor then enters the cryogenic cell. The cavity mirrors are placed on either side of the cell. **(b)** - Room (red) and low (blue) temperature spectra and simulated spectrum with a rotational temperature of 150 K of C_{60}. Reproduced from Changala *et al.* (2019).

enthalpy is converted into kinetic energy, thus drastically cooling down the gas (Georges *et al.*, 2022). The sample gas is seeded in an inert monoatomic buffer gas (usually helium, argon, neon or krypton), leading to a more efficient cooling process through collisions. The technique is generally referred to as supersonic jets or "free jets". The nozzles can be of different geometries (pinholes, slits or de Laval) and either be pulsed or continuous (Franquet *et al.*, 2015). The theory will be reviewed in more details in section 4.1.

Free jets have been paired with various probing techniques. Amirav *et al.* (1980) used LIF to probe iodine I_2 and several large polycyclic aromatic hydrocarbons (PAHs) seeded in rare gases. The gas was expanded through pinholes of various diameters. Amirav *et al.* (1981) later used a slit nozzle to create pulsed planar expansions, in order to increase light-gas interaction pathlength and effectively enhance sensitivity. They probed aniline (C_6H_5-NH_2) and 9,10-dichloroanthracene ($C_{14}H_8C_{12}$) seeded in argon, using both UV absorption spectroscopy and LIF. Works from McClelland *et al.* (1979) and Wallraff *et al.* (1987) showed the less efficient cooling of the vibrational temperature compared to rotational and translational temperatures in supersonic jets.

Infrared spectroscopy has been a prolific tool to study free jets (Arnó & Bevan, 1995). Lovejoy & Nesbitt (1987) used a difference frequency laser, providing cw light tunable in the 2.2-4.2 µm region, to probe N_2HF in a pulsed planar jet from a slit nozzle. A CRDS

study of PAHs (naphthalene, anthracene, phenanthrene, pyrene, and perylene) with a heated supersonic slit jet source was conducted by Huneycutt *et al.* (2004). Brumfield *et al.* (2010) developed a 8.5 µm QCL cavity ring-down spectrometer, and paired it with a slit nozzle expansion to measure methyl bromide (CH_2Br_2) rovibrational structure near 1197 cm^{-1}. After some upgrades to the detector and the laser driver, they revisited their previous measurement of CH_2Br_2 and were able to resolve hyperfine splittings thanks to the increase in resolution and sensitivity (Brumfield *et al.*, 2011). This setup was later modified with a heated slit nozzle to study pyrene in the 1180 cm^{-1} region (Brumfield *et al.*, 2012). Suas-David *et al.* (2016) investigated the measured lineshapes of CO seeded in argon at very high temperature (∼2000 K) in a circular hypersonic jet with cw-CRDS. Fourier transform spectroscopy was also extensively paired with free jets (Herman *et al.*, 2000). Snavely *et al.* (1981) probed a continuous jet of neat ammonia (NH_3) with a FTIR, and later studied two isotopes of methyl chloride ($CH_3{}^{35}Cl$ and $CH_3{}^{37}Cl$) with the same setup (Snavely *et al.*, 1983). Pirali *et al.* (2013) notably presented the rotationaly resolved spectrum of naphtalene at 12.7 µm, obtained with synchrotron radiation and a FTIR.

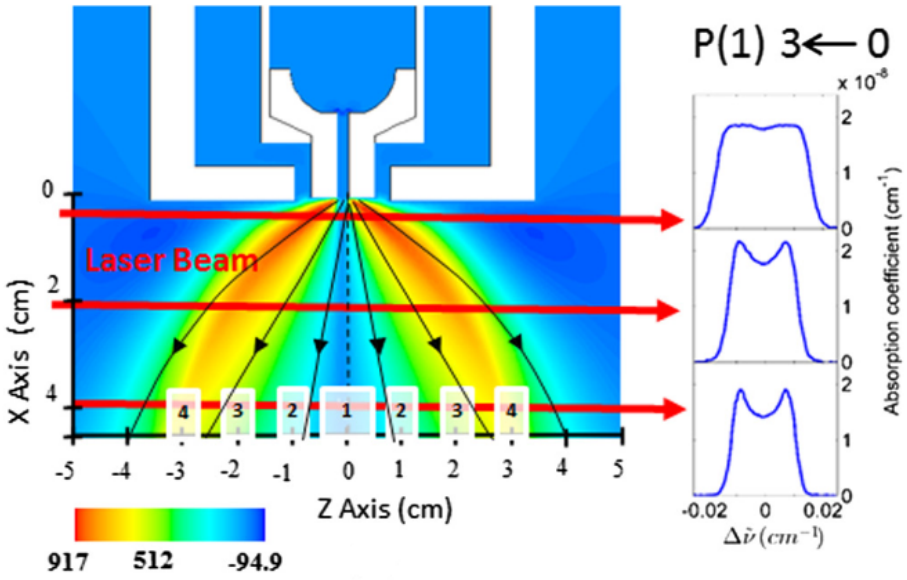

Figure 4.2 : CFD simulation of the transverse velocity distribution of a CO seeded in argon pinhole jet. The red arrows represent three different probing stations with cw-CRDS along the transverse axis. The jet is highly divergent in its boundary layers, leading to the broadened and even double-peaked absorption lineshapes as shown on the right of the figure. Reproduced from Suas-David *et al.* (2016).

Figure 4.2 shows a computational fluid dynamics (CFD) simulation of the transvserse velocity distribution in the pinhole jet. The jet boundary layers appear as highly divergent in the transverse dimension. The red arrows represent the laser beam axis at three different distances from the pinhole. The corresponding absorption line profiles of the P(1) line from the second overtone band of CO are shown on the right of the figure. The lineshapes are Doppler broadened due to the divergence of the jet boundary layers, even presenting double-peaked lineshapes when the probing distance from the pinhole increases.

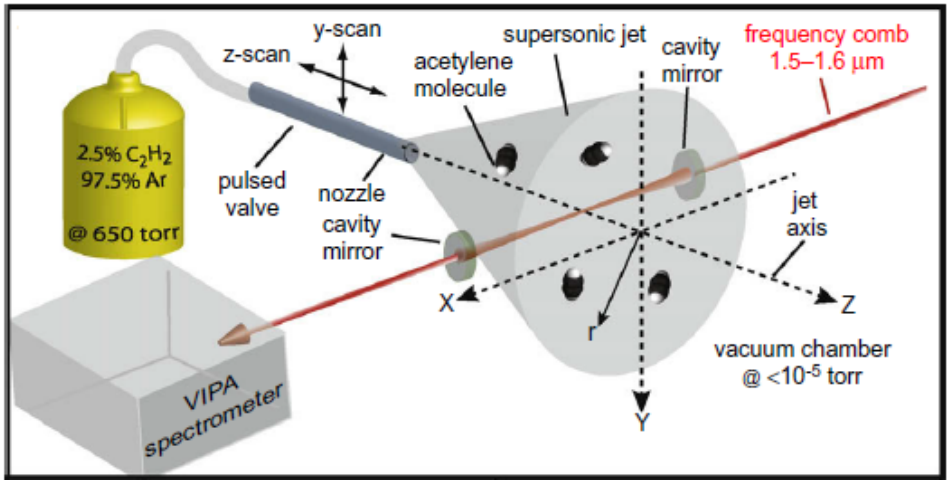

Figure 4.3 : Experimental setup of a pinhole jet of C_2H_2 seeded in argon probed with a near-infrared frequency comb and a VIPA spectrometer. The movable nozzle allowed to probe the jet at different distances and heights from the nozzle. Density and temperature conditions were then mapped using tomographic reconstruction. Reproduced from Thorpe *et al.* (2009).

Recently, free jets have been implemented with frequency comb based spectrometers. Thorpe *et al.* (2009) were the first to use cavity-enhanced direct frequency comb spectroscopy with a VIPA spectrometer to probe a pinhole jet of acetylene at 1.525 μm. The setup is displayed on figure 4.3. The comb had a repetion rate of 100 MHz and was coupled to a 6300 finesse cavity with a FSR of 700 MHz. With the VIPA spectrometer resolution of 1 GHz, the Lorentzian transfer-function of the VIPA etalon and the 700 MHz spacing of the cavity transmitted comb modes, the InGaAs camera frequency channels sampled an average of 2.5 comb modes each. The comb and cavity modes were swept across 1 FSR in 17.5 MHz steps. The VIPA spectrometer records 25 nm at a time, from 1.515 μm to 1.54 μm. The mixture studied contained 2.5% of C_2H_2 seeded in 97.5% Ar at 650 Torr in the reservoir, and expanded through a 1 mm diameter circular valve into a vacuum

chamber at a pressure of $< 10^{-5}$ Torr. By varying the distance and the height between the nozzle and the cavity, they performed a tomographic reconstruction of the density and temperature conditions in the jet. This was the first demonstration of a comb based supersonic jet experiment. Reber *et al.* (2016) demonstrated cavity-enhanced transient absorption spectroscopy (CE-TAS), a comb pump-probe technique with two enhancement cavities, one coupled to the pump comb and the other to the probe comb. They probed I_2 seeded in either He or Ar expanded through a circular nozzle, and were able to follow changes in absorbance with a 120 fs time resolution. Finally, Agner *et al.* (2022) proposed a QCL dual-comb spectrometer operating between 1200 and 1290 cm^{-1}, built from commercially available QCL-DCS devices. They studied CF_4 and $CHCl_2F$ seeded in neon in a pulsed, skimmed, circular free jet. The fast acquisition rate of the DCS approach allowed to probe the jet at different time delays relative to the nozzle valve opening, with a 4 µs time resolution.

As we saw, both buffer gas cells and free jet expansions can be used to cool down molecular rotations down to a few kelvins. Each of the two techniques present advantages and drawbacks, concerning as much the engineering as the interpretation of spectroscopic data. The following lists summarizes the pros and cons of buffer gas cooling cells:

+ longer interaction pathlength, equal to the cell length
+ requires modest pump capacities
+ vibrational relaxation is more efficient through collisions (higher molecular density)
- complex cryogenic engineering
- gas condensation on cell walls.

and of free jets:

+ no condensation on cell walls,
+ temperatures down to 5 K are reachable,
+ relative simple design of the nozzle apparatus,
- requires large pumping capacity,
- mechanical vibrations of the system,
- boundary regions in the jet with different conditions compared to the core and/or highly diverging jets leading to broadened or distorted lineshapes.

The next section will cover the basics of underexpanded free jets.

4.1 Underexpanded free jet

As discussed in the introduction of this chapter, a straightforward technique to cool down a gas sample to a few kelvins is to expand it at supersonic speeds. The gas undergoes an isentropic expansion from a high-pressure reservoir where it is close to rest conditions (temperature T_0, pressure P_0) into a vacuum chamber at a much lower pressure P_b, the so-called background pressure, through a nozzle. The cooling mechanism with underexpanded free jets can be basically described with equation 4.1. As the gas is accelerated through the nozzle into the chamber, the stagnation enthalpy of the gas in the reservoir c_pT_0 is converted into kinetic energy, leading to a decrease of the temperature T in the isentropic core of the jet:

$$c_pT_0 = c_pT + \frac{v_b^2}{2} \tag{4.1}$$

with c_p the gas specific heat capacity through a constant pressure process and v_b the fluid barycentric velocity (Rowe & Canosa, 2022).

A typical nozzle consists of a converging part whose minimal area portion is called the throat, which can be followed by a diverging part. A nozzle can be a conical converging part with an aperture, or even a simple pinhole. As the nozzle area decreases towards the throat, the gas is accelerated by a pressure differential. At the throat, the jet is sonic, meaning that the Mach number M is equal to 1. The Mach number is obtained as:

$$\mathrm{M} = \frac{v_b}{a} \tag{4.2}$$

with a the speed of sound in the medium. For the jet to be sonic, the pressure at the throat needs to be higher than the critical value P_c, which is defined in the isentropic chocking pressure ratio:

$$\frac{P_0}{P_c} = (\frac{\gamma+1}{2})^{\frac{\gamma}{\gamma-1}} \tag{4.3}$$

with $\gamma = c_p/c_v$ the ratio of heat capacities and c_v being the specific heat for a gas in a constant volume process. P_c is then dependent on the gas heat capacities and the pressure in the reservoir P_0. From the isentropic chocking pressure ratio, we can define four categories of supersonic expansions:

- the underexpanded free jet, where the critical pressure P_c is equal to the exit pressure P_e and far exceeds the background pressure P_b,
- the overexpanded free jet, where the nozzle exit pressure P_e is lower than the background pressure P_b,

- the perfectly expanded free jet, where the nozzle exit pressure P_e is matched to the background pressure P_b with a converging-diverging contoured nozzle,
- the molecular beam, where a free jet is collimated using a skimmer.

Underexpanded free jets are usually shortened to "free jets", although all four cases are strictly speaking free jets as well, as they all expand in a "wall-free" medium. Refer to Rowe & Canosa (2022), Georges *et al.* (2022) and Arnó & Bevan (1995) for more details on perfectly expanded free jets and molecular beams.

The underexpanded free jet conditions therefore depend on the P_c/P_b ratio. As the latter increases, the jet is called "moderately underexpanded", "highly underexpanded" or "extremely underexpanded". The moderately underexpanded free jet will present a series of shock waves with a diamond or "X" structure, while the highly underexpanded jet has oblique shock cells in the form of a barrel (Franquet *et al.*, 2015).

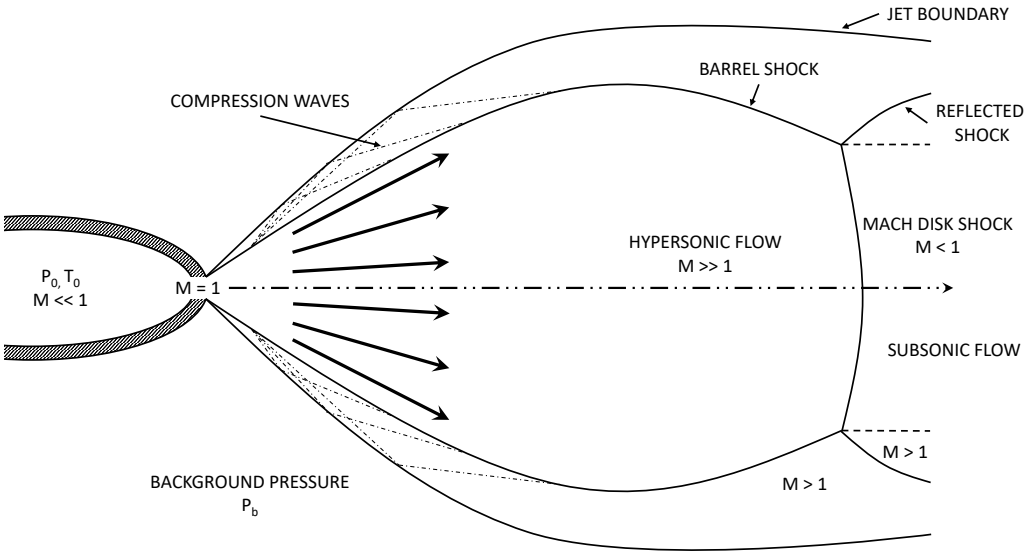

Figure 4.4 : Schematic of an extremely underexpanded free jet expansion (inspired by Rowe & Canosa (2022)).

Figure 4.4 schematizes the extremely underexpanded free jet, where only one barrel cell is present. After the sonic throat, the jet becomes supersonic (or hypersonic) with Mach numbers well above 1. The barrel shock depicts the limits of the isentropic core. The jet boundary represents the outer limit of the mixing layer between the jet and the static gas in the chamber. A curved shock disk is formed at the end of the barrel, called the Mach disk, from which the flow becomes subsonic.

Circular nozzles lead to very divergent jets, resulting in broadened or even double-peaked absorption lines, as was described by Suas-David *et al.* (2016). Instead of a circular nozzle or pinhole, one can use a planar slit nozzle. In this case, the jet is no more circular around an axis but elongated along the slit length dimension. Slit jets present the major advantage of an increased light interaction pathlength and higher column density leading to an increase in sensitivity together with a reduced radial velocity distribution compared to a circular aperture free jet (Veeken & Reuss, 1985). Extensive studies have been conducted both experimentally and numerically on slit nozzles to better comprehend the jet conditions and parameters (Teshima, 1987 ; Raju & Kurian, 1995 ; Putignano & Welsch, 2012). Slit jets are then very well suited to infrared absorption spectroscopy, and have been used with lasers or FTIRs (Arnó & Bevan, 1995 ; Herman *et al.*, 2000).

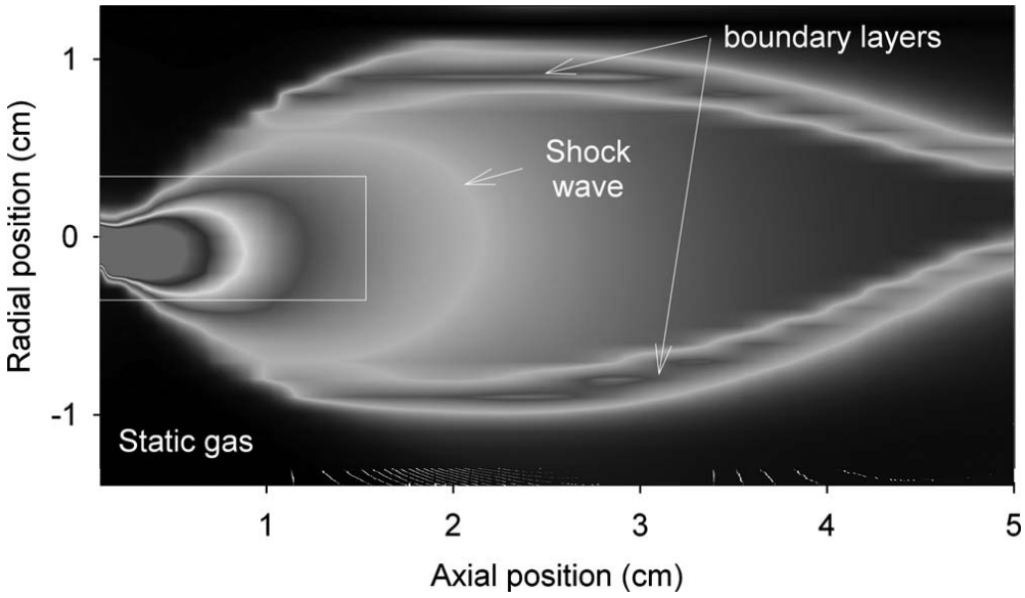

Figure 4.5 : Experimental map of a planar supersonic jet generated with a planar or "slit" nozzle. Reproduced from Moudens *et al.* (2009).

An experimental map of a slit nozzle expansion is shown on figure 4.5, reproduced from Moudens *et al.* (2009). The shock wave delimiting the isentropic core is easily identifiable, as well as the boundary layers between the jet and the static gas in the chamber.

During the second part of my PhD, we developed a comb-based CEAS setup operating in a slit supersonic jet. The slit was designed by Robert GEORGES, Guy PÉCHEUL and Julien LECONTE and has a tunable width. The optical setup allowing to place the enhancement cavity transversally to the jet direction was adapted upon the already

existing CRDS system.

4.2 Experimental setup

The experimental setup is shown on figure 4.6. Before going into technical details, here is summarized the general layout. The comb was coupled to an optical cavity for sensitivity enhancement, with the mirrors mounted on the jet cell, perpendicularly to the gas flow. The comb was locked to the cavity with PDH (see section 2.3.1, and the cavity length was

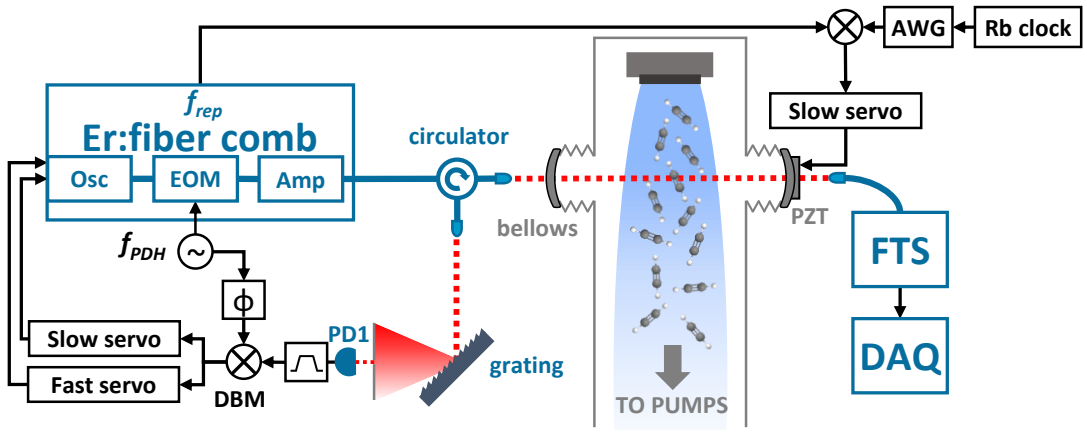

Figure 4.6 : Setup for the comb-jet experiment. The comb amplified output is coupled into a circulator and into a 10 m fiber going to the cavity mounted on the jet cell. The cavity reflected light is retrieved with the circulator, and is coupled to free-space to the PDH optics. The comb is locked with PDH to the cavity, and the cavity length is stabilized with a PZT mounted on one of the mirrors. The cavity transmitted light is coupled back in fiber and analyzed with a fast-scanning FTS.

stabilized with a PZT mounted on one of the mirrors. The cavity output was analyzed with a FTS and data was recorded on an acquisition board (DAQ).

4.2.1 Comb-cavity coupling

The laser is an Er:fiber comb emitting in the near-infrared. It is fibered to an optical circulator. When coupling the comb amplifier light to fiber, we observed a drastic reduction of the comb spectral coverage and power. The comb peak power being too high, leading to non-linear effects in the fiber disrupting the comb pulse, we added a -3 dB attenuator at the comb output. The comb, PDH optics and FTS were located in a neighboring room to

reduce mechanical vibrations due to the pumping system. The circulator is then fibered to a 10 m fiber going to the cavity injection mirrors in the jet cell room.

The optical cavity is made of two plano-concave mirrors with a half-inch diameter, a 6.35 mm thickness and a 1 m radius of curvature. Their reflectivity is 99-99.3% in the 1500-1600 nm range (Layertec, coating 109332). The cavity is 100 cm long, yielding a FSR of 150 MHz. This results in a 3:2 comb-cavity match, where every third comb mode is coupled to every other cavity mode, as shown on figure 4.7, with the comb modes in red and the cavity modes in black. The filtered comb repetition rate is then 300 MHz.

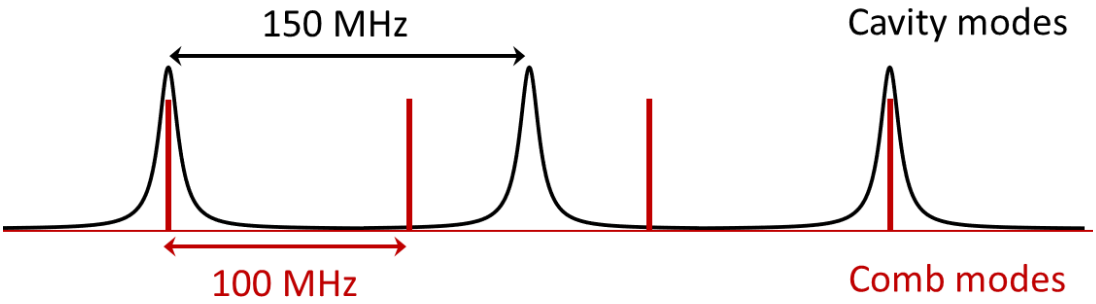

Figure 4.7 : Comb mode spacing of 100 MHz (in red) and cavity FSR of 150 MHz (in black). One out of 3 comb mode is coupled into every other cavity mode. The filtered comb has an effective repetition rate of 300 MHz.

A major issue expected and observed during experiments was the mechanical vibrations induced by the pump system. The vibrations strongly impacted the cavity length, preventing any stabilization at the level required to measure narrow lineshapes. Mount cages were then designed to act as passive stabilization of the mirrors, adding to the active stabilization scheme with the PZT.

4.2.2 Mirror mounts

Originally, the mirror mounts were fixed directly onto a metallic table, sharing the same metallic frame as the vacuum chamber, along the injection mirrors and the fiber collimator. However, as the mirrors were not solidary of the jet cell itself, vibrations from the pumps were clearly observed during experiments and prevented, for example, the optical alignment of the cavity when the pumps were on. Cages for the mounts were designed to dampen the vibrations by mounting the mirrors directly onto the cell flanges.

A 3D model of the mounts is shown on figure 4.8(a) and 4.8(b). Four 25 cm long 1/2" wide optical posts from Thorlabs are screwed in directly onto the cell flange. Two 10 × 10

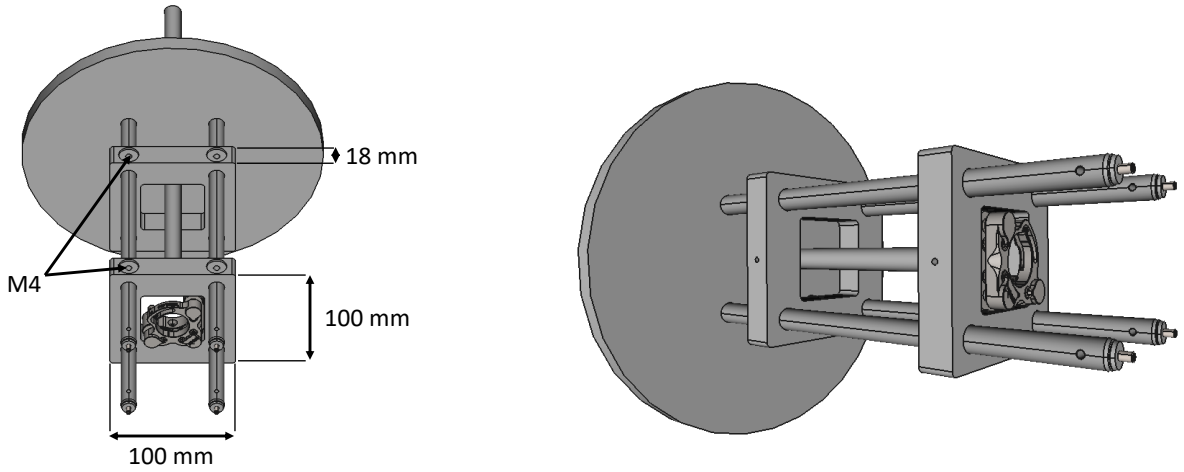

(a) **(b)**

Figure 4.8 : View of mirror mount cage 3D model. **(a)** - Top view. **(b)** - Isometric view.

cm and 2 cm thick squares are sled onto the 4 posts. The first one is meant to rigidify the structure, while the second one is housing the mirror mount. Both squares are tightened on the posts with 4 spring-loaded thumbscrews (Thorlabs, S25H). The whole structure is aligned with the tube centered on the flange, where N_2 is flushed during experiments to prevent static gas from accumulating in front of the mirrors.

The mirrors are encased in a box sealed with o-rings. The box is itself mounted on bellows with o-ring seals, to further dampen mechanical vibrations. The bellows also permit easier cavity alignment as they are deformable. The bellows are then slid onto the flush tubes, and the box sits in the opto-mechanical mount. The whole structure is shown on figure 4.9(a) for the input mirror and figure. 4.9(b) for the output mirror. For the input mirror, we see at the bottom of the picture the 10 m fiber coming from the comb and the fiber collimator. The beam then propagates in free-space to the injection mirrors, and is coupled to the cavity. We see the whole mirror mount structure tightened to the cell flange, and the mirror itself is visible in the center. The same structure is used for the output mirror. The PZT mounted on the mirror is seen in the picture center, and a fiber collimator and the 10 m fiber going to the FTS at the bottom are in view at the bottom of the picture.

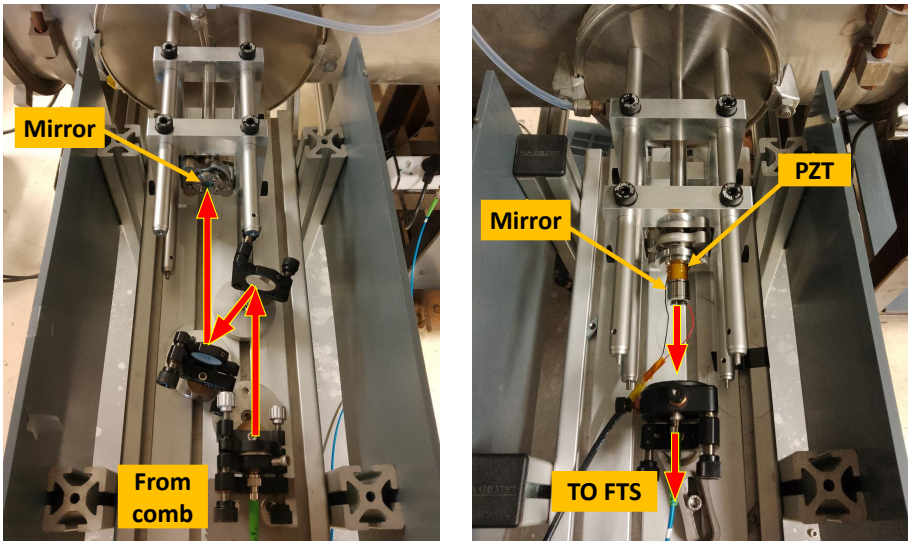

(a) **(b)**

Figure 4.9 : Pictures showing the mirror mounts and cages mounted on the jet cell flanges. The red arrows indicates the path of the comb light. **(a)** - Input mirror cage with comb light coupled to free space from fiber and injections mirrors. **(b)** - Output mirror cage (PZT visible, mounted on the mirror) with collimator and fiber going to the FTS.

4.2.3 Cavity stabilization scheme

The comb is locked to the cavity using a single point PDH lock, as shown on figure 4.6. An electro-optic modulator located in the comb casing is driven at a reference frequency of 10 MHz coming from a GPS-disciplined Rubidium clock, and generates sidebands on each comb mode. Then, the cavity reflected light is retrieved with the fibered circulator. It is then collimated to free space, and dispersed on a reflective diffraction grating (Thorlabs, GR13-0616). A narrow part of the comb spectrum is then filtered through a pinhole, and detected on a 25 MHz bandwidth photodetector (Thorlabs, PDA10D2). Its electrical output is bandpass-filtered at 10 MHz, and demodulated in a DBM (Mini-Circuits, ZAD-1+) with the phase matched Rubidium clock frequency. The obtained PDH error signal is then fed to two servos controlling the comb slow PZT and the oscillator pump current, acting as slow and fast actuators respectively. The PZT servo is a proportional integrator (NewFocus LB1005S) with a PI corner frequency set at 30 Hz. Its output is amplified by a high-voltage amplifier (Vescent SLICE-DHV Dual-Channel PZT Controller and High-Voltage Amplifier). The current servo is a PI^2 (Vescent D2-125 Laser servo) with the first integrator set to off state and the PI corner of the second integrator set to 30 kHz. Once the comb is locked to the cavity, the f_{rep} value is compared to the output of an arbitrary

waveform generator (AWG) in a phase detector (Mini-Circuits ZRPD-1+). Its output is fed to another servo (NewFocus LB1005S) set to pure integrator, which controls the cavity PZT. The servo output is amplified by the high voltage amplifier previously mentioned. The AWG output is finely tuned to match the average value of f_{rep}, then the servo gain is steadily increased to lock f_{rep} by stabilizing the cavity length.

With the locking procedure completed, both the comb repetition rate f_{rep} and the comb offset frequency f_{ceo} are measured on a frequency counter (Tektronix FCA3000). The f_{rep} output from the comb is bandpass filtered around 100 MHz (MiniCircuits, BBP-101+). The f_{ceo} output from the comb built-in *f-2f* interferometer (see section 1.1.3) is lowpass filtered at 50 MHz (MiniCircuits, BLP-50+) and amplified (MiniCircuits, ZFL-500LN+) before the frequency counter, so that only the lower frequency beatnote from the *f-2f* is detected. Each frequency is measured and averaged for 10 ms every second.

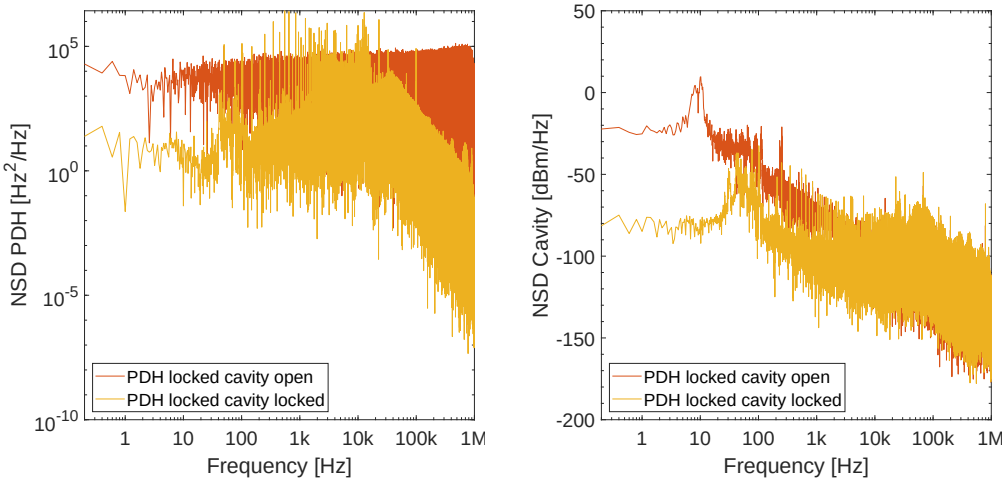

(a) **(b)**

Figure 4.10 : (a) - NSD of the PDH error signal with PDH lock on and cavity free-running (red trace), PDH lock off and cavity locked (yellow trace). When the cavity is locked, a tenfold reduction is observed below 10 kHz compared to the case with the cavity left free-running. **(b)** - NSD of the cavity error signal with PDH lock on and cavity free-running (red trace), PDH lock off and cavity locked (yellow trace). When the cavity is locked, noise corresponding to the mechanical vibrations due to pumps around 10 Hz is reduced by 60 dBm compared to when the cavity is left free-running.

The noise spectral densities (NSD) are presented for both the PDH and cavity error signals (figures 4.10(a) and 4.10(b) respectively) for 2 different cases: comb locked with PDH and cavity length free-running (red) and comb locked and cavity length stabilized (yellow). When both the comb is locked with PDH to the cavity and the cavity is locked

as well, noise decreases by 30 dB up to 30 Hz. However, an increase of noise for discrete frequencies between 30 Hz and 30 kHz is also observed, corresponding to the two servos PI corner frequencies for the slow and fast actuators respectively. As these frequencies are equally spaced by 100 Hz, we assumed they arose from electrical grid at 50 Hz. The noise reduction between 30 Hz and 30 kHz is 8.7 dB. For the cavity error signal on figure 4.10(b) noise mainly corresponds to frequencies below 100 Hz, with the strongest peaks around 10 Hz when the comb is locked to the cavity. This shows the impact of the mechanical vibrations induced by the pumping system on the optical cavity. When the cavity length is then stabilized with the mirror PZT, a noise reduction of 66 dB is observed for frequencies below 30 Hz. Below 10 Hz, noise is decreased by 79 dB. This demonstrates how the locking scheme allows to stabilize the cavity length while the pumps are functioning.

With the comb locked to the cavity and the cavity length stabilized, it is possible to step the cavity length in order to map entire absorption lineshapes using the subnominal and interleaving method (see section 1.4.2). The AWG output can be increased (or decreased) by steps of a few Hz. By doing so, the cavity length will increase (or decrease) and the comb modes spacing will follow. As the comb emits near $\sim$ 196 THz (1525 nm) and its repetition rate is 100 MHz, a change of 1 Hz in the repetition rate results in a change of 1.96 MHz in the optical domain for the comb modes spacing.

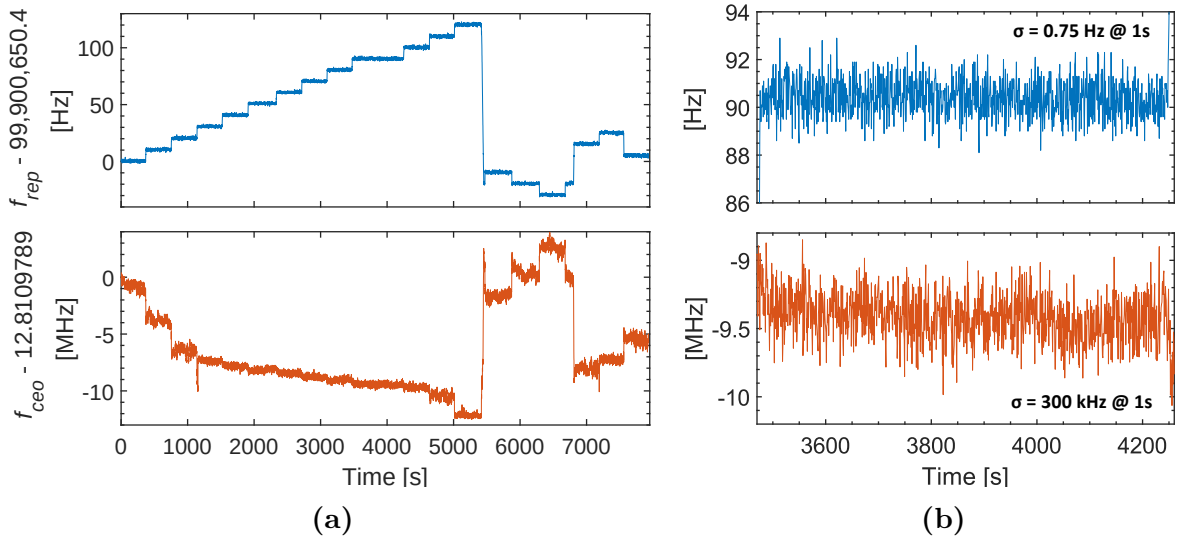

Figure 4.11 : (a) - Monitored values of f_{rep} (upper panel, blue trace) and f_{ceo} (lower panel, red trace) while f_{rep} is swept by 19 steps of 10 Hz (19 MHz in the optical domain). **(b)** - A close-in view of the 10$^{\text{th}}$ step. With σf_{rep} = 0.75 Hz and σf_{ceo} = 300 kHz the uncertainty of the comb mode frequencies is below 2 MHz in the optical domain.

The figure 4.11(a) displays the monitored f_{rep} (upper panel, blue) and f_{ceo} (lower panel, red) values while 19 f_{rep} steps of 10 Hz were acquired. This translates into steps of 19.6 MHz in the optical domain. Both graphs are centered on their starting frequencies. The 19 f_{rep} steps and their corresponding f_{ceo} steps show a "staircase" pattern. A zoom on the 10^{th} step is shown on figure 4.11(b). The standard deviation was typically of 0.75 Hz for f_{rep} (translating to 1.5 MHz in the optical domain) and of 300 kHz for f_{ceo} at 1 Hz measurement cycle for a given step. This yielded a combined uncertainty of the comb mode frequencies below 2 MHz.

The cavity output was then analyzed with the FTS described in section 1.4.3.

4.2.4 Free jet apparatus

Figure 4.12(a) shows a picture of the free jet apparatus. The vacuum chamber continues towards the wall and into the next room where the pumping system is located. The optical cavity is mounted perpendicular to the vacuum chamber. The mirrors are housed in the

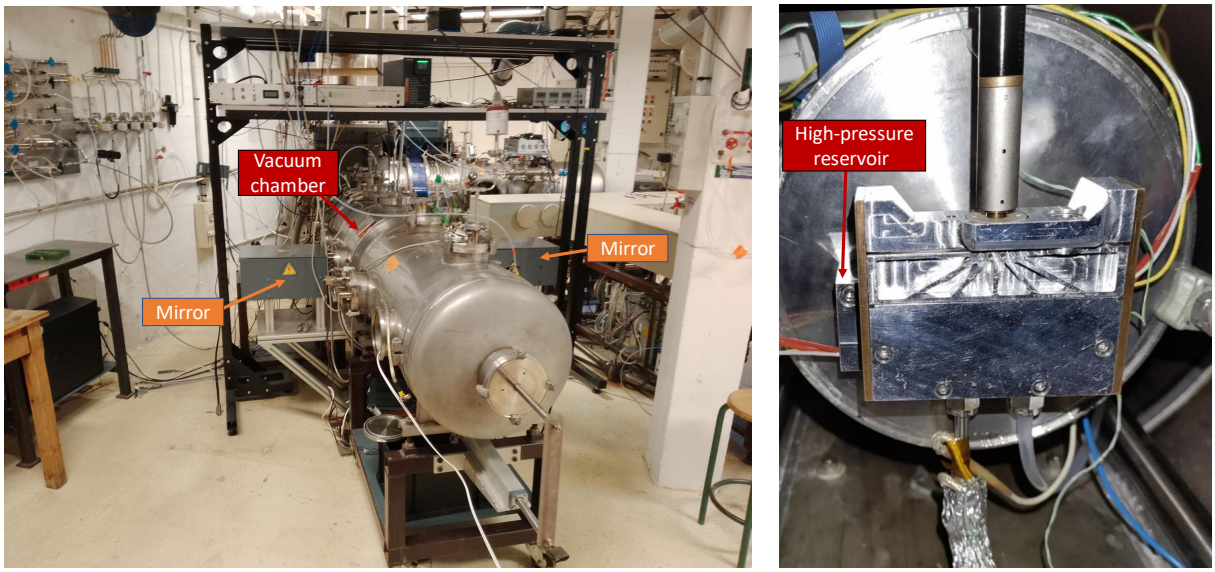

(a) **(b)**

Figure 4.12 : (a) - View of the jet setup in Rennes. The vacuum chamber continues towards the wall and into the pumps room. The cavity mirrors are housed in the grey boxes visible on each side of the vacuum chamber so that the cavity is perpendicular to the flow. **(b)** - Slit nozzle mounted on the reservoir inside the vacuum chamber. The high pressure reservoir sits right behind the nozzle. The slit is 8.1 cm long and its aperture height can be controlled down to 30 µm.

grey boxes visible on each side of the chamber on the picture. The slit nozzle used to expand the gas mixture from the reservoir into the vacuum chamber is showed on figure 4.12(b). The high-pressure reservoir is located right behind the nozzle. It is 8.1 cm long and its width can be varied from 30 µm to 300 µm. The slit was designed by Robert GEORGES, Julien LECOMTE and Guy PÉCHEUL. A CFD simulation was made by LECOMTE, and is shown on figures 4.13(a) and 4.13(b). They respectively represent the density and temperature maps of the free jet expanded through the slit nozzle. The view plane is perpendicular to the slit length and the laser light path through the jet. The consecutive shock cells are easily identifiable on figure 4.13(b), with the cold isentropic core of the first cell reaching temperatures of a few kelvins. The jet can be probed at various distances from the slit. The distance between the optical path and the slit was optimized to probe the coldest part of the jet in the first shock cell, and to minimize absorption in the warm shear and boundary layers (see section 4.1). The optical path was then placed as close as possible to the slit.

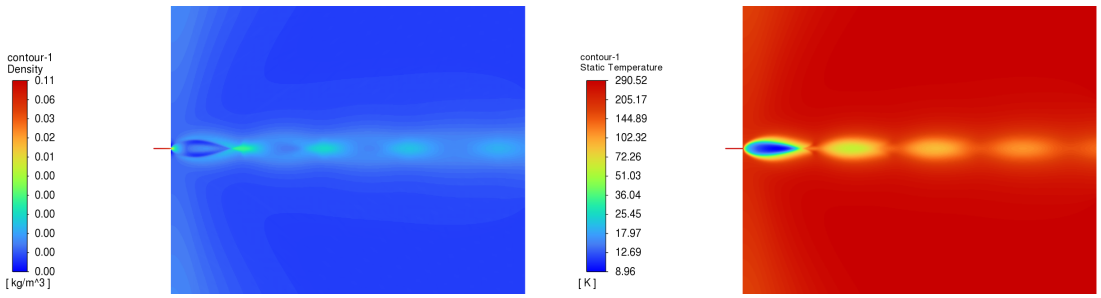

(a) **(b)**

Figure 4.13 : (a) - CFD simulation of a slit nozzle free jet density map seen from the side. **(b)** - CFD simulation of a slit nozzle free jet temperature map seen from the side. The isentropic core surrounded by shear layers is clearly visible in the first shock cell on both figures. The jet here is highly underexpanded, as seen with the successive barrel shock cells. Data and figures come from private communications with Julien LECOMTE.

4.3 Acetylene free jet spectroscopy

A supersonic jet of acetylene in argon expanded through a slit nozzle was then measured with the setup. The experimental conditions are summarized on table A.1.

4.3.1 Interleaved normalized spectrum

Each interferogram was cut relative to the step f_{rep} value, and shifted by the step f_{ceo} value, following the subnominal technique (see section 1.4.2). Then the absolute value of the fast Fourier transform (FFT) of the processed interferogram was computed.

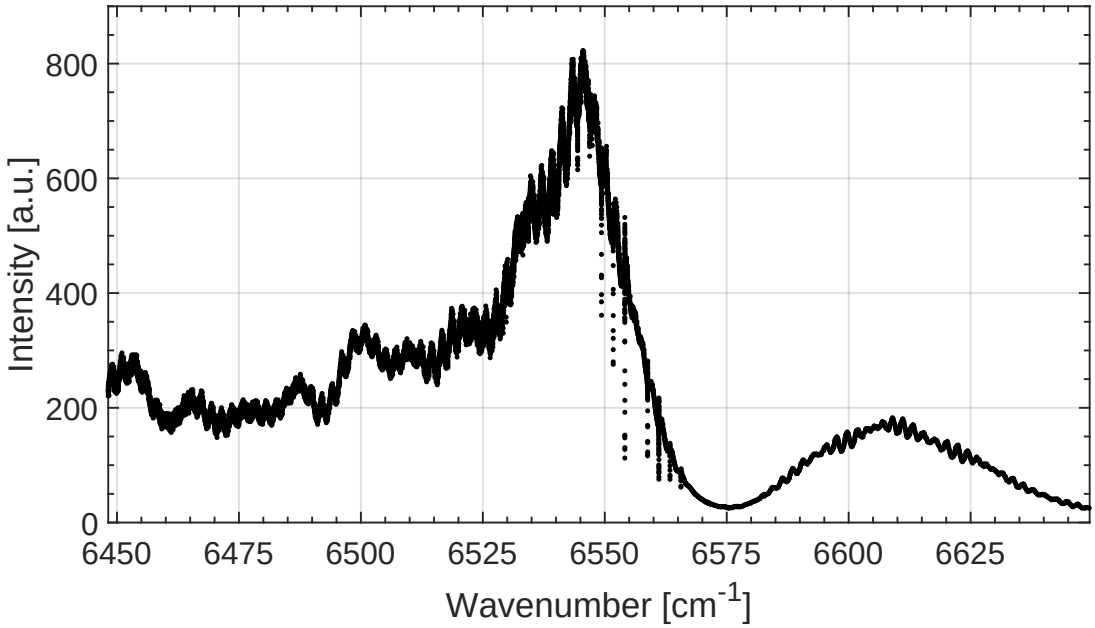

Figure 4.14 : Spectrum obtained after interleaving the averaged 19 f_{rep} steps. Strong absorption features are present in the center of the spectrum. Etalon fringes are visible on the baseline. There is almost no transmitted comb light near 6575 cm^{-1}.

For each step, all 40 spectra were averaged, yielding 19 averaged spectra. All of them were normalized relative to the intensity of the first step spectrum. The spectrum obtained at this step of the data processing is shown on figure 4.14. Strong absorption lines are visible between 6530 and 6565 cm^{-1}. The baseline also displays etalon fringes. It is worth mentioning the absence of comb light near 6575 cm^{-1}.

To subtract the baseline and the etalon fringes from the spectrum, cepstral analysis was used (Cole *et al.*, 2019). Firstly, for each of the 19 spectra, the inverse FFT of the transmission spectrum was computed, yielding the free induction decay (FID) signal shown on figure 4.15(a). This time domain signal is equivalent to the transmission spectrum, with the major difference that the baseline and the etalon fringes are now separated in time from the molecular response to the comb light. The two very intense bursts before 0.6 µs correspond to the baseline, while the burst at 1.3 µs corresponds to the fringes. The rest of the FID signal corresponds to the molecular absorption. The baseline and the

etalons can then be isolated from the molecular response. To do so, a simple weighting function was applied to the FID:

$$w(t) = \begin{cases} 1 & \text{if } t < t_{cut} \\ 0 & \text{if } t > t_{cut} \end{cases} \tag{4.4}$$

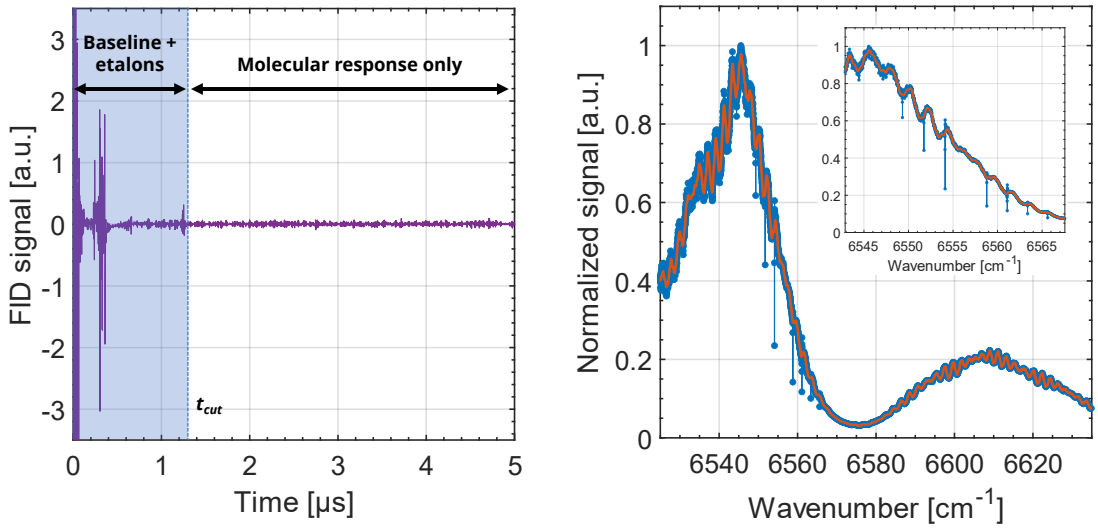

(a) **(b)**

Figure 4.15 : (a) - FID signal obtained from the inverse FFT of the transmission spectrum, for one of the 19 steps. The two intense bursts before 0.6 µs correspond to the baseline component and the burst at 1.3 µs to the etalon fringes. Beyond the limit time t_{cut}, the FID corresponds to the molecular response only. The blue and white regions of the figure show the two different conditions of the weighting functions applied to the FID. **(b)** - After the absolute value of the FFT of the weighted FID is computed, the baseline and fringes components are retrieved in the wavenumber domain. The transmission spectrum of one of the 19 steps is shown in blue, with the retrieved baseline and etalon fringes in red. The zoomed in inset in the top right corner shows that the absorption lines are unaffected by the retrieved baseline.

with t_{cut} the manually estimated time after which the FID contains only the molecular reponse signal. Secondly, the FFT of this weighted FID is performed, and its absolute value is computed. This yields the baseline along with the fringes in the wavenumber domain, which can be subtracted from the raw spectrum. Figure 4.15(b) shows the spectrum from one of the 19 steps on blue, with the baseline and etalon fringes in red retrieved from cepstral analysis. From the zoomed inset located in the figure top right corner, we can see that the absorption lines are not fitted and thus are separated from the baseline.

The 19 baseline-free spectra can then be interleaved again, yielding the normalized cavity transmission spectrum displayed on figure 4.16. The strongest lines between 6545-6570

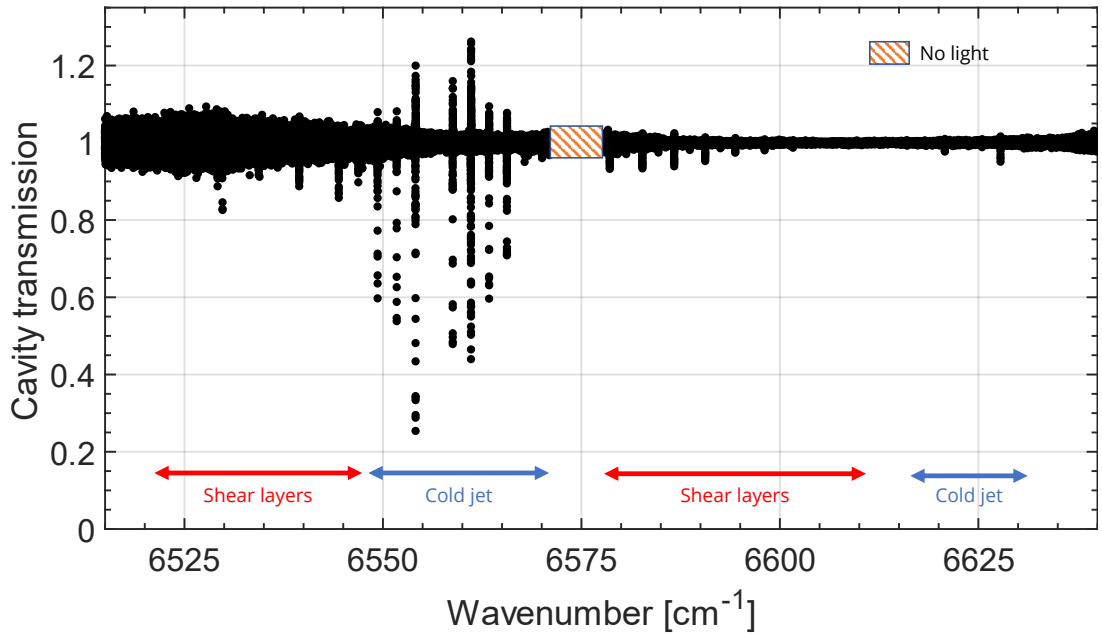

Figure 4.16 : Normalized interleaved spectrum with cepstral analysis. Absorption features corresponding to the cold jet core are present between 6545 and 6570 cm^{-1} and near 6623 cm^{-1} (blue arrows on the figure). Between 6520-6547 cm^{-1} and 6577-6610 cm^{-1} the absorption lines are from the shear layers region of the jet (red arrows on the figure). For both cold and warm regions of the jet, a strong asymmetry is observed on the lines.

cm^{-1} corresponds to the P(3)-P(1) and R(0)-R(3) lines of the $\nu_1 + \nu_3$ combination band of C_2H_2. These lines, along with the lines near 6623 cm^{-1} (P(2), P(1), R(0), R(1) from the $\nu_1 + \nu_2 + (\nu_4 + \nu_5)^0$ band) correspond to light absorption in the core of the jet. Their intensities allow to estimate the temperature in the jet core to be below 10 K. Similarly, the lines lying in the ranges 6520-6547 cm^{-1} and 6577-6610 cm^{-1} from the $\nu_1 + \nu_3$ band correspond to absorption in the shear layers of the jet. From their intensities, the shear layers temperature is estimated to be around 250 K. The near-zero comb light region near 6575 cm^{-1} is not taken into account for further analysis, as shown on the figure. A strong asymmetry is visible for most of the lines, and particularly for the intense absorption lines corresponding to absorption in the isentropic core of the jet. This indicates a mismatch between the comb lines and the center of the cavity modes, leading to these lineshapes when coupled to dispersion from molecular transitions (Foltynowicz *et al.*, 2013). A

closer look at the baseline between absorption lines informs on the achievable sensitivity. The intense lines from the cold jet core lie in the higher noise part of the spectrum, while most of the lines from the hot shear layers lie in the lowest noise part of the spectrum, as shown on figure 4.16. This compares well to the spectrum of the comb amplifier output from figure 1.7. Figure 4.17(a) shows the baseline between 6563.5 and 6565.5 cm^{-1} and figure 4.17(b) the baseline between 6612.8 and 6615.7 cm^{-1} along with their respective standard deviation of 6.0 $\times 10^{-3}$ and 1.4 $\times 10^{-3}$. We observe a 4 times higher signal-to-noise ratio for higher wavenumbers, where the absorption lines from the warm region of the jet reside, compared to lower wavenumbers associated to absorption in the core of the jet.

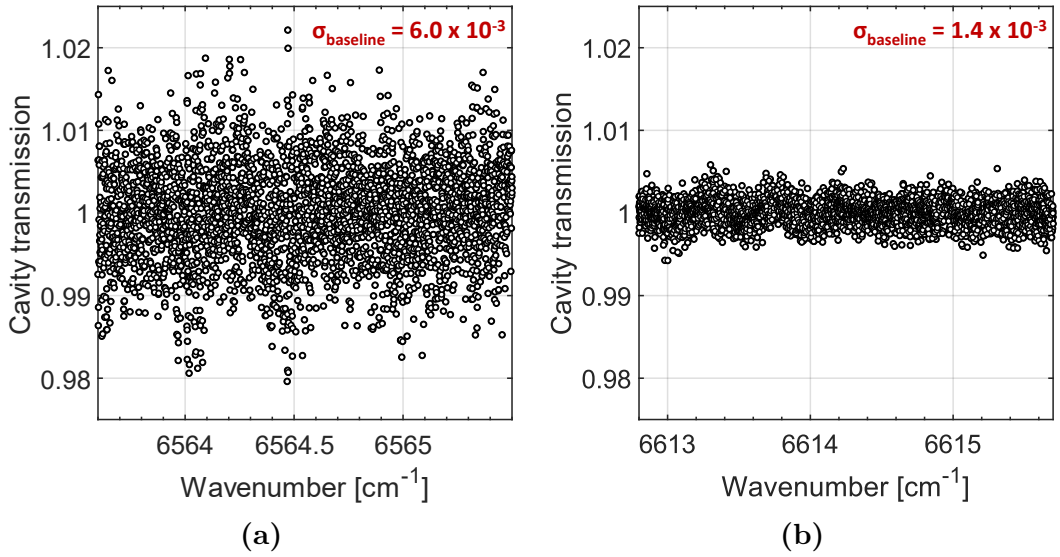

Figure 4.17 : (a) - Zoomed-in view of the baseline between 6563.5 and 6565.5 cm^{-1}. The standard deviation is 6.0 $\times 10^{-3}$. **(b)** - Zoomed-in view of the baseline between 6612.8 and 6615.7 cm^{-1}. The standard deviation is 1.4 $\times 10^{-3}$.

These values correspond to the minimum detectable absorbance. In the highest SNR region near 6613-6614 cm^{-1}, the minimum detectable absorbance is $\alpha_{\min} \times L_{\text{eff}} = 1.4 \times 10^{-3}$, with $\alpha_{\min}$ the minimum detectable absorption coefficient and L_{eff} the effective absorption pathlength through the core of the jet. The length of the slit is $L_{\text{slit}} = 8.1$ cm and the cavity finesse is $F = 350$ at these wavenumbers, yielding an effective absorption pathlength $L_{\text{eff}} = 2FL_{\text{eff}}/\pi = 18$ m. We thus obtain $\alpha_{\min} = 7.8 \times 10^{-7}\,\text{cm}^{-1}$. These results can be compared to the previous work from X. de Ghellinck d'Elseghem Vaernewijck & Herman (2012), where they probed slit supersonic jets of C_2H_4, N_2O and C_2H_2 seeded in Ar with a femtosecond laser coupled into an enhancement cavity and analyzed with a

FTS. The slit had a length $L_{\text{slit}} = 1\,\text{cm}$ and the cavity finesse was $F = 48,960$. Assuming a 5 mm absorption pathlength in the jet, they reported a minimum detectable absorption coefficient of $\alpha_{\text{min}} = 9 \times 10^{-7}\,\text{cm}^{-1}$. While both sensitivities are on the same order of magnitude, they have to be put in perspective as the finesse of the enhancement cavity they used is more than a hundredfold the finesse of our cavity. This demonstrates the significant gain on signal-to-noise ratio obtained by stabilizing both the frequency comb and the optical cavity length.

4.3.2 Cavity-enhanced absorption model

Following equation 2.47, the cavity transmission was modelled with two distinct absorbing media, the jet core and the shear layers. The cavity transmitted electric field with intracavity analyte $E_{analyte}$ is defined as (Johansson *et al.*, 2018):

$$E_{analyte} = E_{inc}\frac{t(\nu)\,e^{-i\phi(\nu)/2-\alpha_{core}(\nu)L/2-\alpha_{shear}(\nu)L/2-i\varphi_{core}(\nu)L/2-i\varphi_{shear}(\nu)L/2}}{1-r(\nu)\,e^{-i\phi(\nu)-\alpha_{core}(\nu)L-\alpha_{shear}(\nu)L-i\varphi_{core}(\nu)L-i\varphi_{shear}(\nu)L}}. \tag{4.5}$$

with E_{inc} the electric field incoming on the cavity, $t(\nu)$ and $r(\nu)$ the frequency-dependent electric field transmission and reflection coefficients of the cavity mirrors (with $t(\nu) = 1 - r(\nu)$), $\phi(\nu)$ a phase parameter accounting for the round trip phase shift in the cavity and the intracavity dispersion due to the mirror coatings, and $\alpha_{core}(\nu)$, $\varphi_{core}(\nu)$, $\alpha_{shear}(\nu)$ and $\varphi_{shear}(\nu)$ the intracavity medium absorption and dispersion coefficients per unit length [cm^{-1}] for the jet core and jet shear layers, respectively. The empty cavity transmitted electric field E_0 is similarly defined as:

$$E_0 = E_{inc}\frac{t(\nu)\,e^{-i\phi(\nu)/2}}{1-r(\nu)\,e^{-i\phi(\nu)}}. \tag{4.6}$$

The normalized intensity cavity transmission is then obtained as:

$$\frac{I_{analyte}}{I_0} = \frac{E_{analyte}E^*_{analyte}}{E_0E^*_0}. \tag{4.7}$$

A simple comparison of the normalized interleaved spectrum from figure 4.16 with this model yielded estimated values for the jet temperature and density in the core and the shear layers, presented on table 4.1. The width of the core was assumed to be the same as the slit length, and the width of the shear layers was estimated from CFD simulations.

It should be emphasized here that the jet spectrum analysis was carried out with the approximation that the rotational temperature of acetylene was equal to the translational temperature of molecules in the isentropic core of the jet. While this approximation is

Table 4.1 : Estimated jet conditions from a preliminary comparison of the spectrum with the model. The width of the isentropic core of the jet was assumed to be equal to the slit nozzle length, while the width of the shear layers is a guess value from CFD simulations.

Jet region	**Temperature**	**C_2H_2 density**	**Width**
Isentropic core	6 K	5×10^{13} cm^{-3}	8.1 cm
Shear layers	250 K	5×10^{14} cm^{-3}	1 cm

seldom true in the case of slit jets, it allowed to fit the data with a rather simple model.

4.3.3 Mirrors reflectivity

To model the cavity transmission as described above, the variation of the cavity mirrors reflectivity over frequency had to be calibrated. To do so, a FT-CRDS measurement was performed with a setup similar to the one described in section 3.2. The retrieved mirror reflectivity is displayed on figure 4.18 as blue circles. The experimental data was fitted with a 2nd order polynomial (red trace). The fit was performed without taking into account the region with no light between 6560 and 6590 cm^{-1} nor the low light region between 6450 and 6530 cm^{-1}. The measured reflectivity shows good agreement with the manufacturer values (99-99.3% in the 6250-6600 nm range).

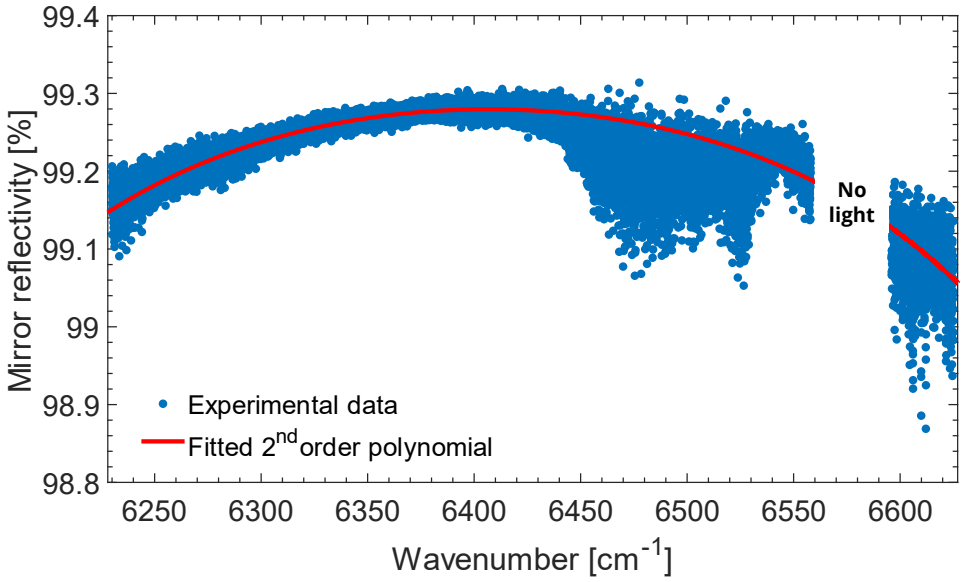

Figure 4.18 : Measured cavity mirrors reflectivity with FT-CRDS. The experimental data points are shown as blue circles with a 2nd order polynomial fit as the red trace.

4.3.4 Fitted spectrum

The spectrum was locally fitted line-by-line with the previously described model. The fit was performed with an algorithm based on the fminsearch function from Matlab. The spectrum was truncated into parts, each one corresponding to a given absorption line. For each line, the fitted parameters were the C_2H_2 densities and temperatures in the jet core and the shear layers, and the phase parameter $\phi(\nu)$ from equation 4.5. The result of the fit is shown on figure 4.19. The top panel displays the experimental spectrum as black circles, and the fitted model as the solid red trace. The lower panel represents the residuals (data - model) of the fit. The model is in good agreement with the experimental data, although intensity discrepancies remain for some of the strongest absorption lines. The discrepancy visible near 6534 cm^{-1} is assumed to come from hot band ro-vibrational lines, which have not yet been taken into account in the model.

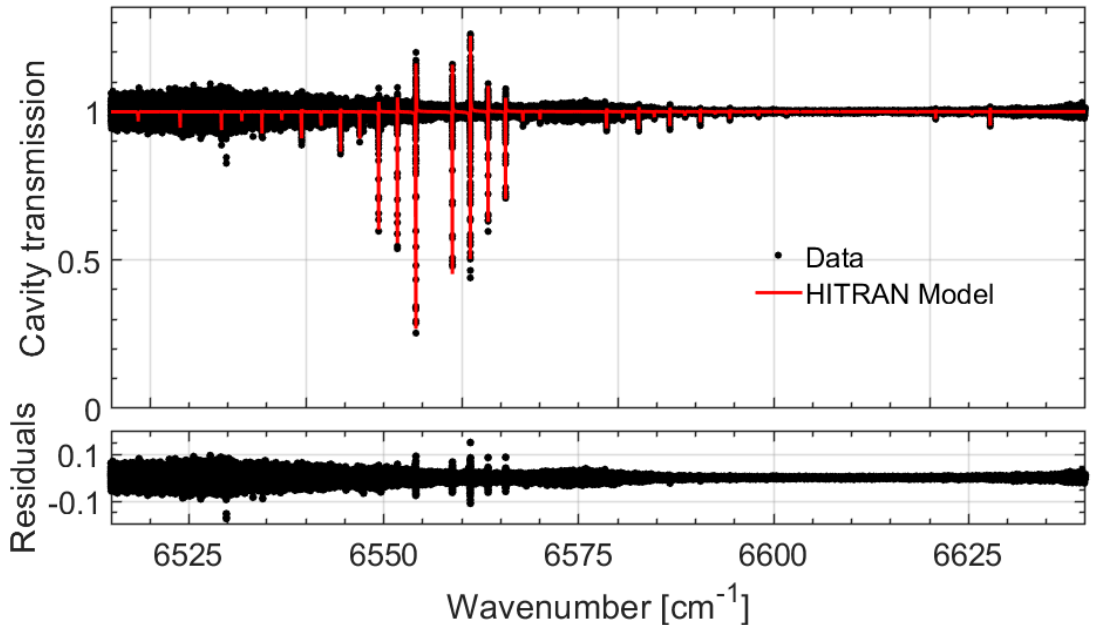

Figure 4.19 : Fitted cavity transmission spectrum after interleaving and normalization. Experimental data points are shown as black circular markers and the fitted model as the red solid trace. The model takes into account two different absorbing media, the jet core and the jet shear layers. The model is able to reproduce both the profiles of the strong "cold" lines and of the less intense "warm" lines.

A closer look at the absorption lineshapes from the P(1) and P(2) lines are displayed on figures 4.20(a) and 4.20(b). The experimental data points are shown as black circular markers and the fitted model as the solid red trace. The asymmetries in both lineshapes

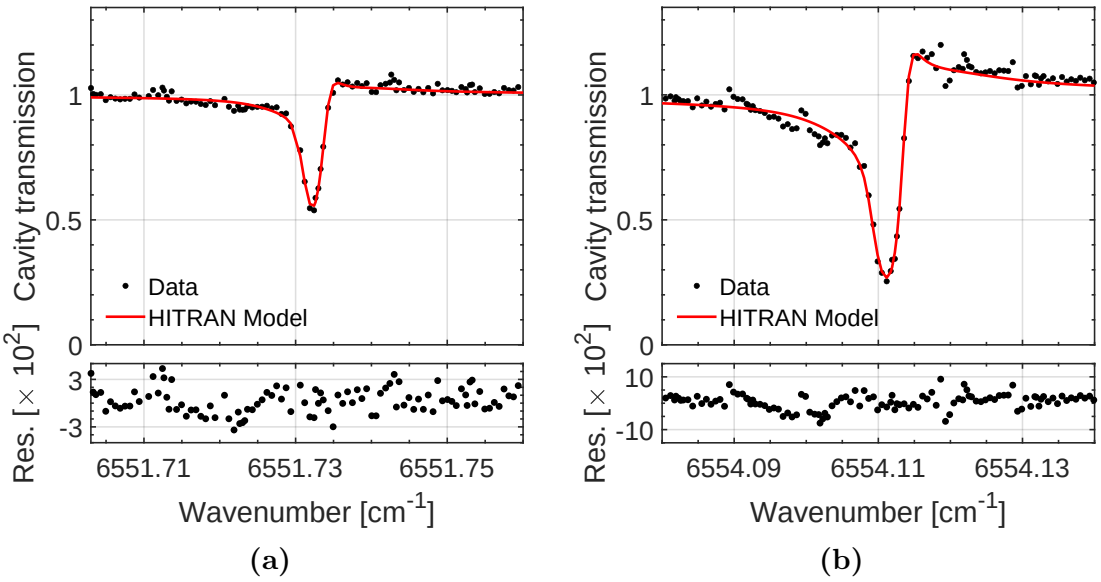

Figure 4.20 : Absorption lineshapes of **(a)** - the P(2) line near 6551.7 cm^{-1} and **(b)** - the P(1) line near 6554.11 cm^{-1}. Black markers represent experimental data, and the fitted cavity transmission model is shown as the red trace. Structure remaining from the interleaving process is visible on the sides of either transition.

coming from the offset between the comb modes and the center of the cavity modes can be reproduced with a good agreement between data and model. However, remaining structure is still visible on the sides of each line due to the current interleaving process. The typical FWHM of the lines are of the order of ∼250 MHz.

A total of 42 lines originating from the $\nu_1 + \nu_3$ and the $\nu_1 + \nu_2 + (\nu_4 + \nu_5)^0$ vibrational bands were fitted, and the 5 parameters retrieved for each line were compared. The lines were separated into two groups: the "cold" lines with J < 4 corresponding to absorption in the cold core of the jet, and the "warm" lines with J > 5 corresponding to absorption in the warmer shear layers (with the exception of the R(6), R(7) and R(8) lines between 6572 and 6577 which belong to the region of the spectrum with almost no light). The C_2H_2 densities were first compared for the two groups. Figure 4.21(a) shows the obtained density of acetylene for each of the cold lines as blue circles as a function of the lines central frequencies. Note the log scale on the density axis. The errorbar on each marker indicates the statistical uncertainty on the fitted density value. The retrieved values are quite spread out around a mean value of 6.0×10^{13} molecules/cm^3 with a standard deviation of 2.6×10^{13} molecules/cm^3, indicated as the dotted red line and the shaded red area. The values from the "warm" lines are shown on figure 4.21(b), as purple circles with errorbars.

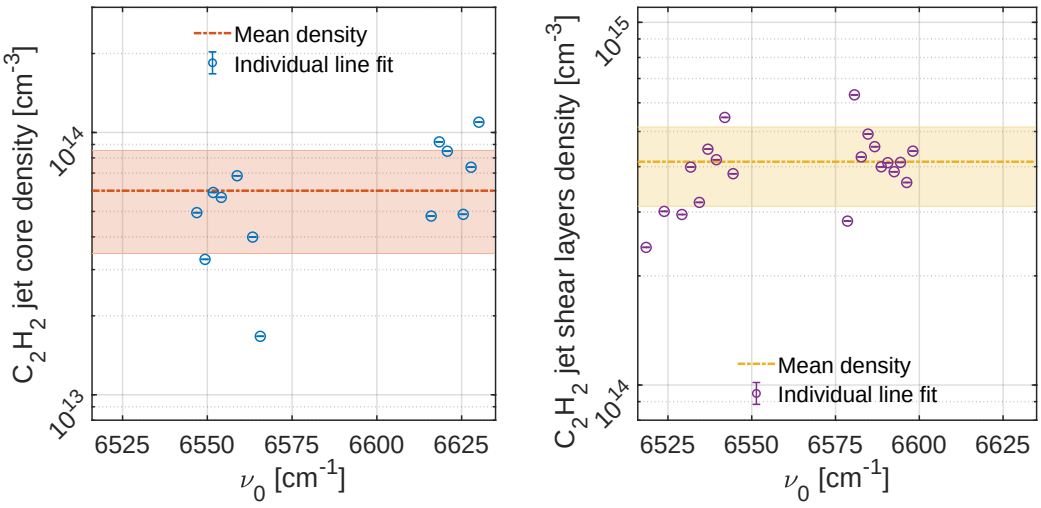

(a) **(b)**

Figure 4.21 : (a) - C_2H_2 density in the isentropic core (blue circles) obtained after independently fitting each line, with the corresponding statistical uncertainty from the fit as the errorbar. The density is shown on the y axis with a log scale. Dotted red trace: mean value. Shaded red region: standard deviation. **(b)** - C_2H_2 density in the shear layers (purple circles) with the corresponding statistical uncertainty from the fit as the errorbar. Dotted yellow trace: mean value. Shaded yellow region: standard deviation.

This yield a mean acetylene density of 4.2×10^{14} molecules/cm^3 with a standard deviation 1.1×10^{14} molecules/cm^3 for the shear layers, shown as the yellow dotted trace and the shaded yellow area. The densities obtained for "warm" lines are relatively tighter around the mean compared to the densities of the "cold" lines.

The same study was conducted with the retrieved temperature for each group. "Temperature" here refers to the both the rotational and the translational temperatures, with the approximation that $T_{rot} = T_{trans}$ in the core of the jet. Figure 4.22(a) shows the fitted values of the temperature of the "cold" lines as the blue circles as a function of the central frequency of absorption lines, leading to a mean value for the temperature in the core of 8.5 K with a standard deviation of 2.6 K. The mean is depicted as the red dotted trace and the std as the shaded red area. It should be noted that the errorbars are larger for most of the less intense lines, especially those from the $\nu_1 + \nu_2 + (\nu_4 + \nu_5)^0$ band. The same observation is made with the fitted temperatures of the "warm" lines, represented on figure 4.22(b) as purple circles. A mean value for the temperature in the shear layers of the jet is retrieved as 266.1 K with a corresponding standard deviation of 45.6 K. As for the "cold" lines, the less intense transitions as well as those in the lower SNR regions

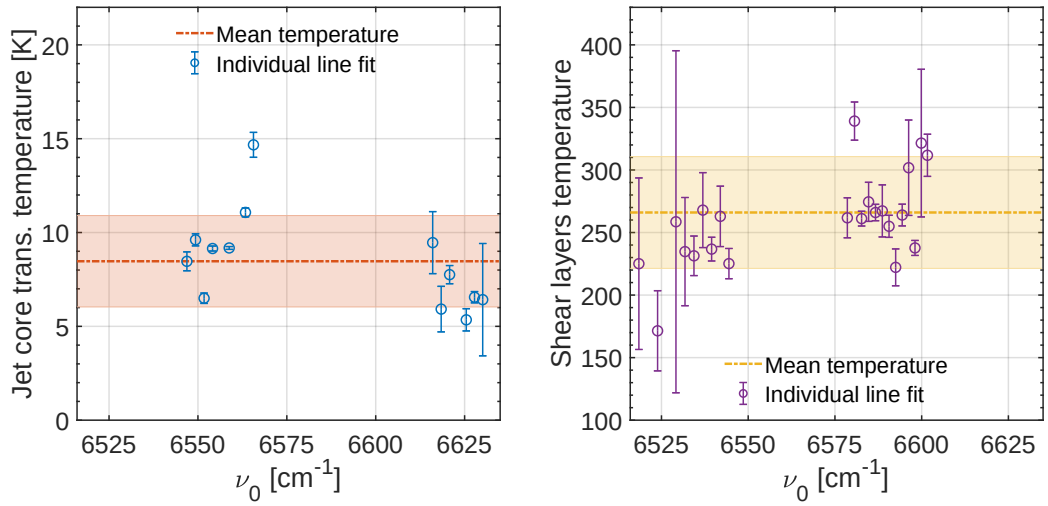

(a) **(b)**

Figure 4.22 : (a) - Temperature in the isentropic core (blue circles) obtained after independently fitting each line, with the corresponding statistical uncertainty from the fit as the errorbar. Dotted red trace: mean value. Shaded red region: standard deviation. **(b)** - Temperature in the shear layers (purple circles) with the corresponding statistical uncertainty from the fit as the errorbar. Dotted yellow trace: mean value. Shaded yellow region: standard deviation.

of the spectrum suffer from much higher uncertainties. The obtained mean and standard deviation values for each fitted jet parameter is summarized in table 4.2.

Table 4.2 : Mean values and standard deviations of temperature and C_2H_2 density in the jet core and shear layers regions obtained from line-by-line fits.

Parameter	Mean value	Standard deviation
Jet core C_2H_2 density [cm^{-3}]	6.0×10^{13}	2.6×10^{13}
Jet shear layers C_2H_2 density [cm^{-3}]	4.2×10^{14}	1.1×10^{14}
Jet core temperature [K]	8.5	2.6
Jet shear layer temperature [K]	266.1	45.6

The fitted phase offset retrieved for each line after the fit is represented on figure 4.23 as a function of the center frequencies of absorption lines. A positive linear trend is observed as frequency increases. This is expected with a single-point PDH lock. Comb modes further away from the locking point are not perfectly centered on the cavity modes due to intracavity dispersion. This in turn leads to the distortion of the absorption lines. The phase offset parameter then increases for absorption lines further away from the comb

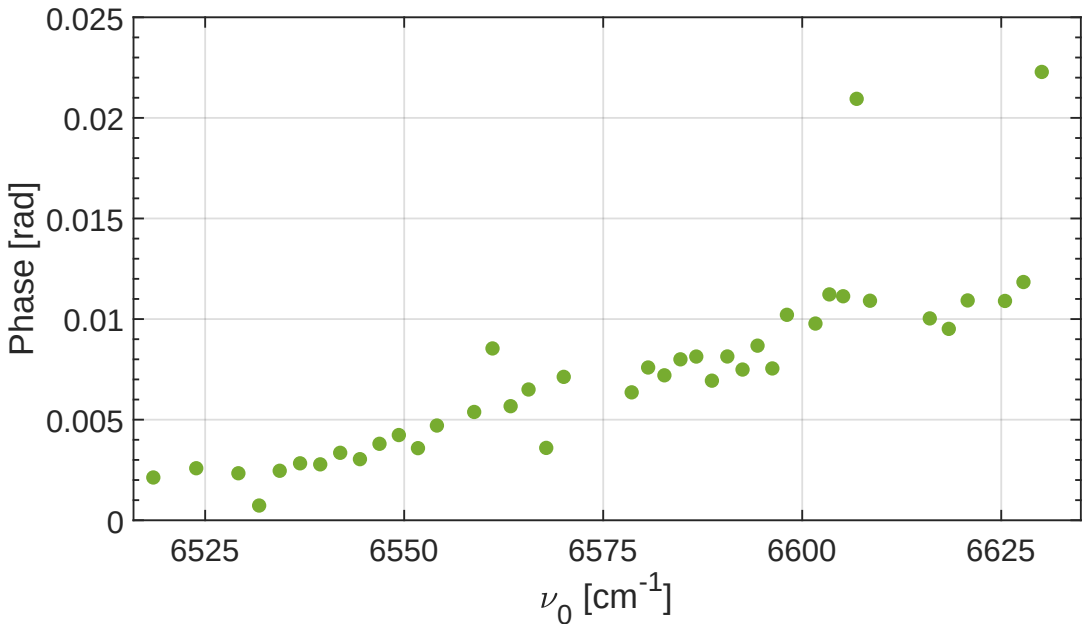

Figure 4.23 : Phase offset fitted for each line as a function of their central frequencies. A linear trend is observed in phase as frequency increases.

locking point. From the figure, the comb locking point is close to 6520 cm^{-1}, where the phase is almost zero.

To conclude, it is noteworthy to mention that these results will be compared to ongoing work on the slit nozzle characterization. All values reported from the fit are temporary results and are subject to change once the jet profile and its density map have been acquired, especially the acetylene densities, as well as the light interaction pathlength in both regions of the jet. Moreover, the present model used to fit the experimental spectrum does not take into account the gradient of densities and temperature present in the shear and boundary layers of the jet. The possibility of absorption by static gas in the chamber should also be explored.

4.4 Conclusion

In this chapter, we presented a setup coupling a slit supersonic jet with cavity-enhanced Fourier transform comb spectroscopy. The measurement analysis procedures were covered. The first spectrum of a slit supersonic expansion of acetylene probed with frequency combs and a Fourier transform spectrometer is reported, yielding a temperature estimated below 10 K in the isentropic core of the jet.

The next step for the technique is to transpose it to the molecular fingerprint region in the mid-infrared, where molecular absorption is 2-3 orders of magnitude higher compared to the near-infrared region around 1.55 µm where this study took place. The demonstrated possibility of cavity-enhanced comb spectroscopy with the pumping system in function paves the way for much more sensitive measurements of molecules cooled down to < 10 K temperatures.

Finally, it is worth mentioning that the relatively low vibrational cooling with free jets, compared to the cooling of rotation and translation (non-LTE conditions), can be exploited to probe hot vibrational bands populated only at high temperatures, without overcrowding the spectrum (Dudás *et al.*, 2023).

Conclusion

On the way to use frequency comb spectroscopy for cold reaction kinetics (see figure 2 in Introduction), we have now developed two essential parts of the system.

Firstly, we have demonstrated time-resolved FTS capable of resolving time-dependent events at the microsecond level. We put it to the most stringent test available by applying to multiplex CRDS. We showed that individual spectral elements could be retrieved without cross-talk after Fourier transformation. Therefore, we believe that we have reached the required specification on time resolution and broad bandwidth for reaction kinetics. In the process, the FT-CRDS technique appeared to be promising enough to be further investigated. The first stage was to increase the cavity finesse to typical values employed in CRDS without reducing the spectral bandwidth, and this was already performed in Torun. There, we show that FT-CRDS has a potential for sensitivity beyond the Voigt profile. The next steps will include: **1)** combination with the sub-nominal and interleaving methods in order to reach calibration-free absorption spectroscopy on both the intensity and frequency axis and **2)** and the technical transfer to the mid-infrared.

Secondly, we have shown cavity-enhanced absorption spectroscopy based on frequency combs in supersonic jets. We applied the system to spectroscopy of a jet of acetylene seeded in argon, and interleaved 18 sub-nominal spectra to yield a spectrum at a temperature of 8.5 K. Nonetheless, the ongoing spectroscopic analysis has highlighted unanswered questions: **1)** the strongest absorption line exhibits an odd profile, unexplained yet ; **2)** slit jets are expected to yield different vibrational, rotational and translational temperatures ($T_{vib} > T_{rot} > T_{trans}$) which was not verified here. The estimated density of acetylene in the core of the jet was 6.0×10^{13} molecule/cm^3, three orders of magnitude higher than the minimum densities of transient species at 10^{10} molecule/cm^3. To increase the sensitivity, one can either increase the interaction length or probe stronger absorption lines. The first option consists in increasing the cavity finesse, which could easily be multiplied by a factor 2-5 to reach a detectable density of 10^{13} without compromising the time resolution. The second will be achieved by transferring the technique to the mid-infrared, where

cross-section are 2-3 orders of magnitude stronger.

The immediate outlook of the experimental setup development is the implementation of a new DFG source, covering the 3-10 µm region (Soboń *et al.*, 2017; Sotor *et al.*, 2018). This source is a comb and can be stabilized on both the repetition rate and the offset frequency thanks to the addition of an AOM on the erbium arm of the DFG (Lee *et al.*, 2017). This will allow to lock this comb source to an enhancement cavity expected to arrive in the coming months. Ultimately, this mid-infrared spectrometer will be combined with a supersonic chamber and a photolysis laser to achieve the first infrared precision spectroscopy of radical species.

A – Experimental conditions for the comb-jet experiment

Table A.1 : Experimental conditions. One slm (standard liter per minute) is the volumetric flow rate per minute measured at 273.15 K and 1 atm.

Slit nozzle	
Length	8.1 cm
Width	30 µm
Gas flows	
C_2H_2 flow	1.5 slm
Ar flow	28 slm
Reservoir pressure	800 Torr
Chamber pressure	0.16 Torr
Data acquisition	
f_{rep} sweep	19 steps of 10 Hz
Interferograms per step	40
Cart travel speed	70 mm/s
Cart travel length	270 mm
Acquisition time per interferogram	10.4 s
Total acquisition time	132 minutes
DAQ sample rate	2.8 MSamples/s
DAQ alias-free bandwidth	1.12 MHz

References

Adler, F., Cossel, K. C., Thorpe, M. J., Hartl, I., Fermann, M. E. & Ye, J., "Phase-stabilized, 1.5 W frequency comb at 2.8–4.8 μm", *Opt. Lett.* **34** (2009), p. 1330-1332, doi : 10.1364/OL.34.001330.

Adler, F., Thorpe, M. J., Cossel, K. C. & Ye, J., "Cavity-Enhanced Direct Frequency Comb Spectroscopy : Technology and Applications", *Annual Review of Analytical Chemistry* **3** (2010), PMID : 20636039, p. 175-205, doi : 10.1146/annurev-anchem-060908-155248.

Agner, J. A., Albert, S., Allmendinger, P., Hollenstein, U., Hugi, A., Jouy, P., Keppler, K., Mangold, M., Merkt, F. & Quack, M., "High-resolution spectroscopic measurements of cold samples in supersonic beams using a QCL dual-comb spectrometer*", *Molecular Physics* **120** (2022), e2094297, doi : 10.1080/00268976.2022.2094297.

Alden, C., Ghosh, S., Coburn, S., Sweeney, C., Karion, A., Wright, R., Coddington, I., Prasad, K. & Rieker, G., "Methane leak detection and sizing over long distances using dual frequency comb laser spectroscopy and a bootstrap inversion technique", *Atmospheric Measurement Techniques Discussions* (2017), p. 1-34, doi : 10.5194/amt-2017-262.

Amirav, A., Even, U. & Jortner, J., "Cooling of large and heavy molecules in seeded supersonic beams", *Chemical Physics* **51** (1980), p. 31-42, doi : 10.1016/0301-0104(80)80077-2.

Amirav, A., Even, U. & Jortner, J., "Absorption spectroscopy of ultracold large molecules in planar supersonic expansions", *Chemical Physics Letters* **83** (1981), p. 1-4, doi : 10.1016/0009-2614(81)80277-1.

Arnó, J. & Bevan, J. W., "Infrared spectroscopy in supersonic free jets and molecular beams", *Jet Spectroscopy and Molecular Dynamics*, sous la dir. de J. M. Hollas & D. Phillips, Dordrecht : Springer Netherlands, 1995, p. 29-73, doi : 10.1007/978-94-011-1314-4_2.

Bagheri, M., Frez, C., Sterczewski, L. A., Gruidin, I., Fradet, M., Vurgaftman, I., Canedy, C. L., Bewley, W. W., Merritt, C. D., Kim, C. S., Kim, M. & Meyer, J. R., "Passively mode-locked interband cascade optical frequency combs", *Scientific Reports* **8** (2018), p. 3322, DOI : 10.1038/s41598-018-21504-9.

Ball, S. M., Povey, I. M., Norton, E. G. & Jones, R. L., "Broadband cavity ringdown spectroscopy of the NO3 radical", *Chemical Physics Letters* **342** (2001), p. 113-120, DOI : 10.1016/S0009-2614(01)00573-5.

Ball, S. M. & Jones, R. L., "Broad-Band Cavity Ring-Down Spectroscopy", *Chemical Reviews* **103** (2003), p. 5239-5262, DOI : 10.1021/cr020523k.

Baltuška, A., Udem, T., Uiberacker, M., Hentschel, M., Goulielmakis, E., Gohle, C., Holzwarth, R., Yakovlev, V. S., Scrinzi, A., Hänsch, T. W. & Krausz, F., "Attosecond control of electronic processes by intense light fields", *Nature* **421** (2003), p. 611-615, DOI : 10.1038/nature01414.

Bernhardt, B., Ozawa, A., Jacquet, P., Jacquey, M., Kobayashi, Y., Udem, T., Holzwarth, R., Guelachvili, G., Hänsch, T. W. & Picqué, N., "Cavity-enhanced dual-comb spectroscopy", *Nature Photonics* **4** (2010), p. 55-57, DOI : 10.1038/nphoton.2009.217.

Bize, S., Diddams, S. A., Tanaka, U., Tanner, C. E., Oskay, W. H., Drullinger, R. E., Parker, T. E., Heavner, T. P., Jefferts, S. R., Hollberg, L., Itano, W. M. & Bergquist, J. C., "Testing the Stability of Fundamental Constants with the $^{199}Hg^{+}$ Single-Ion Optical Clock", *Phys. Rev. Lett.* **90** (2003), p. 150802, DOI : 10.1103/PhysRevLett.90.150802.

Bjork, B. J., Bui, T. Q., Heckl, O. H., Changala, P. B., Spaun, B., Heu, P., Follman, D., Deutsch, C., Cole, G. D., Aspelmeyer, M., Okumura, M. & Ye, J., "Direct frequency comb measurement of OD + CO $\rightarrow$ DOCO kinetics", *Science* **354** (2016), p. 444-448, DOI : 10.1126/science.aag1862.

Brumfield, B. E., Stewart, J. T., Widicus Weaver, S. L., Escarra, M. D., Howard, S. S., Gmachl, C. F. & McCall, B. J., "A quantum cascade laser cw cavity ring-down spectrometer coupled to a supersonic expansion source", *Review of Scientific Instruments* **81** (2010), p. 063102, DOI : 10.1063/1.3427357.

Brumfield, B. E., Stewart, J. T. & McCall, B. J., "High-resolution spectroscopy of the ν_8 band of methylene bromide using a quantum cascade laser", *Journal of Molecular Spectroscopy* **266** (2011), p. 57-62, DOI : 10.1016/j.jms.2011.02.013.

Brumfield, B. E., Stewart, J. T. & McCall, B. J., "Extending the Limits of Rotationally Resolved Absorption Spectroscopy : Pyrene", *The Journal of Physical Chemistry Letters* **3** (2012), p. 1985-1988, doi : 10.1021/jz300769k.

Bui, T. Q., Long, D. A., Cygan, A., Sironneau, V. T., Hogan, D. W., Rupasinghe, P. M., Ciuryło, R., Lisak, D. & Okumura, M., "Observations of Dicke narrowing and speed dependence in air-broadened CO2 lineshapes near 2.06 µm", *The Journal of Chemical Physics* **141** (2014), p. 174301, doi : 10.1063/1.4900502.

Burghoff, D., Kao, T.-Y., Han, N., Chan, C. W. I., Cai, X., Yang, Y., Hayton, D. J., Gao, J.-R., Reno, J. L. & Hu, Q., "Terahertz laser frequency combs", *Nature Photonics* **8** (2014), p. 462-467, doi : 10.1038/nphoton.2014.85.

Burkart, J., Sala, T., Romanini, D., Marangoni, M., Campargue, A. & Kassi, S., "Communication : Saturated CO2 absorption near 1.6 μm for kilohertz-accuracy transition frequencies", *The Journal of Chemical Physics* **142** (2015), 191103, doi : 10.1063/1.4921557.

Changala, P. B., Spaun, B., Patterson, D., Doyle, J. M. & Ye, J., "Sensitivity and resolution in frequency comb spectroscopy of buffer gas cooled polyatomic molecules", *Applied Physics B* **122** (2016), p. 292, doi : 10.1007/s00340-016-6569-7.

Changala, P. B., Weichman, M. L., Lee, K. F., Fermann, M. E. & Ye, J., "Rovibrational quantum state resolution of the C₆₀ fullerene", *Science* **363** (2019), p. 49-54, doi : 10.1126/science.aav2616.

Chen, H., Winderlich, J., Gerbig, C., Hoefer, A., Rella, C. W., Crosson, E. R., Van Pelt, A. D., Steinbach, J., Kolle, O., Beck, V., Daube, B. C., Gottlieb, E. W., Chow, V. Y., Santoni, G. W. & Wofsy, S. C., "High-accuracy continuous airborne measurements of greenhouse gases (CO_2 and CH_4) using the cavity ring-down spectroscopy (CRDS) technique", *Atmospheric Measurement Techniques* **3** (2010), p. 375-386, doi : 10.5194/amt-3-375-2010.

Chen, Z., Yan, M., Hänsch, T. W. & Picqué, N., "A phase-stable dual-comb interferometer", *Nature Communications* **9** (2018), p. 3035, doi : 10.1038/s41467-018-05509-6.

Ciuryło, R., Pine, A. & Szudy, J., "A generalized speed-dependent line profile combining soft and hard partially correlated Dicke-narrowing collisions", *Journal of Quantitative Spectroscopy and Radiative Transfer* **68** (2001), p. 257-271, doi : 10.1016/S0022-4073(00)00024-8.

Coddington, I., Swann, W. C. & Newbury, N. R., "Coherent Multiheterodyne Spectroscopy Using Stabilized Optical Frequency Combs", *Phys. Rev. Lett.* **100** (2008), p. 013902, doi : 10.1103/PhysRevLett.100.013902.

Coddington, I., Newbury, N. & Swann, W., "Dual-comb spectroscopy", *Optica* **3** (2016), p. 414-426, doi : 10.1364/OPTICA.3.000414.

Cole, R. K., Makowiecki, A. S., Hoghooghi, N. & Rieker, G. B., "Baseline-free quantitative absorption spectroscopy based on cepstral analysis", *Opt. Express* **27** (2019), p. 37920-37939, doi : 10.1364/OE.27.037920.

Coleman, T. F. & Li, Y., "An Interior Trust Region Approach for Nonlinear Minimization Subject to Bounds", *SIAM Journal on Optimization* **6** (1996), p. 418-445, doi : 10.1137/0806023.

Cygan, A., Lisak, D., Masłowski, P., Bielska, K., Wójtewicz, S., Domysławska, J., Trawiński, R. S., Ciuryło, R., Abe, H. & Hodges, J. T., "Pound-Drever-Hall-locked, frequency-stabilized cavity ring-down spectrometer", *Review of Scientific Instruments* **82** (2011), p. 063107, doi : 10.1063/1.3595680.

Cygan, A., Lisak, D., Wójtewicz, S., Domysławska, J., Hodges, J. T., Trawi ński, R. S. & Ciuryło, R., "High-signal-to-noise-ratio laser technique for accurate measurements of spectral line parameters", *Phys. Rev. A* **85** (2012), p. 022508, doi : 10.1103/PhysRevA.85.022508.

Cygan, A., Lisak, D., Morzyński, P., Bober, M., Zawada, M., Pazderski, E. & Ciuryło, R., "Cavity mode-width spectroscopy with widely tunable ultra narrow laser", *Opt. Express* **21** (2013), p. 29744-29754, doi : 10.1364/OE.21.029744.

Czyżewski, A., Chudzyński, S., Ernst, K., Karasiński, G., Kilianek, Ł., Pietruczuk, A., Skubiszak, W., Stacewicz, T., Stelmaszczyk, K., Koch, B. & Rairoux, P., "Cavity ring-down spectrography", *Optics Communications* **191** (2001), p. 271-275, doi : 10.1016/S0030-4018(01)01134-8.

Davis, S. P., *Fourier transform spectrometry*, San Diego : Academic Press, 2001.

Del'Haye, P., Schliesser, A., Arcizet, O., Wilken, T., Holzwarth, R. & Kippenberg, T. J., "Optical frequency comb generation from a monolithic microresonator", *Nature* **450** (2007), p. 1214-1217, doi : 10.1038/nature06401.

Demtröder, W., "Widths and Profiles of Spectral Lines", *Laser Spectroscopy 1 : Basic Principles*, Berlin, Heidelberg : Springer Berlin Heidelberg, 2014, p. 75-111, doi : 10.1007/978-3-642-53859-9_3.

Dicke, R. H., "The Effect of Collisions upon the Doppler Width of Spectral Lines", *Phys. Rev.* **89** (1953), p. 472-473, doi : 10.1103/PhysRev.89.472.

Diddams, S. A., Jones, D. J., Ma, L.-S., Cundiff, S. T. & Hall, J. L., "Optical frequency measurement across a 104-THz gap with a femtosecond laser frequency comb", *Opt. Lett.* **25** (2000a), p. 186-188, doi : 10.1364/OL.25.000186.

Diddams, S. A., Jones, D. J., Ye, J., Cundiff, S. T., Hall, J. L., Ranka, J. K., Windeler, R. S., Holzwarth, R., Udem, T. & Hänsch, T. W., "Direct Link between Microwave and Optical Frequencies with a 300 THz Femtosecond Laser Comb", *Phys. Rev. Lett.* **84** (2000b), p. 5102-5105, doi : 10.1103/PhysRevLett.84.5102.

Diddams, S. A., Udem, T., Bergquist, J. C., Curtis, E. A., Drullinger, R. E., Hollberg, L., Itano, W. M., Lee, W. D., Oates, C. W., Vogel, K. R. & Wineland, D. J., "An Optical Clock Based on a Single Trapped $^{199}Hg^{+}$ Ion", *Science* **293** (2001), p. 825-828, doi : 10.1126/science.1061171.

Diddams, S. A., Bartels, A., Ramond, T., Oates, C., Bize, S., Curtis, E. A., Bergquist, J. & Hollberg, L., "Design and control of femtosecond lasers for optical clocks and the synthesis of low-noise optical and microwave signals", *IEEE Journal of Selected Topics in Quantum Electronics* **9** (2003), p. 1072-1080, doi : 10.1109/JSTQE.2003.819096.

Diddams, S. A., Hollberg, L. & Mbele, V., "Molecular fingerprinting with the resolved modes of a femtosecond laser frequency comb", *Nature* **445** (2007), p. 627-630, doi : 10.1038/nature05524.

Diddams, S. A., Vahala, K. & Udem, T., "Optical frequency combs : Coherently uniting the electromagnetic spectrum", *Science* **369** (2020), p. 3676, doi : 10.1126/science.aay3676.

Drever, R. W. P., Hall, J. L., Kowalski, F. V., Hough, J., Ford, G. M., Munley, A. J. & Ward, H., "Laser phase and frequency stabilization using an optical resonator", *Appl. Phys. B* **31** (1983), p. 97-105, doi : doi.org/10.1007/BF00702605.

Dubroeucq, R. & Rutkowski, L., "Optical frequency comb Fourier transform cavity ring-down spectroscopy", *Opt. Express* **30** (2022), p. 13594-13602, doi : 10.1364/OE.454775.

Dubroeucq, R., Charczun, D., Maslowski, P. & Rutkowski, L., "Sensitive Fourier-transform cavity ring down spectroscopy based on a near-infrared frequency comb", *Conference on Lasers and Electro-Optics/Europe and European Quantum Electronics*

Conference, Munich, Germany, 2023a, paper ed_4_2, URL : https://hal.science/hal-04246102.

DUBROEUCQ, R., LE MIGNON, Q., SUAS-DAVID, N., SUAS-DAVID, N., KASSI, S., GEORGES, R. & RUTKOWSKI, L., "Cavity-enhanced frequency comb spectroscopy in a supersonic jet", *Conference on Lasers and Electro-Optics/Europe and European Quantum Electronics Conference*, Munich, Germany, 2023b, paper ed_2_3, URL : https://hal.science/hal-04246135.

DUDÁS, E., VISPOEL, B., GAMACHE, R. R., REY, M., TYUTEREV, V. G., NIKITIN, A. V., KASSI, S., SUAS-DAVID, N. & GEORGES, R., "Non-LTE spectroscopy of the tetradecad region of methane recorded in a hypersonic flow", *Icarus* **394** (2023), p. 115421, DOI : 10.1016/j.icarus.2022.115421.

DUVAL, S., BERNIER, M., FORTIN, V., GENEST, J., PICHÉ, M. & VALLÉE, R., "Femtosecond fiber lasers reach the mid-infrared", *Optica* **2** (2015), p. 623-626, DOI : 10.1364/OPTICA.2.000623.

ENGELN, R. & MEIJER, G., "A Fourier transform cavity ring down spectrometer", *Review of Scientific Instruments* **67** (1996), p. 2708-2713, DOI : 10.1063/1.1147092.

ERNY, C., MOUTZOURIS, K., BIEGERT, J., KÜHLKE, D., ADLER, F., LEITENSTORFER, A. & KELLER, U., "Mid-infrared difference-frequency generation of ultrashort pulses tunable between 3.2 and 4.8 μm from a compact fiber source", *Opt. Lett.* **32** (2007), p. 1138-1140, DOI : 10.1364/OL.32.001138.

FLEISHER, A. J., BJORK, B. J., BUI, T. Q., COSSEL, K. C., OKUMURA, M. & YE, J., "Mid-Infrared Time-Resolved Frequency Comb Spectroscopy of Transient Free Radicals", *The Journal of Physical Chemistry Letters* **5** (2014), p. 2241-2246, DOI : 10.1021/jz5008559.

FOLTYNOWICZ, A., BAN, T., MASŁOWSKI, P., ADLER, F. & YE, J., "Quantum-Noise-Limited Optical Frequency Comb Spectroscopy", *Phys. Rev. Lett.* **107** (2011), p. 233002, DOI : 10.1103/PhysRevLett.107.233002.

FOLTYNOWICZ, A., MASŁOWSKI, P., FLEISHER, A. J., BJORK, B. J. & YE, J., "Cavity-enhanced optical frequency comb spectroscopy in the mid-infrared application to trace detection of hydrogen peroxide", *Applied Physics B* **110** (2013), p. 163-175, DOI : 10.1007/s00340-012-5024-7.

FOLTYNOWICZ, A., RUTKOWSKI, L., SILANDER, I., JOHANSSON, A. C., SILVA DE OLIVEIRA, V., AXNER, O., SOBO Ń, G., MARTYNKIEN, T., MERGO, P. & LEHMANN, K. K., "Sub-

Doppler Double-Resonance Spectroscopy of Methane Using a Frequency Comb Probe", *Phys. Rev. Lett.* **126** (2021), p. 063001, DOI : 10.1103/PhysRevLett.126.063001.

FORTIER, T. & BAUMANN, E., "20 years of developments in optical frequency comb technology and applications", *Communications Physics* **2** (2019), p. 153, DOI : 10.1038/s42005-019-0249-y.

FRANQUET, E., PERRIER, V., GIBOUT, S. & BRUEL, P., "Free underexpanded jets in a quiescent medium : A review", *Progress in Aerospace Sciences* **77** (2015), p. 25-53, DOI : 10.1016/j.paerosci.2015.06.006.

GAMBETTA, A., RAMPONI, R. & MARANGONI, M., "Mid-infrared optical combs from a compact amplified Er-doped fiber oscillator", *Opt. Lett.* **33** (2008), p. 2671-2673, DOI : 10.1364/OL.33.002671.

GEORGES, R., DUDÁS, E., SUAS-DAVID, N. & RUTKOWSKI, L., "Infrared Absorption Spectroscopy in Laval Nozzle Supersonic Flows", *Uniform Supersonic Flows in Chemical Physics*, 2022, chap. 9, p. 479-538, DOI : 10.1142/9781800610996_0009.

GHERMAN, T. & ROMANINI, D., "Mode–locked cavity–enhanced absorption spectroscopy", *Opt. Express* **10** (2002), p. 1033-1042, DOI : 10.1364/OE.10.001033.

GIANFRANI, L., FOX, R. W. & HOLLBERG, L., "Cavity-enhanced absorption spectroscopy of molecular oxygen", *J. Opt. Soc. Am. B* **16** (1999), p. 2247-2254, DOI : 10.1364/JOSAB.16.002247.

GOHLE, C., STEIN, B., SCHLIESSER, A., UDEM, T. & HÄNSCH, T. W., "Frequency Comb Vernier Spectroscopy for Broadband, High-Resolution, High-Sensitivity Absorption and Dispersion Spectra", *Phys. Rev. Lett.* **99** (2007), p. 263902, DOI : 10.1103/PhysRevLett.99.263902.

GORDON, I. *et al.*, "The HITRAN2020 molecular spectroscopic database", *Journal of Quantitative Spectroscopy and Radiative Transfer* **277** (2022), p. 107949, DOI : 10.1016/j.jqsrt.2021.107949.

GOTTI, R., PUPPE, T., MAYZLIN, Y., ROBINSON-TAIT, J., WÓJTEWICZ, S., GATTI, D., ALSAIF, B., LAMPERTI, M., LAPORTA, P., ROHDE, F., WILK, R., LEISCHING, P., KAENDERS, W. G. & MARANGONI, M., "Comb-locked frequency-swept synthesizer for high precision broadband spectroscopy", *Scientific Reports* **10** (2020), DOI : 10.1038/s41598-020-59398-1.

GRIFFITHS, P., DE HASETH, J. & WINEFORDNER, J., *Fourier Transform Infrared Spectrometry*, Chemical Analysis : A Series of Monographs on Analytical Chemistry and

Its Applications, Wiley, 2007, ISBN : 9780470106297, URL : https://books.google.fr/books?id=C_c0GVe8MX0C.

Griffiths, P. R., *Fourier transform infrared spectrometry*, New York : Wiley, 1986.

Grilli, R., Méjean, G., Abd Alrahman, C., Ventrillard, I., Kassi, S. & Romanini, D., "Cavity-enhanced multiplexed comb spectroscopy down to the photon shot noise", *Phys. Rev. A* **85** (2012), p. 051804, DOI : 10.1103/PhysRevA.85.051804.

Hall, J. L., "Nobel Lecture : Defining and measuring optical frequencies", *Rev. Mod. Phys.* **78** (2006), p. 1279-1295, DOI : 10.1103/RevModPhys.78.1279.

Hänsch, T. W., "Nobel Lecture : Passion for precision", *Rev. Mod. Phys.* **78** (2006), p. 1297-1309, DOI : 10.1103/RevModPhys.78.1297.

Hartmann, J.-M., Boulet, C. & Robert, D., "III - Isolated Lines", *Collisional Effects on Molecular Spectra*, sous la dir. de J.-M. Hartmann, C. Boulet & D. Robert, Amsterdam : Elsevier, 2008, p. 63-145, DOI : 10.1016/B978-0-444-52017-3.00003-0.

Heckl, O. H., Bjork, B. J., Winkler, G., Changala, P. B., Spaun, B., Porat, G., Bui, T. Q., Lee, K. F., Jiang, J., Fermann, M. E., Schunemann, P. G. & Ye, J., "Three-photon absorption in optical parametric oscillators based on OP-GaAs", *Opt. Lett.* **41** (2016), p. 5405-5408, DOI : 10.1364/OL.41.005405.

Herman, M., Georges, R., Hepp, M. & Hurtmans, D., "High resolution Fourier transform spectroscopy of jet-cooled molecules", *International Reviews in Physical Chemistry* **19** (2000), p. 277-325, DOI : 10.1080/01442350050020905.

Herriott, D., Kogelnik, H. & Kompfner, R., "Off-Axis Paths in Spherical Mirror Interferometers", *Appl. Opt.* **3** (1964), p. 523-526, DOI : 10.1364/AO.3.000523.

Hjältén, A., Germann, M., Krzempek, K., Hudzikowski, A., Głuszek, A., Tomaszewska, D., Soboń, G. & Foltynowicz, A., "Optical frequency comb Fourier transform spectroscopy of 14N216O at 7.8 µm", *Journal of Quantitative Spectroscopy and Radiative Transfer* **271** (2021), p. 107734, DOI : 10.1016/j.jqsrt.2021.107734.

Hjältén, A., Foltynowicz, A. & Sadiek, I., "Line positions and intensities of the ν1 band of 12CH3I using mid-infrared optical frequency comb Fourier transform spectroscopy", *Journal of Quantitative Spectroscopy and Radiative Transfer* **306** (2023), p. 108646, DOI : 10.1016/j.jqsrt.2023.108646.

Hobbs, P. C. D., "Ultrasensitive laser measurements without tears", *Appl. Opt.* **36** (1997), p. 903-920, DOI : 10.1364/AO.36.000903.

Hoghooghi, N., Chang, P., Burch, S. E. M., Shaik, R., Lynch, P., Diddams, S. & Rieker, G. B., "Complete reactants-to-products observation of a gas-phase chemical reaction with broad, fast mid-infrared frequency combs" (2023), arXiv : 2307.07029 [physics.chem-ph].

Hollberg, L., Diddams, S., Bartels, A., Fortier, T. & Kim, K., "The measurement of optical frequencies", *Metrologia* **42** (2005), S105, doi : 10.1088/0026-1394/42/3/S12.

Hugi, A., Villares, G., Blaser, S., Liu, H. C. & Faist, J., "Mid-infrared frequency comb based on a quantum cascade laser", *Nature* **492** (2012), p. 229-233, doi : 10.1038/nature11620.

Huneycutt, A. J., Casaes, R. N., McCall, B. J., Chung, C.-Y., Lee, Y.-P. & Saykally, R. J., "Infrared Cavity Ringdown Spectroscopy of Jet-Cooled Polycyclic Aromatic Hydrocarbons", *ChemPhysChem* **5** (2004), p. 321-326, doi : 10.1002/cphc.200300776.

Iwakuni, K., Porat, G., Bui, T. Q., Bjork, B. J., Schoun, S. B., Heckl, O. H., Fermann, M. E. & Ye, J., "Phase-stabilized 100 mW frequency comb near 10 μm", *Applied Physics B* **124** (2018), p. 128, doi : 10.1007/s00340-018-6996-8.

Iwakuni, K., Bui, T. Q., Niedermeyer, J. F., Sukegawa, T. & Ye, J., "Comb-resolved spectroscopy with immersion grating in long-wave infrared", *Opt. Express* **27** (2019), p. 1911-1921, doi : 10.1364/OE.27.001911.

Johansson, A. C., Rutkowski, L., Filipsson, A., Hausmaninger, T., Zhao, G., Axner, O. & Foltynowicz, A., "Broadband calibration-free cavity-enhanced complex refractive index spectroscopy using a frequency comb", *Opt. Express* **26** (2018), p. 20633-20648, doi : 10.1364/OE.26.020633.

Jones, D. J., Diddams, S. A., Ranka, J. K., Stentz, A., Windeler, R. S., Hall, J. L. & Cundiff, S. T., "Carrier-Envelope Phase Control of Femtosecond Mode-Locked Lasers and Direct Optical Frequency Synthesis", *Science* **288** (2000), p. 635-639, doi : 10.1126/science.288.5466.635.

Joubert, P., Bonamy, J., Robert, D., Domenech, J.-L. & Bermejo, D., "A PARTIALLY CORRELATED STRONG COLLISION MODEL FOR VELOCITY- AND STATE-CHANGING COLLISIONS APPLICATION TO Ar-BROADENED HF ROVIBRATIONAL LINE SHAPE", *Journal of Quantitative Spectroscopy and Radiative Transfer* **61** (1999), p. 519-531, doi : 10.1016/S0022-4073(98)00038-7.

Jouy, P., Wolf, J. M., Bidaux, Y., Allmendinger, P., Mangold, M., Beck, M. & Faist, J., "Dual comb operation of $\lambda \sim 8.2$ µm quantum cascade laser frequency comb with 1 W optical power", *Applied Physics Letters* **111** (2017), p. 141102, DOI : 10.1063/1.4985102.

Kassi, S., Chenevier, M., Gianfrani, L., Salhi, A., Rouillard, Y., Ouvrard, A. & Romanini, D., "Looking into the volcano with a Mid-IR DFB diode laser and Cavity Enhanced Absorption Spectroscopy", *Opt. Express* **14** (2006), p. 11442-11452, DOI : 10.1364/OE.14.011442.

Kassi, S., Didriche, K., Lauzin, C., de Ghellinck d'Elseghem Vaernewijckb, X., Rizopoulos, A. & Herman, M., "Demonstration of cavity enhanced FTIR spectroscopy using a femtosecond laser absorption source", *Spectrochimica Acta Part A : Molecular and Biomolecular Spectroscopy* **75** (2010), p. 142-145, DOI : 10.1016/j.saa.2009.09.058.

Kassi, S. & Campargue, A., "Cavity ring down spectroscopy with 5 × 10–13 cm–1 sensitivity", *The Journal of Chemical Physics* **137** (2012), p. 234201, DOI : 10.1063/1.4769974.

Keller, U., "Recent developments in compact ultrafast lasers", *Nature* **424** (2003), p. 831-838, DOI : 10.1038/nature01938.

Khodabakhsh, A., Alrahman, C. A. & Foltynowicz, A., "Noise-immune cavity-enhanced optical frequency comb spectroscopy", *Opt. Lett.* **39** (2014), p. 5034-5037, DOI : 10.1364/OL.39.005034.

Khodabakhsh, A., Ramaiah-Badarla, V., Rutkowski, L., Johansson, A. C., Lee, K. F., Jiang, J., Mohr, C., Fermann, M. E. & Foltynowicz, A., "Fourier transform and Vernier spectroscopy using an optical frequency comb at 3–5.4 ; ;&#x03BC ; *Opt. Lett.* **41** (2016), p. 2541-2544, DOI : 10.1364/OL.41.002541.

Khodabakhsh, A., Rutkowski, L., Morville, J. & Foltynowicz, A., "Mid-infrared continuous-filtering Vernier spectroscopy using a doubly resonant optical parametric oscillator", *Applied Physics B* **123** (2017), p. 210, DOI : 10.1007/s00340-017-6781-0.

Kim, J. & Song, Y., "Ultralow-noise mode-locked fiber lasers and frequency combs : principles, status, and applications", *Adv. Opt. Photon.* **8** (2016), p. 465-540, DOI : 10.1364/AOP.8.000465.

Kippenberg, T. J., Holzwarth, R. & Diddams, S. A., "Microresonator-Based Optical Frequency Combs", *Science* **332** (2011), p. 555-559, DOI : 10.1126/science.1193968.

Kowligy, A. S., Timmers, H., Lind, A. J., Elu, U., Cruz, F. C., Schunemann, P. G., Biegert, J. & Diddams, S. A., "Infrared electric field sampled frequency comb spectroscopy", *Science Advances* **5** (2019), eaaw8794, DOI : 10.1126/sciadv.aaw8794.

Kowzan, G., Stec, K., Zaborowski, M., Wójtewicz, S., Cygan, A., Lisak, D., Masłowski, P. & Trawiński, R., "Line positions, pressure broadening and shift coefficients for the second overtone transitions of carbon monoxide in argon", *Journal of Quantitative Spectroscopy and Radiative Transfer* **191** (2017), p. 46-54, DOI : 10.1016/j.jqsrt.2016.12.035.

Lagarias, J. C., Reeds, J. A., Wright, M. H. & Wright, P. E., "Convergence Properties of the Nelder–Mead Simplex Method in Low Dimensions", *SIAM Journal on Optimization* **9** (1998), p. 112-147, DOI : 10.1137/S1052623496303470.

Lee, K. F., Hensley, C. J., Schunemann, P. G. & Fermann, M. E., "Midinfrared frequency comb by difference frequency of erbium and thulium fiber lasers in orientation-patterned gallium phosphide", *Opt. Express* **25** (2017), p. 17411-17416, DOI : 10.1364/OE.25.017411.

Lehmann, K. K. & Romanini, D., "The superposition principle and cavity ring-down spectroscopy", *The Journal of Chemical Physics* **105** (1996), p. 10263-10277, DOI : 10.1063/1.472955.

Leindecker, N., Marandi, A., Byer, R. L. & Vodopyanov, K. L., "Broadband degenerate OPO for mid-infrared frequency comb generation", *Opt. Express* **19** (2011), p. 6296-6302, DOI : 10.1364/OE.19.006296.

Levy, D. H., "Laser Spectroscopy of Cold Gas-Phase Molecules", *Annual Review of Physical Chemistry* **31** (1980), p. 197-225, DOI : 10.1146/annurev.pc.31.100180.001213.

Liao, R., Tian, H., Liu, W., Li, R., Song, Y. & Hu, M., "Dual-comb generation from a single laser source : principles and spectroscopic applications towards mid-IR—A review", *Journal of Physics : Photonics* **2** (2020), p. 042006, DOI : 10.1088/2515-7647/aba66e.

Lisak, D., Charczun, D., Nishiyama, A., Voumard, T., Wildi, T., Kowzan, G., Brasch, V., Herr, T., Fleisher, A. J., Hodges, J. T., Ciuryło, R., Cygan, A. & Masłowski, P., "Dual-comb cavity ring-down spectroscopy", *Scientific Reports* **12** (2022), p. 2377, DOI : 10.1038/s41598-022-05926-0.

Long, D. A., Cygan, A., van Zee, R. D., Okumura, M., Miller, C. E., Lisak, D. & Hodges, J. T., "Frequency-stabilized cavity ring-down spectroscopy", *Chemical Physics Letters* **536** (2012), p. 1-8, DOI : 10.1016/j.cplett.2012.03.035.

Long, D. A., Truong, G.-W., Zee, R., Plusquellic, D. & Hodges, J., "Frequency-agile, rapid scanning spectroscopy : Absorption sensitivity of 2 × 10-12 cm-1 Hz-1/2 with a tunable diode laser", *Applied Physics B* **114** (2014), p. 489-495, doi : 10.1007/s00340-013-5548-5.

Long, D. A., Wójtewicz, S., Miller, C. E. & Hodges, J. T., "Frequency-agile, rapid scanning cavity ring-down spectroscopy (FARS-CRDS) measurements of the (30012)←(00001) near-infrared carbon dioxide band", *Journal of Quantitative Spectroscopy and Radiative Transfer* **161** (2015), p. 35-40, doi : 10.1016/j.jqsrt.2015.03.031.

Long, D. A., Fleisher, A. J., Liu, Q. & Hodges, J. T., "Ultra-sensitive cavity ring-down spectroscopy in the mid-infrared spectral region", *Opt. Lett.* **41** (2016), p. 1612-1615, doi : 10.1364/OL.41.001612.

Lovejoy, C. M. & Nesbitt, D. J., "High sensitivity, high-resolution IR laser spectroscopy in slit supersonic jets : Application to N2HF ν_1 and ν_5+ν_1-ν_5", *The Journal of Chemical Physics* **86** (1987), p. 3151-3165, doi : 10.1063/1.452026.

Maddaloni, P., Bellini, M., Natale, D. & P., *Laser-Based Measurements for Time and Frequency Domain Applications : A Handbook (1st ed.)* CRC Press, 2013.

Mandon, J., Guelachvili, G., Picqué, N., Druon, F. & Georges, P., "Femtosecond laser Fourier transform absorption spectroscopy", *Opt. Lett.* **32** (2007), p. 1677-1679, doi : 10.1364/OL.32.001677.

Mandon, J., Guelachvili, G. & Picqué, N., "Fourier transform spectroscopy with a laser frequency comb", *Nature Photonics* **3** (2009), p. 99-102, doi : 10.1038/nphoton.2008.293.

Maslowski, P., Lee, K. F., Johansson, A. C., Khodabakhsh, A., Kowzan, G., Rutkowski, L., Mills, A. A., Mohr, C., Jiang, J., Fermann, M. E. & Foltynowicz, A., "Surpassing the path-limited resolution of Fourier-transform spectrometry with frequency combs", *Phys. Rev. A* **93** (2016), p. 021802, doi : 10.1103/PhysRevA.93.021802.

McClelland, G. M., Saenger, K. L., Valentini, J. J. & Herschbach, D. R., "Vibrational and rotational relaxation of iodine in seeded supersonic beams", *The Journal of Physical Chemistry* **83** (1979), p. 947-959, doi : 10.1021/j100471a014.

Messer, J. K. & De Lucia, F. C., "Measurement of Pressure-Broadening Parameters for the CO-He System at 4 K", *Phys. Rev. Lett.* **53** (1984), p. 2555-2558, doi : 10.1103/PhysRevLett.53.2555.

Minoshima, K. & Matsumoto, H., "High-accuracy measurement of 240-m distance in an optical tunnel by use of a compact femtosecond laser", *Appl. Opt.* **39** (2000), p. 5512-5517, doi : 10.1364/AO.39.005512.

Moudens, A., Georges, R., Goubet, M., Makarewicz, J., Lokshtanov, S. E. & Vigasin, A. A., "Direct absorption spectroscopy of water clusters formed in a continuous slit nozzle expansion", *The Journal of Chemical Physics* **131** (2009), p. 204312, doi : 10.1063/1.3264576.

Murphy, M. T., Udem, T., Holzwarth, R., Sizmann, A., Pasquini, L., Araujo-Hauck, C., Dekker, H., D'Odorico, S., Fischer, M., Hänsch, T. W. & Manescau, A., "High-precision wavelength calibration of astronomical spectrographs with laser frequency combs", *Monthly Notices of the Royal Astronomical Society* **380** (2007), p. 839-847, doi : 10.1111/j.1365-2966.2007.12147.x.

Ngo, N., Lisak, D., Tran, H. & Hartmann, J.-M., "An isolated line-shape model to go beyond the Voigt profile in spectroscopic databases and radiative transfer codes", *Journal of Quantitative Spectroscopy and Radiative Transfer* **129** (2013), p. 89-100, doi : 10.1016/j.jqsrt.2013.05.034.

Nugent-Glandorf, L., Neely, T., Adler, F., Fleisher, A. J., Cossel, K. C., Bjork, B., Dinneen, T., Ye, J. & Diddams, S. A., "Mid-infrared virtually imaged phased array spectrometer for rapid and broadband trace gas detection", *Opt. Lett.* **37** (2012), p. 3285-3287, doi : 10.1364/OL.37.003285.

O'Keefe, A. & Deacon, D. A. G., "Cavity ring-down optical spectrometer for absorption measurements using pulsed laser sources", *Review of Scientific Instruments* **59** (1988), p. 2544-2551, doi : 10.1063/1.1139895.

Paldus, B. A., Harb, C. C., Spence, T. G., Zare, R. N., Gmachl, C., Capasso, F., Sivco, D. L., Baillargeon, J. N., Hutchinson, A. L. & Cho, A. Y., "Cavity ring-down spectroscopy using mid-infrared quantum-cascade lasers", *Opt. Lett.* **25** (2000), p. 666-668, doi : 10.1364/OL.25.000666.

Patterson, D., Tsikata, E. & Doyle, J. M., "Cooling and collisions of large gas phase molecules", *Physical Chemistry Chemical Physics* **12** (2010), p. 9736-9741, doi : 10.1039/C002764B.

Patterson, D. & Doyle, J. M., "Cooling molecules in a cell for FTMW spectroscopy", *Molecular Physics* **110** (2012), p. 1757-1766, doi : 10.1080/00268976.2012.679632.

Picqué, N. & Hänsch, T. W., "Frequency comb spectroscopy", *Nature Photonics* **13** (2019), p. 146-157, doi : 10.1038/s41566-018-0347-5.

Pirali, O., Goubet, M., Huet, T. R., Georges, R., Soulard, P., Asselin, P., Courbe, J., Roy, P. & Vervloet, M., "The far infrared spectrum of naphthalene characterized by high resolution synchrotron FTIR spectroscopy and anharmonic DFT calculations", *Phys. Chem. Chem. Phys.* **15** (2013), p. 10141-10150, DOI : 10.1039/C3CP44305A.

Potma, E. O., Jones, D. J., Cheng, J.-X., Xie, X. S. & Ye, J., "High-sensitivity coherent anti-Stokes Raman scattering microscopy with two tightly synchronized picosecond lasers", *Opt. Lett.* **27** (2002), p. 1168-1170, DOI : 10.1364/OL.27.001168.

Putignano, M. & Welsch, C., "Numerical study on the generation of a planar supersonic gas-jet", *Nuclear Instruments and Methods in Physics Research Section A : Accelerators, Spectrometers, Detectors and Associated Equipment* **667** (2012), p. 44-52, DOI : 10.1016/j.nima.2011.11.054.

Raju, C. & Kurian, J., "Effect of slit aspect ratio on free jet properties", *Vacuum* **46** (1995), p. 389-395, DOI : 10.1016/0042-207X(94)00085-9.

Reber, M. A. R., Chen, Y. & Allison, T. K., "Cavity-enhanced ultrafast spectroscopy : ultrafast meets ultrasensitive", *Optica* **3** (2016), p. 311-317, DOI : 10.1364/OPTICA.3.000311.

Reichert, J., Holzwarth, R., Udem, T. & Hänsch, T., "Measuring the frequency of light with mode-locked lasers", *Optics Communications* **172** (1999), p. 59-68, DOI : 10.1016/S0030-4018(99)00491-5.

Roberts, F. C., Lewandowski, H. J., Hobson, B. F. & Lehman, J. H., "A rapid, spatially dispersive frequency comb spectrograph aimed at gas phase chemical reaction kinetics", *Molecular Physics* **118** (2020), e1733116, DOI : 10.1080/00268976.2020.1733116.

Rohart, F., Ellendt, A., Kaghat, F. & Mäder, H., "Self and Polar Foreign Gas Line Broadening and Frequency Shifting of CH3F : Effect of the Speed Dependence Observed by Millimeter-Wave Coherent Transients", *Journal of Molecular Spectroscopy* **185** (1997), p. 222-233, DOI : 10.1006/jmsp.1997.7395.

Romanini, D., Kachanov, A., Sadeghi, N. & Stoeckel, F., "CW cavity ring down spectroscopy", *Chemical Physics Letters* **264** (1997), p. 316-322, DOI : 10.1016/S0009-2614(96)01351-6.

Rowe, B. R. & Canosa, A., "Gas Phase Reaction Kinetics at Low and Very Low Temperatures : Fundamentals and Contexts", *Uniform Supersonic Flows in Chemical Physics*, 2022, chap. 1, p. 1-61, DOI : 10.1142/9781800610996_0001.

Roy, J., Deschênes, J.-D., Potvin, S. & Genest, J., "Continuous real-time correction and averaging for frequency comb interferometry", *Opt. Express* **20** (2012), p. 21932-21939, doi : 10.1364/OE.20.021932.

Rutkowski, L. & Morville, J., "Broadband cavity-enhanced molecular spectra from Vernier filtering of a complete frequency comb", *Opt. Lett.* **39** (2014), p. 6664-6667, doi : 10.1364/OL.39.006664.

Rutkowski, L. & Morville, J., "Continuous Vernier filtering of an optical frequency comb for broadband cavity-enhanced molecular spectroscopy", *Journal of Quantitative Spectroscopy and Radiative Transfer* **187** (2017), p. 204-214, doi : 10.1016/j.jqsrt.2016.09.021.

Rutkowski, L., Masłowski, P., Johansson, A. C., Khodabakhsh, A. & Foltynowicz, A., "Optical frequency comb Fourier transform spectroscopy with sub-nominal resolution and precision beyond the Voigt profile", *Journal of Quantitative Spectroscopy and Radiative Transfer* **204** (2018), p. 63-73, doi : 10.1016/j.jqsrt.2017.09.001.

Sadiek, I., Hjältén, A., Senna Vieira, F., Lu, C., Stuhr, M. & Foltynowicz, A., "Line positions and intensities of the ν4 band of methyl iodide using mid-infrared optical frequency comb Fourier transform spectroscopy", *Journal of Quantitative Spectroscopy and Radiative Transfer* **255** (2020), p. 107263, doi : 10.1016/j.jqsrt.2020.107263.

Sadiek, I., Hjältén, A., Roberts, F. C., Lehman, J. H. & Foltynowicz, A., "Optical frequency comb-based measurements and the revisited assignment of high-resolution spectra of CH2Br2 in the 2960 to 3120 cm–1 region", *Phys. Chem. Chem. Phys.* **25** (2023), p. 8743-8754, doi : 10.1039/D2CP05881B.

Scherer, J. J., "Ringdown spectral photography", *Chemical Physics Letters* **292** (1998), p. 143-153, doi : 10.1016/S0009-2614(98)00653-8.

Scherer, J. J., Paul, J. B., Jiao, H. & O'Keefe, A., "Broadband ringdown spectral photography", *Appl. Opt.* **40** (2001), p. 6725-6732, doi : 10.1364/AO.40.006725.

Schibli, T. R., Minoshima, K., Hong, F.-L., Inaba, H., Onae, A., Matsumoto, H., Hartl, I. & Fermann, M. E., "Frequency metrology with a turnkey all-fiber system", *Opt. Lett.* **29** (2004), p. 2467-2469, doi : 10.1364/OL.29.002467.

Schiller, S., "Spectrometry with frequency combs", *Opt. Lett.* **27** (2002), p. 766-768, doi : 10.1364/OL.27.000766.

Schreier, F., "The Voigt and complex error function : A comparison of computational methods", *Journal of Quantitative Spectroscopy and Radiative Transfer* **48** (1992),

Special Issue Conference on Molecular Spectroscopic Databases, p. 743-762, DOI : 10.1016/0022-4073(92)90139-U.

SHIRASAKI, M., "Large angular dispersion by a virtually imaged phased array and its application to a wavelength demultiplexer", *Opt. Lett.* **21** (1996), p. 366-368, DOI : 10.1364/OL.21.000366.

SMITH, G. D. & PALMER, R. A., "Fast Time-Resolved Mid-Infrared Spectroscopy Using an Interferometer", *Handbook of Vibrational Spectroscopy*, John Wiley & Sons, Ltd, 2006, DOI : 10.1002/0470027320.s0217.

SMITH, I. W. M. & ROWE, B. R., "Reaction Kinetics at Very Low Temperatures : Laboratory Studies and Interstellar Chemistry", *Accounts of Chemical Research* **33** (2000), PMID : 10813870, p. 261-268, DOI : 10.1021/ar990099i.

SNAVELY, D. L., COLSON, S. D. & WIBERG, K. B., "Rotational cooling in a supersonic expansion of ammonia", *The Journal of Chemical Physics* **74** (1981), p. 6975-6976, DOI : 10.1063/1.441062.

SNAVELY, D. L., WIBERG, K. B. & COLSON, S. D., "The infrared absorption spectrum of a supersonic expansion of methyl chloride", *Chemical Physics Letters* **96** (1983), p. 319-323, DOI : 10.1016/0009-2614(83)80681-2.

SOBOŃ, G., MARTYNKIEN, T., MERGO, P., RUTKOWSKI, L. & FOLTYNOWICZ, A., "High-power frequency comb source tunable from 2.7 to 4.2 μm based on difference frequency generation pumped by an Yb-doped fiber laser", *Opt. Lett.* **42** (2017), p. 1748-1751, DOI : 10.1364/OL.42.001748.

SOTOR, J., MARTYNKIEN, T., SCHUNEMANN, P. G., MERGO, P., RUTKOWSKI, L. & SOBOŃ, G., "All-fiber mid-infrared source tunable from 6 to 9 μm based on difference frequency generation in OP-GaP crystal", *Opt. Express* **26** (2018), p. 11756-11763, DOI : 10.1364/OE.26.011756.

SPAUN, B., CHANGALA, P. B., PATTERSON, D., BJORK, B. J., HECKL, O. H., DOYLE, J. M. & YE, J., "Continuous probing of cold complex molecules with infrared frequency comb spectroscopy", *Nature* **533** (2016), p. 517-520, DOI : 10.1038/nature17440.

STEINLE, T., MÖRZ, F., STEINMANN, A. & GIESSEN, H., "Ultra-stable high average power femtosecond laser system tunable from 1.33 to 20 μm", *Opt. Lett.* **41** (2016), p. 4863-4866, DOI : 10.1364/OL.41.004863.

STERCZEWSKI, L. A., WESTBERG, J., PATRICK, C. L., KIM, C. S., KIM, M., CANEDY, C. L., BEWLEY, W. W., MERRITT, C. D., VURGAFTMAN, I., MEYER, J. R. & WYSOCKI,

G., “Multiheterodyne spectroscopy using interband cascade lasers”, *Optical Engineering* **57** (2017), p. 011014, DOI : 10.1117/1.OE.57.1.011014.

Suas-David, N., Kulkarni, V., Benidar, A., Kassi, S. & Georges, R., “Line shape in a free-jet hypersonic expansion investigated by cavity ring-down spectroscopy and computational fluid dynamics”, *Chemical Physics Letters* **659** (2016), p. 209-215, DOI : 10.1016/j.cplett.2016.06.082.

Sugiyama, Y., Kashimura, T., Kashimoto, K., Akamatsu, D. & Hong, F.-L., “Precision dual-comb spectroscopy using wavelength-converted frequency combs with low repetition rates”, *Scientific Reports* **13** (2023), p. 2549, DOI : 10.1038/s41598-023-29734-2.

Telle, H. R., Steinmeyer, G., Dunlop, A. E., Stenger, J., Sutter, D. H. & Keller, U., “Carrier-envelope offset phase control : A novel concept for absolute optical frequency measurement and ultrashort pulse generation”, *Applied Physics B* **69** (1999), p. 327-332, DOI : 10.1007/s003400050813.

Tennyson, J., Bernath, P. F., Campargue, A., Császár, A. G., Daumont, L., Gamache, R. R., Hodges, J. T., Lisak, D., Naumenko, O. V., Rothman, L. S., Tran, H., Zobov, N. F., Buldyreva, J., Boone, C. D., Vizia, M. D. D., Gianfrani, L., Hartmann, J.-M., McPheat, R., Weidmann, D., Murray, J., Ngo, N. H. & Polyansky, O. L., “Recommended isolated-line profile for representing high-resolution spectroscopic transitions (IUPAC Technical Report)”, *Pure and Applied Chemistry* **86** (2014), p. 1931-1943, DOI : doi:10.1515/pac-2014-0208.

Teshima, K., “Two-dimensional focusing of a supersonic free jet by a rectangular orifice”, *The Physics of Fluids* **30** (1987), p. 1899-1901, DOI : 10.1063/1.866516.

Thorpe, M. J., Moll, K. D., Jones, R. J., Safdi, B. & Ye, J., “Broadband Cavity Ringdown Spectroscopy for Sensitive and Rapid Molecular Detection”, *Science* **311** (2006), p. 1595-1599, DOI : 10.1126/science.1123921.

Thorpe, M. J. & Ye, J., “Cavity-enhanced direct frequency comb spectroscopy”, *Applied Physics B* **91** (2008), p. 397-414, DOI : 10.1007/s00340-008-3019-1.

Thorpe, M. J., Adler, F., Cossel, K. C., de Miranda, M. H. & Ye, J., “Tomography of a supersonically cooled molecular jet using cavity-enhanced direct frequency comb spectroscopy”, *Chemical Physics Letters* **468** (2009), p. 1-8, DOI : 10.1016/j.cplett.2008.11.064.

Tillman, K. A., Maier, R. R. J., Reid, D. T. & McNaghten, E. D., “Mid-infrared absorption spectroscopy of methane using a broadband femtosecond optical parametric

oscillator based on aperiodically poled lithium niobate", *Journal of Optics A : Pure and Applied Optics* **7** (2005), S408, DOI : 10.1088/1464-4258/7/6/023.

TRAN, H., NGO, N. & HARTMANN, J.-M., "Efficient computation of some speed-dependent isolated line profiles", *Journal of Quantitative Spectroscopy and Radiative Transfer* **129** (2013), p. 199-203, DOI : 10.1016/j.jqsrt.2013.06.015.

TRUONG, G.-W., DOUGLASS, K., MAXWELL, S., ZEE, R., PLUSQUELLIC, D., HODGES, J. & LONG, D. A., "Frequency-agile, rapid scanning spectroscopy", *Nature Photonics* **7** (2013), p. 532-534, DOI : 10.1038/nphoton.2013.98.

UDEM, T., REICHERT, J., HOLZWARTH, R. & HÄNSCH, T. W., "Absolute Optical Frequency Measurement of the Cesium D_1 Line with a Mode-Locked Laser", *Phys. Rev. Lett.* **82** (1999a), p. 3568-3571, DOI : 10.1103/PhysRevLett.82.3568.

UDEM, T., REICHERT, J., HOLZWARTH, R. & HÄNSCH, T. W., "Accurate measurement of large optical frequency differences with a mode-locked laser", *Opt. Lett.* **24** (1999b), p. 881-883, DOI : 10.1364/OL.24.000881.

UDEM, T., HOLZWARTH, R. & HÄNSCH, T. W., "Optical frequency metrology", *Nature* **416** (2002), p. 233-237, DOI : 10.1038/416233a.

VEEKEN, K. & REUSS, J., "Infrared line narrowing and cluster absorption in a planar jet", *Applied Physics B* **38** (1985), p. 117-124, DOI : 10.1007/BF00697450.

WALLRAFF, P., YAMADA, K. & WINNEWISSER, G., "Determination of the vibrational temperature of OCS in a supersonic free jet", *Journal of Molecular Spectroscopy* **126** (1987), p. 78-81, DOI : 10.1016/0022-2852(87)90078-6.

WEICHMAN, M. L., CHANGALA, P. B., YE, J., CHEN, Z., YAN, M. & PICQUÉ, N., "Broadband molecular spectroscopy with optical frequency combs", *Journal of Molecular Spectroscopy* **355** (2019), p. 66-78, DOI : 10.1016/j.jms.2018.11.011.

WHITE, J. U., "Long Optical Paths of Large Aperture", *J. Opt. Soc. Am.* **32** (1942), p. 285-288, DOI : 10.1364/JOSA.32.000285.

X. DE GHELLINCK D'ELSEGHEM VAERNEWIJCK, D. G. & HERMAN, M., "Femto-Fourier transform-cavity enhanced absorption spectroscopy in a supersonic expansion", *Molecular Physics* **110** (2012), p. 2735-2741, DOI : 10.1080/00268976.2012.701342.

XIAO, S. & WEINER, A. M., "2-D wavelength demultiplexer with potential for $\geq$ 1000 channels in the C-band", *Opt. Express* **12** (2004), p. 2895-2902, DOI : 10.1364/OPEX.12.002895.

YE, J., MA, L. S. & HALL, J. L., "Molecular Iodine Clock", *Phys. Rev. Lett.* **87** (2001), p. 270801, DOI : 10.1103/PhysRevLett.87.270801.

Yu, M., Okawachi, Y., Griffith, A. G., Lipson, M. & Gaeta, A. L., "Mode-locked mid-infrared frequency combs in a silicon microresonator", *Optica* **3** (2016), p. 854-860, doi : 10.1364/OPTICA.3.000854.

COLLEGE SCIENCES DE LA MATIERE
DOCTORAL DES MOLECULES
BRETAGNE ET MATERIAUX

Université de Rennes

Titre : Développement d'un spectromètre à transformée de Fourier en cavité par peigne de fréquences optiques pour l'astrophysique de laboratoire

Mot-clés : peignes de fréquences optiques ; cavités optiques ; spectroscopie par transformée de Fourier ; astrophysique de laboratoire.

Résumé : Cette thèse s'inscrit dans le contexte des expériences d'astrophysique de laboratoire menées à l'Institut de Physique de Rennes, qui tentent de reproduire les conditions de basses températures (∼10-50 K) du milieu interstellaire, afin de réaliser des mesures de cinétique réactionnelle avec des molécules d'intérêt pour l'astrochimie. L'objectif de cette thèse est le développement d'un spectromètre d'absorption infrarouge résolu en temps, pour sonder les écoulements supersoniques uniformes utilisés pour refroidir les molécules en phase gazeuse. Le spectromètre est basé sur un peigne de fréquences optiques, qui présente des dizaines de milliers de modes laser équidistants dans le domaine des fréquences, fournissant une large couverture spectrale, une haute résolution et une haute sensibilité, et permettant ainsi de détecter plusieurs espèces moléculaires simultanément. Pour augmenter encore la sensibilité de détection, le peigne de fréquences est couplé à une cavité optique. La détection à large bande de la lumière laser est réalisée avec un spectromètre à transformée de Fourier, qui peut opérer de manière résolue en temps, et est appliqué à une nouvelle approche de la spectroscopie de temps de déclin de cavité large bande avec un peigne de fréquences. La première démonstration d'un jet supersonique continu sondé par spectroscopie à transformée de Fourier basée sur un peigne de fréquences couplé à une cavité optique est également présentée.

Title: Development of a cavity-enhanced Fourier transform spectrometer based on optical frequency combs for laboratory astrophysics

Keywords: optical frequency combs; optical cavities; Fourier transform spectroscopy; laboratory astrophysics.

Abstract: This thesis is set in the context of the laboratory astrophysics experiments conducted at the Institute of Physics of Rennes, which try to reproduce the low temperature conditions (∼10-50 K) of the interstellar medium, to perform reaction kinetics measurements on molecules of interest to astrochemistry. The aim of this thesis was the development of a time-resolved infrared absorption spectrometer, to probe the uniform supersonic flows used to cool down molecules in the gas phase. The spectrometer is based on an optical frequency comb, which displays tens of thousands of equidistant laser modes in the frequency domain, providing a broad spectral coverage, high resolution and high sensitivity, and allowing to monitor several molecular species simultaneously. To further increase detection sensitivity, the frequency comb is coupled to an optical enhancement cavity. The broadband detection of the laser light is performed with a Fourier transform spectrometer, which can be operated in a time-resolved fashion, and applied to a new approach to broadband cavity ringdown spectroscopy with a frequency comb. The first demonstration of a continuous supersonic jet probed by cavity-enhanced Fourier transform spectroscopy based on a frequency comb is also presented.